Searching for New (Dark and Colourful) Sectors at Colliders and Beyond

Dissertation submitted for the award of the title
"Doctor of Natural Sciences"
to the Faculty of Physics, Mathematics and Computer Science of
Johannes Gutenberg University Mainz in Mainz

Christiane Scherb
born in Lörrach, Germany

Mainz, July 12, 2022

JOHANNES GUTENBERG UNIVERSITÄT MAINZ

JG|U

Date of submission: 12.07.2022
Date of defense: 05.10.2022

For my family
we all know without you I wouldn't be where I am today

"I almost wish I hadn't gone down that rabbit-hole-
and yet—and yet—it's rather curious, you know, this sort of life!"

Lewis Carroll, Alice's Adventures in Wonderland

"What we have learned is like a handful of earth;
What we have yet to learn is like the whole world."

Avvaiyar, a 4th century Tamil poet from India

"Walking through darkness with thoughts full of colors."

Prajakta Mhadnak

Abstract

While the Standard Model of particle physics has been confirmed by a variety of measurements and discoveries, there are also observations and considerations that clearly point towards physics beyond the Standard Model. Two of these so far unresolved mysteries are the origin and nature of dark matter and the source of additional CP violation needed for the baryon asymmetry of the universe. In this dissertation the phenomenology of new physics models suggesting solutions for these two questions is studied. Thereby, the focus is on collider probes of the models.

First, two realizations of a t-channel dark sector model are studied. In these the dark sector fields interact with either the right-handed down-type or the up-type quarks via a heavy mediator. In the former case mediator pair production with decays to visible and dark jets is investigated and combined with non-collider probes from flavour and cosmology. The whole range of dark pion lifetimes is considered for a scenario where the dark pion lifetimes are degenerate and for scenarios with two distinguished dark pion lifetimes. Afterwards, for the case where the dark sector couples to up-type quarks via the mediator, the phenomenology of single dark pions is considered exclusively. Single dark pions are, hereby, treated as axion-like particles. The parameter space is studied in detail, including experimental bounds from astrophysics, cosmology and flavour processes, as well as the discovery prospects at fixed target experiments and LHC forward detectors. The combination of these search strategies covers a wide range of axion-like particle masses. Nonetheless, for masses above the charm threshold the parameter space is largely unconstrained. Therefore, a new search strategy for axion-like particles with masses $m_a \sim 1 - 10$ GeV is proposed. The proposed strategy searches for axion-like particles in flavour violating top decays and takes advantage of the fact that the considered axion-like particles can be long-lived and, since they are neutral, leave no tracks in the detector before they decay. Compared to searches for flavour violating top couplings in single top plus missing energy and single top plus jets processes the proposed search strategy can probe approximately two orders of magnitude lower branching ratios $\mathrm{Br}(t \to aq)$, where q is an up or charm quark and a the axion-like particle, in the millimeter to meter lifetime range.

Then, the focus moves to the Two-Higgs-Doublet model which is a minimal model introducing an additional source of CP violation in the scalar sector. After evaluating the constraints on the parameter space three methods to test the CP violation of the model at HL-LHC are investigated. More specifically, the prospect to discover heavy scalars H_i, that are admixtures of CP-even and CP-odd final states, using the angular correlation of the tau decay planes in the process $H_i \to \tau^-\tau^+$, the correlation of final state muons in the process $H_i \to ZZ \to \mu^-\mu^+\mu^-\mu^+$ and the invariant mass spectrum of the latter process is studied and compared.

List of Publications

This thesis is based on the publications and preprints [1–5] listed below. A brief summary of each is provided and the author's contributions highlighted. The additional publications [6–8], to which the work of [1–5] contributed, as well as the previous publication [9] are listed afterwards.

[1] S. Antusch, O. Fischer, A. Hammad and C. Scherb, *Testing CP Properties of Extra Higgs States at the HL-LHC*, JHEP **03** (2021) 200 [2011.10388]

The possibility to discover CP violation in the scalar sector is investigated for the Two-Higgs-Doublet model type-I. The currently allowed parameter space is discussed and for a viable benchmark point the possibility to test the CP properties of the additional neutral Higgs bosons is explored for HL-LHC using the angular distributions of $H_i \to \tau^-\tau^+$ final states. The analysis is done on the reconstructed level using a Boosted Decision Tree for background suppression and a shape analysis to test the CP properties.
This publication forms the basis for the second part of this thesis. Correspondingly, the majority of Chapter VI and Sections VII.1 and VII.2 of Chapter VII are based on this work. The implementation of the model, as well as the evaluation of the parameter space points were performed by the author of this thesis. In particular, the author calculated the electron electric dipole moments and checked all points against all constraints. Scans over the parameter space and Monte Carlo simulations were performed together with a coauthor, while the Boosted Decision Tree and shape analyses were mostly done by coauthors, but cross-checked by all authors. All authors contributed to the published manuscript.

[2] H. Mies, C. Scherb and P. Schwaller, *Collider constraints on dark mediators*, JHEP **04** (2021) 049 [2011.13990]

The complete parameter space of a QCD-like dark sector coupled via a mediator to down-type quarks is explored with a combination of multi-jet, multi-jet plus missing energy and emerging jets searches. The dark sector inherits the flavour structure from QCD leading to dark pions species with various lifetimes. For both, scenarios with degenerate and non-degenerate dark pion lifetimes, the collider phenomenology is studied and combined with non-collider probes.
Based on this publication, as well as the previous studies of QCD-like dark sectors in [10–12] the considered model is introduced in Chapter III. The work of [2], then, forms the basis for Chapter IV. The Monte Carlo simulations for the analyses were performed by a coauthor and evaluated by the author and a coauthor independently. All non-collider constraints were determined by the author. The published manuscript includes contributions from all authors.

[3] A. Carmona, C. Scherb and P. Schwaller, *Charming ALPs*, JHEP **08** (2021) 121 [2101.07803]

The phenomenology of axion-like particles coupling exclusively to up-type quarks at tree-level is studied in detail. This scenario arises naturally in some well-motivated UV completions, such as QCD-like dark sectors or Froggatt-Nielsen models. The phenomenology is investigated for the low energy effective theory and includes all the existing constraints on these models. It is also demonstrated how upcoming

experiments at fixed target facilities and the LHC can probe regions of the parameter space.
This publication is the main foundation of the first part of this thesis and the basis of Chapter V. All model calculations, as well as the determination of the constraints on the parameter space were performed independently by the author and a coauthor. The prospects for fixed target experiments and LHC were determined by the author. The published manuscript was written with contributions from all authors.

[4] S. Antusch, O. Fischer, A. Hammad and C. Scherb, *Explaining excesses in four-leptons at the LHC with a double peak from a CP violating Two Higgs Doublet Model*, [2112.00921]

The Two-Higgs-Doublet model type-I is fitted to the ATLAS four-lepton invariant mass spectrum from [13]. The complementarity of the best-fit benchmark point with the CMS four-lepton data and other decay channels is discussed. This publication was submitted to JHEP and is currently under review.
The last part of the second part of this thesis, Section VII.3, is based on this publication. Again, the evaluation of possible benchmark points from parameter space scans was done by the author, while the scan itself, as well as the Monte Carlo simulations were performed together with a coauthor. The fit to the data was done by a coauthor and cross-checked by all authors. All authors contributed to the investigation of other decay channels, as well as to the manuscript.

[5] A. Carmona, F. Elahi, C. Scherb and P. Schwaller, *The ALPs from the Top: Searching for long lived axion-like particles from exotic top decays*, [2209.09371]

A novel search strategy for light particles with flavour violating couplings and intermediate lifetimes is proposed based on the ratio of energy deposited in the hadronic and electromagnetic calorimeter and the number of tracks. Already existing searches for flavour violating top decays are taken into account. This publication was submitted to and accepted by JHEP.
This publications is the foundation for the second part of Chapter V and forms the foundation of Section V.2. The recast of the already existing searches was done together with a coauthor. The author came up with the details of the new search strategy and performed the analysis thereof with advice and corrections from the coauthors. The results of the analysis were verified independently by a coauthor. The manuscript contains contributions from all authors.

If not mentioned otherwise, the figures presented in this thesis were created by the author. Figures that were produced by collaborators are indicated as such. *All names were removed from the figure credits in the electronic publication of this dissertation.* Most figures from the publications listed above that were produced by collaborators and some of the figures produced by the author herself have been recreated for this thesis to obtain a more uniform colour scheme and plot layout. All Feynman diagrams presented in this thesis were produced using `JaxoDraw` [14, 15].
The above listed publications also lead to contributions in the following publications

[6] L. A. Anchordoqui et al., *The Forward Physics Facility: Sites, Experiments, and Physics Potential*, [2109.10905]

[7] L. Feng et al., *The Forward Physics Facility at the High-Luminosity LHC*, [2203.05090]

[8] G. Albouy et al., *Theory, phenomenology, and experimental avenues for dark showers: a Snowmass 2021 report*, [2203.05093]

Moreover, the publication

[9] S. Antusch, O. Fischer, A. Hammad and C. Scherb, *Low scale type II seesaw: Present constraints and prospects for displaced vertex searches*, JHEP **02** (2019) 157 [1811.03476]

was published before the author started her PhD studies and is not included in the scope of this work.

Contents

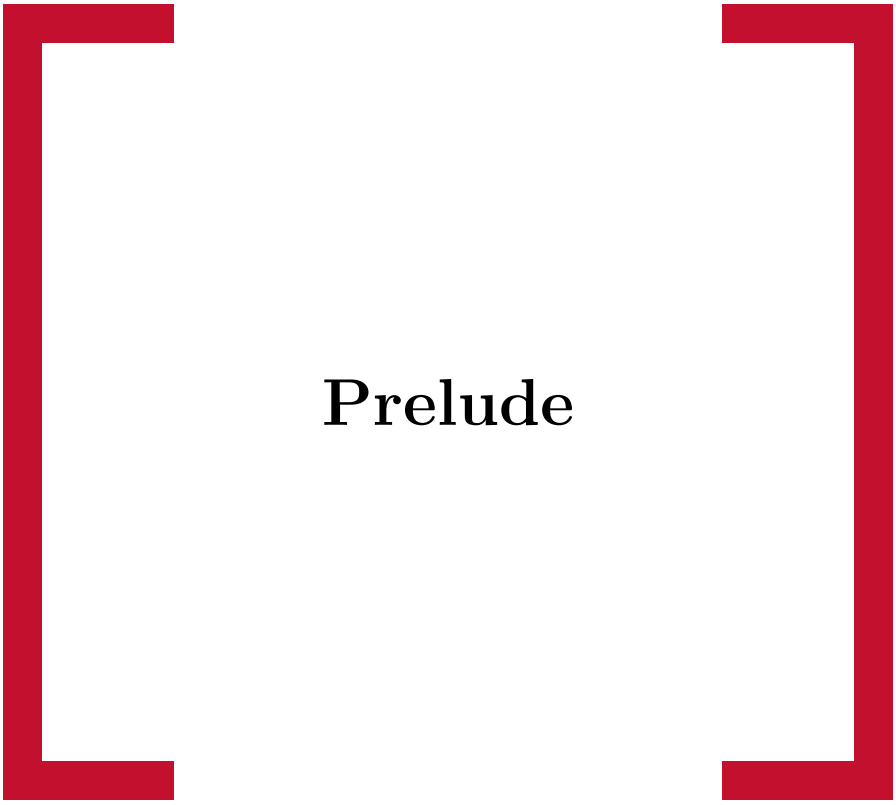

Prelude

CHAPTER I

Introduction

In 1900 Lord Kelvin defined two problems of nineteenth century physics, first, the results of the Michelson-Morley experiment and, second, the Maxwell-Boltzmann doctrine, nowadays known as the equipartition theorem, that was inconsistent with certain specific heat measurements [16]. The Michelson-Morley experiment was supposed to measure the relative velocity of the Earth in the postulated luminiferous aether, which served as an explanation how light could travel through empty space. Its results, however, showed that the movement of Earth through the hypothetical luminiferous aether did not influence the speed of light. These "clouds" as Lord Kelvin called them, could not be solved with classical physics, but only with special relativity and quantum mechanics. Indeed, general relativity and quantum mechanics form the basis of modern physics and have facilitated many advances in physics, for example the development of quantum field theory (QFT). QFT is based on the principles of relativity, quantum mechanics and the field concept. The Standard Model of particle physics (SM), which is one of the most successful theories in physics, is a quantum fields theory. It was developed in the 1960s [17–20] and describes the known elementary particles, as well as their interactions via the strong, weak and electromagnetic forces. It has been investigated with an extensive program of experiments over the past decades. The great agreement found between SM predictions and measurements confirmed its validity. One of the most prominent confirmations was the discovery of the predicted massive, neutral scalar Higgs boson [21–26] in 2012 [27, 28], which had been till then the last missing part of the SM.

Despite the many successful predictions of particles and quantities given by the SM, there are still quite a few "clouds" on the sky of particle physics, meaning that there are still several unanswered questions. They arise on one hand from theoretical - and partly philosophical - considerations, such as the strong CP (CP is the simultaneous flip of charge (C) and parity (P) of all particles in a system) problem and the hierarchy problem and, on the other hand, from experimental observations, such as anomalies in flavour processes, neutrino oscillations, the asymmetry between baryons and antibaryons or the existence of dark matter (DM) and dark energy.

To solve one or more of these problems a multitude of models that extend and/or modify the SM, so called beyond the Standard Model (BSM) models, have been proposed and studied. These new physics (NP) scenarios range from very simple models where only a single field, for example a scalar field, is added to the SM, to models where the SM is extended by complex sectors including additional symmetries and fields.

In this thesis the focus lays on the study of the phenomenology of such BSM models. The first part is dedicated to DM models, including a discussion of a rather complex extension of the SM where a dark sector mimics the structure of quantum chromodynamics (QCD) [29–34], along with a simplified version of the model featuring axion-like particles

(ALPs). In addition, another simple BSM model that only adds one scalar field with the same quantum numbers as the Higgs boson is investigated in the second part of this thesis to explore the CP properties of the scalar sector.
In all studies performed in this thesis hadron collider experiments are used as the main tool for discovering NP. Particle accelerators and colliders have always been valuable means for discovery in the history of particle physics, reaching back to the 1890s when Cathode Ray Tubes were first used by Karl Ferdinand Braun [35]. A few years later, in 1911, Rutherford shot helium nuclei on gold targets [36] leading to a new understanding of the structure of atoms. Since Rutherford's experiments particle accelerators and colliders have become larger, more refined and more powerful. With each new generation of such experiments higher energies and more precision can be reached. Over the decades several variations of collider experiments were used, varying in the mode of acceleration and the particles collided. Both, linear and circular colliders are possible where two electron beams, electron and proton, proton and antiproton or two proton or ion beams are collided. In addition, fixed target experiments where a single particle beam is accelerated and collided with a fixed target, were and are used. Indeed, some of the first larger experiments used cyclotrons, invented by Ernest Lawrence [37], to accelerate particles that were then shot at a fixed target [38]. The various experiments discovered several particles that were predicted from the SM. Examples are the weak gauge bosons W and Z, which were discovered by the CERN (European Organisation for Nuclear Research) experiments UA1 and UA2 [39–42] in 1983. Both were detectors at the antiproton-proton experiment (Sp$\bar{\text{p}}$S). A more recent example is the Higgs boson [27, 28], which was discovered by the ATLAS and CMS detectors at the Large Hadron Collider (LHC) at CERN.
Even with the great success in confirming the SM and the clear hints for BSM physics to date particle colliders have not found any clear evidence of BSM physics. NP might be too weakly coupled or occur at a too high scale to be found with collider experiments. Consequently, alternative probes, such as cosmological, astrophysical or gravitational wave probes, as well as indirect searches via, for example, precision or flavour measurements need to be considered in the search for NP. While gravitational wave probes of BSM physics are not part of this thesis, several complementary non-collider searches to find NP are explored.
This thesis is organized in the following way: First, in Chapter II the SM is reviewed briefly. This chapter also includes a discussion of several open questions in particle physics. Those questions relevant for this thesis are discussed in more detail. Then, Part I is dedicated to the exploration of the phenomenology of strongly coupled dark sectors. After a short introduction to the topic, the t-channel dark sector model which is investigated in this thesis is introduced in detail in Chapter III. Two model setups where the dark sector is coupled to down-type or up-type quarks are considered in Chapters IV and V, respectively. For the case where the dark sector is coupled to down-type quarks the focus lies on collider signatures produced in decays of the mediator that connects the dark and visible sector. They are discussed together with complementary probes, such as flavour observables, fixed target or DM direct detection experiments in Chapter IV. This is followed in Chapter V by a discussion of the phenomenology of ALPs that only couple to up-types quarks at tree-level and represent a simplified version of the considered dark sector model. ALPs can be probed over a wide range of energies with different experimental tests, which are studied in the first part of the chapter. Based on the parameter space, lifetimes and branching ratios found in the first part of Chapter V the second part of this chapter proposes a new search strategy for long-lived ALPs at the LHC. This concludes the discussion of QCD-like dark sectors.

Part II moves away from the question of the origin and nature of DM and, instead, focuses on CP violation in the scalar sector, which could be an additional source of CP violation and part of an explanation for the baryon asymmetry of the universe. As a minimal setup for CP violation in the scalar sector, the complex Two-Higgs-Doublet model (THDM), is studied. It is introduced in Chapter VI, followed by a discussion of strategies to test the CP properties of such a model in Chapter VII. Finally, in Chapter VIII this thesis is summarized and concluded. In addition, a brief outlook on how to improve and extend the studies performed in this thesis is given.

CHAPTER II

Theoretical Background

This chapter lays down the theoretical foundation for this thesis. The SM is reviewed briefly, a more detailed discussion of the SM can be found in textbooks, such as [43–46]. Afterwards, some open questions, that cannot be explained by the SM, but require BSM physics are raised. Then, the open questions, for which possible solutions are proposed in this thesis, are discussed in more detail.

II.1 The Standard Model of Particle Physics

The SM was established based on the work in [17–20] and describes all known elementary particles, as well as three of four fundamental forces, the strong, the weak and the electromagnetic force. These forces govern the interaction between the elementary particles. Note that the fourth fundamental force, gravity, is not included in the SM.
The SM is a renormalizable relativistic QFT based on the symmetry group

$$\mathcal{G}_{SM} = SU(3)_c \times SU(2)_L \times U(1)_Y. \tag{II.1}$$

Here, $SU(3)_c$ refers to the colour group of QCD [29–34], while the $SU(2)_L$ and $U(1)_Y$ gauge groups, corresponding to the weak isospin and hypercharge, respectively, unite the electroweak forces [17–19]. The matter content of the SM consists of three generations of fermionic fields with spin 1/2, further divided in quarks and leptons, as well as spin-1 gauge fields, which mediate the interactions, and one scalar spin-0 field, the Higgs field. The excitations of these fields are called particles. More precisely, fermions form regular matter, while gauge bosons mediate interactions.
These fields are described by the SM Lagrangian density (which we shorten to Lagrangian in the following)

$$\mathcal{L}_{SM} = \mathcal{L}_{kin} + \mathcal{L}_{Yuk} + \mathcal{L}_{Higgs}, \tag{II.2}$$

where $\mathcal{L}_{kin}$ contains the covariant derivatives of the fields describing their dynamics and gauge interactions, $\mathcal{L}_{Yuk}$ contains the coupling of the fermions to the Higgs fields and $\mathcal{L}_{Higgs}$ describes the Higgs potential including self-interactions. The matter content and gauge symmetry completely define the structure of the SM, making only the above Lagrangian possible. Note that strictly speaking one more term that is not included in the SM Lagrangian is possible. This term is discussed as part of the discussion of open questions.
The fermionic matter content of the SM is given in Table II.1 with left-handed (LH) fields labeled with an index L and right-handed (RH) fields with the index R. For all fermions all three families are given explicitly. The LH fields are doublets under $SU(2)_L$, while the

Fields	**Representation under $\mathcal{G}_{\mathrm{SM}}$**	**electric charge**
LH quarks Q_L: $\begin{pmatrix} u_L \\ d_L \end{pmatrix}, \begin{pmatrix} c_L \\ s_L \end{pmatrix}, \begin{pmatrix} t_L \\ b_L \end{pmatrix}$	$(3, 2, \frac{1}{6})$	$\begin{pmatrix} 2/3 \\ -1/3 \end{pmatrix}$
RH up-type quarks: u_R, c_R, t_R	$(3, 1, \frac{2}{3})$	$2/3$
RH down-type quarks: d_R, s_R, b_R	$(3, 1, -\frac{1}{3})$	$-1/3$
LH leptons l_L: $\begin{pmatrix} \nu_e \\ e_L \end{pmatrix}, \begin{pmatrix} \nu_\mu \\ \mu_L \end{pmatrix}, \begin{pmatrix} \nu_\tau \\ \tau_L \end{pmatrix}$	$(1, 2, -\frac{1}{2})$	$\begin{pmatrix} 0 \\ -1 \end{pmatrix}$
RH leptons: e_R, μ_R, τ_R	$(1, 1, -1)$	-1

Table II.1: Fermionic matter content of the SM with the representation under the SM gauge group and electric charges.

RH fields are singlets, making the SM a chiral gauge theory. Moreover, the quarks are triplets under the $SU(3)_c$ symmetry, which distinguishes them from the leptons as leptons are singlets under this symmetry. The up-type quarks are called up (u), charm (c) and top (t) quark, and the down-type quarks down (d), strange (s) and bottom (b) quark. The leptons are electron e, muon μ and tau τ, with the respective neutrinos (ν_e, ν_μ, ν_τ).
The Higgs field

$$H = \begin{pmatrix} \phi^+ \\ \phi^0 \end{pmatrix} \tag{II.3}$$

transforms as $(1, 2, 1/2)$ under the SM gauge group and the Higgs potential is

$$V(H) = \frac{1}{2}\mu^2 H^\dagger H + \frac{1}{4}\lambda (H^\dagger H)^2 \tag{II.4}$$

with the parameter μ having mass dimension, $\mu^2 < 0$ and λ being the dimensionless quartic coupling. By acquiring a vacuum expectation value (vev) $v \approx 246$ GeV, the Higgs field spontaneously breaks the electroweak force to the electromagnetic force $SU(2)_L \times U(1)_Y \to U(1)_{em}$. This process is called the Higgs mechanism, and leads to the gauge bosons and fermionic fields acquiring mass [21–26]. With a global transformation the vev can be rotated into the neutral component, which then can be expanded around it, so that

$$H = \begin{pmatrix} G^\pm \\ 1/\sqrt{2}\left(v + h + iG^0\right) \end{pmatrix}, \tag{II.5}$$

where the physical Higgs mode is denoted h (later also H) and $G^\pm$ and G^0 are would-be Goldstone bosons, which provide the longitudinal degrees of freedom (DOF) for the gauge bosons. By expanding around the vev they acquire mass terms from the covariant derivative of the Higgs in $\mathcal{L}_{kin}$. This results in the mass eigenstates $W^\pm$ and Z, where Z is a linear combination of W_3 and B_0, with masses m_W and m_Z after electroweak symmetry breaking (EWSB). Therefore, it is also common to say the gauge bosons "eat" the would-be Goldstone bosons. The last electroweak gauge boson mass eigenstate is the massless photon γ. The interaction of photons with charged particles are described by quantum electrodynamics (QED) [47–52]. The final SM gauge bosons are gluons, which are the carrier of the strong force. As they are the gauge bosons of $SU(3)_c$, there are eight gluons, which carry colour charge.
As mentioned above, the Higgs mechanism not only provides masses for the $W^\pm$ and Z bosons, but also for the fermions. The Yukawa part of the Lagrangian in Equation II.2 is

$$\mathcal{L}_{Yuk} = -(Y_u)_{ij}\bar{Q}^i_L \tilde{H} u^j_R - -(Y_d)_{ij}\bar{Q}^i_L H d^j_R - -(Y_e)_{ij}\bar{l}^i_L H e^j_R \tag{II.6}$$

with Q_L^i and l_L^i the LH quark and lepton doublets, u_R^j, d_R^j, e_R^j the RH quark and lepton singlets (as defined in Table II.1), $i,j = 1,2,3$ and $H = i\sigma_2 H^*$, where σ_2 is the second Pauli-matrix. After EWSB and inserting the expansion around the vev in the above Lagrangian one obtains the following mass terms for the fermions

$$\mathcal{L}_{Yuk} \supset -(M_u)_{ij}\,\bar{u}_L^i u_R^j - (M_d)_{ij}\,\bar{d}_L^i d_R^j - (M_l)_{ij}\,\bar{l}_e^i e_R^j\,. \tag{II.7}$$

Here, M_f are 3×3 mass matrices defined by $M_f = Y_f v/\sqrt{2}$ with $f = u,d,e$. Via singular value decomposition the mass matrices M_f can be diagonalized by independently rotating the LH and RH fields by unitary 3×3 matrices $U_{L,R}^f$. The rotations are then of the form $f_{L,R}^i \to (U_{L,R}^f)^{ij} f_{L,R}^j$ and result in six massive quark and three massive charged lepton mass eigenstates, while the three neutrino are massless in the SM.
More specifically, the mass matrices of the quark sector, M_u and M_d are diagonalized by transforming to the basis (u'_L, d'_L) via

$$u'_L = U_u^{ij} u_L^i, \quad d'_L = U_d^{ij} d_L^i. \tag{II.8}$$

Then, the unitary matrices U_u^{ij} and U_d^{ij} also appear in the kinematic terms of $\mathcal{L}_{kin}$, which for fermions have the form $\bar{\psi}^i \not{D} \psi^i$ with $\psi = Q_L, u_R, d_R, l_L, e_R$. With the exception of the charged current J_W^μ the SM currents remain unchanged because the U_i combine to unity. The charged current, however, changes to

$$J_W^\mu = \frac{1}{\sqrt{2}} \bar{u}_L^i \gamma^\mu d_L^i \to \frac{1}{\sqrt{2}} \bar{u}_L^{i\prime} \gamma^\mu \left(U_u^\dagger U_d\right) d_L'^i = \bar{u}_L'^i \gamma^\mu V^{ij} d_L'^i\,, \tag{II.9}$$

where the unitary mixing matrix $V = U_u^\dagger U_d$, the *Cabibbo-Kobayashi-Maskawa* (CKM) matrix, was introduced [53, 54]. The off-diagonal entries of the CKM matrix lead to interactions between quarks of different families in the charged current.
Since the CKM matrix is a unitary 3×3 matrix, it has nine DOF, namely three rotation angles and six phases. Of the six phases five can be absorbed by the rotation of the quark fields with a global phase because the mass terms are invariant under phase change. Consequently, three rotation angles and one phase are left as the physical parameters of the CKM matrix.
In contrast, such a matrix does not occur in the lepton sector. Since the neutrinos remain massless in the SM, they can be transformed in the same way as the LH charged leptons. Due to this additional freedom, no mixing, but a unity matrix appears in the leptonic charged current.
Before discussing some of the open questions in particle physics, a very brief overview of QCD [29–34] is given. For more detailed discussion see for example [55–61]. The QCD Lagrangian is

$$\mathcal{L}_{QCD} = \sum_q \bar{\psi}_{q,a} \left(i\not{D} - m_q \delta_{a,b}\right) \psi_{q,b} - \frac{1}{4} G_{\mu\nu}^A \tilde{G}^{\mu\nu A}, \tag{II.10}$$

where ψ are the quarks-field spinors, q and a the quark flavour and colour indices, m_q the quark masses and $G_{\mu\nu}^A$ the field-strength tensor

$$G_{\mu\nu}^A = \partial_\mu \mathcal{A}_\nu^A - \partial_\nu \mathcal{A}_\mu^A - g_s f_{ABC} \mathcal{A}_\mu^B \mathcal{A}_\nu^C \tag{II.11}$$

with its dual $\tilde{G}_{\mu\nu} = \frac{1}{2}\epsilon_{\mu\nu\alpha\beta} G^{\alpha\beta A}$. Here, the gluon fields are denoted $\mathcal{A}$ $(A = 1,...,8)$, g_s is the QCD coupling constant, often also used in the form $\alpha_s = \frac{g_s^2}{4\pi}$, and f_{ABC} are the structure constants of $SU(3)_c$ given by

$$\left[t^A, t^B\right] = i f_{ABC} t^C \tag{II.12}$$

with t_A the eight generators of $SU(3)_c$. Finally, the running of the coupling as a function of a renormalization scale μ_R is given by the renormalization group equation (RGE)

$$\mu_R^2 \frac{d\alpha_s^2}{d\mu_R^2} = \beta(\alpha_s) = -(b_0\alpha_s^2 + b_1\alpha_s^3 + ...)\,. \tag{II.13}$$

In the above expression the β − function is expressed as a perturbative series with the n-loop coefficients b_{n-1} in the ultraviolet (UV). The negative sign in Equation II.13 implies that the coupling α_s is large for small scales μ_R and becomes weak for large μ_R. This leads to a phenomenon called "asymptotic freedom" [33, 34], which means that quarks and gluons behave asymptotically like free-particles, when close to each other (μ_R large). On the other hand, at low energies (μ_R small) the value of α_S becomes so large that perturbation theory can no longer be used. This is called confinement. In this limit, the relevant particle are no longer quarks and gluons, but rather composite stated. These states, which are called hadrons, are colour-neutral. In other words, the $SU(3)_c$ symmetry is dynamically broken and in the vacuum quark condensates $\langle \bar{q}_i q_j \rangle$ are formed.
Hadrons can be further divided in mesons (consisting of a quark and an anti-quark with opposite colour charge) and baryons (made of three quarks, which each have a different colour charge). The confinement scale Λ_{QCD} is defined as the scale where the strong coupling constant diverges. The point of divergence is called the *Landau Pole*. More details about the running of the QCD coupling and the consequences can be found in [62] and references therein.
Under the assumption of massless quarks the QCD Lagrangian simplifies to

$$\mathcal{L}_{QCD} = \sum_q \bar{\psi}_{q,a} i \not{D} \psi_{q,b} - \frac{1}{4} G^A_{\mu\nu} \tilde{G}^{\mu\nu A}\,. \tag{II.14}$$

Then, the above Lagrangian is invariant under the chiral symmetry group

$$SU(N_f)_L \times SU(N_f)_R, \tag{II.15}$$

as LH and RH quarks are decoupled. Here, N_f is the number of quark flavours. However, in nature, quarks are massive, so that the above chiral symmetry is not an exact symmetry of QCD. Since the lightest quarks u, c and s have masses much below Λ_{QCD}, the chiral symmetry associated with these quarks can be studied. It approximately is

$$SU(3)_L \times SU(3)_R\,. \tag{II.16}$$

Still, this symmetry is broken spontaneously by the quark condensate to $SU(3)_L \times SU(3)_R \to SU(3)_V$, where the V stands for vector, and also explicitly by the quark masses. According to the Goldstone theorem [63, 64] eight light pseudo-Nambu-Goldstone bosons (pNGB) emerge, which are the pions, Kaons and the η meson.
The SM is very successful at describing the fundamental interactions of nature, for example it correctly predicted the existence of the weak gauge bosons, gluons, heavy quarks and the Higgs boson, which by now have all been confirmed experimentally [27, 28, 39–42, 65–73]. Furthermore, a lot of the from the SM predicted quantities are in great agreement with measurements. One of the most famous examples is the electron magnetic dipole moment where the predicted value agrees with the experimental data with a precision of 10^{-12} [74, 75]. Nonetheless, the SM is not able to explain all observations and measurements, leaving a variety of open questions and unexplained anomalies. A few of them are listed below:

- **Neutrino Masses:** While non-zero masses of neutrinos are confirmed by the observation of neutrino oscillations [76, 77], the SM does not provide a mechanism for the generation of neutrino masses.

- **Hierarchy Problem:** The hierarchy problem poses the questions, why the two fundamental scales of nature, the Planck-scale and the weak scale show a large hierarchy. Even before the Higgs boson was discovered, it was known that the Higgs field has to have a size about 250 GeV to produce the correct masses of the W and Z bosons. Naturally, however, the Higgs field should be zero or at the Planck scale to be stable. Thus, the hierarchy problem poses the question, why the non-zero value of the Higgs field is so small compared to the Planck-scale. Note that the hierarchy problem is a problem related to the Higgs field, not the Higgs boson mass. Nonetheless, the question how the Higgs mass is protected from Planck-scale radiative corrections, is related. As the Higgs boson is a scalar, its mass is affected by the presence of heavy particles and receives quantum corrections that destabilize the weak scale [20, 78]. This can be seen, when considering the loop corrections to the Higgs mass in the SM, which read [79]

$$\frac{\Delta m_h^2}{m_h^2} = \frac{3\Lambda^2}{8\pi^2 v^2}\left[4\frac{m_t^2}{m_h^2} + \frac{m_Z^2}{m_h^2} - 2\frac{m_W^2}{m_h^2} - 1 + ...\right] \approx \left(\frac{\Lambda}{500\ \text{GeV}}\right)^2, \tag{II.17}$$

  where the loop integrals have been regularized due to limiting the virtual momentum to the cut-off scale Λ, which should be considered as the scale of NP. The loop corrections have a quadratic divergence. Therefore, if the SM is considered to be an effective field theory (EFT), the Higgs mass will be quadratically sensitive to the scale of NP, that appears in the UV. The loop corrections to the Higgs mass are not proportional to the Higgs mass itself and exceed the physical value for scales above $\Lambda \sim 500$ GeV.

- **Cosmological Constant Problem:** The cosmological constant problem describes the discrepancy between the very large energy density for the vacuum, which predicts large gravitational effects in QFT, and the non-observation of such effects.

- **Grand Unified Theories:** The question is posed if there is a *Grand Unified Theory* at a high scale where the SM is described by one single gauge group.

- **Unification of Gravity and QFT:** So far no theory that reconciles general relativity with QFT has been found.

- **Dark Matter:** While the existence of DM is established by observations of gravitational effects over a wide range of length scales [80] reaching back to nearly a century ago (for a review of DM observations over time see [81]), the origin and nature of DM is to date unknown. A more detailed discussion follows in Section II.2.

- **Dark Energy:** Around 68 % of the universe are made up of dark energy, which is the energy needed to explain the observed accelerated expansion of the universe.

- **Strong CP Problem:** The SM gauge group allows for an additional term in the Lagrangian of the form

$$\mathcal{L}_\theta = -\frac{g_a^2}{32\pi}\theta \tilde{G}_{\mu\nu A} G^{\mu\nu A}, \tag{II.18}$$

which violates CP. Even though Equation II.18 can, in principle, be written as a total derivative, it gives rise to non-perturbative instanton effects and, thus, cannot be discarded from the Lagrangian. However, via the chiral rotation $q \to e^{i\alpha\gamma_5}q$ the parameter θ can be moved to a complex phase in the quark mass matrix. This changes θ to the physical CP violating parameter $\bar{\theta} = \theta + \arg\det(M_q)$, where M_q is the quark mass matrix. Then, a contribution to the electric dipole moment (EDM) of the neutron arises [82]. The current measured limit from the neutron EDM [83] leads to an upper bound on θ at $|\bar{\theta}| < 5 \times 10^{-12}$. The natural expectation, however, would be $\theta \sim \mathcal{O}(1)$.
Thus, the strong CP problem is a naturalness problem. It addresses, why θ is small, or in other words, why QCD does not violate CP.

- **Baryon Asymmetry of the Universe:** In a universe that consists of equal amount of matter and antimatter particles and antiparticles would annihilate each other, leaving only radiation. However, as matter exists in the universe, there has to be an asymmetry of matter and anti-matter. Based on the observed anisotropies in the cosmic microwave background (CMB) and light element abundance produced during BigBang Nucleosynthesis (BBN) the baryon asymmetry of the universe can be quantified as

$$Y_B = \frac{n_B - n_{\bar{B}}}{s} \approx 8.7 \times 10^{-11}, \tag{II.19}$$

  where n_B and $n_{\bar{B}}$ are the number densities of baryons and antibaryons, and s is the co-moving entropy density in the universe [84]. Three conditions need to be fulfilled to generate a baryon-antibaryon asymmetry [85]. First, baryon number has to be violated. Second, C and CP have to be violated and, third, interactions out of the thermal equilibrium are necessary. In general, these conditions can be fulfilled in the SM with electroweak baryogenesis [86–88] as C and CP are violated in the electroweak interactions of the SM, baryon number is violated by non-perturbative sphalerons in such a setup and a first-order phase transition can provide the necessary non-equilibrium conditions. However, the amount of CP violation in the SM can not explain the observed baryon asymmetry of the universe and, thus, NP is required. Furthermore, according to the content of the SM the electroweak phase transition is expected to be a crossover transition.

- **Flavour Anomalies:** Measurements of meson decays [89,90], for example B meson decays, hint that lepton flavour universality might not be a correct assumption.

- **Muon Anomalous Magnetic Moment:** A recent measurement confirmed the tension of the measured value of the muon anomalous magnetic moment and the SM prediction [91].

II.2 Dark Matter

One of the biggest and most studied open question in contemporary particle physics is the origin and nature of DM. A multitude of observations at various length scales [80, 84, 92–103], imply the existence of non-luminous, gravitationally (and possible also strong and/or electroweak) interacting matter, which is called DM.

The first hint of DM was observed nearly a century ago by Zwicky in 1933, who found that the velocity dispersion in the Coma cluster had larger values than expected from the visible matter [92]. He concluded that this points to a larger amount of "dark matter" than visible matter in the universe. A similar result on galactic scales was obtained from the analysis of the rotation curves of the Andromeda galaxy by Rubin and Ford in 1970 [93]. A flat velocity distribution was found for stars at large radii instead of the expected $1/\sqrt{r}$ dependence. This observation could be explained by a DM halo, in which the galaxies are embedded. Further observations of rotation curves of galaxies support this theory [96–98]. Another very compelling hint for DM comes from the observation of the Bullet cluster [94, 95] where the collision of two galaxies was observed. It was seen that, while the hot baryonic gas parts of both galaxies were affected and slowed down by the collision, the bulk mass was mostly unaffected. Strong [99, 100] and weak [101] gravitational lensing further confirm the existence of DM in galaxies and large-scale structures, respectively. The total energy density of "cold" dark matter (CDM) can be determined precisely from measurements of the power spectrum of the CMB [84, 102, 103]. The current value is $h^2\Omega_{DM} = 0.120 \pm 0.001$ [84], where h is the renormalized Hubble parameter. Here, CDM refers to DM that is non-relativistic at the point of matter-radiation equality and the beginning of structure formation. Then, perturbations in the CDM component can collapse to form structures, when the universe becomes matter-dominated, leading to an early formation of small scale structures. The same is not the case for baryonic matter, which cannot collapse until the time of photon decoupling due to radiation pressure. "Hot" dark matter (HDM), in contrast, stays relativistic at the beginning of structure formation and, thus, has a non-negligible free-streaming length. HDM does not form structures until it becomes non-relativistic. Consequently, the observed small-scale structures imply that most of the DM is cold. Lastly, the amount of visible matter is constrained by the light element abundance generated during BBN [104], which again leads to the conclusion that most of the matter in the universe is DM.

In general, most of the above observations could also be explained by massive, baryonic, non-radiating objects, such as primordial black holes and other *massive astrophysical compact halo objects* (MACHOs). However, due to the power spectrum of the CMB and the light element abundance they can not be the sole explanation for the missing mass. Alternate explanations, especially for the rotation curves of galaxies, also include modifications of gravity, for example the *modified newtonian dynamics* (MOND). However, they lack a comprehensive framework as the fitting of the rotation curves does not lead to a unique parameter to modify newtonian dynamics. In addition, these models are also very strongly constrained from limits on the deviation of the speed of gravity from the speed of light, which were found from observing gravitational waves and electromagnetic radiation from a neutron star binary merger [105]. Consequently, here, DM is considered to be made up of elementary or composite particles, that explain the above discussed observations.

By now, it is well established that DM makes up 27% of the universe (corresponding to 85% of the total matter), while only around 5% of the universe consist of the baryonic

matter of the SM [84]. As mentioned above, the remaining 68% are dark energy, an unknown form of energy required to explain the observed accelerated expansion of the universe. The standard model of cosmology includes both CDM and dark energy, the latter via the cosmological constant Λ, leading to its name ΛCDM Standard Model of cosmology. Further, it is known that DM is electrically neutral with the exception of possible milli-charges [106–108]. DM particles also have to be stable or at least have lifetimes larger than the age of the universe [109]. From the observations of collisions of galaxy clusters, as, for example, the already discussed Bullet cluster, an upper bound on the self interactions can be found [110]. On the range of the DM masses, however, there is no strong constraint. The upper bounds on the DM mass arise, on one hand, from the fact that too heavy DM would disrupt star clusters and similar structures while passing through and is set at $m_{DM} \leq 5M_{\odot}$ [111] with the solar mass $M_{\odot} \approx 2 \times 10^{30}$ kg, and, on the other hand, from the particle physics perspective at the Planck scale $\sim 1.2 \times 10^{19}$ GeV. The lower limits on the DM mass depend on the type of DM. For fermionic DM Pauli's exclusion principle puts a strong limit at $m_{DM} \geq 70$ eV from the mass and size of white dwarfs [112]. For bosonic DM the bounds are less stringent. The de Broglie wavelength $\lambda \sim 1/m_{DM}$ gives a lower bound on the DM mass because it has to be smaller than the size of dwarf galaxies. However, a stronger bound arises from structure formation and the Lyman - α - forest observations, which set a limit at $m_{DM} \geq 10^{-21}$ eV [113]. The strongest bound is found for thermal DM, again from Lyman - α - forest observations, at $m_{DM} \geq 5.3$ keV since otherwise the small-scale structure formation would be erased due to its large free-streaming length at matter-radiation equality [114].
Generally, two production mechanisms for the generation of the DM abundance of the universe can be distinguished, namely thermal and non-thermal production [115]. In thermal production scenarios the DM energy distribution is proportional to the one of particles in thermal equilibrium because the DM is produced from particles which are in thermal equilibrium. For non-thermal production this is not the case, so that the DM does not show a thermal distribution. Examples for non-thermal DM production is the generation from the decay of out-of-equilibrium particles or by coherently oscillating scalars [115]. Similarly, there are several possibilities how DM can be produced thermally. Here, merely two standard scenarios for DM production are considered, "freeze-out" [116, 117] and "freeze-in" [118, 119]. In the standard thermal freeze-out scenario DM particles have a large initial thermal density. When the temperature of the thermal bath falls below the DM mass, the thermal density dilutes due to the annihilation to lighter states. The DM abundance is then given by the temperature of decoupling from the plasma, which happens, when the annihilation becomes slower than the expansion of the universe. In freeze-in scenarios, on the other hand, DM is only weakly coupled to the thermal bath at very high temperatures and there is a negligible DM abundance. When the universe cools, the DM abundance is produced from scattering or the decay of particles in the thermal bath. When the temperature drops below the DM mass, no more DM particles can be produced, which gives the DM abundance.
Since the SM does not provide an explanation for the origin and nature of DM, a plethora of DM candidates and models have been proposed, studied and searched for. Despite these efforts, other than the above listed gravitational signals, no signs of DM have been found so far. Therefore, the first part of this thesis is dedicated to the study of DM models. The focus lies on a specific class of DM models, strongly coupled dark sectors, but a discussion of ALPs is also included. In the following, these two concepts, as well as another historically important DM candidate, *weakly interacting massive particles* (WIMP), are briefly reviewed.

Weakly Interacting Massive Particles and the WIMP miracle

WIMP are a thermal DM candidate. As the name implies, WIMP are massive particles, which couple weakly to some SM particles. For example, in supersymmetric models, the lightest supersymmetric particle can be a WIMP candidate if it is electrically neutral [120]. The WIMP DM abundance is produced via thermal freeze-out: In the early universe the interactions with SM particles keep the DM number density changing processes in equilibrium, meaning the WIMP DM thermalizes. Once the temperature of the universe falls below the WIMP mass the universe does not have enough energy to produce WIMP. However, the annihilation of WIMP continues, and, thus, the co-moving number density of WIMP depletes until the expansion rate of the universe, called the Hubble rate, dominates the interaction rate of DM. At this stage WIMP DM chemically decouples and, consequently, its co-moving number density is conserved. The time evolution of the corresponding DM number density is determined using the Boltzmann equations [121], and is approximately found to be [122]

$$h^2\Omega_{DM} \simeq \frac{0.1 \text{ pb } c}{\langle \sigma v \rangle}, \tag{II.20}$$

where h is again the renormalized Hubble constant, c is the speed of light and $\langle \sigma v \rangle$ the thermally averaged cross-section times velocity. The fact that WIMP reproduce the observed DM abundance for masses and annihilation cross section values that are typical for the weak scale, making them ideal CDM candidates, is called the "WIMP miracle". In addition, WIMP can be tested at experiments in several ways as the process responsible for the thermal freeze-out is closely related to various processes used in astrophysical or laboratory probes. This includes indirect detection experiments, which aim to detect the products of the DM annihilation, such as gamma - rays, cosmic rays of charged antiparticles or neutrinos, direct detection experiments where DM is probed due to its scattering off SM particles [123], and the production of DM particles at particle colliders like the LHC. Indirect detection experiments are, for example, the Cherenkov telescopes Fermi-LAT, MAGIC and H.E.S.S., which observe nearby dwarf galaxies in the Milky Way [124–126] and the galactic center [127]. Direct detection experiments include experiments using nobel gases, such as XENON1T [128] in the mass region between $\mathcal{O}(10)$ MeV and 1 TeV with various analysis techniques, but also the cyrogenic solid-state detectors CRESST-III [129] and SuperCDMS [130], which cover masses down to $m_{DM} \sim 1$ MeV, and detectors based on charged coupled devices, such as DAMIC [131] and SENSEI [132], that can probe the sub-MeV and eV region. Despite the experimental efforts, to date no clear evidence of WIMP DM has been observed leading to strong bounds on its mass and couplings. There are some results, however, that could arguably be hints for WIMP DM. One of these is the observation of an excess of gamma - rays from the galactic center in the few GeV range by Fermi-LAT [133]. If this excess is, indeed, caused by DM annihilation is of yet an unanswered question [134]. Cosmic ray anti-proton data show a similar excess [135, 136]. Moreover, another debatable observation was made by the DAMA/LIBRA collaboration. An annually-modulated DM annihilation signal was reported [137], which is, however, in conflict with the non-observation of such a signal in other direct detection experiments [138], and is, therefore, controversial. As a consequence of the non-discovery of WIMP DM in recent years the focus has shifted more and more towards other DM models.

Strongly Coupled Dark Sectors

Strongly coupled dark sectors, or QCD-like dark sectors, are a class of asymmetric DM models. In asymmetric DM models the particle content of the DM sector typically has similar properties to SM baryons and a common origin of the DM and the SM baryon abundance in the present-day universe is assumed. This can either be the sharing of a primordial asymmetry, which is produced in an arbitrary sector, or the production of both asymmetries by the same process. Reviews of asymmetric DM can, for example, be found in [139, 140].

In contrast to models with WIMP DM dark sectors consist not of a single DM field, but several. These dark sector fields typically do not interact directly with SM particles, but via a portal interaction. Generally, dark sectors can couple to the visible sector via SM portals, which are gauge singlet operators with mass dimension less than four. Three SM portals exist: the Hypercharge gauge boson $B_{\mu\nu}$ [141], the Higgs bi-linear $|H|^2$ [142] and the neutrino portal via Hl_L [143]. Interactions between the visible and the dark sector can also be mediated by NP fields, so called mediators. Another difference to WIMP DM is the fact that the DM candidate of models with a strongly coupled dark sector is not an elementary particle, but a dark hadron composed of several dark sector particles. This type of model is realized by enhancing the SM gauge symmetry group in Equation II.1 by an additional gauge group $SU(N_D)_D$, and the SM particle content by a set of n_D light particles and a mediator, that facilitates interactions between the dark and the visible sector, more precisely SM quarks. Such a setup was first proposed under the name *Hidden Valley Model* in [144].

Analogous to QCD quarks the introduced light dark sector particles are fermions which are charged under the new $SU(N_D)_D$ and are called dark quarks in the following. Furthermore, these models feature dark gauge bosons, namely the dark gluons. The SM particles have no charge under the dark gauge symmetry. Consequently, to allow couplings to both SM quarks and dark sector particles the mediator has to be charged under both the SM $SU(3)_c$ and the dark sector $SU(N_D)_D$.

We differentiate between two types of mediators, *s-channel mediators* and *t-channel mediators*, based on how the dark quarks are produced, cf. Figure II.1. Typical s-channel mediators are a Z', as was proposed in [144] and further studied in, for example, [145–156]. Bi-fundamental scalars X_D [11,157–161] act as t-channel mediators. If a mediator is heavy,

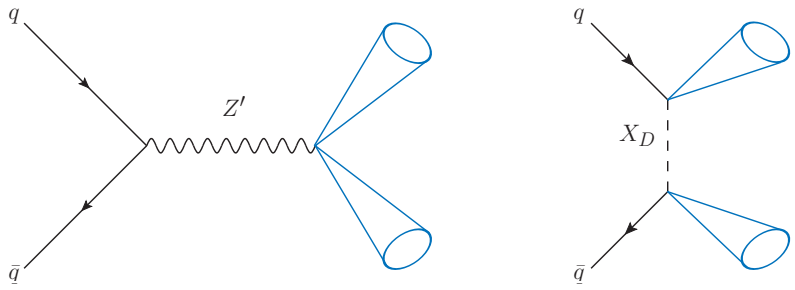

Figure II.1: Production of dark quarks via a s-channel mediator, e.g. a Z' (**left**) and a t-channel mediator X_D (**right**). The blue cones represent dark jets. Here, we only consider t-channel mediators.

it can be integrated out leading to the contact operator

$$\mathcal{L} \supset \frac{c_{ij\alpha\beta}}{\Lambda_D} \left(\bar{q}_i \gamma^\mu q_j\right) \left(\bar{Q}_{D\alpha} \gamma_\mu Q_{D\beta}\right), \tag{II.21}$$

where Roman indices are used for SM flavour indices and Greek ones for dark flavour. Moreover, the dark sector features a strong "dark force" with a coupling constant g_D with a similar running as the strong coupling constant g_s. Therefore, the dark quarks confine below a scale Λ_D, forming dark hadrons and dark mesons. It was shown, for example, in [11] that mechanisms exist, so that the dark confinement scale is similar to the QCD confinement scale.
As there are no indications on the number of dark colours (N_D) and flavours (n_D) or the mass scales of either the dark quarks or the dark hadrons a wide variety of models with different properties is possible. Consequently, there are also several mechanisms possible to obtain the observed relic DM density [154, 162–166] as there can be stable and unstable dark sector species present. Most notable is $3 \to 2$ annihilation.
In the type of dark sector models considered here, which feature a bi-fundamental scalar X_D as the mediator, the lightest dark baryon is stable due to a conserved dark hadron symmetry and, thus, a viable DM candidate. Dark mesons, in contrast, are not protected by a symmetry and decay back to SM particles. This makes strongly coupled dark sectors especially interesting from a collider perspective as they lead to spectacular signatures, such as semi-visible or emerging jets [12, 167, 168]. Note that it is a common feature of strongly coupled dark sector models that the collider phenomenology is governed by the dark mesons, specifically the dark vector meson ρ_D and the pseudoscalar dark pion π_D. The concrete phenomenology depends on the lifetimes, masses and mass hierarchy of these two dark sector particles. A recent overview about dark sector signatures and searches at LHC can be found in [8]. Along with collider searches strongly coupled dark sectors can also be searched for in other ways, for example with direct detection experiments.
A detailed introduction of the specific dark sector model investigated in this thesis can be found in Chapter III.
In addition to the strongly coupled dark sector models investigated in this thesis a variety of similar hidden dark sector models exists. Examples of other hidden dark sectors are twin Higgs models [169–172], composite and/or asymmetric DM scenarios [11, 159, 163, 173–186] and models discussed in the context of string theory [187, 188]. Phenomenological studies of these models can be found for example in [144, 189–203].

Axions and Axion-Like Particles

Axions and ALPs are (very) light, neutral pseudo-scalar particles that, generally, arise as the (pseudo-)Nambu-Goldstone bosons of a spontaneous broken, global $U(1)$ symmetry. If this symmetry is only broken spontaneously, the corresponding axion/ALP will be a massless Nambu-Goldstone boson, while a small additional explicit symmetry breaking leads to small masses for the axion/ALP. The couplings of axions/ALPs to SM particles are suppressed by their decay constant f_a, leading to small couplings to both matter fields and radiation. Here, the term "axion" refers to the QCD axion generated from the breaking of the Peccei-Quinn (PQ) symmetry $U(1)_{PQ}$ [204, 205]. The QCD axion can be a solution to the above described strong CP problem [204–207]. In this case, a dynamical pseudo-scalar field, the axion a, is introduced and added to Equation II.18, leading to

$$\mathcal{L}_a = -\frac{g_s^2}{32\pi}\left(\bar{\theta} + \frac{a}{f_a}\right)\tilde{G}_{\mu\nu^A} G^{\mu\nu A}\,. \tag{II.22}$$

In presence of such an axion field the QCD vacuum energy $E(\bar{\theta}) = -m_\pi^2 f_\pi^2 \cos(\bar{\theta})$ [44], with m_π and f_π the pion mass and decay constant, respectively, becomes $E(\bar{\theta}) = -m_\pi^2 f_\pi^2 \cos(\bar{\theta} + a/f_a)$ [208]. Consequently, the energy is minimized, when the axion acquires a vev $\langle a \rangle$ that exactly cancels $\bar{\theta}$. Then, Equation II.18 vanishes in the vacuum,

explaining, why QCD does not violate CP. The mass of the QCD axion can be calculated in chiral perturbation theory (ChPT) and is

$$m_a \approx 6 \text{ meV} \left(\frac{10^9 \text{ GeV}}{f_a/C} \right), \tag{II.23}$$

where C is an integer and arises from the colour anomaly of the PQ symmetry [206, 207]. Constraints arising from accelerators, reactors and cosmology generally set a lower bound on f_a at $f_a > 10^7$ GeV, resulting in $m_a \lesssim 10$ meV [209].
ALPs, on the other hand, are a more general type of pNGB of a spontaneously broken $U(1)$, where m_a and f_a are not related. They are predicted as the lightest degree of freedom in composite models [210–214], strongly coupled dark sectors [10–12, 144, 155, 196, 215], supersymmetric models [216, 217], Froggatt-Nielsen (FN) models of flavour [218], string theory [219,220] or in models with horizontal symmetries [108,221–232]. The independence of m_a and f_a for ALPs opens up a larger parameter space than is viable for the QCD axion, that can be probed using various approaches. ALPs can be produced at colliders and, thus, searched for via their decay products [3, 233, 234]. Another possibility are "light shining through a wall" experiments, for example the ALPS [235], ALPS-II [236] or OSQAR [237] experiments. Here, using strong magnetic fields photons are converted to axions/ALPs, which can travel freely through a wall, before being converted back into photons. Helioscopes, such as CAST [238] or IAXO [239], aim to observe solar axions/ALPs that are turned into photons in the magnetic field of the Earth. Furthermore, DM direct detection experiments such as XENON1T can also be used to constrain the parameter space. A recent electron recoil data set from XENON1T shows an excess of recoil events in the $2-3$ keV region [240], which could be explained by solar axions/ALPs [240, 241]. However, stellar bound on axions/ALPs disfavour the best fit parameter point for solar axions/ALPs [242]. The origin of the excess in the recoil events is still an open question. Further bounds on the parameter space arise from astrophysics, for example from the ratio of horizontal branch stars to red giant in galactic globular clusters [243], red giant bursts and supernova cooling [225, 244–246].
If it is assumed that ALPs are DM, additional constraints will arise from haloscope searches where the conversion rate of ALPs to photons is resonantly enhanced using a cavity, so that a detectable signal is produced [247], and also from experiments searching for cosmic ALPs such as ABRACADABRA [248], searches in gamma ray spectra for the process $a \to \gamma\gamma$ [249] and from analyzing the acoustic peaks and anisotropies of the CMB matter power spectrum in the ultra light ALP mass region [250, 251].

II.3 Extending the SM Scalar Sector

A common way to address one or more open questions of particle physics is to enhance the SM scalar sector. Here, additional scalars, that are singlets, doublets, triplets, etc. under $SU(2)_L$, are added to the SM particle content. The study of extended scalar sectors is compelling for several reasons. After the discovery of a scalar resonance at the LHC [27,28], that is consistent with the SM predictions, the knowledge of the scalar sector in general, for example the scalar potential including the Higgs self-coupling, is still rather limited. Therefore, one of the main goals of contemporary particle physics is to measure its properties and establish, whether the scalar sector is minimal, containing only one scalar field, or if there are several.
Extended scalar sectors are one of the simplest possible extension of the SM. Nonetheless, they allow addressing several open questions in particle physics. One of them is the hierarchy problem, for which, for example, supersymmetric models provide solutions [252–254].
Moreover, adding scalar fields to the SM can also solve the problem of the stability of the electroweak vacuum. For large field values the Higgs potential $V(h)$ in Equation II.4 is approximately

$$V(h) \simeq \lambda(h)\frac{h^4}{4}\,, \tag{II.24}$$

where $\lambda(h)$ describes the renormalization group running of the Higgs quartic coupling λ. From the RGE the $\beta-$ function that governs the running is

$$\beta_\lambda = \frac{d\lambda}{d\log\mu} = \frac{1}{16\pi^2}\left[12\lambda^2 + 6\lambda Y_t^2 - 3Y_t^4\right]\,, \tag{II.25}$$

where Y_t is the top Yukawa coupling. For the measured Higgs and top masses the Higgs vacuum is not bounded from below and not stable [255, 256] because of this running. However, the corresponding tunneling probability is very small, leading to a lifetime of the vacuum that exceeds the age of the universe by orders of magnitude. That means the electroweak vacuum is a meta-stable vacuum very close to actual stability [255]. Models with an enhanced scalar sector can change the running of λ and, thus, lead to a stable vacuum. Note that the opposite can also be true, so thar the addition of scalars spoils the (meta-)stability of the SM electroweak vacuum.
The type-II sea-saw mechanism [257–262], which provides a mechanism for generating Majorana neutrino masses, is also based on an extension of the scalar sector. A $SU(2)_L$ triplet field Δ is added to the SM, which obtains a vev v_T after spontaneous symmetry breaking. Expanding around the triplets vev in analogy to Equation II.5 leads to Majorana mass terms for the SM neutrinos from the coupling to two lepton doublets

$$Y_\Delta \bar{l}_L^c i\sigma^2 \Delta l_L + h.c.\,, \tag{II.26}$$

where Y_Δ is the Yukawa coupling of the new triplet, the superscript c denotes the charge conjugation of a given particle and σ^2 is the second Pauli matrix. Then, the resulting neutrino mass term is

$$(Y_\Delta)_{ij} v_T/\sqrt{2}\nu_{L_i}\bar{\nu}_{L_j}^c. \tag{II.27}$$

In this thesis, a model with an extended scalar sector is used to discuss an additional source of CP violation and, thus, address the baryon asymmetry of the universe. Here,

an additional source of CP violation is introduced in the scalar sector. More precisely, additional CP violation is introduced by adding a complex $SU(2)_L$ scalar field with the same quantum numbers as the SM Higgs field. This type of model where a (complex) $SU(2)_L$ doublet scalar is added to the SM is called (complex) Two-Higgs-Doublet model [263].
Besides providing solutions to several open questions of the SM extended scalar sectors also feature a rich phenomenology, not only leading to additional states, but also modifying the SM Higgs couplings. Consequently, measurements of the Higgs signal strength and electroweak precision variables set bounds on the parameter space of models with extended scalar sectors. On the other hand, the additional physical scalar states, that arise in these models, can lead to new signatures and, as a result, inspire new search channels at experiments. Then, the study of extended scalar sector models helps to use current experiments to their most complete potential. This way, models with extended scalar sectors cannot only give insight into the properties of the SM scalar sector, but also into other missing parts of the SM.

Part I

Colourful Dark Sectors

THE nature and origin of DM is one of the biggest unsolved mysteries in particle physics (cf. Section II.2). A lot of effort, both on the theoretical and the experimental side, is invested in solving this puzzle. As part of this endeavor a wide variety of DM models is considered. The first part of this thesis is dedicated to the study of one specific type of DM models, namely theories with strongly coupled dark sectors.

As discussed in Section II.2, such theories introduce an additional non-Abelian gauge group, as well as dark gauge and matter fields in analogy to SM gluons and quarks, hence the name QCD-like dark sectors. Given the complex structure of the SM, especially of QCD, it is a valid assumption that a dark sector would also be highly non-trivial. In fact, no a priori predictions exist for the gauge group dimension, which defines the number of colours, nor for the number of flavours, and, thus, the number of matter fields in a QCD-like dark sector. Similarly, the mass hierarchies of the matter fields of strongly coupled dark sectors are not set by any such expectations. Consequently, the structure of the dark sector can be arbitrarily complex. Nonetheless, assumptions on these types of models can be made to classify and study them.

First, we assume that the visible and dark sector communicate via a portal. Here, we do not consider the above described SM portal interactions, but the case of a NP mediator as a portal, which couples the visible sector fermions to the dark sector fermions. More specifically, we investigate a mediator that couples to SM quarks, denoted as q, and dark quarks Q_D. As was discussed already, a typical s-channel mediator is a Z', studied, for example, in [144–156]. In contrast, t-channel mediators are new bi-fundamental scalars [11, 157–161].

A common feature of QCD-like dark sector is that the dark sector particles confine below a dark confinement scale Λ_D and form dark hadrons independently of the exact details of QCD-like dark sector models. The stable dark hadrons, here, serve as DM candidates. Depending on the model's symmetries dark baryons and/or dark mesons can be the DM candidate(s).

QCD-like dark sectors lead to rich and spectacular collider phenomenology. In addition to the model parameters, also the dark confinement scale influences the expected phenomenology: Dark quark masses and a dark confinement scale much smaller than the center-of-mass energy $\sqrt{s}$ of the LHC at CERN, $m_{Q_D} \lesssim \Lambda_D \ll \sqrt{s}$, lead to spectacular signatures at LHC, such as semi-visible jets and emerging jets [12, 167, 168]. Increasing the value of Λ_D leads to heavier bound states and as a consequence to smaller final state multiplicities for a given $\sqrt{s}$ since the parameter space decreases. In the limit where $\Lambda_D \sim \sqrt{s}$ depending on the production mechanism $2 \to 2$ processes can become dominant. Thus, in this limit resonance-like searches for dark bound states can be used [183, 202, 264, 265]. On the other hand, for the case of $m_{Q_D} \gg \Lambda_D, m_{Q_D} \lesssim \sqrt{s}$, the unusual signature of quirks can be observed [195, 266, 267].

In this thesis, the focus is the study of the phenomenology of t-channel models under the assumption of the first case, $m_{Q_D} \lesssim \Lambda_D \ll \sqrt{s}$. For the investigation of such models hadron colliders such as the LHC are great testing grounds for several reasons. Since the particles of QCD-like dark sectors, as they are considered here, solely couple to SM quarks, they can only be produced directly at hadron colliders, but not at electron colliders. In addition, circular hadron colliders generally provide larger center-of-mass energies than circular lepton colliders since the maximum energy obtained at a circular lepton collider is limited as a result of synchroton radiation. Currently, the energy frontier is set by LHC with a center-of-mass energy of $\sqrt{s} = 13$ TeV. LHC provides and accelerates protons or heavy ions before colliding them at the four different experiments ALICE [268], ATLAS [269], CMS [270] and LHCb [271]. Both ATLAS and CMS are general-purpose

detectors with the aim of studying the SM, searching for extra dimensions and new particles Thus, they are well suited for phenomenological studies of QCD-like sectors. The focus of LHCb is the investigation of the baryon-antibaryon asymmetry through the study of bottom quarks. For the study of dark-sectors coupled to down-type quarks LHCb can also be used as a testing ground. ALICE, finally, is dedicated to heavy-ion physics.
The data taking of LHC started in 2011/2012 at $\sqrt{s}$ = 7-8 TeV. In total an integrated luminosity of about $\mathcal{L} = 25$ fb^{-1} of data was collected [272, 273]. The second run of LHC from 2015 until the end of 2018 collected additional 139 fb^{-1} luminosity [274]. After a long shut-down run 3 will start in 2022 and is planned to continue until 2025 with a center of mass energy up to $\sqrt{s} = 14$ TeV, even though currently the center of mass energy is at $\sqrt{s} = 13.6$ TeV [275]. It is expected that up to $\sim 300\,\text{fb}^{-1}$ of proton-proton (pp) collision data will be collected. In addition, during run 3 new experiments will take data for the first time, such as FASERν [276] or SND@LHC [277]. During another shut-down LHC will be upgraded to the High Luminosity Large Hadron Collider (HL-LHC) [278]. HL-LHC aims for collecting $\mathcal{L} = 4000$ fb^{-1} at $\sqrt{s} = 14$ TeV starting 2029.
Collider experiments such as the LHC, but also fixed target experiments such as NA62 [279], can search for NP directly or indirectly. Direct searches look for distinct signatures from new particles, for example for large missing energy signatures, signatures of displaced decaying particles or exotic signatures such as emerging jets. Multiple NP searches have been performed by ATLAS and CMS. The results of these searches, however, are not always presented in a model-independent way. Nonetheless, results cited in a model-specific framework can be used to constrain other models by recasting the results with the help of Monte Carlo (MC) simulations. Similarly, predictions for signatures that have not yet been considered in experimental searches can be given with the help of such simulations. On the other hand, bounds can be put on the parameter space from indirect searches since new particles also contribute to SM processes, such as electroweak precision measurements or flavour observables.
In the following, we explore the parameter space of several setups of QCD-like dark sectors, making use of both approaches. More specifically, Chapter III outlines the QCD-like dark sector model we consider here. Afterwards, Chapters IV and V focus on the phenomenology of coupling the dark sector to RH down- and up-type quarks, respectively. Chapter IV presents the most recent bounds on the complete parameter space for couplings to down-type quarks, while Chapter V discusses the parameter space of and a new search strategy for a simplified model coupled solely to the up-type quarks.

CHAPTER III

A t-channel Dark QCD Model

In the following, we study a specific UV-completion of the contact operator in Equation II.21 where the dark sector couples to RH SM-quarks via a heavy mediator. There are many options for mediators, acting both in the s-channel [144–156] and in the t-channel [10–12, 157–161] cf. Figure II.1 in Section II.2, but only the case where dark sector particles are mainly produced in t-channel processes, is considered in this thesis. The specific model investigated here was first introduced in [11]. In addition to the SM gauge group (cf. Equation II.1) a dark flavour symmetry $SU_D(N_D)$ with $N_D \geq 2$ is introduced, so that the complete symmetry group of the model is

$$SU(3)_c \times SU(2)_L \times U(1)_Y \times SU(N_D)_D. \tag{III.1}$$

Furthermore, n_D Dirac fermions, so called dark quarks Q_D, are added to the SM particle content. In the following, we nearly always assume $n_D = N_D = 3$ and discuss this scenario in detail. All SM particles are neutral under $SU(3)_D$, while the dark quarks transform in its fundamental representation, but are not charged under the SM gauge group. A bi-fundamental scalar mediator X_D, transforming as $(3, \bar{3})$ under $SU(3)_c \times SU(3)_D$, connects SM quarks and dark quarks via Yukawa-like interactions. In Table III.1 the relevant particle content and charges under the model's symmetry group are given. The model is

field	$\mathbf{SU(3)_c \times SU(2)_L \times U(1)}$	$\mathbf{SU(3)_D}$
X_D	$(3, 1, \frac{2}{3}/-\frac{1}{3})$	$(\bar{3})$
Q_D	$(1, 1, 0)$	(3)
d_R	$(3, 1, -\frac{1}{3})$	(0)
u_R	$(3, 1, \frac{2}{3})$	(0)

Table III.1: Charges under the SM and dark gauge group for RH SM quarks, dark quarks and the bi-fundamental mediator X_D.

then described by

$$\mathcal{L} \supseteq \mathcal{L}_{SM} - \frac{1}{4} G_{D,\mu\nu} G_D^{\mu\nu} + i\bar{Q}_D \not{D} Q_D - m_{Q_D} \bar{Q}_D Q_D + D_\mu X_D^\dagger D^\mu X_D + m_X |X_D|^2 + \mathcal{L}_{Yuk}, \tag{III.2}$$

with

$$\mathcal{L}_{Yuk} = -\kappa_{\alpha i} \bar{q}_{R_i} Q_{D_{L_\alpha}} X_D + h.c. \tag{III.3}$$

in the UV. Here, G_D is the $SU_D(3)$ field strength tensor, m_Q the Dirac mass of the dark quarks and D_μ, $\not{D}$ the appropriate covariant derivatives. The Yukawa-like coupling of visible to dark sector $\kappa_{\alpha i}$ is a 3×3 matrix and q_R are RH SM quarks. Again, Roman indices are SM flavour indices and Greek one dark flavour indices. In the full Lagrangian in Equation III.2 the flavour indices are suppressed. Depending on the hypercharge of X_D the dark sector interacts either with the up-type quarks ($Y_X = \frac{2}{3}$) or the down-type quarks ($Y_X = -\frac{1}{3}$). In Chapter IV, we focus on the latter and discuss the phenomenological consequences of this choice. Then, in Chapter V the case of $Y_X = \frac{2}{3}$ is studied.
An interesting feature of this model is the fact that due to this Yukawa-like coupling the SM flavour gets imprinted on the dark sector. The coupling κ can be decomposed as

$$\kappa = VDU, \tag{III.4}$$

where for $n_D = 3$ V and U are unitary 3×3 matrices and D is a non-negative diagonal 3×3 matrix of the form [280]

$$D = (\kappa_0 \cdot \mathbb{1} + \mathrm{diag}\,(\kappa_1, \kappa_2, -\kappa_1 - \kappa_2))\,. \tag{III.5}$$

Choosing $m_{Q_{\alpha\beta}} = \delta_{\alpha\beta} m_{Q_{\alpha\beta}}$, meaning the dark quark masses are degenerate on the Lagrangian level, the resulting dark flavour symmetry $U(3)_d$ can be used to rotate V away. Then, κ is the only source of flavour violation in the dark sector. An interesting consequence arises in the case of $n_D > 3$. For $n_D > 3$ there is an unbroken $U(n_D - 3)$ symmetry in the dark sector resulting in stable dark pions. For example, in case of $n_D = 4$, there are six (three) stable dark pions, for the CP phases $\delta_{ij} \neq 0$ $(= 0)$, $i, j = 1, 2, 3, 4$. This case, however, is not studied in the scope of this work. Finally, U can be written as

$$U = U_{23} U_{13} U_{12}, \tag{III.6}$$

with U_{ij} the rotational matrices for ij, e.g.

$$U_{12} = \begin{pmatrix} \cos\theta_{12} & \sin\theta_{12} e^{-i\delta_{12}} & 0 \\ -\sin\theta_{12} e^{-i\delta_{12}} & \cos\theta_{12} & \\ 0 & 0 & 1 \end{pmatrix}, \tag{III.7}$$

where θ_{ij} are the rotation angles and we set the CP phases $\delta_{ij} = 0$.
Similarly to QCD, the dark sector confines below the dark confinement scale Λ_D, which is approximately the mass of the majority of dark hadrons. In the limit $m_{Q_D} \to 0$ and $m_X \to \infty$ the model features a global dark chiral symmetry $SU(3)_{d_L} \times SU(3)_{d_R}$. The spontaneous symmetry breaking of $SU(3)_{d_L} \times SU(3)_{d_R}$ to its diagonal group $SU(3)_{dV}$ by the dark quark condensate $\langle \bar{Q}_{D\alpha} Q_{D\beta} \rangle \propto \delta_{\alpha\beta} \Lambda_d^3$ leads to eight Nambu-Goldstone bosons $\pi_{D_1}, ..., \pi_{D_8}$. However, we consider massive dark quarks with $m_{Q_D} \ll \Lambda_D$. In this case $\pi_{D_1}, ..., \pi_{D_8}$ are pNGBs, that are parametrically lighter than the other dark hadrons. In the following, we refer to them as *dark pions*.
Opposite to the dark mesons, that have no conserved charge and can decay to SM states, the dark baryons carry a conserved *dark baryon number*. Therefore, the lightest dark baryon is stable and the DM candidate of the model. With the exception of the DM candidate all dark hadrons and glueballs decay promptly into dark pions, so that the dark pions are governing the phenomenology of such models. The model setup is shown in Fig. III.1. Besides the dark confinement scale Λ_D the dark mediator mass m_X, the DM mass m_{p_D} and the dark pion mass m_{π_D} are the relevant mass scales, that need to be considered in this model setup. In asymmetric DM models where the DM candidate has similar properties to SM baryons a common origin of the DM and the SM baryon abundance in

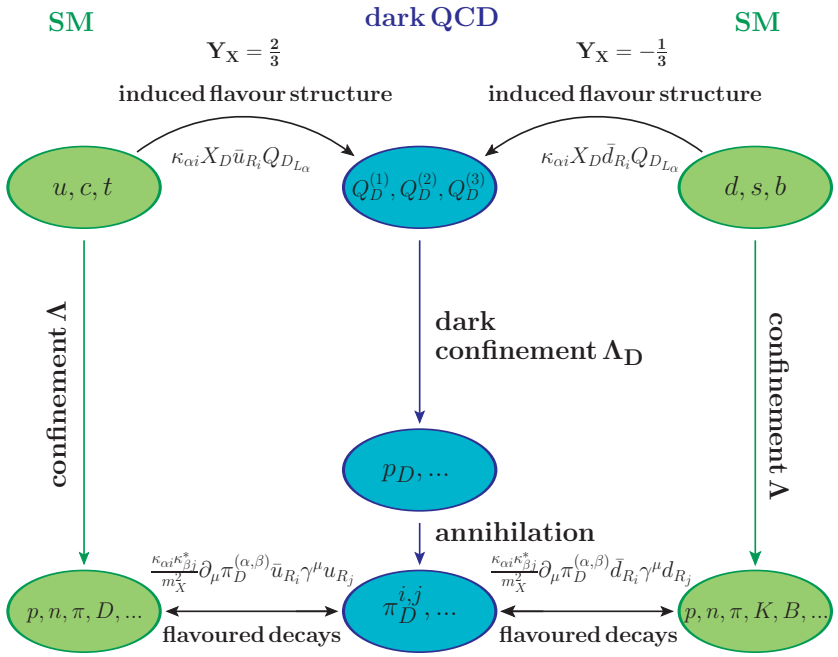

Figure III.1: Schematic view of the here considered dark QCD model for hypercharge $Y_X = \frac{2}{3}$ and $Y_X = -\frac{1}{3}$. In the middle in blue the dark quarks are shown, which confine at the scale Λ_D to form dark baryons. The heavier dark hadrons denoted p_D decay to the light dark pions. On the left and right the SM quark-type is shown in green, to which the dark sector quarks couple for $Y_X = \frac{2}{3}$ and $Y_X = -\frac{1}{3}$. SM quarks confine at the confinement scale Λ. The resulting SM hadrons interact with the dark pions as shown in the lowest part of the figure.

the present-day universe is assumed, either by both sectors sharing a primordial asymmetry produced in an arbitrary sector, or from the fact that both asymmetries are produced by the same process. Consequently, DM and SM baryons also should have similar number density leading to

$$\frac{m_{DM}}{m_{proton}} \simeq \frac{\Omega_{DM}}{\Omega}, \tag{III.8}$$

where m_{DM} and m_{proton} are the masses of the DM candidate and the SM proton, while Ω denotes the mass density of the respective component. From observation $\frac{\Omega_{DM}}{\Omega} \simeq 5$ is known [103, 281] and, thus, we assume $m_{DM} \simeq 5 \times m_{proton}$ up to factors of order one depending on the actual mechanism of symmetry sharing. This motivates a choice of $\Lambda_D \sim \mathcal{O}(1-10)$ GeV since in the here considered model the DM candidate is the lightest stable dark baryon with a mass of order of the confinement scale Λ_D of the dark gauge group. In [11] it was shown how a dynamical mechanism can relate the QCD and dark QCD confinements scales at the GeV scale. Other possibilities for GeV scale DM can be found in e.g. [172, 174, 175, 178, 179, 282–306].
Here, the asymmetry is shared via the mediator X_D. The coupling of dark and visible sector via X_D also allows for an efficient annihilation of the symmetric relic DM density back into SM particles. For QCD-like dark sectors pairs of dark baryons and dark anti-baryons annihilate into dark pions. Then, the dark baryon relic density is determined by the DM asymmetry. The entropy transfer to the visible sector for models with $n_D \leq 3$ happens due to dark pions decaying to SM particles.

An upper bound for the mediator mass can be found from Big Bang Nucleosynthesis: In order to not interfere with BBN dark pions should have a lifetime of less than a second. This leads to an upper bound of the mediator mass of order of 100 TeV. However, in [11] it was shown that lower mediator masses are more likely leading to $\Lambda_D \sim \Lambda$. Due to the mechanism considered in [11] a specific ratio of the QCD and dark QCD gauge couplings is ensured at the scale m_X due to the mediator. Therefore, we generally assume $m_X \sim \mathcal{O}(1)$ TeV.
To understand the phenomenology of the model first the dark pion spectroscopy needs to be studied. As $N_D = n_D = 3$ was chosen, the effective theory for the dark pions can be written analogously to QCD pions and Kaons with the three dark quarks acting as the dark sector counterparts to the three light SM quarks u, d and s. Using

$$\Pi_D = \pi_{D_a}\frac{\lambda_a}{2} = \frac{1}{2}\begin{pmatrix} \pi_{D_3} + \frac{\pi_{D_8}}{\sqrt{3}} & \pi_{D_1} - i\pi_{D_2} & \pi_{D_4} - i\pi_{D_5} \\ \pi_{D_1} + i\pi_{D_2} & -\pi_{D_3} + \frac{\pi_{D_8}}{\sqrt{3}} & \pi_{D_6} - i\pi_{D_7} \\ \pi_{D_4} + i\pi_{D_5} & \pi_{D_6} + i\pi_{D_7} & -\frac{2\pi_{D_8}}{\sqrt{3}} \end{pmatrix} \tag{III.9}$$

with λ_a, $a = 1, ..., 8$ the Gell-Mann matrices, the corresponding Goldstone matrix is

$$U_D(\Pi_D) = \exp\left(\frac{2i}{f_d}\Pi_D\right), \tag{III.10}$$

where f_d is the dark pion decay constant. Generally, f_d is a free parameter, however, we will later use $f_d = m_{\pi_D}$. In absence of interactions with the SM for small masses the dark pions are described in ChPT with

$$\mathcal{L}_{d\text{ChPT}} = \frac{f_d^2}{4}\text{Tr}\left(\partial_\mu U_D \partial^\mu U_D^\dagger\right) + \frac{f_d^2 B_D}{2} m_Q \text{Tr}\left(U_D^\dagger + U_D\right), \tag{III.11}$$

where B_D is a constant related to the dark pion mass via

$$m^2_{\pi_{D_a}} = m^2_{\pi_D} = 2m_Q B_d. \tag{III.12}$$

Analogously, the purely SM chiral Lagrangian is

$$\mathcal{L}_{\text{ChPT}} = \frac{f_\pi^2}{4}\text{Tr}\left(\partial_\mu U \partial^\mu U^\dagger\right) + \frac{f_\pi^2 B_0}{2}\text{Tr}\left(m_q U^\dagger + U m_q^\dagger\right) \tag{III.13}$$

with $B_0 \approx m_\pi / (m_u + m_d)$.
Besides small radiative corrections from the interactions with SM particles the dark pions are degenerate in mass. The radiative corrections define the new mass eigenstates

$$\begin{aligned} \pi_D^{(1,2)} &= \frac{1}{\sqrt{2}}\left(\pi_{D_1} - i\pi_{D_2}\right), \\ \pi_D^{(1,3)} &= \frac{1}{\sqrt{2}}\left(\pi_{D_3} - i\pi_{D_4}\right), \\ \pi_D^{(2,3)} &= \frac{1}{\sqrt{2}}\left(\pi_{D_6} - i\pi_{D_7}\right), \\ \pi_D^3 &= \pi_D^3, \\ \pi_D^8 &= \pi_D^8. \end{aligned} \tag{III.14}$$

The dark quark content of the mass eigenstates in Equation III.14 is given in Table III.2. For small dark pion masses $m_{\pi_D} \lesssim 4\pi f_\pi$ also the interactions with the SM particles are

Dark Pion	Dark Quark Content
$\pi_D^{(1,2)}$	$\bar{Q}_{D2}Q_{D1}$
$\pi_D^{(1,3)}$	$\bar{Q}_{D3}Q_{D1}$
$\pi_D^{(2,3)}$	$\bar{Q}_{D3}Q_{D2}$
π_D^3	$\frac{1}{\sqrt{2}}\left[\bar{Q}_{D1}Q_{D1} - \bar{Q}_{D2}Q_{D2}\right]$
π_D^8	$\frac{1}{\sqrt{6}}\left[\bar{Q}_{D1}Q_{D1} + \bar{Q}_{D2}Q_{D2} - 2\bar{Q}_{D3}Q_{D3}\right]$

Table III.2: Dark quark content of the dark pion mass eigenstates.

best described in ChPT. The Lagrangian describing the interaction between the visible and dark sector is

$$\mathcal{L}_{\text{ChPT}}^{\text{mix}} = -\frac{f_d^2 f_\pi^2}{2m_{X_D}^2}\kappa_{\alpha i}\kappa_{\beta j}^*\text{Tr}\left(c_{\beta\alpha}U_D^\dagger\left(\partial_\mu U_D\right)\right) \times \text{Tr}\left(c_{ij}U\left(\partial^\mu U\right)^\dagger\right) \tag{III.15}$$

with the projection matrices

$$c_{\alpha\beta}^{mn} = \delta_\alpha^m\delta_n^\beta, \quad \alpha,\beta = 1,2,3, \quad c_{ij}^{mn} = \delta_i^m\delta_j^n, \quad i,j = 1 \tag{III.16}$$

and zero otherwise. On the other hand, for larger dark pion masses quark-hadron duality [307, 308] gives

$$\mathcal{L}_{\text{mix}} = i\frac{f_d^2}{2m_{X_D}^2}\kappa_{\alpha i}\kappa_{\beta j}^*\text{Tr}\left(c_{\beta\alpha}U_D^\dagger\left(\partial_\mu U_D\right)\right)(\bar{u}_{Ri}\gamma^\mu u_{Rj}). \tag{III.17}$$

From Equations III.15 and III.17 the parts describing interactions of SM quarks and dark pions decays are

$$\mathcal{L}_{\text{ChPT}}^{\text{mix}} \supset -\frac{f_d f_\pi^2}{2m_{X_D}^2}\sum_{a=3,8}\sum_{\alpha\beta}\kappa_{\alpha i}\kappa_{\beta j}^*\left(\lambda^a\right)_{\alpha\beta}\partial_\mu\pi_D^a \times \text{Tr}\left(c_{ij}U\left(\partial^\mu U\right)^\dagger\right) \tag{III.18}$$

and

$$\mathcal{L}_{\text{mix}} \supset -\frac{f_d}{2m_{X_D}^2}\sum_{a=3,8}\sum_{\alpha\beta}\kappa_{\alpha i}\kappa_{\beta j}^*\left(\lambda^a\right)_{\alpha\beta}\partial_\mu\pi_D^a(\bar{u}_{Ri}\gamma^\mu u_{Rj}), \tag{III.19}$$

for π_D^3 and π_D^8, while for $\pi_D^{(\alpha,\beta)}$ they are

$$\mathcal{L}_{\text{ChPT}}^{\text{mix}} \supset -\frac{f_d f_\pi^2}{2m_{X_D}^2}\sum_{\alpha\beta}\kappa_{\alpha i}\kappa_{\beta j}^*\partial_\mu\pi_D^{(\alpha,\beta)} \times \text{Tr}\left(c_{ij}U\left(\partial^\mu U\right)^\dagger\right) \tag{III.20}$$

and

$$\mathcal{L}_{\text{mix}} \supset -\frac{f_d}{2m_{X_D}^2}\sum_{\alpha\beta}\kappa_{\alpha i}\kappa_{\beta j}^*\partial_\mu\pi_D^{(\alpha,\beta)}(\bar{u}_{Ri}\gamma^\mu u_{Rj}), \tag{III.21}$$

respectively. For the phenomenological studies of this model we focus on $m_{\pi_D} \sim \mathcal{O}(1-10)$ GeV where the quark-hadron duality picture is valid and dark pions decay mostly to light quarks. Consequently, we are most interested in these decays. For the chosen dark pion mass range the dark pion decay width to a pair of quarks is

$$\Gamma(\pi_D^b \to q_i\bar{q}_i) = \frac{N_c f_D^2 m_{\pi_D}}{64\pi m_{X_D}^4}\left|\kappa_{\alpha i}\kappa_{\beta j}^*(\lambda^b)_{\alpha\beta}\right|^2\left[\left(m_{q_i}^2 + m_{q_j}^2\right) - \frac{\left(m_{q_i}^2 - m_{q_j}^2\right)^2}{m_{\pi_D}^2}\right]$$

$$\times \sqrt{\left(1-\frac{\left(m_{q_i}+m_{q_j}\right)^2}{m_{\pi_D}^2}\right)\left(1-\frac{\left(m_{q_i}-m_{q_j}\right)^2}{m_{\pi_D}^2}\right)}\Theta(m_{\pi_D}-(m_{q_i}+m_{q_j})) \tag{III.22}$$

for π_D^b with $b = 3, 8$ and

$$\Gamma(\pi_D^{(\alpha,\beta)} \to q_i\bar{q}_i) = \frac{N_c f_D^2 m_{\pi_D}}{32\pi m_{X_D}^4}\left|\kappa_{\alpha i}\kappa_{\beta j}^*\right|^2\left[\left(m_{q_i}^2+m_{q_j}^2\right)-\frac{\left(m_{q_i}^2-m_{q_j}^2\right)^2}{m_{\pi_D}^2}\right]$$
$$\times \sqrt{\left(1-\frac{\left(m_{q_i}+m_{q_j}\right)^2}{m_{\pi_D}^2}\right)\left(1-\frac{\left(m_{q_i}-m_{q_j}\right)^2}{m_{\pi_D}^2}\right)}\Theta(m_{\pi_D}-(m_{q_i}+m_{q_j})) \tag{III.23}$$

for $\pi_D^{(\alpha,\beta)}$. Depending on the choice of κ and m_{π_D} one or more dark pions can decay at tree-level, while the others decay via one-loop level processes and are, therefore, long-lived. For smaller dark pion masses one needs to consider dark pion decays to light mesons in the chiral picture. However, as mentioned above, in our phenomenological studies of dark pions we always assume dark pion masses $m_{\pi_D} \sim \mathcal{O}(1-10)$ GeV where the partonic picture is valid. For details about the dark pion decay width in the ChPT picture see for example [10]. Decays to mesons in ChPT only appear for $m_{\pi_D} > 3m_\pi$ as pions are the lightest SM mesons and the decay to two pions is forbidden by CP. Below this mass the dark pions can only decay to two photons. The decay to photons arises from the dimension-5 operator $\pi_D \tilde{F}_{\mu\nu}F^{\mu\nu}$ and the corresponding decay width is [10]

$$\Gamma_{\pi_D^{\alpha,\beta}} \approx \sum_{k=1}^{3}\frac{\alpha_{em}^2}{2304\pi^3}\frac{f_{\pi_D}^2 m_{\pi_D}^3}{m_X^4}\left|\kappa_{\alpha k}\kappa_{\beta k}^*\right| \tag{III.24}$$

with the fine structure constant α_{em}.

CHAPTER IV

Dark QCD Coupled to the Down Sector

IV.1 Searches for Dark Mediators at LHC

In this chapter the phenomenology of a dark sector as introduced in [11] and described in Chapter III is studied for the whole range of dark pion masses. Here, $Y_X = -\frac{1}{3}$ has been chosen, so that the mediator connects RH down-type quarks with dark quarks. Previous phenomenological studies have been carried out in [10–12, 156–161, 166, 264, 280, 305, 306, 309]. A particularly interesting phenomenological feature of t-channel dark sectors is the *emerging jets* signature proposed in [12]. Emerging jets arise when dark quarks are produced at a collider experiment and form dark jets consisting of dark hadrons, which then decay back to SM particles at a displaced vertex: Similar to their SM counterparts dark quarks undergo showering (the process of radiating (dark) gluons off (dark) quarks and the splitting of (dark) gluons into (dark) quark or gluon pairs) and hadronization, meaning the conversion of dark partons to dark hadrons, forming a dark jet. As explained in Chapter III, dark hadrons, with the exemption of the stable lightest dark baryon, decay fast to dark pions, which in turn decay back into SM particles. Each dark pion decays at a different length due to its characteristic lifetime in the laboratory frame $\beta\gamma c\tau_{\pi_D}$ depending on its boost $\beta\gamma = p_T/m_{\pi_D}$, where p_T is the transverse momentum, and, therefore, on its individual momentum. In addition, the actual decay points for a given lifetime $c\tau_{\pi_D}$ are exponential distributed. Consequently, from a radial perspective, a dark jet deposits very little energy at the interaction point and then emerges with every dark pion that decays into visible particles. This is shown in Figure IV.1 where the dashed grey lines represent dark pions and the colourful lines SM particles. Based on this, a respective search at CMS has been carried out in [310]. However, a search for emerging jets only covers the intermediate lifetime regime of dark pions. Dark pions with very small lifetimes look like prompt SM jets, while large lifetimes lead to a missing energy signal. Here, we recast three experimental searches including the emerging jets search [310] to cover the complete lifetime range of dark pions and combine them with constraints from flavour, cosmology and direct detection experiments as has been discussed in detail in [10] for a non-trivial flavour structure for the QCD-like dark sector.

IV.1.1 Implementation and Phenomenological Parameters

In QCD-like dark sectors low-energy parameters cannot be calculated from the UV using perturbative techniques. Equally, since strongly interactive theories inherently depend on UV parameters, minimal models, which do not rely on top-down priors are not a viable

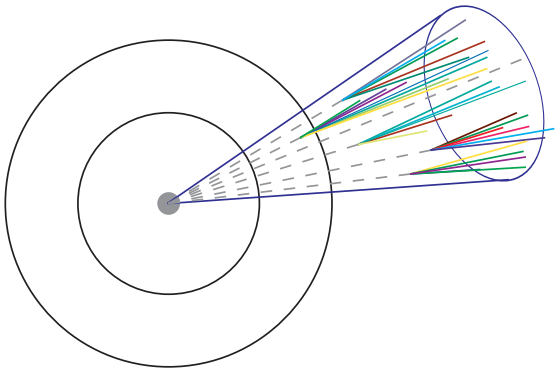

Figure IV.1: Schematic view of an emerging jet: dark pions (depicted as grey dashed lines) are produced at the interaction point, for example from the decay of mediators, and, according to their respective boosts, decay at various points in the detector to SM particles (illustrated by the coloured lines) producing an emerging jet.

option to reliably describe the infrared (IR) parameters of QCD-like dark sectors. Instead, we use our experience with low-energy QCD to choose parameters.
We start with the UV theory where the model is specified by four parameters: the masses of the dark quarks m_{Q_D}, the mediator mass m_X, the dark confinement scale Λ_D determining the dark strong coupling and the Yukawa-coupling κ_{ij}. For $\kappa_{ij} = \kappa_0$ the dark pion lifetime is [2, 12]

$$c\tau_{\pi_D} = 80\ mm \cdot \frac{1}{\kappa_0^4} \cdot \left(\frac{2\ \text{GeV}}{f_{\pi_D}}\right)^2 \left(\frac{100\ \text{MeV}}{m_{d_i}}\right)^2 \left(\frac{2\ \text{GeV}}{m_{\pi_D}}\right) \left(\frac{m_X}{1000\ \text{GeV}}\right)^4 \tag{IV.1}$$

with m_{d_i} the heaviest down-type quark mass kinematically accessible. In Equation IV.1 the phenomenological parameters f_{π_D} and m_{π_D} were introduced. As explained above, these two parameters cannot be calculated analytically. However, since the dark quark mass term in Equation III.2 explicitly breaks the dark chiral symmetry, the dark pion mass is proportional to the dark quark mass. Consequently, we can use m_{π_D} instead of m_{Q_D} as a free parameter. In QCD we find that $m_\pi \approx f_\pi$ and accordingly we use $f_{\pi_D} = m_{\pi_D}$. From naive dimensional analysis one would expect $f_{\pi_D} \approx \Lambda_D/(4\pi)$. In this case f_{π_D} would be independent of m_{π_D}. For our purpose, however, we always vary m_{π_D}, so that this relation is not grossly violated. Then, the remaining free parameters are

$$m_X, \quad m_{\pi_D}, \quad \tau_{\pi_D}. \tag{IV.2}$$

In our analysis we vary these parameters independently.
In case of non-universal Yukawa-couplings κ_{ij} the number of free parameters grows drastically. But even in this case, the main distinguishable parameter between the different dark pions are still the different lifetimes, while the masses remain nearly degenerate. In the case of $n_D = 3$ and in absence of CP violation the five dark pions in Equation III.14 arise, which generally can all have different lifetimes. More generally, for n_D dark quarks there are $n_D^2 - 1$ Goldstone bosons, which reduce to $n_D\,(n_D + 1)\,/2 - 1$ without CP violations as the off-diagonal dark pions form particle-antiparticle pairs (cf. Equations III.10 and III.14). For modelling reasons in Section IV.1.3 we only distinguish between two different dark pion lifetimes with varying relative probabilities. In this case the free parameters are

$$m_X, \quad m_{\pi_D}, \quad \tau_{\pi_{D_1}}, \quad \tau_{\pi_{D_2}}. \tag{IV.3}$$

The process under consideration is mediator pair-production with each mediator subsequently decaying into a quark and a dark quark ($pp \to X_D X_D^\dagger$, $X_D \to \bar{d}_i Q_D$). For couplings $\kappa \sim \mathcal{O}(1)$ the mediator decays before SM and dark showering and hadronization begin. We, therefore, treat $X_D \to \bar{d}_i Q_D$ as a hard process. The down-type quark d_i then undergoes normal SM showering and hadronization, forming a visible jet. Similarly, also the dark quark Q_D undergoes showering and hadronization in the dark sector. The showering of dark partons is theoretically well understood and described by the DGLAP (Dokshitzer-Gribov-Lipatov-Altarelli-Parisi) evolution equations [311–313]. Hadronization, on the other hand, is a non perturbative process that so far can only be modelled for QCD and we infer from it to dark QCD.
Unlike in [12] we didn't perform the event generation, showering and hadronization in [2] solely in `Pythia v8.240` [314, 315]. Instead, the mediator X_D and the dark quarks Q_D were implemented in the `FeynRules` package [316] and the *Universal Feynrules Output* (UFO) [317] was produced. Then, the UFO was used to generate parton level events of the process $pp \to X_D X_D^\dagger$ in `MadGraph5_aMC@NLO v2.6.4` [318]. Generated events were showered and hadronized, both in the dark and visible sector, using the *HiddenValley* (HV) implementation [200, 201, 319] of `Pythia v8.240`. Note that dark baryon production was not implemented in `Pythia v8.2` because it is suppressed by $1/N_D$ as (dark) baryons consist of $N = 3$ ($N_D = 3$) (dark) quarks and additionally by kinematics. In QCD baryon production is a 10% effect, and we expect it to be similar in dark QCD [201]. Heavier dark mesons decay promptly to dark pions which then decay back into SM particles and, thus, govern the phenomenology.
In the HV implementation several more phenomenological parameters appear. We choose them in a way that gives the best agreement of the shower multiplicity with the theoretical prediction. In [12] it was found that the best agreement is obtained using

$$2m_{\pi_D} = m_{Q_D} = \Lambda_D = \frac{1}{2} m_{\rho_D}, \tag{IV.4}$$

where m_{ρ_D} is the mass of the dark vector meson ρ_D. Due to naive spin counting and neglecting kinematic we expect a production rate of dark vector mesons to dark pions of $\#\rho_D : \#\pi_D = 3 : 1$. However, with the mass ordering in Equation IV.4 the dark vector meson ρ_D decays promptly to dark pions and, therefore, not effect the phenomenology. It is important to point out that the dark quark mass in Equation IV.4 is not the same as introduced in the dark sector Lagrangian III.2, but should rather be considered as a "constituent" quark mass. We study the parameter space for the three benchmark points

Parameter	**point A**	**point B**	**point C**
m_{Q_D}	10	4	20
m_{π_D}	5	2	10
m_{ρ_D}	20	8	40

Table IV.1: Summary of the different benchmark points used to analyze the dark QCD parameter space. All masses are given in GeV.

in Table IV.1, which all fulfill Equation IV.4.
The various production channels for pairs of mediators are shown in Figure IV.2. The upper panel shows the s-channel diagrams and the four-point gluon fusion production, while the lower panel shows the t-channel diagrams. The advantage of using `MadGraph5_aMC@NLO v2.6.4` for simulating mediator pair production in comparison to

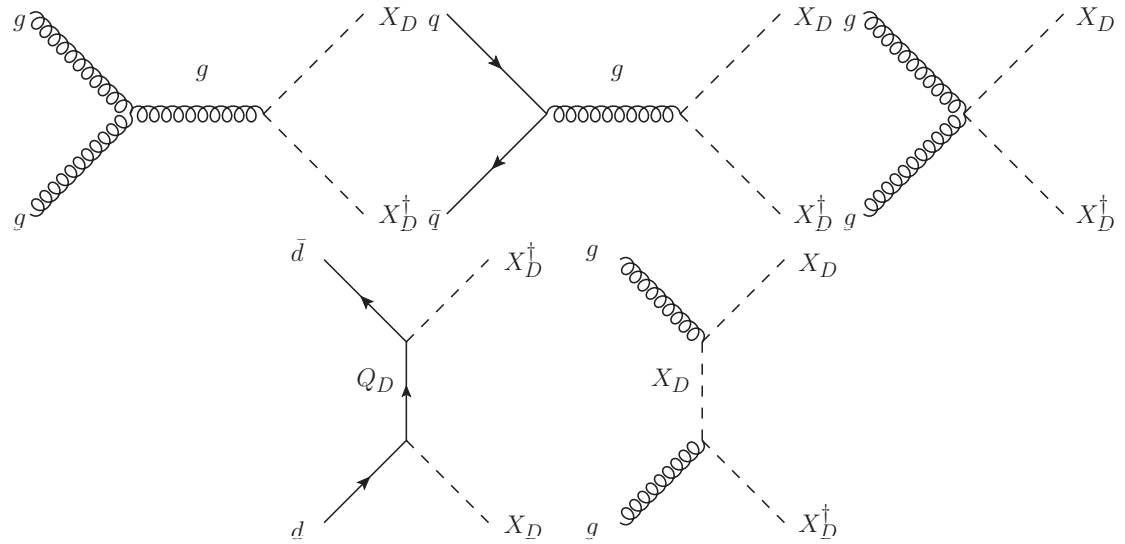

Figure IV.2: Feynman diagrams for the pair production of mediators. The **upper** panel shows the s-channel modes and the four-point gluon fusion process, while the **lower** panel shows the t-channel modes.

`Pythia v8.240` is that additional production channels can be taken into account. Especially, including the production via t-channel exchange of a dark quark can have a significant impact on the production cross section. In Figure IV.3 the pair production cross section is shown as a function of the mediator mass for $\kappa_0 = 1$ (left) and as a function of κ_0 for $m_X = 1.2$ TeV (right) for LHC at $\sqrt{s} = 13$ TeV. It can be seen that

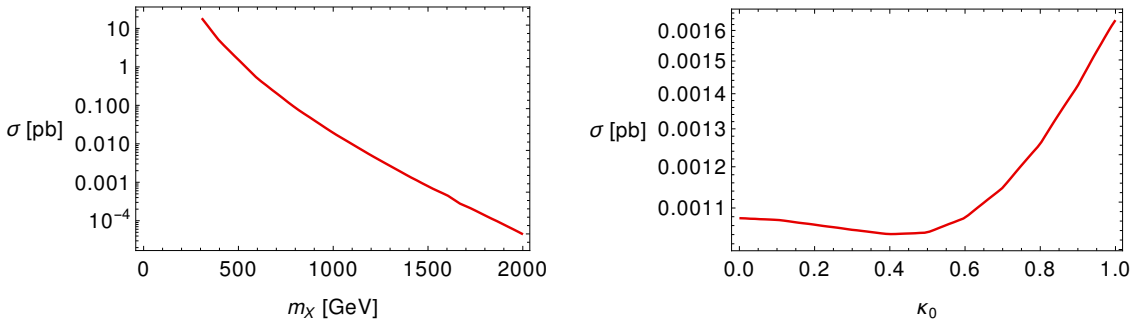

Figure IV.3: Cross section for mediator pair production at LHC with $\sqrt{s} = 13$ TeV as a function of the mediator mass m_X for $\kappa_0 = 1$ (**left**) and as a function of κ_0 for $m_X = 1200$ GeV (**right**).

the cross section decreases slightly for $\kappa_0 \lesssim 0.5$, before increasing for larger values of κ_0. The decrease for $\kappa_0 \lesssim 0.5$ originates from a destructive interference from the t-channel exchange of Q_D. In the following, we consider τ_{π_D} instead of κ_0 as a free parameter.

IV.1.2 Recast of the LHC Searches

As mentioned above, we focus here on the pair production of mediators, that both decay to a visible and a dark jet. Generally, mediators could also be produced via single production modes, exemplary parton level Feynman diagrams are shown in Figure IV.4, leading to a slightly different signature. In this section, we use $\kappa = \mathbb{1}\kappa_0$ with $\kappa_0 = 1$, so that all dark pions are degenerate in mass and lifetime. Following the experimental search

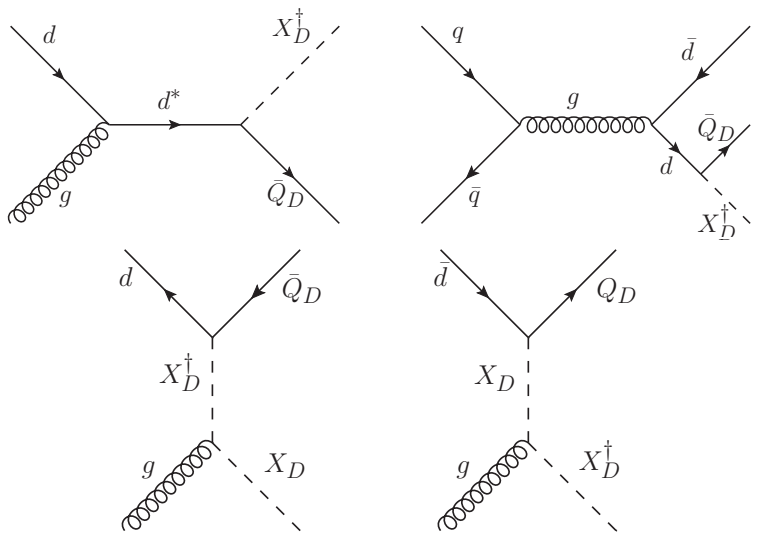

Figure IV.4: Exemplary Feynman diagrams for the single production of mediators in the s-channel (**top**) and t-channel (**bottom**).

in [310] where the only non-negligible Yukawa-coupling to the dark sector is the one to down quarks we consider for the recasts only mediator decays to a dark quark and a down quark in `Pythia v8.240`. Mediator pair production leads to a final state consisting of two SM jets and two jets containing mainly dark pions (as all other dark hadrons except of the lightest dark baryon decay promptly to dark pions), which then decay back into SM particles. Depending on the dark pion lifetime three different scenarios are possible: (1) If the dark pions are stable on detector scales ($c\tau_{\pi_D} \geq 0.05$ m), they will appear as missing transverse energy (MET), (2) for intermediate lifetimes (0.001 m $\leq c\tau_{\pi_D} \leq 1$ m) dark pions will appear as the described emerging jets and (3) if they decay prompt ($c\tau_{\pi_D} \leq 0.1$ m), they will appear as visible jets. In addition, there are always two jets originating from the SM down-type quarks, so that the corresponding final states are (1) two QCD jets and missing energy, (2) two QCD jets and two emerging jets and (3) four QCD jets. The signatures of jets plus long-lived dark pions and jets plus promptly decaying dark pions also occur in the SM as jets plus missing energy and prompt jets, and can also arise in various other NP scenarios. Therefore, already existing experimental searches that are not specific for our model can be recast to find bounds in the respective lifetime regions. On the other hand, after the proposal of the emerging jets signature a specific search has been done in [310] and sets boundaries on the mediator mass in the intermediate lifetime regime. Nonetheless, we also recast this search. Doing so allows us to verify our recast procedure before using it in a flavoured scenario. While each recast follows a different procedure depending on the search strategy of the original search, for each of them 10000 events have been simulated for various lifetimes as described in Section IV.1.1.

Jets plus MET and Four Jets Search Recast

For the long-lived dark pions (2 jets + MET) and the prompt dark pions (4 jets) scenarios the LHC searches in [320] and [321] have been recast to find the allowed parameter space. The jets plus MET search in [320] requires at least two jets inside $|\eta| \leq 2.4$. The sum of scalar momenta of jets (H_T) with $|\eta| \leq 2.4$ is required to be $H_T > 300$ GeV. Similarly, the magnitude of $\vec{H}_T^{miss}$, which is the negative vector sum of the transverse momenta of

jets with $|\eta| < 5$ for better representation of the missing energy of an event, has to satisfy $H_T^{miss} > 300$ GeV. Furthermore, no isolated electron or muon with $p_T > 10$ GeV, no isolated track with transverse mass $m_T < 100$ GeV and $p_T > 10$ GeV and no isolated photon candidate with $p_T > 100$ GeV are allowed. Finally, criteria on the azimuthal angle difference between the jets and $\vec{H}_T^{miss}$ are used.
On the other hand, the four jets search in [321] only considers events with at least two tracks with $p_T > 400$ MeV originating from the primary vertex (PV). Events need to have at least four jets with $p_T > 120$ GeV and $|\eta| < 2.4$. More selection criteria based on the distance of jet pairs are applied in the analysis. The signal selection requirements we used are summarised for both searches in Table IV.2. We apply them as follows:

For the jets plus MET search the dark pions need to decay outside of the hadronic

jets+MET search	**4 jets search**
$N_{jet} \geq 2$ for jets with $\|\eta\| \leq 2.4$	$N_{jet} \geq 4$ for jets with $\|\eta\| \leq 2.4$
$H_T > 300$ GeV, where H_T is the scalar p_T sum of the jets	$p_T > 120$ GeV for each jet
$H_T^{miss} > 300$ GeV, magnitude of negative $\vec{p}_T$ sum with $\|\eta\| < 5$	at least two tracks with $p_T > 400$ MeV

Table IV.2: Summary of the requirements for an event to count as signal for the jets plus MET search and the four jets search.

calorimeter to fulfill the missing energy requirement of the search. To ensure this for each event the decay point of the dark pions is recorded and checked. If dark pions decay outside of the hadronic calorimeter, their momenta in x- and y-direction will be summed to obtain $\vec{p}_T^{miss}$. The sum over the $\vec{p}_T^{miss}$ of all dark pions in an event gives $\vec{H}_T^{miss}$, from which H_T^{miss} is found. Here, all particles with $|\eta| < 5$ are considered for better accuracy on the MET. If $H_T^{miss} > 300$ GeV and the two additional requirements in Table IV.2 are fulfilled, an event will be counted as signal. This procedure is performed for lifetimes $0.05 \text{ m} \leq c\tau_{\pi_D} \leq 100$ m.
In case of the four jets search we make use of the `Pythia v8.240` variables *ParticleDecays:xyMax* and *ParticleDecays:limitCylinder*, so that all particles decaying outside the detector are now considered as stable. From all particles visible to the detector jets are formed with *SlowJet* using the anti-k_T algorithm [322] with a cone size $R = 0.4$ and a pseudorapidity limit $|\eta| < 2.4$. If an event fulfills the requirements of Table IV.2, it will be counted as signal. The lifetime range where we employ the requirements for the four jets search is $0.001 \text{ mm} \leq c\tau_{\pi_D} \leq 100$ mm.
By using varying lifetimes for both scenarios, we find how the signal acceptance depends on the lifetime. We denote the number of events fulfilling the respective search requirements $N(c\tau_{\pi_D})$ with $N(c\tau_{\pi_D}) \leq 10000$. To get the actual acceptance rate we set baseline points for both searches and compare all other lifetimes to them. If the dark pions have large lifetimes $c\tau_{\pi_D} \geq 100$ m, they will be stable on detector scales. Thus, we can use this as an "infinite" lifetime limit for the jets plus MET search. In the "infinite" lifetime limit all dark pions decay outside of the detector, while with decreasing lifetimes an increasing number of dark pions decays inside of the detector and, thus, less events are counted as signal. Inversely, for the four jets search, the smallest lifetime gives the most events compared to events with larger dark pion lifetimes and can, therefore, be used as a baseline. Here, the smallest considered lifetime is $c\tau_{\pi_D} = 0.001$ mm. Based on the two baseline points $N_{MET}(100 \text{ m})$ and $N_{jets}(0.001 \text{ mm})$ we define the acceptance rates as a function

of the dark pion lifetime as

$$N_{MET}(c\tau_{\pi_D})/N_{MET}(100\text{ m}) \quad \text{and} \quad N_{jet}/N_{jets}(0.001\text{ mm}) \tag{IV.5}$$

for the jets plus MET and four jets scenario, respectively. The acceptance rates are shown in Figure IV.5. It can clearly be seen that both acceptance rates behave as expected,

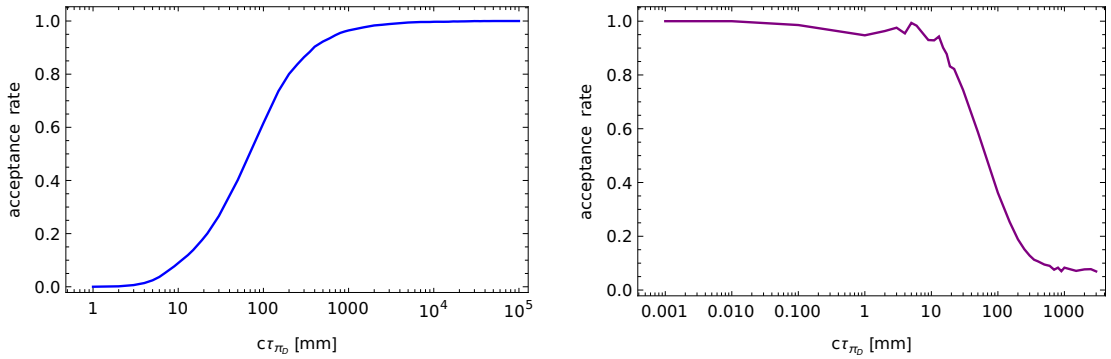

Figure IV.5: Acceptance rates as defined in Equation IV.5 as a function of the dark pion lifetime for the jets plus MET (**left**) and four jets search (**right**). This figure was created by a collaborator.

justifying our choice of baseline lifetimes. For lifetimes below a few millimeters (nearly) all dark pions decay in the detector, so that they are seen as QCD-like jets and do not contribute to the missing energy. Thus, the acceptance rate for the jets plus MET search (left panel) is zero and the one for the four jets (right panel) is approximately one. In the few millimeter to one meter region an increasing amount of dark pions decays outside of the detector, therefore, contributing to the missing energy. Consequently, the acceptance rate for the jets plus MET search increases, while it decreases for the four jets search. The fluctuations around $c\tau_{\pi_D} \sim 10$ mm are due to statistical fluctuations in the simulation and not due to some physical process. Finally, for lifetimes $c\tau_{\pi_D} \gtrsim 1$ m most of the dark pions decay outside of the detector, so that the acceptance rates of the jets plus MET search and the four jets search approach one and zero, respectively.
The effective signal production cross section in our model for these two searches can now be calculated by multiplying the mediator pair production cross section in the left panel of Figure IV.3 with the respective acceptance rate

$$\sigma_{eff} = \sigma_{X_D X_D} \times \frac{N(c\tau_{\pi_D})}{N(c\tau_0)}, \tag{IV.6}$$

where $c\tau_0$ is the baseline lifetime of the respective search. By comparing the effective cross section in Equation IV.6 to the at LHC observed cross section of the respective search exclusion limits on m_X are obtained. For each lifetime all m_X that lead to $\sigma_{eff} > \sigma_{LHC}$ are excluded. The exclusion limits from the jets plus MET search in [320] are shown in blue in Figure IV.7, IV.16 and IV.17 for the three benchmark points A, B and C in Table IV.1, while the same is shown for the four jets search in [321] in purple.

Emerging Jets Recast

Next, we recast the emerging jets search performed in [310] at $\mathcal{L} = 16.1$ fb^{-1}, which, in the following, we denote *experimental emerging jets search*. While we could also directly use the exclusion limits obtained in the experimental emerging jets search, a successful recast

of the search justifies the use of the same procedure to predict the discovery prospects in flavoured scenarios. To classify an emerging jet four new variables have been introduced in [310]. The first two variables are the median of the unsigned transverse impact parameters of associated tracks ($\langle IP_{2D} \rangle$), and second, the distance between the z position of the track at its distance of closest approach to the PV and the z position of the PV (PU_{dz}). As the third variable the parameter D_N is defined as

$$D_N = \sqrt{\left[\frac{z_{PV} - z_{trk}}{0.01 \text{ cm}}\right] + [IP_{sig}]} \tag{IV.7}$$

with z_{PV} the z position of the PV, z_{trk} the z position of the track at its closest approach to the PV, and IP_{sig} the transverse impact parameter significance of the track at its closest approach to the PV. Lastly, the fourth variable is called α_{3D}, which is the scalar p_T sum of the associated tracks with values of D_N smaller than a threshold, divided by the scalar p_T sum of all associated tracks [310].
These variables were tested in several selection sets. Additionally, every signal event is required to have at least four jets with $|\eta| < 2.0$. Two of these jets have to be tagged as emerging jets *or* one of them has to be tagged as an emerging jet and be associated with a large amount of missing energy. Finally, a requirement on the momentum of the sum of hadronic jets is imposed. Events will be counted as signal if all of these requirements are fulfilled. Based on this, in the experimental emerging jets search the signal acceptance rate is given as a function of the mediator mass m_X and the dark pion lifetime $c\tau_{\pi_D}$. Again, the acceptance rate is multiplied by the mediator pair production cross section to obtain the effective signal cross section σ_{eff}. Similar to the acceptance rate the expected number of background events is also given in [310] for each $(m_X, c\tau_{\pi_D})$ point. With this information the recast exclusion limit can be found by excluding all points with $\frac{S}{\sqrt{S+B}} \geq 2$ as for these points the signal would have been seen already.
In the experimental emerging jets search $m_{\pi_D} = 5$ GeV is used, corresponding to our benchmark point A. The exclusion limits from the actual search in [310] and the exclu-

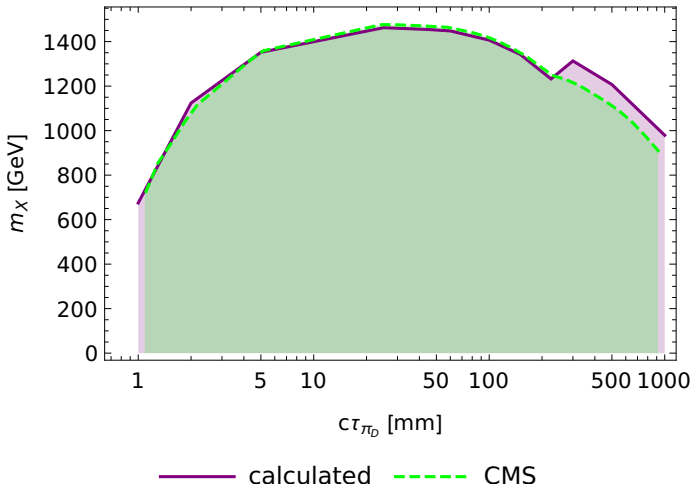

Figure IV.6: Constraints on the mediator mass from the jets plus emerging jets search, both from the CMS search in [310] (green) and the recast of this search (purple) with $m_{\pi_D} = 5$ GeV. This figure was created by a collaborator.

sion limits derived with the above described recast procedure are shown in Figure IV.6 in

green and purple, respectively. The recast constraint matches the CMS constraint well. Consequently, in the following it is assumed that the recast procedure can be safely generalised for flavoured scenarios. Nonetheless, in the parameter space plots in Figures IV.7, IV.16 and IV.17 we show the limits from the CMS search [310]. In a previous technical report of this search, the exclusion limit has been given for various values of m_{π_D} [323], which we use to set the appropriate bounds for the three benchmark points considered here. We show them together with the bounds from the recast of the jets plus MET and four jets search in the left panel of Figure IV.7 for benchmark point A, as well as in Figures IV.16 and IV.17 in Appendix IV.A for points B and C with solid green lines. As

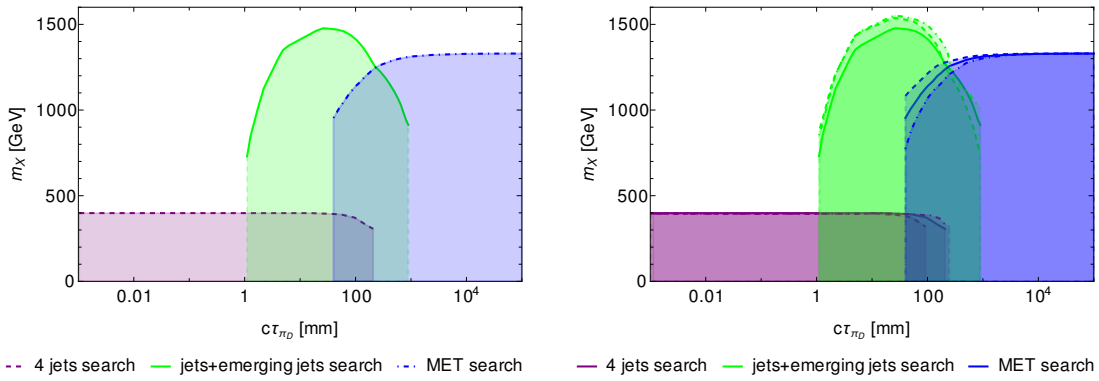

Figure IV.7: **Left:** Constraints on the mediator mass for the jets plus MET search (dashed, purple), jets plus emerging jets search (solid, green) and the four jets search (dot-dashed, blue). **Right:** Summary of the constraints for all benchmark points. Here, solid lines refer to benchmark point A, dashed (dot-dashed) lines to benchmark point B (C) of Table IV.1. Again, the purple shaded region on the left is excluded from the four jets search, the green shaded region in the middle from the jets and emerging jets search and the blue shaded region on the right from the jets plus MET search.

expected each of the three searches covers a different part of the parameter space. The least stringent search is the four jets search, covering mediator masses $m_X \lesssim 400$ GeV. Nonetheless, it is the most sensitive search for lifetimes $c\tau_{\pi_D} \lesssim 1$ mm. For larger lifetimes, the jets plus emerging jets search becomes more sensitive excluding mediator masses up to $m_X \sim 1500$ GeV for benchmark point A and slightly higher for benchmark points B and C. Finally, for $c\tau_{\pi_D} \gtrsim 100$ mm the jets plus MET search is the best search strategy and excludes mediator masses $m_X \lesssim 1300$ GeV. While this is comparable to the bound from the jets plus emerging jets search, it should be noted that for the latter only $\mathcal{L} = 16.1$ fb^{-1} have been used, while for the four jets search $\mathcal{L} = 36.7$ fb^{-1} [321] and for the jets plus MET search $\mathcal{L} = 137$ fb^{-1} [310] have been used. The latter is essentially the full LHC run 2 data set. Therefore, it can be expected that the jets plus emerging jets constraint will improve once the search is updated with the full LHC run 2 data set. The same should be true for the four jets search.

The right panel of Figure IV.7 shows the constraints for all three benchmark points. Solid lines refer to benchmark point A and dashed (dot-dashed) lines to benchmark point B (C) of Table IV.1. As before, the purple shaded region on the left is excluded from the four jets search, the green shaded region in the middle from the jets and emerging jets search, and the blue shaded region on the right from the jets plus MET search. Comparing the constraints from the three benchmark points we find that they are mostly robust for small changes of the dark pion mass. Only slight differences can be seen at the edges where the

searches lose sensitivity. Consequently, the here obtained bounds on the mediator mass are largely independent on the details of the dark sector.

IV.1.3 Beyond the Minimal Case

After finding the allowed parameter space for $\kappa_{ij} = \kappa_0$, we now consider a flavoured scenario, meaning a scenario with non-universal couplings κ_{ij} and, thus, varying dark pion lifetimes. Different lifetimes for dark pions can be achieved in `Pythia v8.240` by setting the *HiddenValley:nFlav* function to *on*. At the time the work of [2] was completed, `Pythia v8.240` could only distinguish between on- and off-diagonal dark pions, but did not include the possibility to handle the properties of individual dark pions. Consequently, it is also only possible to implement two dark pion lifetimes. Nonetheless, taking advantage of the possibility of distinguishing between the characteristic lifetimes of diagonal and off-diagonal dark pions, one can capture the main effects various lifetimes have on the phenomenology. In this case, the relative abundance of dark pions with one of the two lifetime is indirectly controlled by the number of dark flavours n_D. Generally, the ratio of diagonal to off-diagonal dark pions would be $(n_D - 1) / \left(n_D^2 - 1 - (n_D - 1)\right) = 1/n_D$. This means, for $n_D = 2$ there are $n_D - 1 = 1$ diagonal and $n_D^2 - 1 - (n_D - 1) = 2$ off-diagonal dark pions, while for $n_D = 3$ there are two diagonal and six off-diagonal dark pions. However, the string fragmentation model implemented in `Pythia v8.240` actually gives a ratio of $n_D / \left(n_D^2 - n_D - 1\right) = 1/(n_D - 1)$. Then, the ratio of diagonal to off-diagonal dark pions is $1:1$ for $n_D = 2$ and $1:2$ for $n_D = 3$. For both cases we vary the lifetime of diagonal and off-diagonal dark pions independently while keeping the dark pion mass for all dark pions fixed at $m_{\pi_D} = 5$ GeV (benchmark point A). This way we redo the recast of the three search strategy described in Section IV.1.2 with multiple combinations of dark pions lifetimes.

For the jets plus MET and the four jets searches the same recast procedure as for the unflavoured case can be used. For various combinations of dark pion lifetimes the respective acceptance rate is calculated as described in Equation IV.5, with the only difference that the baseline lifetime $c\tau_0$ refers now to the case where both diagonal and off-diagonal dark pions have $c\tau_{\pi_D} = c\tau_0$. Then, for each $(c\tau_{\pi_{D_{diagonal}}}, c\tau_{\pi_{D_{off-diagonal}}})$ point the effective signal cross section is calculated according to Equation IV.6 and the constraint on m_X is found by excluding all m_X with $\sigma_{eff} > \sigma_{LHC}$. The resulting exclusion limits for the jets plus MET search and the four jets search are shown in Figures IV.8 and IV.9. The left panel in both figures corresponds to $n_D = 2$ and the right one to $n_D = 3$. We use $c\tau_1$ for the lifetime of the diagonal dark pions and $c\tau_2$ for the lifetime of the off-diagonal ones. The contour lines show the maximal allowed value for m_X at each given point.

On the other hand, in case of the jets plus emerging jets search we have to adjust the recast strategy slightly. For the unflavoured scenario we used the experimental acceptance rate and number of background events from the experimental emerging jets search. However, to date no search for a flavoured scenario has been performed and, thus, no data on the acceptance rate and number of background events exists that could be used. Instead, we weight the acceptance rate from the experimental emerging jets search according to the probability with which the diagonal and off-diagonal dark pions are produced. As discussed above, due to the string fragmentation model used in `Pythia v8.240`, the probability to find a diagonal dark pion is $1/n_D$. Thus, for $n_D = 2$ ($n_D = 3$) the ratio of diagonal to off-diagonal dark pions and the corresponding acceptance rates is $1:1$ ($1:2$). The obtained total acceptance rate is again multiplied with the mediator pair production cross section. For the number of background events for every lifetime pair we also use the data from the experimental emerging jets search. In case the two lifetimes fall into different

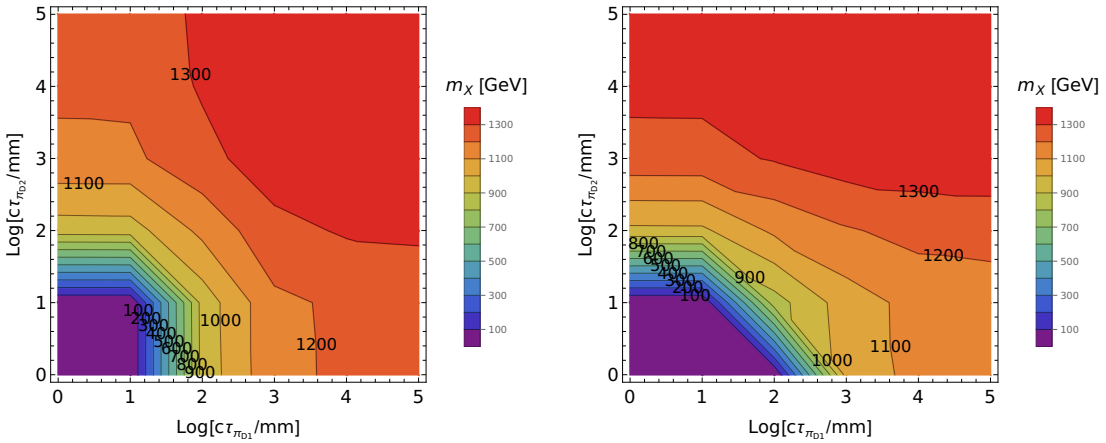

Figure IV.8: Constraints on the mediator mass as a function of $(c\tau_1, c\tau_2)$ for the jets plus MET search, where $c\tau_1$ ($c\tau_2$) is the lifetime of the (off-)diagonal dark pions. **Left** panel corresponds to $n_D = 2$, **right** to $n_D = 3$. This figure was created by a collaborator.

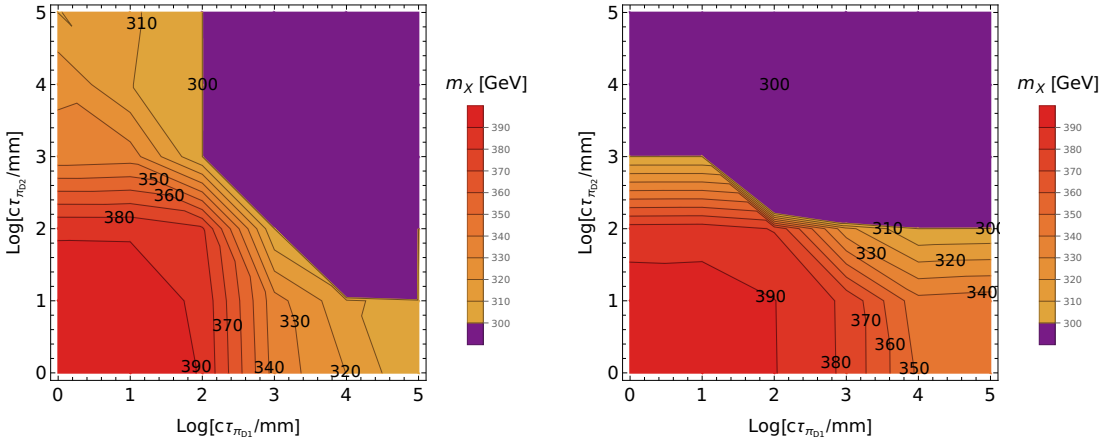

Figure IV.9: Constraints on the mediator mass as a function of $(c\tau_1, c\tau_2)$, same as Figure IV.8, but for the four jets search. This figure was created by a collaborator.

background bins for the same mediator mass, the larger number of background events is chosen to be conservative. Multiplying the effective signal cross section with the integrated luminosity of the search $\mathcal{L} = 16.1$ fb^{-1} and knowing the respective number of background events all points with $\frac{S}{\sqrt{S+B}} > 2$ are excluded. The resulting constraints on the mediator mass are shown in Figure IV.10. The results of the recast of the jets plus MET, four jets and jets plus emerging jets search for the flavoured scenario, which are shown in Figures IV.8, IV.9 and IV.10, are as expected. For $n_D = 2$ the constraint is symmetric, as suggested by the ratio of diagonal to off-diagonal dark pions being 1 : 1. The constraints following the diagonal where the lifetimes of the diagonal and off-diagonal dark pions are equal are in agreement with the constraints in the unflavoured scenario. In contrast, for $n_D = 3$ the limits depend more strongly on the off-diagonal dark pions. Besides the ratio of diagonal to off-diagonal dark pions being 1 : 2, the asymmetry also arises partly due to the used search strategies: More specifically, the jets plus MET search will stay partly sensitive even if the diagonal dark pions decay promptly, as the long-lived off-diagonal dark pions carry enough energy to fulfill the missing energy requirement of the search. Analogously, the four jets search remains partly sensitive for one of the dark pion times

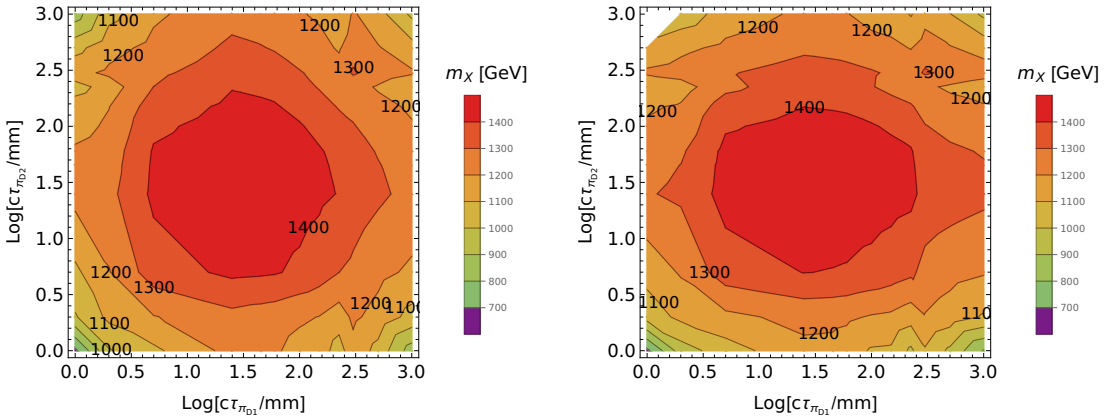

Figure IV.10: Constraints on the mediator mass as a function of $(c\tau_1, c\tau_2)$, same as Figure IV.8, but for the jets plus emerging jets search. This figure was created by a collaborator.

being long-lived, as long as enough of the other dark pion type decay promptly. The same symmetry can also be seen for the jets and emerging jets search. At this point it is worth pointing out that for this search only the lifetime range for which experimental data is available can be shown. Nonetheless, similar conclusions can be made for one dark pion species having a larger lifetime than considered in the experimental emerging jets search. Even if one of the dark pion lifetimes would be sent to infinity, the search would retain some sensitivity as long as the other dark pion species fulfill the search requirements. The opposite is not true, however. If one of the dark pions decays promptly, the effect on the acceptance rate will depend crucially on how the search is implemented experimentally: If prompt or almost-prompt jets are vetoed, as was proposed in the original emerging jets paper [12], the acceptance rate will drop to zero. This, however, does not rule out a search for emerging jets in a flavoured scenario where at least one dark pion decays prompt, but merely requires a new dedicated search strategy without a veto on prompt jets.

IV.2 Additional Constraints on Dark QCD

After having found the current collider constraints on the considered dark QCD model for both an unflavoured and a minimal flavoured scenario, the next step is to compare these to constraints and detection possibilities from other experimental searches. As the model provides a DM candidate and additional possibly long-lived states (the dark pions), constraints from direct detection experiments, such as XENON1T [128] and DARWIN [324] and a possible interference with BBN due to the long-lived dark pions need to be taken into account. In addition, in scenarios where the Yukawa matrix κ is not diagonal the dark sector content of the model can contribute to flavour processes, such as neutral meson mixing and exotic meson decays shown on parton level in Figure IV.11. Dark

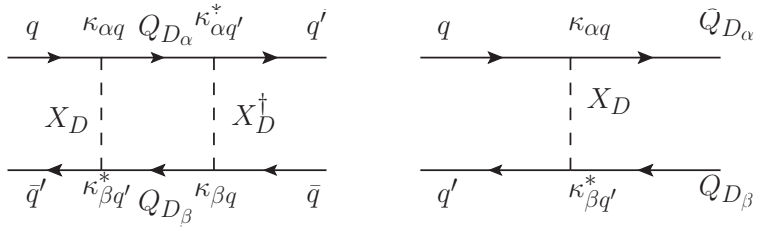

Figure IV.11: Parton level Feynman diagrams for flavour violating processes involving dark quarks and dark pions. **Left:** Neutral meson mixing. **Right:** Flavour violating meson decays of the form $M \to N\pi_D$, where M and N are mesons. Only the partons that are part of the flavour violation process are shown.

pions can also be produced at e.g. fixed target experiments in the above mentioned exotic meson decays, leading to a complementary probe. The impact of all mentioned probes has been discussed in great detail in [10]. Here, these additional constraints and detection possibilities are investigated for the unflavoured and flavoured scenarios discussed above. As part of this a scheme to translate the collider bounds to the more commonly used mediator mass - DM mass frame is introduced.

IV.2.1 Unflavoured Scenario

First, we consider the unflavoured scenario with $\kappa = \mathbb{1}\kappa_0$. In this case, no flavour violating processes via dark quarks and mediators are possible (cf. Figure IV.11). Nonetheless, the bounds from BBN and direct detection experiments need to be considered.
BBN is the formation of light elements out of a thermal bath of protons and neutrons at $T <$ MeV. This process is very sensitive to additional energy from late decaying particles. Very light decays still affect the photon to neutrino temperature ratio even after BBN has ended. Consequently, such decays are very likely in conflict with the number of relativistic DOF at the time of CMB formation. The number of relativistic DOF is determined accurately from Planck and WMAP (Wilkinson Microwave Anisotrope Probe) data [84, 325]. To evade constraints from BBN all unstable particles need to have lifetimes shorter than $\tau < 1$ s. In our case where the various dark pions can have varying lifetimes it is enough to require that at least one of the dark pions has lifetime $\tau_{\pi_D} < 1$ s, as was discussed in [10]. For the unflavoured scenario all dark pions have the same couplings and masses, and, consequently, also the same lifetime. Thus, the lifetime of all dark pions must be $\tau_{\pi_D} < 1$ s.
The DM direct detection experiment XENON1T and the proposed experiment DARWIN search for DM being scattered at nuclei of liquid xenon, which is operated as a dual

liquid/gas phase target. Then, interactions between the DM particles and the liquid xenon generate scintillation light recorded by photo-multipliers at the top and bottom of the chamber. In addition, free electrons are produced, which are drifted to the liquid-gas interface by an electric field and then extracted as scintillation light by a strong electric field.
Dark quarks with degenerate masses form a dark baryon octet, which can be detected by DM direct detection experiments. For the dominant spin-independent cross section the matrix element reads [123]

$$\mathcal{M}_{p,n} = \sum_a \frac{|\kappa_{\alpha i}|^2}{8m_X^4} J^0_{D\alpha} J^0_{p,n}, \tag{IV.8}$$

with $J^0_{D\alpha} = \sum_k \langle p_{D_k} | \bar{Q}_{D\alpha} \gamma^0 Q_{D\alpha} | p_{D_k} \rangle = 1$ and $J^0_{p,n} = \sum_k \langle p, n | \bar{d} \gamma^0 d | p, n \rangle \approx 1,2$ where $J^0_{D\alpha}$ corresponds to the number of valence quarks Q_{D_α} in all eight dark baryons averaged over the number of dark baryons. As it is evaluated by summing over all dark baryons, $J^0_{D\alpha} = 1$ is obtained for $n_D = 3$. Then, we obtain averaged spin-independent cross section [10]

$$\begin{aligned} \sigma^{SI}_{N-D} &= \frac{1}{A} \sum_a \frac{(J^0_{Da})^2 |\kappa^4_{\alpha 1} \mu^2_{n-D}}{32\pi m_X^4} (J^0_n (A - Z) + J^0_p Z)^2 \\ &= \frac{1}{A} \sum_a \frac{|\kappa^4_{\alpha 1} \mu^2_{n-D}}{32\pi m_X^4} (2(A - Z) + Z)^2, \end{aligned} \tag{IV.9}$$

where μ_{n-D} is the reduced mass of the dark baryon-nucleus system and $Z = 54$ and $A = 131$ for xenon. It is important to note that the bounds from direct detection put constraints on the mediator and DM candidate mass (hereafter denoted as dark proton) and not on the dark pion lifetime and the mediator mass as the collider constraints. Therefore, we translate the collider bounds to the mediator mass - dark proton mass plane, before applying the direct detection bounds.
We do this using Equation IV.1. With our assumption $m_{\pi_D} = f_{\pi_D}$ Equation IV.1 connects the dark pion lifetime with the Yukawa coupling κ and the dark pion mass m_{π_D} for a given mediator mass m_X. Given a specific choice of κ one can easily translate the constraint on the lifetime to a constraint on the dark pion mass and translate Figure IV.7 to a mediator mass - dark pion mass plane. However, the dark pion is not the DM candidate of the model. Thus, to map Figure IV.7 to the mediator mass - dark proton mass plane assumptions on the relation between the dark pion and the dark proton mass must be made. We consider here two cases, $m_{p_D} = 10 m_{\pi_D}$, inspired by SM QCD, and $m_{p_D} = 3 m_{\pi_D}$ with m_{p_D} the dark proton mass. First, we study the case of $\kappa_0 = 1$. The resulting bounds from the collider recasts, as well as from XENON1T (red) and the projected bounds from DARWIN (dark turquoise, dotted) are shown in Figure IV.12 for $m_{p_D} = 10 m_{\pi_D}$ (left) and $m_{p_D} = 3 m_{\pi_D}$ (right). The coloured regions are excluded by the various constraints, while in the grey regions the dark pion mass would be heavier than the mediator mass. For this choice of coupling the direct detection experiments give the most stringent bound on the parameter space, excluding mediator masses up to $m_X \sim 20$ TeV. This can be explained by the large coupling of the dark quarks to down quarks. By choosing a smaller coupling $\kappa_0 = 0.1$ this bound can be relaxed, as can be seen in Figure IV.13. Finally, we consider a *strange dark sector* scenario with $\kappa_{11} = 0.01$, $\kappa_{22} = \kappa_{33} = 1$. Since in this scenario the coupling of dark quarks to down quarks is suppressed, the main interaction is with strange and bottom quarks. In this case, the emerging jets constraint is the most stringent one, as can be seen in Figure IV.14. The direct detection bounds, on the other hand, are relaxed due to the

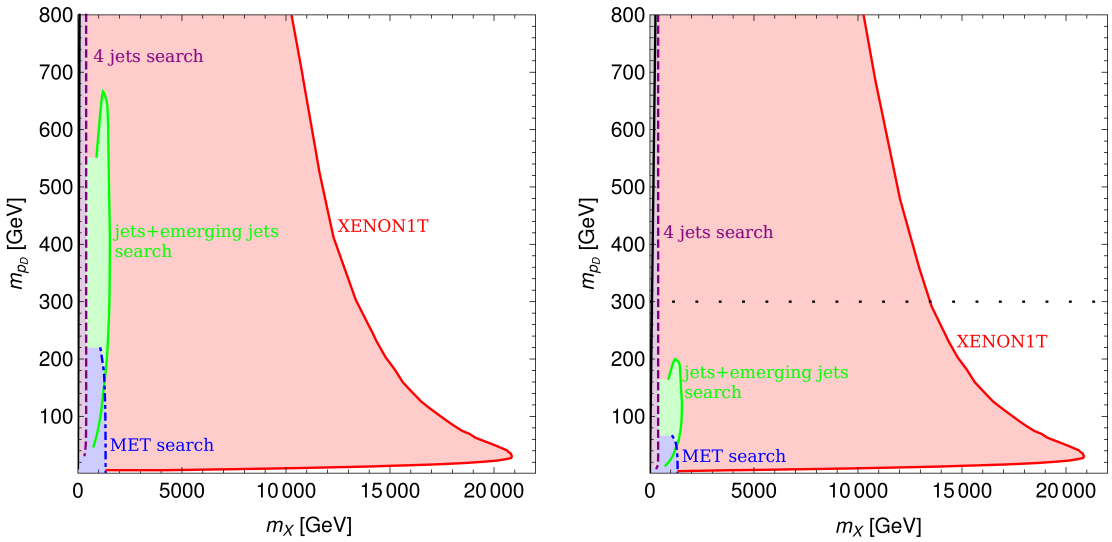

Figure IV.12: Constraints on dark QCD in the DM - mediator mass plane for $\kappa_0 = 1$ with $m_{p_D} = 10 m_{\pi_D}$ (**left**) and $m_{p_D} = 3 m_{\pi_D}$ (**right**). The red region is excluded by XENON1T, while the blue, green and purple regions are excluded by the jets plus MET (dot-dashed), jets plus emerging jets (solid) and four jets searches (dashed) respectively. In the grey region to the left of the black line the dark pion mass would be heavier than the mediator mass, while above the loosely dotted line $m_{\pi_D} > 100$ GeV.

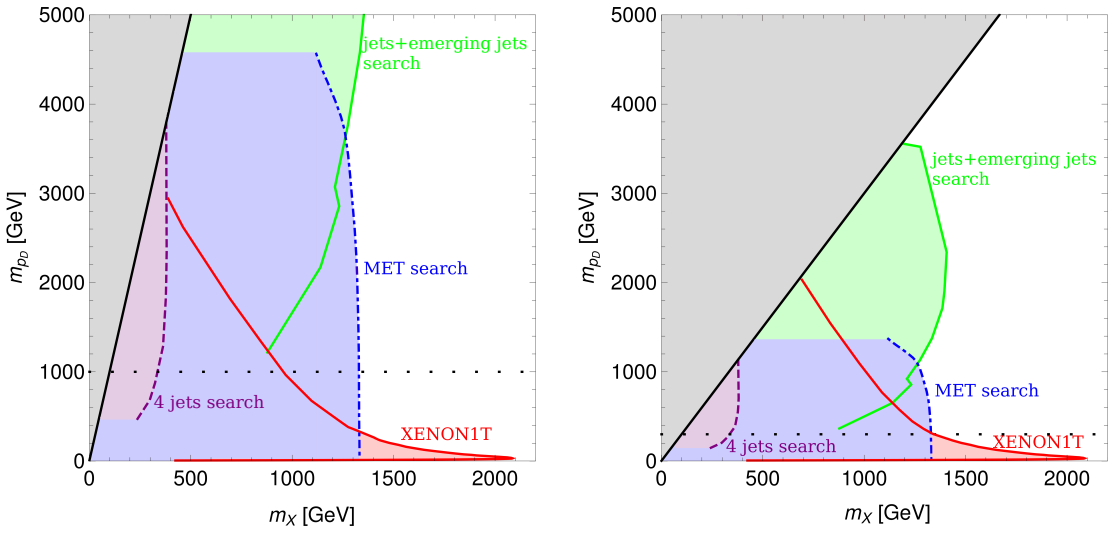

Figure IV.13: Constraints on dark QCD in the DM - mediator mass plane, same as Figure IV.12, but for $\kappa_0 = 0.1$.

small coupling to down quarks. Consequently, the strange dark sector scenario has the prospect to be discovered by a collider search, while for scenarios with κ_{11} of equal strength as κ_{22} and κ_{33} DM direct detection experiments are the most promising testing grounds. Comparing the bounds and resulting discovery channels in Figures IV.12, IV.13 and IV.14 it is worth noting that different ranges of DM masses are displayed. The DM mass ranges arise from translating the lifetime to the DM mass according to Equation IV.1. There, the coupling occurs with the fourth power, thus, leading to different dark proton mass regions for different coupling choices. For all three figures it should also be considered that the

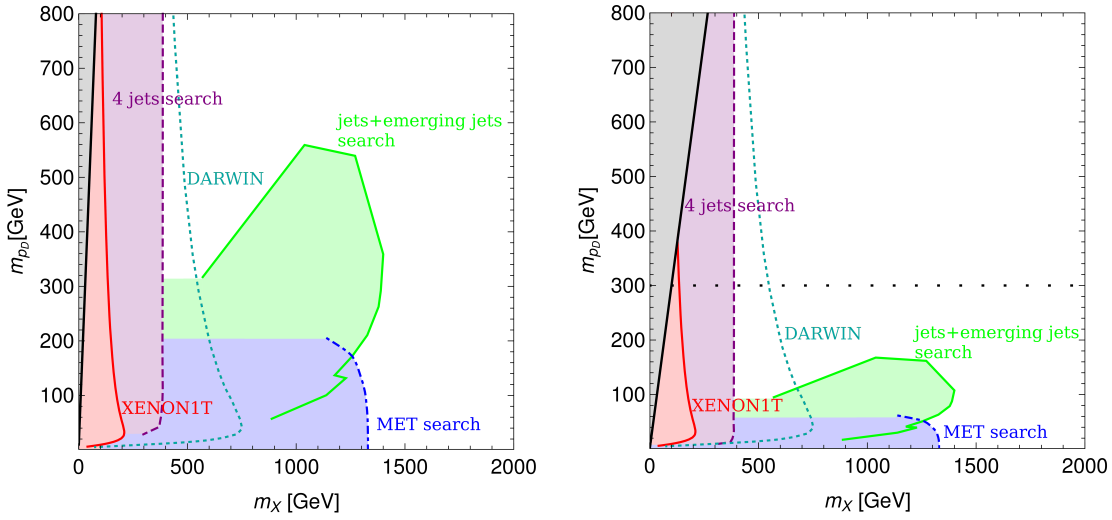

Figure IV.14: Constraints on dark QCD in the DM - mediator mass plane, same as Figure IV.12, but for $\kappa_{11} = 0.01$, $\kappa_{22} = \kappa_{33} = 1$. Here, in addition, the expected DARWIN exclusion region is shown with the dotted dark turquoise line. DARWIN would exclude the region to the left of the line.

dark proton mass exceeds 100 GeV in a part of the parameter space illustrated by the loosely black dotted line, so the limits in this region should be considered with caution.

IV.2.2 Flavoured Scenario

For the study the additional flavour and BBN constraints, as well as the direct detection prospects in a flavoured scenario with $n_D = 3$ we use the decomposition of κ in Equation III.4 in Chapter III. With this parameterization off-diagonal coupling arise in κ, allowing flavour-violating interactions. Even with the choice to set the CP violating phases to zero there are six free parameters for this choice of decomposition: three mixing angles θ_{12}, θ_{13} and θ_{23}, and three parameters to define the diagonal entries of D κ_0, κ_1 and κ_2. In [10] it was found that if two entries of the diagonal matrix D are degenerate, i.e. $\Delta_{ij} = D_{ii} - D_{jj} = 0$, the corresponding mixing angle θ_{ij} will drop out of the formula for neutral meson mixing, which is proportional to

$$\left(\sum_{\alpha} \kappa_{\alpha q} \kappa^*_{\alpha q'} \right)^2 , \tag{IV.10}$$

where q and q' are the quarks of the considered neutral meson. Consequently, for $\Delta_{ij} = D_{ii} - D_{jj} = 0$ the angle θ_{ij} can be chosen arbitrarily large, without impacting the neutral meson mixing. This leads to the following three scenarios

$$\boldsymbol{ij = 12:}\ \kappa_0 = 1,\ \kappa_1 = \kappa_1,\ \kappa_2 = 0,\ \theta_{12} = \theta_{12},\ \theta_{13} = 0,\ \theta_{23} = 0, \tag{IV.11}$$

$$\boldsymbol{ij = 13:}\ \kappa_0 = 1,\ \kappa_1 = \kappa_1,\ \kappa_2 = 0,\ \theta_{12} = 0,\ \theta_{13} = \theta_{13},\ \theta_{23} = 0, \tag{IV.12}$$

$$\boldsymbol{ij = 23:}\ \kappa_0 = 1,\ \kappa_1 = \kappa_1,\ \kappa_2 = 0,\ \theta_{12} = 0,\ \theta_{13} = 0,\ \theta_{23} = \theta_{23}, \tag{IV.13}$$

which allow studying the impact of moving away from the degenerate case on the constraints on the respective mixing angle by varying κ_1. For combining the flavour, BBN and direct detection constraints with the discovery prospect at collider and fixed target experiments κ_0 has been chosen as the free parameter, with κ_1 defined by $\Delta_{ij} = 0.5\kappa_0$

for each scenario. The respective non-zero mixing angle is set to the largest from neutral meson mixing allowed angle ($\theta_{12} = 0.1$, $\theta_{13} = 0.05$, $\theta_{23} = 0.3$ in the respective scenario). With this new parameterization flavour, BBN and direct detection constraints, as well as discovery prospects at NA62 [326] and SHiP [327] have been calculated for $m_X = 1$ TeV and displayed in the κ_0 - m_X plane for the three scenarios in [10]. However, from our recast of the collider searches in Section IV.1 for parts of the parameter space where the jets plus emerging jets and the jets plus MET searches are sensitive $m_X = 1$ TeV is already excluded. Nonetheless, to find the analogous bounds for larger values of m_X we do not need to recalculate these bounds, but merely rescale them since all involved processes are proportional to $\left(\frac{\kappa_0}{m_X}\right)^4$. We rescale them for $m_X = 1.55$ TeV, which is close to the smallest allowed mediator mass according to the jets and emerging jets search. In addition, we combine the results from our recast of the LHC searches with the from [10] rescaled constraints. This is possible since in the here considered parameterization only small off-diagonal couplings appear and it has already been seen in Section IV.1.3 that the overall result of the searches remains the same for flavoured scenarios. Figure IV.15 shows the rescaled bounds and detection prospects from [10] for $m_X = 1.55$ TeV together with the regions in which the jets plus emerging jets search and the jets plus MET searches are sensitive for the $ij = 13$ and $ij = 23$ scenarios. The constraints arising from flavour pro-

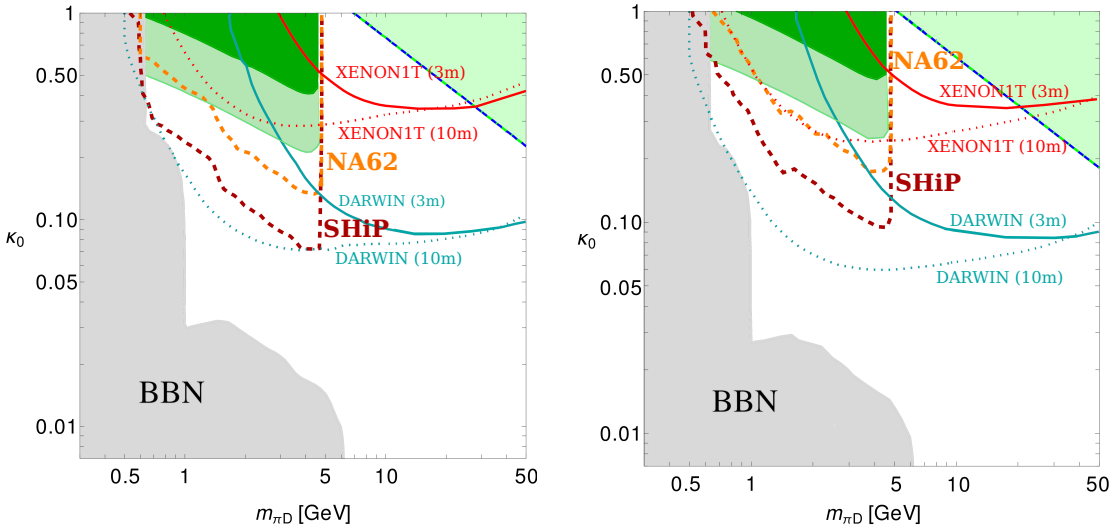

Figure IV.15: Constraints on dark QCD in the flavoured 13 (**left**) and 23 scenarios (**right**) of [10] in the κ_0 - m_{π_D} plane for $m_X = 1.55$ TeV. The grey region is excluded by BBN, the dark green one by the BaBar measurement of $B \to K\nu\bar{\nu}$ [328], while the light green shaded region below shows the projected exclusion bound for the Belle II Br($B \to K\nu\bar{\nu}$) measurement [329,330]. Above the red and orange dashed lines more than three dark pion decays are expected in the decay volumes of SHiP and NA62. The red and dark turquoise solid (dotted) lines show the regions excluded from XENON1T and the expected exclusion limits from DARWIN for $m_{p_D} = 3m_{\pi_D}$ ($m_{p_D} = 10m_{\pi_D}$). Finally, the light green shaded regions in the upper right corner show where the jets plus emerging jets search is sensible. Below the green and blue line the jets plus MET search is sensible.

cesses are shown as the dark and light green shaded regions where the dark green region is excluded from the BaBar measurement of $B \to K\nu\bar{\nu}$ [328], while the light green shaded region below shows the projected exclusion bound for the Belle II measurement of the same process [329, 330]. In the grey region at least one of the dark pions has lifetime $\tau > 1$ s,

consequently the parameter space region is ruled out from BBN. Above the red and dark turquoise solid (dotted) lines, the model does not satisfy the constraints from XENON1T and the expected exclusion limits from DARWIN for $m_{p_D} = 3m_{\pi_D}$ ($m_{p_D} = 10m_{\pi_D}$). Upwards of the red and orange dashed lines, more than three dark pion decays are expected in the decay volumes of SHiP and NA62 which is the expected number of events required for discovery. Finally, in the light-green shaded region in the upper right corner the dark pions have lifetimes of $c\tau_{\pi_D} \lesssim 1$ m and, thus, the jets plus emerging jets search is sensible, while below the blue and green line the jets plus MET search would be sensitive, covering most of the parameter space under consideration. Only for large values of both κ_0 and m_{π_D} the jets plus emerging jets search becomes more sensitive, however part of that region is already excluded by XENON1T. Note that for this choice of mediator mass, the collider searches do not exclude any parameter space yet.

IV.3 Conclusion

In this chapter, the constraints on a QCD-like dark sector with $n_D = 3$ coupling via a mediator with $Y_X = -\frac{1}{3}$ to the down-type quarks were studied and updated. For the first time, the whole range of possible dark pion lifetimes was investigated by recasting three different LHC searches for $\kappa = \mathbb{1}\kappa_0$. It was found that mediator masses $m_X \gtrsim 400$ GeV are excluded for small dark pion lifetimes below one millimeter, while for intermediate lifetimes the jets plus emerging jets search constrains mediator masses up to $m_X \sim 1.5$ TeV. Lastly, for large lifetimes $c\tau_{\pi_D} \gtrsim 1$ m mediator masses below $m_X \sim 1.3$ TeV are excluded. Additionally, the study of various benchmark points showed that these constraints are independent of the dark pion mass in the considered dark pion mass range.
The resulting bounds are not only shown in the $c\tau_{\pi_D}$ - m_X plane, but also in the common DM - dark mediator mass plane for two different dark pion to dark proton mass ratios. There, the collider constraints are combined with bounds from BBN and DM direct detection for three different choices of κ_0. For $\kappa_0 = 1$ direct detection imposes the strongest bound on the parameter space. Choosing a smaller value of κ_0 relaxes the direct detection bound. While for $\kappa_0 = 0.1$ in the small dark baryon mass region the direct detection bound is still the most stringent constraint, in the high dark baryon mass region the collider searches rule out dark baryon masses of $m_{p_D} \sim \mathcal{O}(1000\text{ GeV})$. Similarly, one can consider a *strange dark sector*. There, the coupling to down quarks and, consequently, the direct detection bounds, are suppressed. Meanwhile the production at colliders is not suppressed, so the jets plus emerging jets search poses the strongest constraint. Therefore, for the strange dark sector, a collider experiment such as the LHC has the best discovery prospect.
The unflavoured scenario can be generalized to multiple flavours, as discussed in Section IV.1.3. By redoing the recast for scenarios where diagonal and off-diagonal dark pions have different lifetimes it was found that the general form of the constraints from the recasts remains the same. Due to the overall shape of the constraints from the recasts remaining the same in the unflavoured and flavoured scenario, the collider constraints on the unflavoured scenario can be combined with the non-collider constraints for the flavoured scenario in [10]. These arise from BBN, direct detection and flavour observables. The discovery prospects from fixed target experiments is also shown. While a part of the still allowed parameter space with large κ_0 and m_{π_D} can be probed with an emerging jets search, for most of the remaining parameter space the jets plus MET search is the most sensitive one.
For flavoured scenarios with two or more dark pions with different lifetimes the sensitivity of collider searches could be further improved by utilizing more dedicated search strategies. A relatively simple option would be, for example, to add a missing energy requirement to the emerging jets search. More sophisticated search strategies could focus on searching for displaced subjets inside multi-jet signatures, or require reconstructed vertices in the muon system in addition to prompt or displaced signatures at shorter distances from the interaction point. While most existing searches attempt to isolate these new signatures radially, here, they are expected to be aligned along the dark jets due to the nature of the dark shower.

Appendix

IV.A Benchmark Points B and C

In this appendix, for completeness, in Figures IV.16 and IV.17 the constraints on the mediator mass for the benchmark points B and C of Table IV.1 are shown. Again, the bounds from the four jets search are illustrated by the dashed purple lines, the jets plus emerging jets search bounds by solid green lines and the jets plus MET search bounds as dot-dashed blue lines. All shaded regions are excluded from one of the three searches.

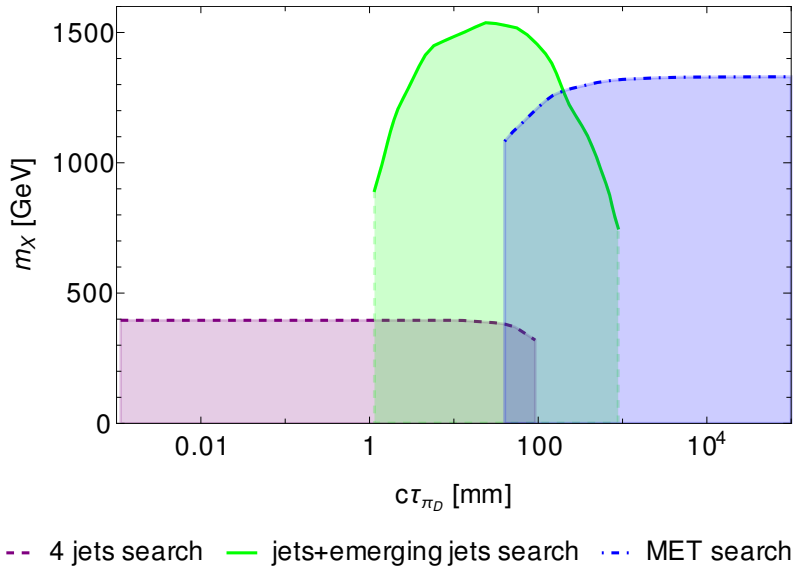

Figure IV.16: Constraints on the mediator mass for the jets plus MET search (dashed, purple), jets plus emerging jets search (solid, green) and the four jets search (dot-dashed, blue) for benchmark point B of Table IV.1.

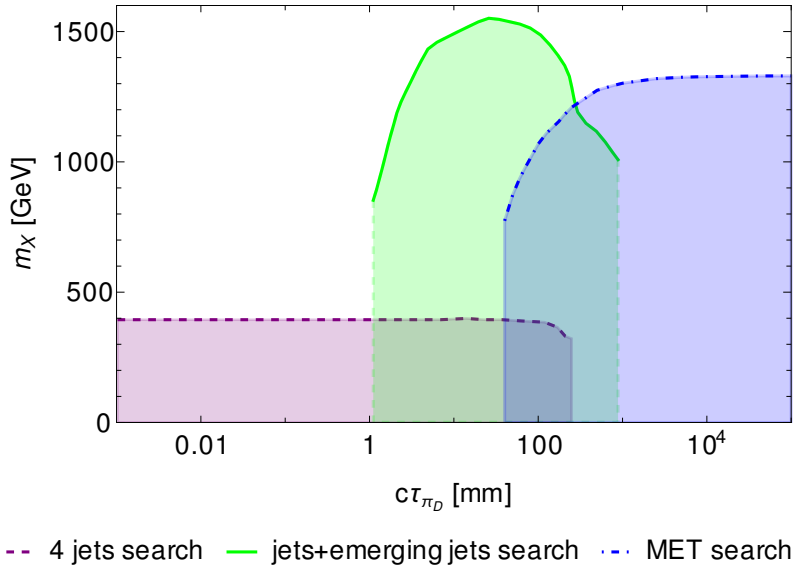

Figure IV.17: Constraints on the mediator mass for the jets plus MET search (dashed, purple), jets plus emerging jets search (solid, green) and the four jets search (dot-dashed, blue) for benchmark point C Table IV.1.

CHAPTER V

Charming ALPs

V.1 Charming ALP Parameter Space

After exploring the t-channel dark QCD model with $n_D = N_D = 3$ and $Y_X = -\frac{1}{3}$ in the previous chapter, in this chapter the case of $n_D = N_D = 3$ and $Y_X = \frac{2}{3}$ and, thus, a dark sector coupled to the up-type quarks is investigated. Unlike in Chapter IV where the full model with eight dark pions was considered, here, we exclusively study the phenomenology of two dark pions, specifically the phenomenology of the diagonal dark pions π_D^3 and π_D^8. At the phenomenological level, the main difference between the couplings of the two diagonal dark pions is the presence of a tree-level coupling with the RH top quark for π_D^8, that is not present for π_D^3. The off-diagonal dark pions are either an interpolation between the two diagonal dark pion scenarios or be stable at collider scales in the mass range of interest.

V.1.1 Charming ALP Effective Field Theory

Dark pions are neutral pseudo-scalar particles. Therefore, a single dark pion can be described by the general ALP effective Lagrangian [331, 332]

$$\begin{aligned}\mathcal{L} = &\frac{1}{2}(\partial_\mu a)(\partial^\mu a) - \frac{m_a^2}{2}a^2 + \frac{\partial_\mu a}{f_a}\left[(c_{u_R})_{ij}\bar{u}_{Ri}\gamma^\mu u_{Rj} + c_H H^\dagger i\overleftrightarrow{D_\mu} H\right] \\ &- \frac{a}{f_a}\left[c_g\frac{g_3^2}{32\pi^2}G^a_{\mu\nu}\tilde{G}^{\mu\nu a} + c_W\frac{g_2^2}{32\pi^2}W^I_{\mu\nu}\tilde{W}^{\mu\nu I} + c_B\frac{g_1^2}{32\pi^2}B_{\mu\nu}\tilde{B}^{\mu\nu}\right],\end{aligned} \tag{V.1}$$

where the gauge couplings of $U(1)_Y$, $SU(2)_L$ and $SU(3)$ are denoted g_1, g_2 and g_3, respectively, and $B_{\mu\nu}$, $W^I_{\mu\nu}$, $I = 1,2,3$, and $G^a_{\mu\nu}$, $a = 1,\dots,8$, are their corresponding field-strength tensors with $\tilde{B}_{\mu\nu} = \frac{1}{2}\varepsilon_{\mu\nu\alpha\beta}B^{\alpha\beta}, \dots$ the respective duals. H stands for the SM Higgs doublet and c_g, c_W, c_B, c_H and c_{u_R} are the Wilson coefficients (WCs). Here, c_g, c_W, c_B and $c_H \in \mathbb{R}$, whereas c_{u_R} is a hermitian matrix. This Lagrangian arises under the assumption that an ALP a is the pNGB of the spontaneous breaking of some global $U(1)$ symmetry, which is softly broken and may be anomalous.
The couplings to the gauge bosons are the only non-derivative couplings in the Lagrangian. For a given field-strength tensor $F_{\mu\nu}$ with $Tr\left[F_{\mu\nu}\tilde{F}^{\mu\nu}\right] \equiv \partial_\mu A_X^\mu$ and A_X^μ the appropriate gauge field the shift symmetry $a \to a + \alpha$ with $\alpha = const$ leads to [333]

$$\partial_\mu A_X^\mu \frac{a}{f_a} \to \partial_\mu A_X^\mu \frac{a+\alpha}{f_a} = -A_X^\mu \partial_\mu \frac{a}{f_a} + \frac{\alpha}{f_a}\partial_\mu A_X^\mu\,. \tag{V.2}$$

The corresponding associated current $\delta\mathcal{L} = \frac{\alpha}{f_a}\partial_\mu K^\mu_X$ is anomalous. In the limit $m_a \to 0$ without this anomalous couplings the ALP would be a true Goldstone boson with only derivative couplings [331, 334].
Here, we use ALPs to study the phenomenology of a single dark pion. Consequently, contrary to the QCD axion case, we treat m_a and f_a as independent parameters. Furthermore, since the dark pions of the dark QCD-like sector with $Y_X = \frac{2}{3}$ only interact with up-type quarks, we also assume that the couplings to leptons, SM quark doublets and RH down-type quarks vanish in Equation V.1.
The operator $\mathcal{O}_H = (\partial^\mu a/f_a)H^\dagger i\overleftrightarrow{D_\mu}H$ with $H^\dagger\overleftrightarrow{D_\mu}H = H^\dagger(D_\mu H) - (D_\mu H)^\dagger H$ induces a mixing between the ALP and the would-be Goldstone boson that is eaten by the Z. In other words, a is acting as an additional contribution to the longitudinal component of the electroweak gauge fields [331]. This mixing term can be rotated away by an ALP-dependent rotation of the Higgs field

$$H \to He^{ic_H a/f_a}. \tag{V.3}$$

Using this field redefinition and applying equations of motions, the operator $\mathcal{O}_H$ can be traded by the flavour-blind and chirality conserving operator

$$\frac{\partial_\mu a}{f_a}\left[\frac{1}{3}\bar{q}_{Li}\gamma^\mu q_{Li} + \frac{4}{3}\bar{u}_{Ri}\gamma^\mu u_{Ri} - \frac{2}{3}\bar{d}_{Ri}\gamma^\mu d_{Ri} - \bar{l}_{Li}\gamma^\mu l_{Li} - 2\bar{e}_{Ri}\gamma^\mu e_{Ri}\right], \tag{V.4}$$

(see e.g. [331, 334, 335]). This operator together with the operator for the coupling to W bosons,

$$\mathcal{O}_W = \frac{a}{f_a}\frac{g_2^2}{32\pi^2}W^I_{\mu\nu}\tilde{W}^{\mu\nu I}, \tag{V.5}$$

induces flavour-changing neutral currents (FCNCs) at one-loop, which were studied, for example, in [335] in the framework of B and K-meson decays. In the following, it is assumed that both WCs are small enough, so that the leading flavour-violating effects are parameterized by c_{u_R}. Moreover, the chirality conserving operator in Equation V.4 can be expressed as a function of

$$-i\frac{a}{f_a}\bar{q}_{Lk}\tilde{H}u_{Rj}\,(Y_u)_{ks}\,(c_{u_R})_{sj} + \text{h.c.} \tag{V.6}$$

and some extra contributions to the anomalous terms in Equation V.1 after integrating by parts and using equations of motion. Here, $\tilde{H} = i\sigma^2 H^*$ and Y_u is the up Yukawa matrix, which appears in the SM in the Yukawa term for the up-type quarks as

$$-\bar{q}_{Lk}\tilde{H}u_{Rj}\,(Y_u)_{kj} + \text{h.c.}\,. \tag{V.7}$$

A basis where Y_u is diagonal can always be chosen without loss of generality. We use such a basis, so that

$$Y_u = \lambda_u, \qquad Y_d = \tilde{V}\lambda_d, \tag{V.8}$$

with $\lambda_{u,d}$ diagonal matrices with real and positive entries and $\tilde{V}$ a unitary matrix, which will be just the CKM mixing matrix V if there is no extra contribution to the fermion masses. In this case we also have $\lambda_u = \sqrt{2}\mathcal{M}_u/v$ and $\lambda_d = \sqrt{2}\mathcal{M}_d/v$ with $\mathcal{M}_u = \text{diag}(m_u, m_c, m_t)$, $\mathcal{M}_d = \text{diag}(m_d, m_s, m_b)$ and $v = 246\,\text{GeV}$ the Higgs vev. For

this choice of basis, the RH up-quarks do not need to be rotated to diagonalize the mass matrices generated after spontaneous EWSB. Instead, one can just use

$$U_L^d = \tilde{V}, \quad U_R^d = U_L^u = U_R^u = \mathbb{1}. \tag{V.9}$$

Subsequently, it is always assumed that the EFT Lagrangian in Equation V.1 is defined in this basis. Then, the operator in Equation V.6 can be rewritten as

$$-i\frac{a}{f_a}\bar{q}_{Li}\tilde{H}u_{Rj}\mathcal{C}_{ij} + \text{h.c.} \tag{V.10}$$

with the WC

$$\mathcal{C}_{ij} = (\lambda_u)_{ii}(c_{u_R})_{ij}. \tag{V.11}$$

For small ALP masses, $m_a \lesssim 1$ GeV where QCD is confined a mostly decays to hadrons. These decays are described by the following chiral ALP Lagrangian [331, 332, 336, 337]

$$\begin{aligned}\mathcal{L}_{\text{aChPT}} = &\frac{1}{2}(\partial_\mu a)(\partial^\mu a) - \frac{m_a^2}{2}a^2 - \frac{a}{f_a}\frac{e^2}{32\pi^2}c_\gamma F_{\mu\nu}\tilde{F}^{\mu\nu} + \frac{f_\pi^2}{4}\text{Tr}\left(\partial_\mu U\partial^\mu U^\dagger\right)\\ &+ \frac{f_\pi^2 B_0}{2}\text{Tr}\left(\hat{m}_q(a)U^\dagger + U\hat{m}_q^\dagger(a)\right) + i\frac{f_\pi^2}{2}\frac{\partial_\mu a}{f_a}\text{Tr}\left[(\hat{c} + \varkappa_q c_g)\left(UD^\mu U^\dagger\right)\right],\end{aligned} \tag{V.12}$$

where B_0 is the low-energy constant related to the quark masses [338], $f_\pi \approx 93\,\text{MeV}$ is the pion decay constant and m_q is the quark mass matrix $m_q = \text{diag}(m_u, m_d, m_s)$. Furthermore, in the above equation the chiral field is given by

$$U = U(\Pi) = \exp\left(2i\Pi/f_\pi\right), \tag{V.13}$$

where

$$\Pi = \varphi^a\frac{\lambda^a}{2} = \frac{1}{\sqrt{2}}\begin{pmatrix}\frac{1}{\sqrt{2}}\pi^0 + \frac{\eta_8}{\sqrt{6}} & \pi^+ & K^+\\ \pi^- & -\frac{1}{\sqrt{2}}\pi^0 + \frac{\eta_8}{\sqrt{6}} & K^0\\ K^- & K^0 & -\frac{2}{\sqrt{6}}\eta_8\end{pmatrix} \tag{V.14}$$

is the Goldstone matrix describing the spontaneous symmetry breaking $SU(3)_L \otimes SU(3)_R \to SU(3)_V$ of QCD obtained using the Gell-Mann matrices λ^a, $a = 1, \ldots, 8$. In Equation V.12 we also use

$$\hat{c} = \text{diag}((c_{u_R})_{11}, 0, 0), \tag{V.15}$$

$$\varkappa_q = \frac{m_q^{-1}}{\text{Tr}(m_q^{-1})}, \tag{V.16}$$

$$\hat{m}_q(a) = \exp\left(-i\varkappa_q c_g\frac{a}{2f_a}\right)m_q\left(-i\varkappa_q c_g\frac{a}{2f_a}\right), \tag{V.17}$$

$$D_\mu U = \partial_\mu U + ieA_\mu\Big[Q_q, U\Big], \tag{V.18}$$

$$c_\gamma = c_W + c_B - 2\,N_c c_g\text{Tr}\left(\varkappa_q Q_q^2\right), \tag{V.19}$$

with the electric charge $e = g_2 g_1/\sqrt{g_1^2 + g_2^2}$ and $Q_q = 1/3\,\text{diag}(2, -1, -1)$. It is important to note that in order to get the above Lagrangian we rotated the gluon coupling away by the following chiral transformation

$$q \to \exp\Big(-i\frac{a}{2f_a}c_g\varkappa_q(1+\gamma_5)\Big)q. \tag{V.20}$$

We can use the above transformation because choosing an arbitrary diagonal matrix for the vectorial part of the quark rotation does not affect QCD at very low energies, as discussed in [331]. This holds true because up, down, and strange quark numbers are conserved separately. The here considered charming ALPs only interact with RH quarks, so that we can choose the same diagonal matrix for both the vectorial and axial parts of the rotation and still effectively only transform RH quarks, which leads to a simpler EFT. It is worth pointing out that the Lagrangian in Equation V.12 gives an irreducible contribution to the ALP mass via

$$m_{a\,\mathrm{QCD}}^2 = c_g^2 \frac{m_\pi^2 f_\pi^2}{(m_d+m_u) f_a^2} \frac{m_u m_d m_s}{m_u m_d + m_u m_s + m_d m_s} + \mathcal{O}\left(\frac{m_\pi^2 f_\pi^4}{f_a^4}\right) \tag{V.21}$$

with

$$m_\pi^2 = B_0(m_u+m_d) + \mathcal{O}\left(\frac{m_\pi^2 f_\pi^4}{f_a^4}\right). \tag{V.22}$$

In addition, kinetic mixing arises from the last term in Equation (V.12) and induces a mass mixing between the different neutral pions. Specifically, one obtains

$$\pi \to \pi - \frac{f_\pi}{f_a}\frac{m_a^2}{m_a^2-m_\pi^2}\left(\mathcal{K}_\pi - \frac{\mathcal{K}_\eta \delta_I m_\pi^2}{\sqrt{3}(m_a^2-m_\eta^2)}\right) a - \frac{\delta_I m_\pi^2}{\sqrt{3}(m_\eta^2-m_\pi^2)}\eta_8 + \mathcal{O}(f_\pi^2/f_a^2) + \mathcal{O}(\delta_I^2), \tag{V.23}$$

where

$$\delta_I = \frac{m_d-m_u}{m_d+m_u} \approx \frac{1}{3}, \qquad m_\eta^2 = \frac{m_d+m_u+4m_s}{3(m_u+m_d)} m_\pi^2 \tag{V.24}$$

and

$$\mathcal{K}_\pi = c_g \frac{m_s(m_d-m_u)}{2(m_s m_u + m_d m_u + m_d m_s)} + \frac{(c_{u_R})_{11}}{2}, \tag{V.25}$$

$$\mathcal{K}_\eta = c_g \frac{m_s(m_d+m_u)-2m_d m_u}{2\sqrt{3}((m_s m_u + m_d m_u + m_d m_s))} + \frac{(c_{u_R})_{11}}{2\sqrt{3}}. \tag{V.26}$$

In the following, pseudo-scalar particles described by the Lagrangian in Equation V.1 are denoted as "charming ALPs" instead of dark pions. Nonetheless, the charming ALPs are studied as if they are the diagonal dark pions of a QCD-like dark sector. More precisely, the couplings of the charming ALPs to RH up-type quarks are defined via the couplings of the diagonal dark pions. Comparing Equation V.1 with the mixing terms in Equation III.21 one finds

$$f_a = \frac{m_X^2}{f_{\pi_D}} \tag{V.27}$$

and

$$(c_{u_R}^{(a)})_{ij} = -\sum_{\alpha\beta} \kappa_{\alpha i}\kappa_{\beta j}^* \left(\lambda^a\right)_{\alpha\beta}, \qquad a = 3, 8. \tag{V.28}$$

More explicitly, with κ defined as in Equation III.4 and the $ij = 12$ scenario in Equation IV.11

$$c_{u_R}^{(3)} = \frac{\kappa_0^2}{4}\begin{pmatrix} 4s_{12}^2 - 9c_{12}^2 & -13c_{12}s_{12} & 0 \\ -13c_{12}s_{12} & 4c_{12}^2 - 9s_{12}^2 & 0 \\ 0 & 0 & 0 \end{pmatrix}, \tag{V.29}$$

$$c_{u_R}^{(8)} = \frac{-\kappa_0^2}{4\sqrt{3}} \begin{pmatrix} 4s_{12}^2 + 9c_{12}^2 & 5c_{12}s_{12} & 0 \\ 5c_{12}s_{12} & 4c_{12}^2 + 9s_{12}^2 & 0 \\ 0 & 0 & -2 \end{pmatrix}. \tag{V.30}$$

Additionally, at tree-level $c_H = 0$, as well as $c_g = c_W = c_B = 0$ and $\kappa_0 \in \mathbb{R}^+$ and $c_{12} = \cos\theta_{12}$, $s_{12} = \sin\theta_{12}$, with $\theta_{12} \in [0, \pi]$. Following [10] $D^0 - \bar{D}^0$ - mixing is used to set the value of θ_{12}: For the $ij = 12$ scenario in Equation IV.11 there is no constraint from $D^0 - \bar{D}^0$ − mixing if $\theta_{12} \leq 0.022$ when considering the full QCD-like model. Therefore, for concreteness, in the following, $\theta_{12} = 0.022$ is used. Here, it is worth to point out that, while all non-zero entries of the two choices for c_{u_R} vary slightly, the main difference between them is the coupling of charming ALPs to top quarks, which is present for $a = \pi_D^8$, but not for π_D^3. In the following, we will see that this difference has a significant impact on the resulting allowed parameter space.

The charming ALP Lagrangian in Equation V.1 can also be naturally UV-completed in another class of models, generically known by the name of flavons or familions (see [108, 221–225] and e.g. [226–232, 339–341] for more recent implementations). These are pNGBs of some spontaneously broken flavour symmetry $U(1)$, which may be anomalous. They generically feature flavour-violating couplings to quarks or leptons. This class of models is attractive as such models naturally feature enhanced Yukawa couplings, while still being in agreement with existing flavour bounds. They were studied in a slightly different context in [342–344], but without considering the phenomenology of the light scalar degree of freedom, *the flavon*. Here, we consider a specific setup of the FN model where only the RH up-type quarks have charge under the new global $U(1)$ flavour symmetry. This symmetry is broken by the vev of an extra scalar $\langle S \rangle = f_a$ with

$$S = \frac{1}{\sqrt{2}}(f_a + s)e^{ia/f_a}, \tag{V.31}$$

and S has charge -1 under this new $U(1)$. The charges of the RH up-type quarks under the new flavour symmetry $U(1)$ are n_i^u, leading to higher dimensional Yukawa couplings for up-type quarks

$$\mathcal{L} \supset -(y_u)_{ij} \left(\frac{S}{\Lambda}\right)^{n_j^u} q_{Li}\tilde{H}u_{Rj} + \text{h.c.}, \tag{V.32}$$

where one typically assumes that $f_a < \Lambda$, while leaving all other Yukawa couplings unchanged. This term generates interactions like in Equation (V.6)

$$-\frac{ia}{f_a}\bar{q}_{Li}\tilde{H}u_{Rj}n_j^u = -\frac{ia}{f_a}\bar{q}_{Li}\tilde{H}u_{Rj}(Y_u)_{ij}n_j^u \tag{V.33}$$

with the effective up Yukawa matrix,

$$(Y_u)_{ij} = (y_u)_{ij}\left(\frac{f_a}{\Lambda}\right)^{n_j^u}. \tag{V.34}$$

With this setup and under the assumption of order one Yukawa couplings $(y_u)_{ij} = \mathcal{O}(1)$ and $f_a/\Lambda = \epsilon \sim m_c/m_t$ the correct up-type quark masses arise by choosing $n_j^u = (2, 1, 0)$. Using $n_j^u = (2, 1, 0)$ gives

$$(m_u, m_c, m_t) \sim \frac{1}{\sqrt{2}} v\,(\epsilon^2, \epsilon, 1) \tag{V.35}$$

with

$$\frac{m_u}{m_t} \sim \epsilon^2, \qquad \frac{m_c}{m_t} \sim \epsilon. \tag{V.36}$$

Moreover, the Yukawa coupling matrix Y_u can be diagonalized by

$$u_R \to U_R^u u_R, \qquad u_L \to U_L^u u_L, \tag{V.37}$$

with

$$U_R^u \sim \begin{pmatrix} 1 & \epsilon & \epsilon^2 \\ \epsilon & 1 & \epsilon \\ \epsilon^2 & \epsilon & 1 \end{pmatrix}, \qquad (U_L^u)_{ij} \sim \mathcal{O}(1). \tag{V.38}$$

In the basis where Y_u is diagonal one finally obtains

$$c_{u_R} = U_R^u n_j^u \, (U_R^u)^\dagger \sim \begin{pmatrix} 2 & 3\epsilon & 3\epsilon^2 \\ 3\epsilon & 1 & \epsilon \\ 3\epsilon^2 & \epsilon & \epsilon^2 \end{pmatrix}. \tag{V.39}$$

The coupling in Equation V.39 defines a third charming ALP benchmark point. Again, $c_H = 0$ is used, the concrete values of the anomalous couplings c_g, c_W, c_B, however, depend on the specific UV completion of the FN model. They may all be zero, which is the case we consider in the following. Similarly to the scenario with $a = \pi_D^3$ in the FN inspired scenario the coupling to top quarks is small, but non-zero.
As a fourth benchmark point an IR motivated scenario where $(c_{u_R})_{ij} = 1 \; \forall i, j$ at the scale f_a is studied. This scenario represents the anarchic limit with no hierarchies present in c_{u_R}, but all the entries are of the same order. As always we assume that the anomalous gauge couplings and c_H are negligible.

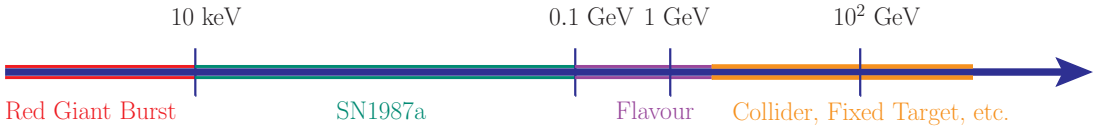

Figure V.1: Possible search strategies for charming ALPs for ALP masses $m_a \lesssim \mathcal{O}(100)$ GeV. Coloured regions show up to which ALP mass the possible search strategy can probe the charming ALP parameter space.

Independent of which of the UV completions introduced above is chosen to define the coupling c_{u_R} the mass of the charming ALP is always a free parameter. The rich phenomenology of the charming ALP model allows us to study a wide range of ALP masses. In Figure V.1 we show the various ways of probing the ALP parameter space for a given charming ALP mass regime. Note that Figure V.1 shows up to which charming ALP mass a given search can be used to probe the charming ALP parameter space. Probes, that can be used in the high m_a region typically can also probe the low mass region. However, for illustrative reasons, in the lower mass region only the additional ways to probe charming ALPs opening up are shown in the coloured regions. Nonetheless, the various search strategies are complementary to each other, as will be seen in the discussion of the charming ALP parameter space below.

V.1.2 ALP Lifetime and Branching Ratios

First, we discuss the various charming ALP decay modes, the resulting total decay width and lifetime. The decay modes of charming ALPs mainly depend on their mass m_a. We investigate them both, for small ALP masses where QCD is confined and we can use ChPT, as well as for larger values of the ALP mass where the dominant ALP decays can be computed using quark-hadron duality [308, 345]. To separate these two regions we follow [10] and find the energy scale separating both pictures by demanding that the total decay width to hadrons or SM quarks is of the same order in both regimes. In the following, we discuss the various ALP decay channels to find the scale of the matching. As a result we will see that the matching condition is fulfilled for $m_a \sim 1\,\text{GeV}$ for the benchmark models at hand.

For small ALP masses the only possible decay channel for the here considered charming ALPs is to photons. This decay occurs due to the mixing in Equation V.23 and the subsequent decay $\pi \to \gamma\gamma$, plus one-loop contributions coming from integrating out heavy quarks. The corresponding decay width is

$$\Gamma(a \to \gamma\gamma) \approx \frac{\alpha_{\text{em}}^2 m_a^3}{(4\pi)^3 f_a^2} \left| \sum_{i=2}^{3} \frac{4}{3} (c_{u_R})_{ii} B_1(\tau_i) - \frac{m_a^2}{2(m_\pi^2 - m_a^2)} (c_{u_R})_{11} \right|^2 \tag{V.40}$$

with the loop-function $B_1(\tau_i) = 1 - \tau_i f^2(\tau)$, $\tau_i = 4(\mathcal{M}_u)_{ii}^2/m_a^2$, and

$$f(\tau_i) = \begin{cases} \arcsin\left(1/\sqrt{\tau_i}\right) & \tau_i \geq 1 \\ \frac{\pi}{2} + \frac{i}{2} \ln\left(\frac{1+\sqrt{1-\tau_i}}{1-\sqrt{1-\tau_i}}\right) & \tau_i < 1 \end{cases} . \tag{V.41}$$

This channel is only open as long as the decays to leptons $a \to \ell^+\ell^-$ are kinematically forbidden. The leptonic decays of charming ALPs arise due to the one-loop coupling of the flavour blind operator $\mathcal{O}_H$. The running of the WC is described by [346–350]

$$16\pi^2 \frac{dc_H}{d\ln\mu} = -6\text{Tr}\left(\lambda_u c_{u_R} \lambda_u\right) \Rightarrow c_H = \frac{3}{8\pi^2 v^2} \text{Tr}\left(\mathcal{M}_u c_{u_R} \mathcal{M}_u\right) \ln\left(\frac{f_a^2}{\mu^2}\right). \tag{V.42}$$

After field redefinition we obtain

$$-c_H \frac{\partial_\mu a}{f_a} \left(\bar{l}_{Li} \gamma^\mu l_{Li} + 2\bar{e}_{Ri} \gamma^\mu e_{Ri}\right), \tag{V.43}$$

which leads after EWSB to

$$\mathcal{L} \supset \frac{i c_H a}{f_a} m_\ell (\bar{\ell}\gamma_5 \ell) = i\, a\, g_{a\ell\ell} (\bar{\ell}\gamma_5 \ell), \quad \ell = e, \mu, \tau. \tag{V.44}$$

Specifically, at the scale $\mu \sim m_t$ the ALP lepton coupling is

$$g_{all} = \frac{c_H m_l}{f_a} = \frac{3 m_l}{8\pi v^2 f_a} \ln\left(\frac{f_a^2}{m_t^2}\right) \sum_{i=1}^{3} (\mathcal{M}_u)_{ii} (c_{u_R})_{ii}. \tag{V.45}$$

It is obvious from Equation V.45 that this coupling will be relatively large if the ALP couples to top quarks since this coupling contributes the most significantly to the running. Finally, the leptonic decay width can be written as

$$\Gamma(a \to \ell^+\ell^-) = \frac{m_a m_\ell^2}{8\pi f_a^2} \sqrt{1 - \frac{4m_\ell^2}{m_a^2}} |c_H|^2. \tag{V.46}$$

Due to the strong dependence on the ALP top quark coupling the di-photon final state dominates over the e^+e^- and $\mu^+\mu^-$ decays in models where $(c_{u_R})_{33}$ is absent or negligible. On the other hand, if the ALP top quark coupling is non-negligible, once the leptonic decay channels $a \to e^+e^-$ and $a \to \mu^+\mu^-$ open up, they become the dominant decays, at least for large values of f_a leading to log-enhanced $g_{a\ell\ell}$ couplings. In both cases, the m_a^3 dependence of the di-photon decay leads to a faster increase of $\Gamma(a \to \gamma\gamma)$ compared to the di-lepton decay widths, which increase proportional to m_a. This can, in some cases, lead to the di-photon decay becoming the leading channel for larger m_a, at least until the $a \to 3\pi$ channel opens kinematically. The decay width for this channel reads [233]

$$\Gamma(a \to \pi^a\pi^b\pi^0) = \frac{\pi}{12}\frac{m_a m_\pi^4}{f_a^2 f_\pi^2}\left[\frac{(c_{u_R})_{11}}{32\pi^2}\right]^2 g_{ab}\left(\frac{m_\pi^2}{m_a^2}\right), \tag{V.47}$$

with

$$g_{00}(x) = \frac{2}{(1-x)^2}\int_{4x}^{(1-\sqrt{x})^2} dz\sqrt{1-\frac{4x}{z}} \times \lambda^{1/2}(1,z,x), \tag{V.48}$$

$$g_{+-}(x) = \frac{12}{(1-x)^2}\int_{4x}^{(1-\sqrt{x})^2} dz\sqrt{1-\frac{4x}{z}}(z-x)^2 \times \lambda^{1/2}(1,z,x), \tag{V.49}$$

and $\lambda(a,b,c) = a^2+b^2+c^2-2(ab+ac+bc)$. For charming ALPs this decay mode always dominates the di-photon decay, while, for $(c_{u_R})_{33}$ and/or f_a large enough to have significant $g_{a\ell\ell}$ couplings, $a \to \mu^+\mu^-$ can be the dominant decay channel in this region of ALP masses.

Going to even larger ALP masses $m_a \gtrsim 1\,\text{GeV}$, equation (V.12) becomes invalid and the dominant ALP decays into hadrons can be computed using quark-hadron duality. The ALP can decay to both, quarks and gluons in this mass region. While the decays to up-type quarks are at tree-level, decays to gluons are loop-induced. Lastly, decays to down-type quarks originate from the one-loop running of c_{u_R} and, if the decay is flavour conserving, c_H. In contrast to the decay to leptons, which can be dominant in the low mass region for large couplings to top quarks, the decay to pairs of down-type quarks is always suppressed. This difference stems from the fact that in the region where leptonic decays can be dominant the only other kinematically allowed decay is the decay to photons. In the region where the decays to down-type quarks open up, however, tree-level decays to up-type quarks are possible and dominate over the loop-suppressed decays to down-type quarks. The decay width for the tree-level decays to up-type quarks is

$$\begin{aligned}\Gamma(a \to u_i\bar{u}_j) = \frac{N_c m_a}{16\pi f_a^2}\left|(c_{u_R})_{ij}\right|^2 \times \left((m_i^2+m_j^2) - \frac{(m_i-m_j)^2}{m_a^2}\right) \\ \times \sqrt{\left(1-\frac{(m_i+m_j)^2}{m_a^2}\right)\left(1-\frac{(m_i-m_j)^2}{m_a^2}\right)},\end{aligned} \tag{V.50}$$

where q_i, q_j and m_i, m_j with $i,j = 1,2,3$ are the up-type quarks and the respective masses. We take the one-loop decay rate to gluon pairs from Equation 28 of [233], which reads

$$\Gamma(a \to gg) = \frac{32\pi\alpha_s^2(m_a)m_a^3}{f_a}\left[1+\left(\frac{97}{4}-\frac{7n_q}{6}\right)\frac{\alpha_s(m_a)}{\pi}\right]\left|c_{gg}+\sum_{q=1}^{n_q}\frac{(c_{u_R})_{qq}}{32\pi^2}\right|^2 \tag{V.51}$$

with α_s the fine structure constant, $c_{gg} = 0$ the WC for the coupling to gluons and n_q the number of light quarks, for the case of charming ALPs $n_q = 1$. As mentioned above, the

decay to down-type quarks arises from the one-loop running of c_{u_R} from the UV scale f_a to the IR scale μ. Due to the running a term of the form

$$(c_{q_L})_{ij}\frac{\partial_\mu a}{f_a}\left(\bar{q}_{Li}\gamma^\mu q_{Lj}\right) \tag{V.52}$$

arises. From Equation V.52 one obtains [346–349]

$$16\pi^2\frac{dc_{q_L}}{d\ln\mu} = -\lambda_u c_{u_R}\lambda_u \Rightarrow c_{q_L} = \frac{\lambda_u c_{u_R}\lambda_u}{32\pi^2}\ln\left(\frac{f_a^2}{\mu^2}\right), \tag{V.53}$$

which leads after EWSB to

$$\frac{\partial_\mu a}{f_a}\left[(c_{u_L})_{ij}\bar{u}_{Li}\gamma^\mu u_{Lj} + (c_{d_L})_{ij}\bar{d}_{Li}\gamma^\mu d_{Lj}\right] \tag{V.54}$$

with $c_{u_L} = c_{q_L}$ and $c_{d_L} = V^\dagger c_{q_L} V$. Finally, the WCs for the decay to down-type quarks from c_{u_R} are

$$(c_{d_L})_{ij} = \frac{1}{16\pi^2 v^2}V^*_{ri}(\mathcal{M}_u)_{rr}(c_{u_R})_{rs}(\mathcal{M}_u)_{ss}V_{sj}\ln\left(\frac{f_a^2}{\mu^2}\right), \tag{V.55}$$

while the WC c_H, that contributes to flavour conserving decays, can be found analogously to the one for leptons. The decay width can now be written as in Equation V.50, replacing c_{u_R} with the above WCs and using the respective down-type quark masses. It is clear that the decays to down-type quarks are always suppressed compared to the decays to gluons and up-type quarks. Thus, we assume that they do not play a role for the phenomenology of charming ALPs. The decay width to photons in this regime is given by

$$\Gamma(a\to\gamma\gamma) \approx \frac{\alpha_{\text{em}}^2 m_a^3}{(4\pi)^3 f_a^2}\left|\sum_{i=1}^{3}\frac{4}{3}(c_{u_R})_{ii}B_1(\tau_i)\right|^2. \tag{V.56}$$

To find the scale, at which to transition from ChPT to quark-hadron duality, in Figure V.2 the total decay width in both, the ChPT and the hadronic picture are shown. The left panel shows $a = \pi_D^3$ and $a = \pi_D^8$ with the blue and yellow lines, while on the right side the anarchic and FN scenario are shown in green and red, respectively. The dashed lines correspond to the decay width in the ChPT picture, which includes the decays to photons according to Equation V.40, the decays to leptons, as well as the decays to three pions. We do not include decays to Kaons and pions as the matching of the two pictures happens below the kinematic threshold of these decays. On the other hand, the decay width in the quark-hadron duality picture includes in addition to the leptonic decays, all decays to up-type quarks, the decay to hadrons via gluons and the decay to photons from Equation V.56. It is shown by the solid lines in Figure V.2. In both panels $f_a = 10^4$ TeV and $\kappa_0 = 1$ is chosen. For all four scenarios, in the chiral picture one can clearly see the dimuon channels opening at $m_a = 2m_\mu \sim 0.2$ GeV, and, in the cases with small or zero couplings to top quarks also the opening of the three pion channel at $m_a = 3m_\pi \sim 0.4$ GeV. Similarily, in the partonic picture one the various diquark channel thresholds are clearly visible. This is less prominent in the chiral picture. One can also see that for the anarchic scenario and $a = \pi_D^8$ for $m_a \sim 1$ GeV, illustrated by the grey band in Figure V.2, the decay width in both pictures are close to each other. Especially for the anarchic scenario they are within $\mathcal{O}(1)$ of each other. While the $a = \pi_D^8$ scenario would favour the matching to be at slightly lower scale, the choice of $m_a = 1$ GeV for the

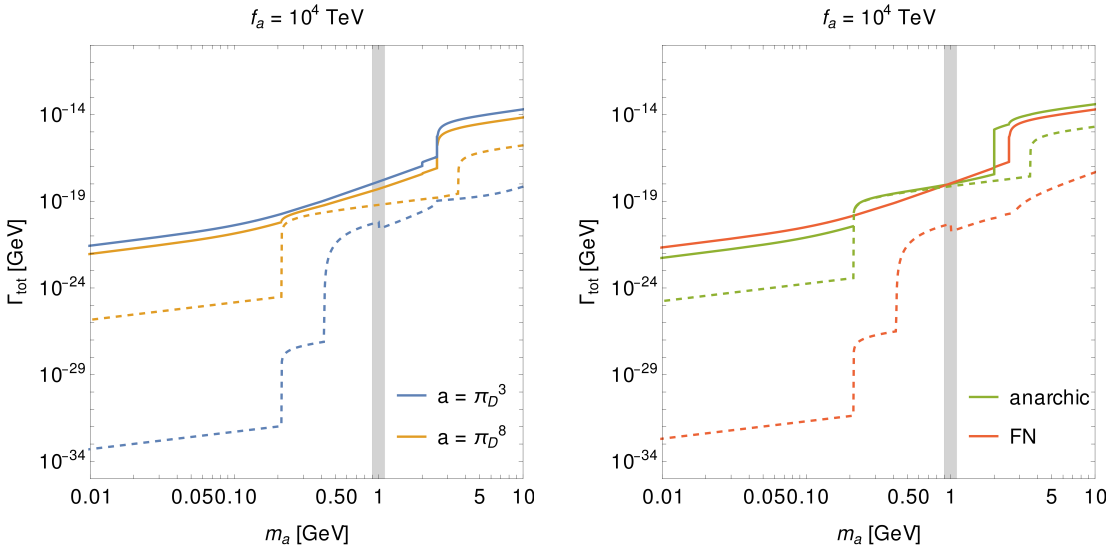

Figure V.2: Total decay width of charming ALPs calculated with ChPT (dashed lines) and with quark-hadron duality (solid lines). The **left** panel shows $a = \pi_D^3$ and $a = \pi_D^8$ in blue and yellow, while the **right** panel depicts the total decay width for the anarchic and FN scenario in green and red, respectively. Here, $f_a = 10^4$ TeV and $\kappa_0 = 1$ are used.

matching is still reasonable. Both scenarios with negligible ALP top couplings ($a = \pi_D^3$ and FN scenario) also have the two pictures closest at around $m_a = 1$ GeV. Therefore, as mentioned above, we use ChPT for ALPs with $m_a \leq 1$ GeV and quark-hadron duality for $m_a > 1$ GeV in the following.

We show the resulting total decay width of charming ALPs in all four benchmark scenarios as a function of m_a for $f_a = 10^4$ TeV and $\kappa_0 = 1$ in Figure V.3, now only using the chiral picture for $m_a \leq 1$ GeV and the partonic picture for $m_a > 1$ GeV. Again, we illustrate with the blue and yellow lines the total decay width for $a = \pi_D^3$ and $a = \pi_D^8$, respectively, while the green lines and the red lines depict the total decay width for the anarchic and FN scenarios. The grey band around $m_a \sim 1$ GeV shows where we transition from the ChPT picture to quark-hadron duality. Similarly to Figure V.2, in the anarchic and the $a = \pi_D^8$ scenario where $(c_{u_R})_{33}$ is of the same order of magnitude as the other entries of c_{u_R} the opening of the di-muon channel at $m_a = 2m_\mu \sim 0.2$ GeV is clearly visible, while in the other two scenarios the three pion channel opening can be seen at $m_a = 3m_\pi \sim 0.4$ GeV. Above $m_a = 1$ GeV the opening of the $c\bar{c}$ channel is visible for all four scenarios. However, only in the anarchic scenario the opening of the uc channel has a visible impact.

Both, in Figure V.2 and V.3 f_a is fixed to $f_a = 10^4$ TeV. Changing the value of f_a only influences the magnitude, but not the overall shape of the decay width. Thus, it also does not change the scale of matching between the chiral and the partonic picture. Smaller values of f_a lead to larger decay widths, while larger values result in smaller decay widths and correspondingly in larger ALP lifetimes through $\tau = \hbar/\Gamma$. Finally, the branching ratios for the charming ALPs are depicted in Figure V.4 for $f_a = 10^4$ TeV as a function of the ALP mass m_a, also assuming $\kappa_0 = 1$ for the dark-QCD motivated benchmark scenarios. It can be seen that in the scenarios where the ALP top quark coupling is zero or negligible small (π_D^3 (top left) and FN scenario (bottom right)) the di-photon decay is the leading decay mode for most of the region $m_a \lesssim 1$ GeV up to ALP masses where $a \to 3\pi$ is kinematically allowed. Meanwhile, in the cases with non-negligible $(c_{u_R})_{33}$

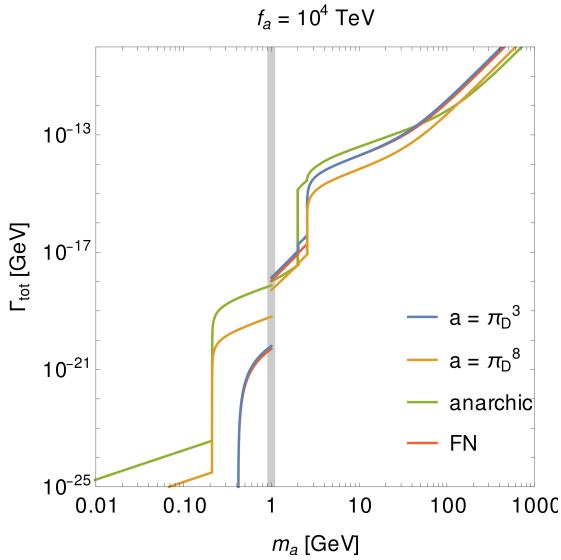

Figure V.3: Total decay width in GeV for charming ALPs as a function of m_a for $f_a = 10^4$ TeV and $\kappa_0 = 1$. The blue and yellow lines show the total decay width for $a = \pi_D^3$ and $a = \pi_D^8$, respectively, while the green lines and the red lines illustrate the total decay width for the anarchic and FN scenarios. The grey shaded band around $m_a = 1$ GeV depicts the matching between the calculations in ChPT and quark-hadron duality.

(π_D^8 (top right) and anarchic scenario (bottom left)) and for the choice of $f_a = 10^4$ TeV the leptonic channels $a \to e^+e^-$ and $a \to \mu^+\mu^-$ become dominant once the respective channel opens up. For all four benchmark scenarios for ALP masses $\gtrsim 1$ GeV, decays into hadrons are by far the dominant channels. While the $a \to \bar{q}^{(\prime)}q$ is the leading decay channel close to its respective kinematical threshold, for larger values of m_a $a \to gg$ takes over and becomes the leading channel at large masses. The decays to leptons and photons are subdominant in this region.

V.1.3 Flavour Constraints

As can be seen in Equation V.1 charming ALPs induce flavour-changing couplings to RH up-type quarks. This leads to contributions to several flavour-violating processes which constrain the parameter space significantly. Here, we consider two types of processes,

1. the $\Delta F = 2$ process of $D^0 - \bar{D}^0$ − mixing displayed in Figure V.5 and
2. $\Delta F = 1$ processes like the exotic decays of D, B and K mesons (cf. Figure V.6).

While in the considered model exotic D meson decays occur at tree-level, exotic Kaon and B meson decays can only happen at loop level, cf. Figure V.6. In addition, we also study radiative decays of J/ψ, displayed in Figure V.7.

V.1.3.1 $D^0 - \bar{D}^0$ − Mixing

The relevant Hamiltonian for $D^0 - \bar{D}^0$ −mixing is

$$\mathcal{H}_{\text{eff}}^{\Delta C=2} = \sum_{i=1}^{5} C_i \mathcal{O}_i + \sum_{i=1}^{3} \tilde{C}_i \tilde{\mathcal{O}}_i, \tag{V.57}$$

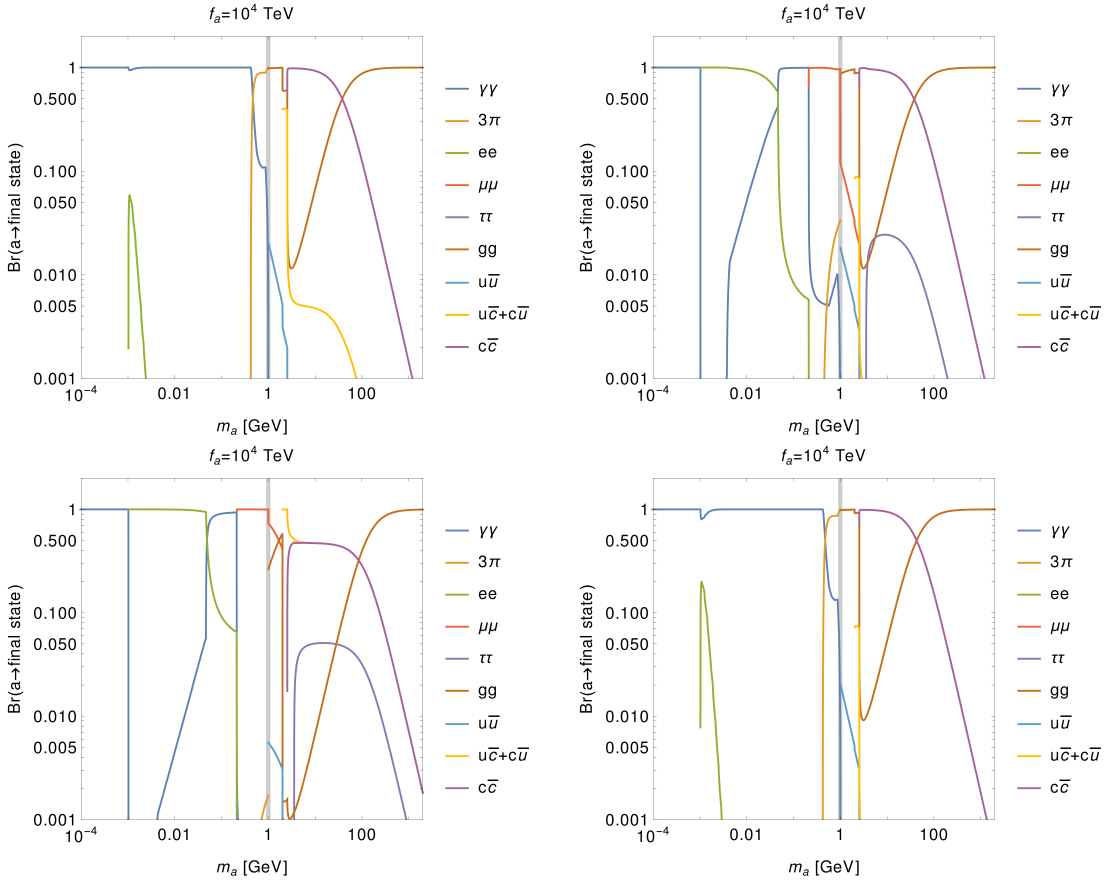

Figure V.4: Branching ratios of the charming ALP as a function of its mass m_a for the four different benchmark models. The **top** panels correspond to the dark-QCD inspired scenarios with $a = \pi_D^3$ being on the **top left** and $a = \pi_D^8$ on the **top right**. The **bottom** panels show the anarchic scenario on the **left** and the FN motivated benchmark on the **right**, respectively. In all cases, we have assumed $f_a = 10^4$ TeV. Moreover, for the dark-QCD motivated scenarios depicted in the upper panel we have taken $\kappa_0 = 1$. The gray narrow band around 1 GeV illustrates the matching between the calculations performed using ChPT and quark-hadron duality.

with the operators

$$\mathcal{O}_1 = (\bar{c}_L^\alpha \gamma^\mu u_L^\alpha)(\bar{c}_L^\beta \gamma_\mu u_L^\beta), \tag{V.58}$$

$$\mathcal{O}_2 = (\bar{c}_R^\alpha u_L^\alpha)(\bar{c}_R^\beta u_L^\beta), \quad \mathcal{O}_3 = (\bar{c}_R^\alpha u_L^\beta)(\bar{c}_R^\beta u_L^\alpha), \tag{V.59}$$

$$\mathcal{O}_4 = (\bar{c}_R^\alpha u_L^\alpha)(\bar{c}_L^\beta u_R^\beta), \quad \mathcal{O}_5 = (\bar{c}_R^\alpha u_L^\beta)(\bar{c}_L^\beta u_R^\alpha). \tag{V.60}$$

The operators $\tilde{\mathcal{O}}_{1,2,3}$ arise from $\mathcal{O}_i$ after exchanging both chiralities, i.e., $L \leftrightarrow R$. Thus, in the following, we only focus on NP contributions to the above WCs, namely $C_i = C_i^{\rm NP}$ and $\tilde{C}_i = \tilde{C}_i^{\rm NP}$. The NP contribution are either from short or long distance physics depending on the mass of the ALP: Short distance effects occur for heavy ALPs ($m_a \gg m_c$), that can be integrated out. On the other hand, long distance physics contribution arise for small ALP masses $m_a \ll m_c$ where the operator product expansion (OPE) in powers of $1/m_c$ can be applied to the $D^0 - \bar{D}^0$ − mixing system.
A detailed calculation of the WCs in both cases can be found in Appendix V.A. There,

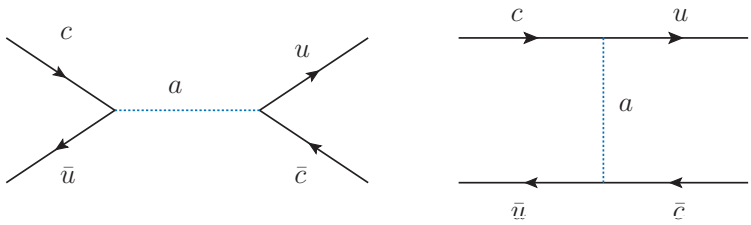

Figure V.5: Parton level Feynman diagrams for ALP-mediated $D-\bar{D}$ mixing via s- (**left**) and t-channel (**right**).

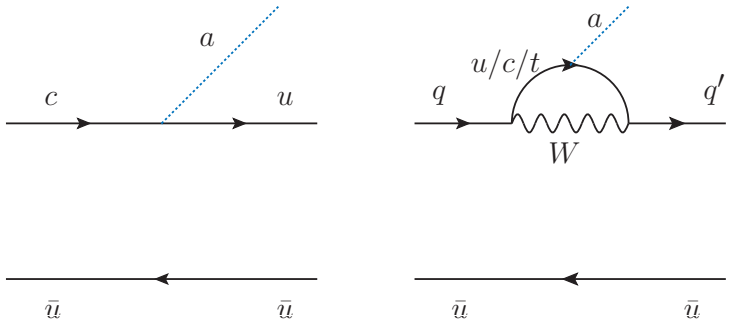

Figure V.6: Parton level Feynman diagrams for exotic D (**left**), K and B meson (**right**) decays involving charming ALPs.

for the short distance effects ($m_a \gg m_c$) the only non-zero WCs are given by

$$\tilde{C}_2 = \frac{(c_{u_R})_{21}^2}{2m_a^2}\frac{m_c^2}{f_a^2},\ C_2 = \tilde{C}_2\frac{m_u^2}{m_c^2},\ C_4 = -2\tilde{C}_2\frac{m_u}{m_c}\,, \tag{V.61}$$

and zero is obtained for all other operators. Here, $(c_{u_R})_{21}$ is the WC from Equation V.11 at the matching scale m_a and the running from the cut-off scale $4\pi f_a$ has been neglected. Moreover, for small ALP masses (large distance effects), the WCs are found to be

$$\tilde{C}_2 = -\frac{(c_{u_R})_{21}^2}{2f_a^2},\ C_2 = \tilde{C}_2\frac{m_u^2}{m_c^2},\ C_4 = -2\tilde{C}_2\frac{m_u}{m_c}, \tag{V.62}$$

while again all other WCs vanish.
In general, the NP contributions to $D^0-\bar{D}^0-$ mixing are parameterized by

$$2m_D M_{12}^{\mathrm{NP}} = \sum_{i=1}^{5} C_i(\mu)\langle D^0|\mathcal{O}_i|\bar{D}^0\rangle(\mu) + \sum_{i=1}^{3}\tilde{C}_i(\mu)\langle D^0|\tilde{\mathcal{O}}_i|\bar{D}^0\rangle(\mu), \tag{V.63}$$

with $\langle D^0|\tilde{\mathcal{O}}_i|\bar{D}^0\rangle = \langle D^0|\mathcal{O}_i|\bar{D}^0\rangle$ for $i=1,2,3$ because of parity conservation in QCD and we use $m_D = 1.865\,\mathrm{GeV}$ [351]. For small ALP masses we obtain

$$|M_{12}^{\mathrm{NP}}| = \frac{1}{2m_D}\frac{(c_{u_R})_{21}^2}{2f_a^2}\,(0.1561\,\mathrm{GeV}^4), \tag{V.64}$$

using the WCs in Equation V.62, $\langle\mathcal{O}_2\rangle = -0.1561\,\mathrm{GeV}^4$ at $\mu = 3\,\mathrm{GeV}$ from [352], and neglecting contributions that are suppressed with $\mathcal{O}(m_u/m_c)$ ($C_2 \sim 0, C_4 \sim 0$).

On the other hand, for studying short distance physics it is necessary to run the WCs from the scale of integration $\Lambda = m_a$ to the scale $\mu \sim m_c \sim 3\,\text{GeV}$. The running of the WCs was, for example, studied in [353] and, here, taken from its appendix A. However, to obtain the correct running of the relevant WCs we first have to transform them to our operator basis as described in Appendix V.B.
Again, neglecting $\mathcal{O}(m_u/m_c)$ effects at the UV we find for the running of the WCc

$$\begin{aligned}\tilde{C}_2(\mu) &= \left[r(\mu,\Lambda)^{\frac{1-\sqrt{241}}{6}} \left(\frac{1}{2} - \frac{52}{\sqrt{241}}\right) \right. \\ &\quad \left. + r(\mu,\Lambda)^{\frac{1+\sqrt{241}}{6}} \left(\frac{1}{2} + \frac{52}{\sqrt{241}}\right) \right] \tilde{C}_2(\Lambda), \\ \tilde{C}_3(\mu) &= \frac{705}{32\sqrt{241}} \left[r(\mu,\Lambda)^{\frac{1-\sqrt{241}}{6}} - r(\mu,\Lambda)^{\frac{1+\sqrt{241}}{6}} \right] \tilde{C}_2(\Lambda)\end{aligned} \tag{V.65}$$

with

$$r(\mu,\Lambda) = \left(\frac{\alpha_s(\Lambda)}{\alpha_s(m_t)}\right)^{2/7} \left(\frac{\alpha_s(m_t)}{\alpha_s(m_b)}\right)^{6/23} \left(\frac{\alpha_s(m_b)}{\alpha_s(\mu)}\right)^{6/25}, \tag{V.66}$$

where α_s is the strong coupling constant at the given scale. The running of α_s is done with `RunDec` [354, 355].
Due to the running $\tilde{C}_2$ is no longer the only non-zero WC, but also a contribution from $\tilde{C}_3$ to M_{12} occurs. Therefore, we also need $\langle \mathcal{O}_3 \rangle$. Here, we use $\langle \mathcal{O}_3 \rangle = 0.0464\,\text{GeV}^4$ at $\mu = 3\,\text{GeV}$ [352]. Then, for example, the value of M_{12} for $\Lambda = m_a = 2\,\text{TeV}$ and $\mu = 3\,\text{GeV}$ is

$$|M_{12}^{\text{NP}}| = \frac{1}{2m_D} \frac{(c_{u_R})_{21}^2}{2f_a^2} (8.95 \cdot 10^{-9}\,\text{GeV}^4). \tag{V.67}$$

The choice of $m_a = 2$ TeV corresponds to the largest value we consider in the phenomenological analysis. Consequently, the effect of the running is smaller for all other values of m_a shown. To find the parameter space allowed from $D^0 - \bar{D}^0$ − mixing, we demand that the NP contribution to $x_{12} = 2|M_{12}|/\Gamma$ do not exceed its upper bound at 95% confidence level (CL) [356], i.e.

$$x_{12}^{\text{NP}} = \frac{2|M_{12}^{\text{NP}}|}{\Gamma_D} < 0.63 \cdot 10^{-2}. \tag{V.68}$$

To determine the bound $\Gamma_D = 1.60497 \cdot 10^{-12}\,\text{GeV}$ [351] is used.

V.1.3.2 Exotic D, B and Kaon Decays

Next, we study $\Delta F = 1$ decays of mesons of the type $M \to Na$, where $M = D^{\pm,0}, B^{\pm,0}, K^{\pm,0}$ and $N = \pi^{\pm,0}$, $K^{\pm,0}$. The parton level Feynman diagrams of the processes are depicted in Figure V.6. For these decays the matrix element can be composed as

$$\langle N(p')|\bar{q}_i \gamma_\mu q_j|M(p)\rangle = (p+p')_\mu f_+^{MN}(k^2) + k_\mu f_-^{MN}(k^2), \tag{V.69}$$

where the momentum transfer is $k_\mu = (p-p')_\mu$, and q_i and q_j are the relevant quarks for the decay at the parton level. Then, the scalar form factor is defined as

$$f_0^{MN}(k^2) = f_+^{MN}(k^2) + \frac{k^2}{m_M^2 - m_N^2} f_-^{MN}(k^2). \tag{V.70}$$

Finally, the decay width for the decays is following [338]

$$\Gamma(M \to Na) = \frac{m_M^3 |\varkappa_{MN}|^2}{64\pi f_a^2} \left(1 - \frac{m_N^2}{m_M^2}\right)^2 (f_0^{MN}(m_a^2))^2 \times \sqrt{\left(1 - \frac{(m_N + m_a)^2}{m_M^2}\right)\left(1 - \frac{(m_N - m_a)^2}{m_M^2}\right)}, \tag{V.71}$$

where the effective coupling $\varkappa_{MN}$ is defined by

$$\mathcal{L} \supset \varkappa_{MN} \frac{\partial^\mu a}{2f_a} \bar{q}_i \gamma_\mu q_j + \text{h.c.}. \tag{V.72}$$

Again, q_i and q_j are the quarks of M and N that are part of the FCNC. Note that in [357] additional contributions from the diagonal couplings to the FCNCs were found, which are not yet included here.
If one neglects small isospin breaking effects, the exotic D meson decays $D^{\pm,0} \to \pi^{\pm,0} a$ will be induced by the dimension-5 operator

$$\mathcal{L} \supset (c_{u_R})_{ij} \frac{\partial_\mu a}{f_a} \left(\bar{u}_R^i \gamma^\mu u_R^j\right). \tag{V.73}$$

Then, the decay width for this specific process can easily be read from Equation V.71 by replacing $\varkappa_{MN}$ with $(c_{u_R})_{12}$, $m_M = m_D$, $m_N = m_\pi$ and using $f_0^{D\pi}(m_a^2)$ from [358].
On the other hand, the WCs for the flavour violating decays of B mesons and Kaons arise from the one-loop running of c_{u_R}, as discussed in Section V.1.2. Due to the running the term in Equation V.52 arises at low energies. Generally, through the one-loop running there also arises a non-zero WC for $\mathcal{O}_H$. This generator, however, is flavour blind, and, thus, does not contribute to the here considered $\Delta F = 1$ flavour violating processes. In contrast, the contribution is relevant for the astrophysical constraints on the model, as discussed in Section V.1.4. The WCs responsible for the exotic decays $B \to Ka$, $B \to \pi a$ and $K \to \pi a$, where $B = B^{\pm,0}, K = K^{\pm,0}$ and $\pi = \pi^{\pm,0}$ are the ones found in Equation V.55. For completeness they are written down again below:

$$(c_{d_L})_{ij} = \frac{1}{16\pi^2 v^2} V_{ri}^* (\mathcal{M}_u)_{rr} (c_{u_R})_{rs} (\mathcal{M}_u)_{ss} V_{sj} \ln\left(\frac{f_a^2}{\mu^2}\right). \tag{V.74}$$

Knowing the WCs the corresponding decay widths again can be read from Equation V.71, using $\mu \sim m_t$ and

$$\begin{array}{llllll}
(B \to Ka): & \varkappa_{MN} = (c_{u_{d_L}})_{32}, & m_N = m_B, & m_M = m_K & f_0^{MN}(m_a^2) = f_0^{BK}(m_a^2) & [359], \\
(B \to \pi a): & \varkappa_{MN} = (c_{u_{d_L}})_{31}, & m_N = m_B, & m_M = m_\pi, & f_0^{MN}(m_a^2) = f_0^{B\pi}(m_a^2) & [360], \\
(K \to \pi a): & \varkappa_{MN} = (c_{u_{d_L}})_{21}, & m_N = m_K, & m_M = m_\pi, & f_0^{MN}(m_a^2) = f_0^{K\pi}(m_a^2) & [361].
\end{array}$$

The form factors used here are calculated in the isospin preserving limit. Therefore, in the following we do not distinguish between e.g. $B^\pm \to K^\pm a$ and $B^0 \to K^0 a$.
To date no constraint on the branching ratio $\text{Br}(D \to \pi + \text{invisible})$ exists, however there are measurements of the three-body decay $D^+ \to (\tau^+ \to \pi^+ \nu)\bar{\nu}$ [362,363]. In the analysis the distributions are given as a function of the missing mass squared M_{miss}^2, which corresponds to m_a^2 in the ALP case. Thus, we can recast the analysis to find a constraint on the ALP parameter space. A similar recast was done, for example, in [347] for massless ALPs by concentrating on the bins with $M_{\text{miss}}^2 \leq 0.05\,\text{GeV}^2$. Here, however, we are interested in the case of massive ALPs. For all four considered benchmark points, including the two

benchmark points inspired by the diagonal dark pions π_D^3 and π_D^8, the FN benchmark point and the anarchic benchmark point, the total ALP decay width is small, as was seen in Section V.1.2. Even for f_a as small as $f_a \sim \mathcal{O}(1\text{ GeV})$ the total decay width for charming ALPs is still smaller than the bin width in the mass region of interest. Consequently, we can safely produce bounds similar to the ones in [347] for different values of m_a by comparing the observed number of events with the predicted background for every bin with $M^2_{\text{miss}} \geq 0$. In detail, to obtain the 90% CL bounds on $\text{BR}(D \to \pi a)$ the `TLimit` class of `ROOT` [364], which implements the CL_s method [365] and allows to include systematic errors in the background and signal, is used. Comparing the bounds produced with this method for the analyses in [362] and [366], it turns out that the bound from the former are stronger than the more recent ones from the latter.

There are several searches for exotic meson decays involving down quarks, e.g. $K^+ \to \pi^+ X^0$ [367] and $B^\pm \to \pi^\pm X^0$, $B^\pm \to K^\pm X^0$ [368], where X^0 is a *massless* ALP, but, with the exception of the recent analysis in [369] where bounds on $K^+ \to \pi^+ a$ were presented as a function of m_a, no searches for *massive* ALPs exist. Similarly to the $D^\pm \to \pi^\pm a$ case this gap can be filled by recasting existing searches on three-body decays where the relevant kinematic information is provided. In particular, we recast the searches performed in [328] and [370] to derive constraints on $B \to Ka$ and $B \to \pi a$, respectively. Again, we set 90% CL on $B \to Ka$ and $B \to \pi a$. More precisely, for $B \to Ka$ we combine the observed number of events and the predicted background for $B^+ \to K^+ \nu\bar{\nu}$ and $B^0 \to K^0 \nu\bar{\nu}$ for every $s_B = k^2/m_B^2 = m_a^2/m_B^2$ bin in Figure 5 of [328] with the CL_s method. With the same method the 90% CL limits for $B \to \pi a$ are derived comparing the observed number of events with the predicted background for every $p_\pi \equiv \sqrt{\vec{p}_\pi^{\,2}}$ bin in the right panel of Figure 4 in [370]. This is in direct correspondence with the ALP mass via $m_a^2 = m_B^2 + m_\pi^2 - 2m_B\sqrt{m_\pi^2 + \vec{p}_\pi^{\,2}}$).

It is expected that future measurements of Belle II will be sensitive to the SM $\text{Br}(B^\pm \to K^\pm \nu\bar{\nu}) = (4.0 \pm 0.5) \times 10^{-6}$ [329] at 10% accuracy with 50 ab^{-1} of data [330]. Furthermore, NA62 will measure the branching ratio $\text{Br}(K^\pm \to \pi^\pm \nu\bar{\nu})$ to within 10% of its SM value $\text{Br}(K^\pm \to \pi^\pm \nu\bar{\nu}) = (8.4 \pm 4.1) \times 10^{-11}$ [371, 372]. Independently of whether the results of future measurements are published directly on a two-body decay or a recast of the three-body decay analysis is needed their numbers are a great improvement compared to current bounds.

V.1.3.3 Radiative J/ψ Decays

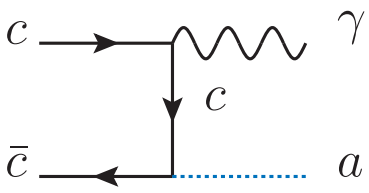

Figure V.7: Parton level Feynman diagram for the decay $J/\psi \to a\gamma$.

After discussing the impact of charming ALPs on flavour violating processes, we now focus on the radiative charmonium decay $J/\psi \to a\gamma$ as first proposed by [207] (later studied by many others, see e.g. [373–378]) and displayed on parton level in Figure V.7. This process strongly constrains the diagonal ALP coupling $(c_{u_R})_{22}$. It is convenient to normalize the corresponding branching ratio by the one of $J/\psi \to \mu^+\mu^-$. This way one can absorb

some of the QCD uncertainties of the calculation. The $J/\psi \to \mu^+\mu^-$ branching ratio is accurately measured to be $\mathrm{Br}(J/\psi \to \mu^-\mu^+) = 5.973\ \%$ [366]. The normalized branching ratio for the radiative decay then is

$$\frac{\mathrm{Br}(J/\psi \to a\gamma)}{\mathrm{Br}(J/\psi \to \mu^-\mu^+)} = \frac{G_F m_c^2 v^2}{\sqrt{2}\pi\alpha_{\mathrm{em}}} \left(\frac{(c_{u_R})_{22}}{f_a}\right)^2 \times \left(1 - \frac{m_a^2}{m_{J/\psi}^2}\right) F. \tag{V.75}$$

$F \sim \mathcal{O}(1/2)$ is a correction factor taking into account QCD effects [379, 380], contributions related to bound-state formation [381, 382], as well as relativistic corrections [383]. Henceforth, for the sake of concreteness, we assume that $F = 1/2$. Then, for the radiative branching ratio we have

$$\mathrm{Br}(J/\psi \to a\gamma) = (1.05\,\mathrm{GeV}^2) \left(\frac{(c_{u_R})_{22}}{f_a}\right)^2 \left(1 - \frac{m_a^2}{m_{J/\psi}^2}\right). \tag{V.76}$$

The decay $J/\psi \to a\gamma$ has been searched for by the CLEO collaboration [384], which we use to constrain the charming ALP parameter space.

V.1.4 Astrophysical and Cosmological Constraints

In addition to constraints from flavour processes, bounds from astrophysical and cosmological processes also set limits on the ALP parameter space. In the following, we discuss these constraints in detail.

V.1.4.1 Bounds from Astrophysical Processes

Supernova SN1987a

The first bound we discuss arises from the observed neutrino burst due to the core-collapse supernova SN1987a. The main cooling mechanism of the proto-neutron star left after the core-collapse is neutrino emission. Consequently, a too large amount of ALP emission could lead to ALP emission becoming the main cooling mechanism and, eventually, to ALP emission being in conflict with the observed amount of neutrinos. To impose a bound on the parameter space, we follow [385] and demand that the ALP luminosity in the proto-neutron star L_a does not exceed the neutrino one L_ν, i.e. $L_a \leq L_\nu = 3 \cdot 10^{52}\,\mathrm{erg/s}$. Here, it is worth to point out that in [386] some serious doubts on supernova cooling bounds for ALPs have been brought up by drawing attention to the fact that the cooling of the proto-neutron star is not the only neutrino production mechanism in core-collapse supernovae and current simulations are not sufficient to definitely exclude parts of the ALP parameter space. Nonetheless, we calculate and show the supernovae bound on the charming ALP parameter space.

To do so we first need to find the ALP nucleon couplings. At leading order this coupling can be obtained from the Lagrangian

$$\begin{aligned}\mathcal{L}_{\mathrm{int}} = \left(\frac{\partial_\mu a}{4f_a}\right) \Big\{ &\mathrm{Tr}\left((\hat{c} + \varkappa_q c_g)\lambda^a\right) \left(F\,\mathrm{Tr}\left(\bar{B}\gamma^\mu\gamma_5\left[\lambda^a, B\right]\right) + D\,\mathrm{Tr}\left(\bar{B}\,\gamma^\mu\gamma_5\left\{\lambda^a, B\right\}\right)\right) \\ &+ \frac{1}{3}\mathrm{Tr}\left(\hat{c} + \varkappa_q c_g\right)\, S\,\mathrm{Tr}\left(\bar{B}\,\gamma^\mu\gamma_5 B\right) + \mathrm{Tr}\left((\hat{c} + \varkappa_q c_g)\lambda^a\right)\mathrm{Tr}\left(\bar{B}\,\gamma^\mu\left[\lambda^a, B\right]\right)\Big\}. \end{aligned} \tag{V.77}$$

In this Lagrangian B is the baryon matrix

$$B = \frac{1}{\sqrt{2}} B^a \lambda^a = \begin{pmatrix} \frac{\Sigma^0}{\sqrt{2}} + \frac{\Lambda}{\sqrt{6}} & \Sigma^+ & p \\ \Sigma^- & -\frac{\Sigma^0}{\sqrt{2}} + \frac{\Lambda}{\sqrt{6}} & n \\ \Xi^- & \Xi^0 & -\frac{2\Lambda}{\sqrt{6}} \end{pmatrix}, \tag{V.78}$$

and the axial-vector coupling constants F and D are defined by

$$\langle B_i' | J_j^{(8)} | B_k \rangle = i f_{ijk} F + d_{ijk} D. \tag{V.79}$$

Finally, $J_j^{(8)}$ is the weak axial-vector hadronic current transforming as an $SU(3)$ octet, while f_{ijk} are the totally antisymmetric structure constants of $SU(3)$ and d_{ijk} the totally symmetric ones. Moreover, S is defined by the singlet current which can be renormalized independently. The constants F and D are found from hyperon semileptonic decays [387] and are $F = 0.463 \pm 0.008$, $D = 0.804 \pm 0.008$, while $S \approx 0.13 \pm 0.2$ [388]. Here, we are only interested in the $a\bar{N}N$ couplings, with $N = p, n$ defined by

$$\mathcal{L}_{\text{int}} \supset \frac{1}{12} \frac{\partial_\mu a}{f_a} (c_{u_R})_{11} \Big(\big[S - 4D\big] (\bar{n} \gamma^\mu \gamma_5 n) + \big[2D + 6F + S\big] (\bar{p} \gamma^\mu \gamma_5 p) + 6 \bar{p} \gamma^\mu p \Big). \tag{V.80}$$

The last part of Equation V.80 can be neglected because it is a total derivative. Ultimately, the ALP nucleon coupling reads

$$\mathcal{L}_{aNN} = \sum_{N=p,n} \frac{\partial_\mu a}{2 f_a} c_{aNN} \bar{N} \gamma^\mu \gamma_5 N \tag{V.81}$$

with

$$c_{app} = (c_{u_R})_{11} \left(F + \frac{1}{3} D + \frac{1}{6} S \right) = (c_{u_R})_{11} \left(0.75 \pm 0.03 \right), \tag{V.82}$$

$$c_{ann} = (c_{u_R})_{11} \left(\frac{1}{6} S - \frac{2}{3} D \right) = (c_{u_R})_{11} \left(-0.51 \pm 0.03 \right). \tag{V.83}$$

In the proto-neutron star the ALP luminosity is

$$L_a = \int_{r \leq R_\nu} dV \int_{m_a}^{\infty} d\omega \left(\frac{dP_a}{dV d\omega} \right) e^{-\tau}. \tag{V.84}$$

In the above expression ω is the ALP energy and $R_\nu \sim \mathcal{O}(40\,\text{km})$ is the radius of the neutrinosphere. Beyond this radius neutrinos free stream until arriving on Earth. We also take into account the probability for an ALP produced within the neutrinosphere to reach $R_{\text{far}} \sim \mathcal{O}(100 - 1000\,\text{km})$. Neutrinos are not produced efficiently outside of this radius. This probability shows up in the term $e^{-\tau}$ in Equation V.84. If ALPs produced in the neutrinosphere do not reach R_{far}, they will get "trapped" due to their large couplings. In this case, the energy of the ALPs is eventually converted back into neutrinos. The probability for ALPs to reach R_{far} is computed using the optical depth $\tau = \tau(m_a, \omega, r, R_{\text{far}})$, for which we take $R_{\text{far}} = 100\,\text{km}$ [389]. The term $\frac{dP_a}{dV d\omega}$ in Equation V.84 describes the ALPs differential power. Since charming ALPs solely couple to RH up-type quarks and, therefore, to nucleons, the dominant production mode in a proto-neutron star is the bremsstrahlung process $N + N \to N + N + a$. For this process the differential power is [244, 385]

$$\frac{dP_a}{dV d\omega} = \frac{1}{2\pi^2} \omega^3 \Gamma_a e^{-\omega/T} \beta^2, \tag{V.85}$$

where T is the temperature as a function of the radius and $\beta = \sqrt{1 - m_a^2/\omega^2}$ is a phase space factor. Moreover, Γ_a is the ALP absorption width

$$\Gamma_a = \Gamma_a^{pp} + \Gamma_a^{nn} + \Gamma_a^{pn} + \Gamma_a^{np} \tag{V.86}$$

with [390]

$$\Gamma_a^{NN'} = \frac{c_{aNN}^2 Y_N Y_{N'}}{4f_a^2}\frac{\omega}{2}\frac{n_B^2\sigma_{np\pi}}{\omega^2}\gamma_{\rm f}\gamma_{\rm p}\gamma_{\rm h}, \quad N^{(\prime)} = n, p. \tag{V.87}$$

The relevant ALP-nucleon coupling c_{aNN}, with $N = p, n$, has been calculated above. The values for c_{app} and c_{ann} are given in Equations V.82 and V.83. In the ALP absorption width in Equation V.87 $Y_{N^{(\prime)}}$ is the mass fraction of the nucleon $N^{(\prime)}$, $n_B = \rho/m_N$ is the baryon density and $\sigma_{np\pi}$ is given by

$$\sigma_{np\pi} = 4\alpha_\pi^2\sqrt{\pi T/m_N^5} \tag{V.88}$$

with $\alpha_\pi \approx 15$. For concreteness we take $Y_p = 0.3$ and $Y_n = 1 - Y_p = 0.7$. Moreover, we use [391]

$$1/\gamma_{\rm f} = 1 + \left(n_B\sigma_{np\pi}/(2\omega)\right)^2, \tag{V.89}$$

while $\gamma_{\rm p} = s(n_B, Y_N, \omega/T, m_\pi/T)$ with s given by Equation 49 of [392]. Note that s is divided by an extra factor $(1 - \exp(-x))$ in order to preserve the detailed balance more explicitly. Lastly, we take [393]

$$\gamma_{\rm h} = -0.0726502\ln(\rho) + 10^{10}/\rho^{0.9395710} + 2.5558616, \tag{V.90}$$

where the density ρ is expressed in $\mathrm{g\,cm^{-3}}$. Following [394] we assume for $\rho(r)$ and $T(r)$ the "fiducial" profiles of [389]

$$\rho(r) = \rho_c \times \begin{cases} 1 + k_\rho(1 - r/R_c) & r < R_c \\ (r/R_c)^{-\nu} & r \geq R_c \end{cases}, \tag{V.91}$$

$$T(r) = T_c \times \begin{cases} 1 + k_T(1 - r/R_c) & r < R_c \\ (r/R_c)^{-\nu/3} & r \geq R_c \end{cases}. \tag{V.92}$$

Concretely, the following values are used: $k_\rho = 0.2$, $k_T = -0.5$, $\nu = 5$, $R_c = 10\,\mathrm{km}$, $T_c = 30\,\mathrm{MeV}$ and $\rho_c = 3\cdot 10^{14}\,\mathrm{g/cm^3}$.
The last part missing to calculate the ALP luminosity in the proto-neutron star is the optical depth, for which we take [394]

$$\tau = (R_{\rm far} - R_\nu)\beta^{-1}\Gamma_a(R_\nu) + \beta^{-1}\int_r^{R_\nu} d\tilde{r}\,\Gamma_a(\tilde{r}). \tag{V.93}$$

With this information we can, finally, calculate L_a and put a bound on the charming ALP parameter space.

Red Giant Burst

As seen above in Section V.1.2, the one-loop running of the dimension-5 effective charming ALP Lagrangian in Equation V.1 generates a non-zero WC for the flavour-blind operator $\mathcal{O}_H$. In addition to couplings to up- and down-type quarks, this operator also induces a coupling to leptons. For small m_a the coupling to electrons faces strong astrophysical bounds, more specifically it is constrained by data from red giant bursts.

The running of the WC has been discussed in Section V.1.2. Here, we are specifically interested in the ALP electron coupling at the scale $\mu \sim m_t$, which from Equation V.45 is

$$g_{aee} = \frac{c_H m_e}{f_a} = \frac{3m_e}{8\pi v^2 f_a} \ln\left(\frac{f_a^2}{m_t^2}\right) \sum_{i=1}^{3} (\mathcal{M}_u)_{ii} (c_{u_R})_{ii}. \tag{V.94}$$

It is obvious from Equation V.94 that the bound on the parameter space will be strong if the ALP couples to top quarks since this coupling contributes the most significantly to the running. For ALP masses below the temperature of the red giant ($T_{core} \sim 10$ keV) the bound on the ALP electron coupling is $g_{aee} \lesssim 1.6 \cdot 10^{-13}$ [225, 244–246].

V.1.4.2 Cosmological Bounds

Cosmological bounds are very sensitive to the total decay width and the different branching ratios of the ALP. Therefore, we make use of the discussion of these properties in Section V.1.2. It is important to note that most cosmological constraints on ALPs are calculated under the assumption that ALPs only couple to photons. Nonetheless, following the discussion in [395] the cosmological bounds can also be applied to the more general case where other couplings are present. Couplings to other SM particles than photons lead to a smaller temperature for the ALP decoupling and, therefore, a higher primordial abundance. Thus, the bound for the relic ALP production from the case with only couplings to photons can be considered as conservative bounds. Fermionic ALP decays only dominate close to their threshold over the decays to photons and gluons. Therefore, at low masses, the ALP phenomenology relevant for the cosmological constraints is similar to the one of ALPs with only photon couplings, while at higher masses of a few GeV the coupling to gluons leads to mixing with hadrons and, consequently, to additional decay modes to photons. Making use of this, we can recast the limits from [395–397] by using the ALP lifetime $1/\Gamma$, with Γ the total decay width. The cosmological bounds studied in [395–397] include the possible impact on N_{eff}, potential distortions of the CMB spectrum, as well as modifications of the predicted BBN. For ALP decays to lepton pairs being the dominant decay channel, which is the case when there is a sizeable coupling ALP top quark coupling present, these bounds can also be directly applied interpreting $1/\Gamma$ as the ALP lifetime. In fact, if $a \to \mu^+\mu^-$ is the dominant decay channel, this approach will over-estimate the excluded region slightly because the subsequent decay of the muons heats the neutrino bath, which in turn reduces the impact on the effective number of DOF N_{eff}. On the other hand, in the region where $a \to 3\pi$ is the dominating decay mode, the bound from ^{4}He overproduction poses the dominant constraint. Since only a minimal amount of charged pions is necessary for this bound to apply, it holds regardless of the changes in the branching ratios. Lastly, for even larger ALP masses, more decay channels open up, and the hadronic decays eventually make the lifetime of charming ALPs shorter than one second. Then, the BBN constraint is harmless and we can apply the corresponding bounds if we interpret τ as the total lifetime even for these masses.

V.1.5 Collider Probes

As has been seen above, charming ALPs are long-lived in parts of the parameter space. Consequently, fixed target experiments and LHC forward detectors may be able probe this part of the parameter space. Here, we study the prospects of NA62 [279] and the proposed SHiP experiment [398] as examples for fixed target experiments, as well as the prospects of the LHC forward detector FASER [6, 7, 399] and the proposed MATHUSLA detector

[400, 401]. We compare the prospect of these experiments with the bounds imposed by the CHARM experiment in [402]. For all experiments we consider the decay of D mesons as the main ALP production mode. The geometrical structure and detector parameters for all here considered experiments are given in Table V.1.

Experiment	distance from IP	length of decay volume	radius/opening angle	N_D
FASER	480 m	1.5 m	0.1 m	1.1×10^{15}
FASER2	480 m	5 m	1 m	2.2×10^{16}
MATHUSLA	68 m downstream, 60 m above	100 m	25 m high	2.2×10^{16}
NA62	80 m	65 m	$\theta_{\max} = 0.05$	2×10^{15}
SHiP	60 m	50 m	2.5 m	6.8×10^{17}
CHARM	480 m	35 m	$0.0068 < \theta < 0.0126$	4.08×10^{15}

Table V.1: Detector parameters for the different fixed target experiments and LHC forward detectors considered.

V.1.5.1 Fixed Target Experiments

The NA62 experiment is a fixed target experiment at the CERN Super Proton Synchrotron (SPS). Its main purpose is the search for rare Kaon decays. Nonetheless, when operating in the beam dump mode, so that the target is lifted and the 400 GeV proton beam hits the Cu collimator located 20 m downstream, NA62 can also be used to search for hidden sector particles [326]. From a short run in beam dump mode in November 2016 useful information about the background have been extracted and it has been found that an upstream veto in front of the decay volume could reduce the backgrounds to nearly zero [403]. Similarly, the design of the proposed SHiP experiments aims to reduce the background to 0.1 events [327, 398]. Consequently, for both experiments three charming ALP decay events correspond to an expected exclusion limit at over 95% CL.
The expected number of events in the decay volume of the respective detector can be calculated as

$$N_a = N_D \cdot \mathrm{Br}(D \to \pi a) \cdot \varepsilon_{\mathrm{geom}} \cdot F_{\mathrm{decay}} \,. \tag{V.95}$$

Here, N_D is the number of D mesons produced at the interaction point. This number is listed in Table V.1. The branching ratio $\mathrm{Br}(D \to \pi a)$ was defined in Section V.1.3, and $\varepsilon_{\mathrm{geom}}$ is the geometric acceptance. It describes the fraction of ALPs with lab frame momentum at the acceptance angle of the respective detector. Lastly, F_{decay} is the fraction of ALPs that decay inside the decay volume of the detector, which depends on the charming ALP lifetime and boost. In the following, it is also always assumed that the number of ALPs directly produced in the beam dump is negligible.
We follow [10] for the calculation of F_{decay} and $\varepsilon_{\mathrm{geom}}$. The probability for a particle with lab-frame decay length L to decay in a detector volume, that starts at the distance L_1 from the interaction point and ends at L_2 is

$$p_{decay}(L) = e^{-L_1/L} - e^{-L_2/L}. \tag{V.96}$$

The length of the detectors can be found in Table V.1. To get F_{decay} this probability has to be convoluted with the distribution for L. The distribution for the lab-frame decay length

L and $\varepsilon_{\text{geom}}$ can be obtained from the lab-frame distribution of longitudinal momenta and angles for the charming ALPs. For calculating these it is assumed that, in analogy to the B mesons in [10], the D mesons are produced close to threshold. That means the D mesons have very small transverse momenta compared to their lab-frame longitudinal momenta. For the considered two-body decay $D \to \pi a$ one finds the magnitude of the charming ALP momenta in the rest frame of the D meson given by [10]

$$p_{CM} = \frac{1}{2m_D}\sqrt{\left(m_D^2 - (m_\pi + m_a)^2\right)\left(m_D^2 - (m_\pi - m_a)^2\right)}. \tag{V.97}$$

Then, the expected distribution of longitudinal and transverse momenta for the charming ALPs in the frame of the D meson are found by taking a random sample of angles θ_{CM} from a flat distribution between $-\pi$ and π for each charming ALP mass in a sampled range and setting the magnitude to p_{CM}. Finally, the distribution of longitudinal and transverse momenta is boosted by the D meson momentum distribution to obtain the lab-frame distribution of longitudinal momenta and angles for the charming ALPs. For both, NA62 and SHiP the D meson momentum distribution is taken from [404] since both experiments have the same proton beam energy. Using the above formalism the expected discovery regions for NA62 and SHiP can be found by using Equation V.95 and demanding $N_a \geq 3$.
Searches for ALPs decaying into pairs of photons, electrons and muons have been carried out by the CHARM experiment. The analysis in [402] record no decay events at 90% CL. Based on this the upper limit on the number of charming ALP events at CHARM is then found using a Poisson distribution with $0.1 = \lambda^k e^{-\lambda}/k!_{|k=0}$ [405]. The solution of this equation is $\lambda = 2.3$ and, thus, we set a limit at $N_{\text{obs}} = 2.3$ to recast the bound for charming ALPs. Again, we assume that charming ALPs are produced in the $D^\pm \to \pi^\pm a$. As CHARM also has a proton beam energy of 400 GeV, we use the same momentum distribution for the D mesons as for NA62 and SHiP. The number of D mesons produced can be found from the number of protons hitting the target $N_{proton} = 2.4 \times 10^{18}$ [402] and multiplying it by the probability of such a proton beam to produce a pair of c quarks [406] $p_{c\bar{c}} = 1.7 \times 10^{-3}$, leading to $N_D = 4.08 \times 10^{15}$ produced D mesons. Following the same procedure as for NA62 and SHiP we use the detector parameters in Table V.1 to calculate with Equation V.95 the expected number of charming ALPs decaying inside the CHARM detector volume and impose the 90% CL bound. It is important to note that the CHARM experiment only searches for the di-photon, di-electron and di-muon final states, so that for the recast Equation V.95 has to be multiplied by $\sum_{i=\gamma,e,\mu} \text{Br}(a \to ii)$ to only take these decays into account.

V.1.5.2 LHC Forward Detectors

FASER as part of the Forward Physics Facility (FPF) [6,7] and the proposed MATHUSLA detector are experiments designed to search for long-lived particles at LHC. Their prospect to search for charming ALPs produced in D meson can be determined in analogy to the fixed target experiments. The D meson momentum distribution at LHC and HL-LHC is simulated using `FONLL` with `CTEQ6.6` [407]. For LHC run 3 where FASER will operate the expected number of produced D mesons is $N_D = 1.1 \times 10^{15}$ and this number increases by a factor 20 for the HL-LHC, for which both FASER2 and MATHUSLA are proposed. With the detector parameters given in Table V.1 the number of expected charming ALP decays is calculated from Equation V.95.

V.1.6 Resulting Charming ALP Parameter Space

All the above discussed constraints on the parameter space are shown together with the detection lines for the four discussed experiments in Figures V.8 and V.9. More specifi-

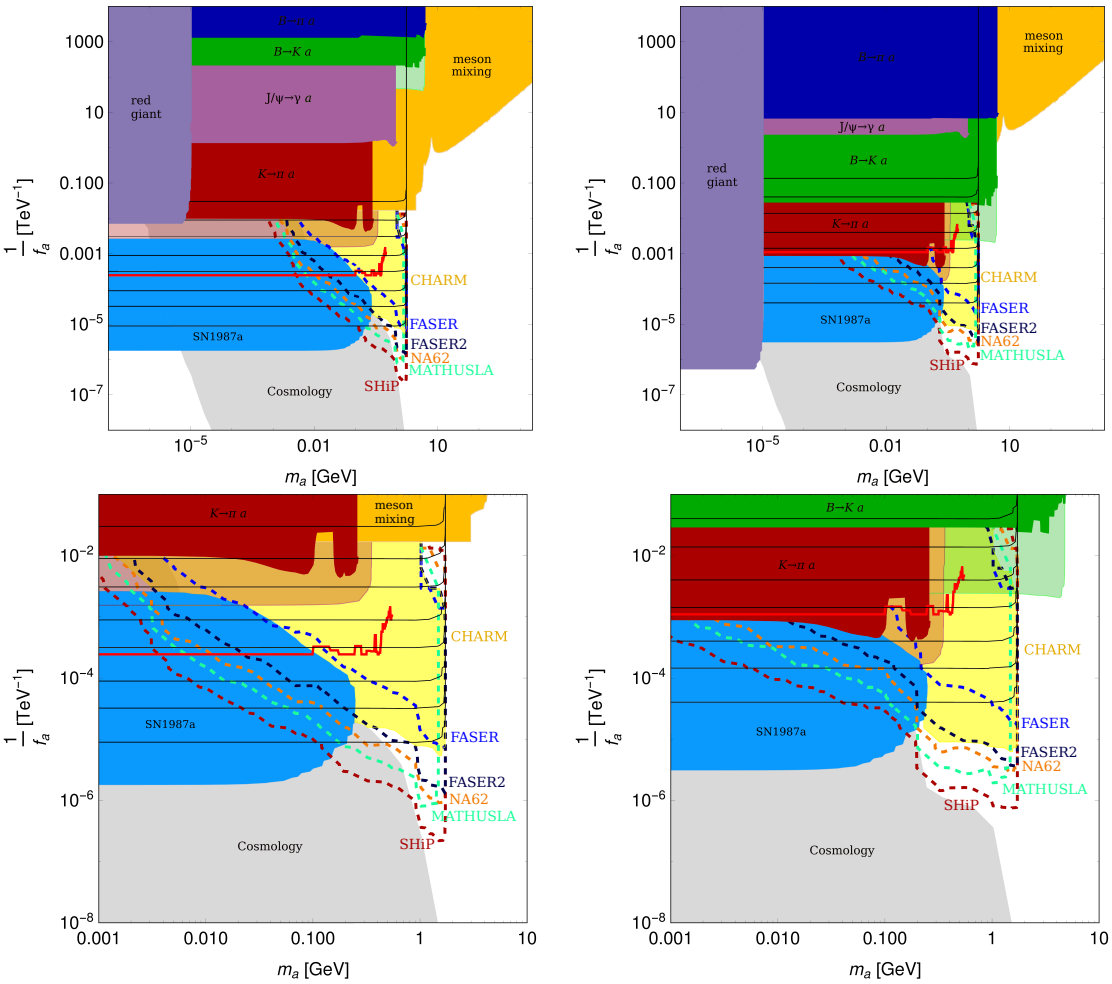

Figure V.8: Experimental constraints and expected detection lines for $1/f_a$ as a function of m_a for the dark-QCD inspired benchmark models. The case $a = \pi_D^3$ is shown in the **left** panels, while **right** panels illustrate the scenario $a = \pi_D^8$. The light green and light red areas depict the expected constraints coming from Belle II and NA62, respectively. The constraint arising from the recast of the three-body decay $D^+ \to (\tau^+ \to \pi^+ \bar{\nu})\nu$ is shown by the red line, whereas the impact of a direct measurement of $\mathrm{Br}(D \to \pi a)$ is represented by black lines with values going from 10^{-1} to 10^{-8}, each one a decade smaller. Finally, dashed lines correspond to the different considered fix-target experiments and collider probes of the model. **Lower** panels zoom in the regions where upcoming experiments are sensitive. For both scenarios we assume $\kappa_0 = 1$.

cally, in Figure V.8 the resulting allowed parameter space for the two dark-QCD inspired benchmark points is shown, the case of $a = \pi_D^3$ in the left panels and $a = \pi_D^8$ in the right ones. For both scenarios we assume $\kappa_0 = 1$ to be able to evaluate the logarithmic dependence in the ALP electron coupling, which only depends on f_a, while all other here considered quantities are proportional to factors of $\frac{\kappa_0}{f_a}$. Choosing a different value for κ_0 with $\kappa_0 \sim \mathcal{O}(1)$ does not change the parameter space significantly. In Figure V.9, on the

other hand, the resulting parameter space for the anarchic scenario is shown in the left panels, while the right panels illustrate the resulting allowed parameter space of the FN scenario. For all four scenarios shown, the parameter space excluded by $D^0 - \bar{D}^0$ – mixing

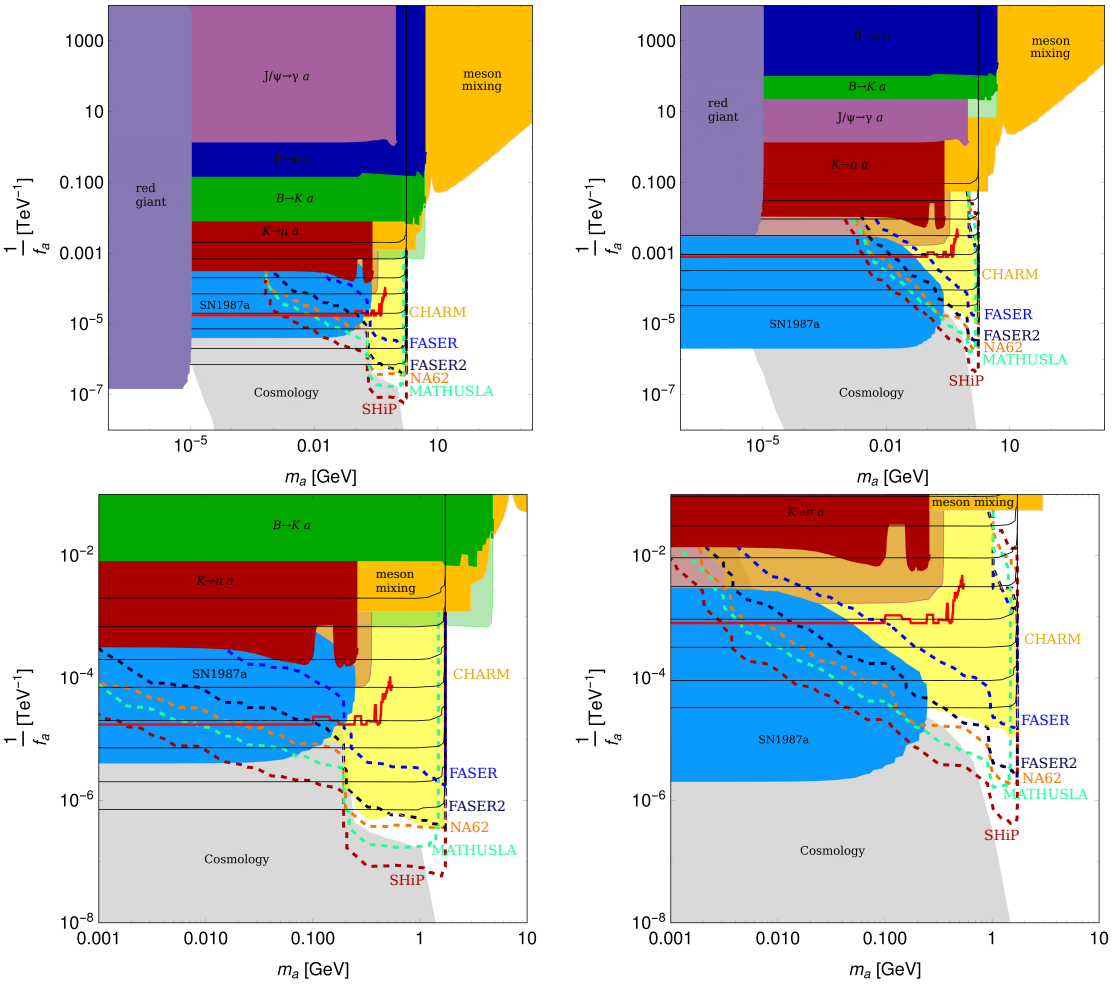

Figure V.9: Experimental constraints and expected detection lines for $1/f_a$ as a function of m_a, same as figure V.8, but for the anarchic (**left**) and the FN inspired models (**right**). **Lower** panels again zoom in the regions where upcoming experiments are sensitive.

is shown as the dark yellow region, whereas the regions excluded from $B \to Ka$, $B \to \pi a$ and $K \to \pi a$ are displayed in green, blue and red, respectively. To give a prospect where the future bounds of Belle II and NA62 would be we interpret the expected bounds on $B \to K\nu\bar{\nu}$ and $K \to \pi\nu\bar{\nu}$ as sensitive to $B \to Ka$ and $K \to \pi a$ and show them in light green and light red. However, a proper recast of these bounds, once they are measured, will most likely result in slightly weaker bounds. For the constraints from exotic Kaon and B meson decays, the impact of the ALP top quark coupling is quite visible: If the ALP has a non-negligible coupling to top quarks, couplings arising on one-loop level will be larger and, therefore, the bounds from Kaon and B meson decays will be stronger for the $a = \pi_D^8$ (Figure V.8 right) and anarchic scenario (Figure V.9 left) than for the $a = \pi_D^3$ (Figure V.8 left) and FN scenario (Figure V.9 right). The limits arising from the recast of $D^+ \to (\tau^+ \to \pi^+\nu)\bar{\nu}$ are illustrated with the red line. The last constraint from flavour processes shown in Figures V.8 and V.9 is the constraint from the radiative $J\psi \to a\gamma$

decay, which is shown in purple.
The astrophysical bounds from SN1987a and red giant bursts are represented by the blue and lilac regions. Finally, the cosmological bounds are depicted by the grey region. Again, the impact of the ALP top quark coupling to the ALP electron coupling, which arises from the one-loop running of c_H, is clearly visible as the red giant burst bound is more stringent for larger couplings to top quarks.
Independent of the choice of benchmark model the parameter space above the D and B meson mass is mostly unconstrained by flavour. This opens the possibility to probe this region at the energy frontier, i.e. at the LHC. A detailed study how this region could be probed with flavour-violating top decays can be found in Section V.2. Similarly, below the D meson mass, some viable regions remain as well and can be probed by the upcoming or proposed collider experiments discussed in section V.1.5. The projected detection regions for the fixed target experiments NA62 and SHiP are shown by the dashed orange and red lines, while for the LHC forward experiments FASER at LHC run 3, and FASER2 and MATHUSLA at HL-LHC the same is shown by the light blue, dark blue and turquoise dashed lines. Above the lines more than three charming ALP decay events are expected inside the respective decay volume, corresponding by non-discovery to an exclusion limit at over 95% CL. In addition, we show the region excluded by the recast of the results of the CHARM experiment as the light yellow region.
For better assessment of the regions that can be probed by these experiments we show a zoomed in view to these regions in the lower panels of Figures V.8 and V.9. It can be seen that FASER will mostly validate the CHARM bounds, while FASER2 at the HL-LHC, as well as NA62 will probe new regions of parameter space, with SHiP and MATHUSLA covering the remaining unexplored areas below the charm mass threshold. When comparing the scenarios with small $(c_{u_R})_{33}$ ($a = \pi_D^3$ and FN scenario) with the benchmark models with sizable ALP top quark coupling, it is clear that $(c_{u_R})_{33}$ also impacts the regions probable by future experiments. For small ALP top quark couplings the total decay width for small ALP masses is smaller and, consequently, the lifetime larger. If the ALP lifetime grows too large, ALPs will not decay inside the considered detectors, but even further away from the interaction point. This explains the bump at around $m_a \sim 1$ GeV in the $a = \pi_D^3$ and FN scenario for all detection lines. Contrariwise, for the $a = \pi_D^8$ and anarchic scenario the couplings to leptons are larger, leading to smaller ALP lifetimes, and, thus, to the plateau-like feature of the detection lines between twice the muon mass and the kinematic threshold of the D meson decay.
Finally, a possible measurement of $\mathrm{Br}(D \to \pi + \text{invisible})$ could provide a complementary test of the parameter space close to the charm threshold. In fact, this measurement might be crucial to probe the region close to the charm mass at relatively large coupling. In both, the FN and the $a = \pi_D^3$ benchmark models the parameter space in this region is not otherwise accessible. Meanwhile, this region can also be probed by Belle II to higher ALP masses in the $a = \pi_D^8$ scenario and is already excluded by CHARM and $D^0 - \bar{D}^0$ − mixing in the anarchic scenario. In the same way, the low mass region ($m_a \lesssim 10^{-6}$ GeV) is only accessible via $\mathrm{Br}(D \to \pi + \text{invisible})$ and future NA62 measurements. The discovery prospect of a measurement of $\mathrm{Br}(D \to \pi + \text{invisible})$ is illustrated by the black contour lines in Figures V.8 and V.9, which correspond to the branching ratio values $\mathrm{Br}(D^\pm \to \pi^\pm \text{invisible}) \in \{10^{-8}, 10^{-7}, 10^{-6}, 10^{-5}, 10^{-4}, 10^{-3}, 10^{-2}, 10^{-1}\}$. They show that an experimental measurement of $\mathrm{Br}(D^\pm \to \pi^\pm \text{invisible})$ is a valuable piece in the quest for discovering NP in the up-type quark sector, for example the well motivated scenario of charming ALPs.
It is important to mention that some of the phenomenology studied here may change when

considering the whole picture in the dark-QCD case due to non-trivial interplay between the complete set of dark pions, see Chapter IV for details.
Lastly, a region of parameter space was so far left unexplored in the study of charming ALPs. It is the region with very small ALP masses and couplings, i.e. the lower left regions of our figures. In these regions the charming ALP would be a DM candidate. Due to DM overproduction the freeze-out of such a DM candidate is excluded for $m_a \gtrsim 100$ eV [395] and in the whole parameter region if structure formation bounds are also taken into account [408]. Oppositely, if considering a freeze-in mechanism for the charming ALP DM production, a region of parameter space will remain in principle viable [408].

V.2 Charming ALPs and Exotic Top Decays

By studying the various constraints on the charming ALP parameter space in Section V.1 it was found that a large region above the D meson mass is mostly unconstrained. The only bound in this region comes from $D^0 - \bar{D}^0$ − mixing. If the charming ALP has non-zero couplings $(c_{u_R})_{13} = (c_{u_R})_{31} \neq 0$ and/or $(c_{u_R})_{23} = (c_{u_R})_{32} \neq 0$, charming ALPs can be produced in exotic top decays, as well as directly in association with a top quark. Consequently, precision top quark physics, as well as new search strategies for flavour violating top decays involving charming ALPs where the top quark is used as a trigger object can be used to probe this region. As has been found above, in the here considered parameter region ALPs decay mostly hadronically (cf. Figure V.4) and have varying lifetimes depending on their mass and the choice of couplings. If the ALP lifetime is large, ALPs will be stable on detector scales, while for small lifetimes they will be seen as a prompt event at colliders. In both cases they can contribute to single top events. Finally, in the intermediate lifetime region ALPs decay to displaced jets. In the following, we first show that precision measurements of the single top cross section are able to probe the charming ALP model by performing recasts of existing single top searches. From the recasts we obtain new constraints on the parameter space of the ALP for both prompt ALP decays to jets and for detector stable ALPs. Afterwards, we propose a new search strategy for long-lived ALPs in events with top quark pairs. Since the top pair production cross section at LHC is humongous ($\sigma_{t\bar{t}} \sim 830$ pb [409]), even a small branching ratio of top to an ALP and a light jet from an up or charm quark leads to a large amount of top plus ALP events. If the ALP decays displaced from the PV, its decay will be easily distinguishable from SM decays. Charming ALPs decay displaced for masses at the lower end of the allowed mass range. For ALP decays in the hadronic calorimeter we expect only a small energy deposit in the electromagnetic calorimeter and at the same time fewer tracks associated with the jet. We exploit this in our proposed search to suppress the backgrounds by several orders of magnitude. Thus, our proposed search facilitates to reach sensitivity to very small exotic top branching ratios.

V.2.1 Charming ALP Parameterization

While we continue to study the charming ALP model described by the effective Lagrangian in Equation V.1, we move away from the in the previous Section V.1 introduced benchmark scenarios. Instead, we introduce a parameterization of c_{u_R}, that is more convenient for the study of the constraints and search possibilities of charming ALPs in exotic top decays and precision top quark physics. As before, we set all WCs except c_{u_R} to zero, so that the ALP effective Lagrangian simplifies to

$$\mathcal{L} = \frac{1}{2}(\partial_\mu a)(\partial^\mu a) - \frac{m_a^2}{2}a^2 + \frac{\partial_\mu a}{f_a}(c_{u_R})_{ij}\bar{u}_{Ri}\gamma^\mu u_{Rj}\,. \tag{V.98}$$

For now, we simply assume that

$$c_{u_R} = \begin{pmatrix} c_{11} & c_{12} & c_{13} \\ c_{21} & c_{22} & c_{23} \\ c_{31} & c_{32} & c_{33} \end{pmatrix} \tag{V.99}$$

is a not further specified hermitian matrix. Couplings to vector bosons and to other SM fermions (down-type quarks and leptons) are generated via top loops and from the RGEs [346–350, 410], as was discussed in Section V.1.2. We have seen before that these

operators are suppressed relative to the tree-level interactions of Equation (V.98), but induce decays, that can be relevant in some regions of the parameter space, where the hadronic channels are kinematically inaccessible. We show the branching ratios of charming ALPs again as a function of the ALP mass in the left panel of Figure V.10, this time for a specific choice of the general form of c_{u_R} defined in Equation V.99. Since the only constraint in the region $m_a \gtrsim m_D$ is the one from $D^0 - \bar{D}^0$ − mixing, which depends on $(c_{u_R})_{12}$, we use $(c_{u_R})_{12} = 0 = (c_{u_R})_{21}$. For all other entries we choose $(c_{u_R})_{ij} = 1$, as well as $f_a = 10^6$ GeV. Here, $f_a = 10^6$ GeV is chosen because it allows a wide range of lifetimes while keeping $(c_{u_R})_{3i} = 1$ and $(c_{u_R})_{ii} \sim 0.1 - 10$ $(i = 1, 2, 3)$. Changes in f_a are later absorbed in changes of the couplings, as, with the exception of the leptonic branching ratio, all considered quantities are only proportional to powers of c_{u_R}/f_a, but not c_{u_R} or f_a independently. In addition, in Figure V.10 we only show the for the collider searches relevant ALP masses, more precisely $m_a > 1$ GeV and, thus, always use quark-hadron duality [308,345]. All decay widths were calculated using the expressions in Section V.1.2. For ALP masses where $a \to \bar{c}c$ is not kinematically allowed $a \to gg$ dominates the ALP branching ratio. Then, when the $a \to \bar{c}c$ channel opens up, it is the dominant decay channel, until for large enough values of the ALP mass $a \to gg$ takes over again since the loop generated vector boson decays grow with m_a^3, while the fermionic decay widths are linear in the ALP mass. Note that the fermionic decays induced from RGE-running (couplings to leptons and flavour blind couplings to down-type quarks) have a logarithmic dependence on the scale of the matching $\Lambda \sim f_a$, so smaller values of f_a reduce their relative impact, cf. Equation V.45.

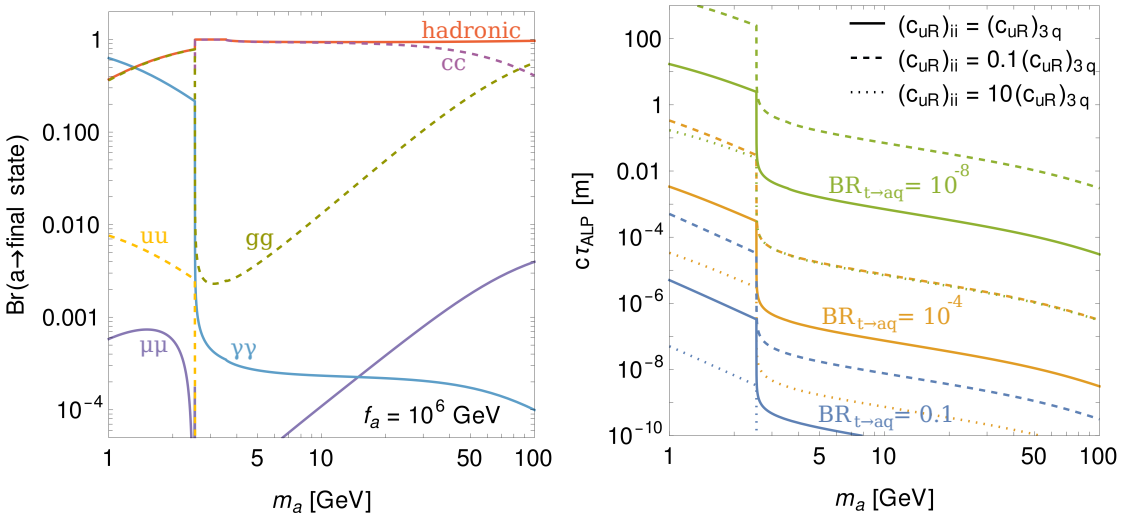

Figure V.10: **Left:** ALP branching ratios as a function of the ALP mass m_a for $f_a = 10^6$ GeV. The dashed lines show the contributions to the hadronic channel. ma **Right:** Lifetime of the ALPs as a function of the ALP mass. The blue, orange and green lines show $\mathrm{Br}(t \to aq) = 10^{-1}, 10^{-4}$ and 10^{-8}, respectively. Solid, dashed and dotted lines refer to $(c_{u_R})_{ii}/(c_{u_R})_{3q} = 1, 0.1$ and 10.

Generally, light particles that mainly decay to hadrons, like charming ALPs, are difficult to find at hadron colliders such as the LHC because of the large amount of hadronic background events. However, the charming ALP model has two specific features allowing it to be clearly distinguishable from hadronic SM backgrounds: first, the presence of flavour violating decays in the up-quark sector and, second, the possible long lifetime of charming ALPs. Due to the constraint from $D^0 - \bar{D}^0$ − mixing $(c_{u_R})_{12}$ and $(c_{u_R})_{21}$ have to be ex-

traordinarily small. Consequently, flavour violating decays involving charm and up quarks are most likely not a promising way to search for charming ALPs. Instead, we concentrate on flavour-violating top decays involving long-lived ALPs with masses $m_a \sim (1-10)$ GeV as a novel and interesting way of searching for ALPs at colliders.
The choice of this mass range becomes clear from the right panel of Figure V.10. There, the ALP decay length is shown as a function of the ALP mass for three different choices of c_{u_R} defined by the branching ratio $\mathrm{Br}(t \to aq)$ and the ratio of diagonal to off-diagonal couplings. The choice of $\mathrm{Br}(t \to aq)$ and the ratio of diagonal to off-diagonal couplings as the free parameters can be justified by the following: To simplify the parameter space, the couplings are chosen as $(c_{u_R})_{ii} \equiv (c_{u_R})_{11} = (c_{u_R})_{22} = (c_{u_R})_{33}$ and $(c_{u_R})_{3q} \equiv (c_{u_R})_{13} = (c_{u_R})_{23} = (c_{u_R})_{31} = (c_{u_R})_{32}$. This choice of simplification of c_{u_R} is convenient for the study of exotic top decays since the ALPs lifetime is mainly set by the diagonal coupling $(c_{u_R})_{ii}$ and the exotic top decay depends on the off-diagonal couplings $(c_{u_R})_{3q}$ via

$$\mathrm{Br}(t \to aq) = \frac{N_c}{96\pi} \frac{|(c_{u_R})_{3q}|^2}{f_a^2} \frac{m_a^2}{m_t} \left(\frac{\left(m_q^2 - m_t^2\right)^2}{m_a^2} - \left(m_t^2 + m_q^2\right) \right) \times \sqrt{\left(1 - \frac{(m_a + m_q)^2}{m_t^2}\right)\left(1 - \frac{(m_a - m_q)^2}{m_t^2}\right)} \times \frac{1}{\Gamma_t}, \quad q = u, c \tag{V.100}$$

with Γ_t the total top decay width. Furthermore, since all branching ratios just depend on the ratio c_{u_R}/f_a, and the exotic decays only involve off-diagonal couplings, we can use $\mathrm{Br}(t \to aq)$ and the ratio $(c_{u_R})_{ii}/(c_{u_R})_{3q}$ as free parameters. In particular, we present $c\tau_{\mathrm{ALP}}$ as a function of m_a for $\mathrm{Br}(t \to aq) = 10^{-1}, 10^{-4}$ and 10^{-8} as well as hierarchies of diagonal versus non-diagonal couplings of $(c_{u_R})_{ii}/(c_{u_R})_{3q} = 0.1, 1, 10$. Then, it is clear from Figure V.10 that the ALPs decay length can easily reach the typical length scales of LHC detectors for masses in the 1 GeV $-$ 10 GeV range, without going to tiny $\mathrm{Br}(t \to aq)$. Finally, as a last step we can exchange $\{\mathrm{Br}(t \to aq), (c_{u_R})_{ii}/(c_{u_R})_{3q})\}$ with $\{\mathrm{Br}(t \to aq), c\tau_{\mathrm{ALP}}\}$ as free parameters. This is possible because we chose $(c_{u_R})_{12} = 0 = (c_{u_R})_{21}$ and other flavour violating ALP decays are kinematically inaccessible in the mass range where we "naturally" get the right ALP lifetimes, so that all relevant branching ratios only involve the diagonal couplings $(c_{u_R})_{ii}$. In the following, for our phenomenological studies we use the ALP lifetime and exotic top branching ratio as our independent model parameters. As already mentioned, changing the scale f_a does not have a large impact since it can always be absorbed in a redefinition of the couplings (up to small logarithmic corrections to the branching ratios of the leptonic decays). Thus, f_a can be fixed to an arbitrary scale which we choose to be $f_a = 10^6$ GeV.

V.2.2 Experimental Constraints

Before proposing a new strategy to search for ALPs in flavour violating top decays, we study existing bounds arising from measurements of top quark properties and single top searches.

V.2.2.1 Model Independent Limits on Exotic Top Decays

Although the top quark was discovered more than two decades ago [72,73] and its properties studied ever since, measuring the top decay width is still a challenging process. Due

to the low experimental resolution to reconstruct jet-related properties, such as jet reconstruction, jet energy resolution, jet energy scale or jet vertex fraction [411–414] direct measurements of the top quark width, which avoid model-dependent assumptions, have large uncertainties. The value of the top quark width from direct measurements is 0.6 GeV $< \Gamma_t <$ 2.5 GeV at 95% CL [415, 416]. New methods using a combination of resonant and non-resonant cross-sections to extract a model independent top quark decay width measurement have been proposed [417–419] and reduce the uncertainty significantly to $\Gamma_t = 1.28 \pm 0.30$ GeV [420]. Nonetheless, the $O(10\%)$ uncertainties still leave room for large NP contributions. While indirect measurements of the top width further decrease the uncertainty, they are performed under certain SM assumptions [421, 422], for example on the top branching ratios, and are, thus, not applicable to the search of NP in top decays.
On the other hand, several experimental searches for FCNCs in top decays have been performed, mainly studying the tqX coupling with $q = u, c$ and $X = h/Z/\gamma/g$ [423–432]. In the SM this coupling is tiny, as it is loop and CKM suppressed, leading to $\mathrm{Br}(t \to qX) \ll 10^{-10}$ [433]. Consequently, NP contributions to this coupling can be easily analyzed, see for example [434–438]. Since light quark jets resemble b-jets, measurements of the FCNC top quark coupling focus mostly on exotic top quark production in the form of single top plus X searches and not on exotic top quark decays. In analyses that focus on exotic top decays the properties of X, i.e. mass, decay products, etc., are used to extract the signal [423–425, 428–430]. Thus, recasting such searches would only be meaningful if the ALP had very similar properties to X. In the following, we, therefore, focus on the single top plus jets and single top plus MET searches to find the current bounds on the ALP parameter space. As explained above, the top plus jets final state arises for promptly decaying ALPs, while the single top plus MET final state corresponds to the case where the ALPs are long-lived.

V.2.2.2 Recast of Searches for Exotic Top Decays

Charming ALPs can be produced at LHC in association with a top quark as shown in the Feynman diagrams in Figure V.11. Here, we first study the bounds arising from

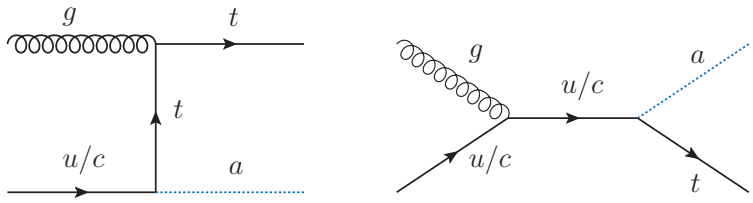

Figure V.11: The Feynman diagrams representing top plus ALP production at the LHC.

measurements of the top plus jets process since charming ALPs with small lifetimes decay mostly hadronically in the mass range of interest. To do so, we recast the CMS search in the top plus jets channel probing the anomalous tqg coupling in [432]. The analysis specifically searched for a leptonic top in association with one or two jets where at least one of them fails the b-tagging secondary vertex algorithm. In the b-tagging secondary vertex algorithm jets with 0.01 cm $< r <$ 2.5 cm are selected [439]. Here, r is the radial distance between the secondary vertex and the PV. Due to the fact that at least one jet is required to fail the b-tagging algorithm and gluon and light quark jets tend to have prompt vertices, it is clear that jets with $r <$ 0.01 cm are considered in the search. Meanwhile, it is not obvious that also jets with $r >$ 2.5 cm are considered as failing in the

algorithm or taken into account at all. To be conservative in our recast we assume that jets with 2.5 cm $< r <$ 2 m are not rejected. Charming ALPs decaying with $r <$ 2 m decay outside of the hadronic calorimeter and, thus, cannot be detected as a regular jet. The upper limit on the cross section of NP contributing to $pp \to t + j$ is $\sigma_{tj} \simeq 0.29$ pb at $\sqrt{s} = 13$ TeV [440]. Using `MadGraph5_aMC@NLO v2.6.4` [318] an upper bound on $(c_{u_R})_{3q}/f_a$ with $q = u, c$ can be found from the upper limit on the cross section and, in turn, be translated to an upper limit on $\mathrm{Br}(t \to aq)$ using Equation V.100. When doing so we also have to take into account the probability that the jet(s) resulting from ALP decays are (most likely) accepted by the search. More specifically, that means that ALPs should decay with 0.01 cm $< r <$ 2.5 cm. We do so by calculating the probability that the ALPs decay in that range. The efficiency factor for ALPs to decay with $r <$ 0.01 cm is

$$\int_0^{10^{-4}\,\mathrm{m}} (\gamma c\tau_{\mathrm{ALP}})^{-1} e^{-\frac{ct}{\gamma c\tau_{\mathrm{ALP}}}}\, d(ct)\,, \tag{V.101}$$

where $\gamma = p_T/m_a$ is the boost factor along the transverse direction for the ALP mass m_a and transverse momentum p_T. We weight the MC generated events by this boost factor. Analogously, for ALPs decaying with 2.5 cm $< r <$ 2 m, we use an efficiency factor

$$\int_{2.5\times10^{-2}\,\mathrm{m}}^{2\,\mathrm{m}} (\gamma c\tau_{\mathrm{ALP}})^{-1} e^{-\frac{ct}{\gamma c\tau_{\mathrm{ALP}}}}\, d(ct)\,. \tag{V.102}$$

Figures V.15 and V.16 show the ALP parameter space for $m_a = 2$ GeV (upper panels) and $m_a = 10$ GeV (lower panels) in the $c\tau_{ALP}$ - $\mathrm{Br}(t \to aq)$ frame. The from the top plus jets search at CMS obtained constraint is shown as the purple region in both figures. There, the dashed line represents the constraint from $\mathrm{Br}(t \to au)$ and the solid line the one from $\mathrm{Br}(t \to ac)$. As we are mainly interested in long-lived charming ALPs and show the corresponding part of parameter space, the bound from ALPs decaying with $r <$ 0.01 cm is not visible in Figures V.15 and V.16. Due to the larger boost factor for smaller masses the constraints are pushed to lower $c\tau$ values for $m_a = 2$ GeV.

For our second recast, we consider charming ALPs with large lifetimes that are stable on collider scales. Then, the ALPs appear as missing energy and measurements of single top production rates impose constraints on the couplings of the ALP. SM single top production is suppressed by the b quark parton distribution function (PDF) and, therefore, relatively small. We use a search of the ATLAS experiment [431] for top quark FCNC with a gluon mediator in the single top channel to constrain charming ALPs with large lifetimes. An upper limit on the cross section ($\sigma_t \lesssim 0.10$ pb at $\sqrt{s} = 13$ TeV) was reported in [440]. The analysis requires exactly one jet, one lepton and missing energy. Multivariate analysis was used to find the limit where one of the variables used as an input is the transverse mass

$$m_T(W) = m_{T_{\ell\nu}} = \sqrt{2\left(p_T(l)E_T^{miss} - \vec{p}_T(l)\cdot\vec{E}_T^{miss}\right)}, \tag{V.103}$$

where E_T^{miss} and $\vec{E}_T^{miss}$ are the negative scalar and vector sums over all momenta. The transverse mass in Equation V.103 should have an upper limit of m_W in the case of true single top production. In this process the neutrino that originates from the decay of the W is the only source of missing energy. In the case of top production in association with a charming ALP, on the other hand, the ALP is an additional source of missing energy, so that the distribution of $m_T(W)$ would differ. Nonetheless, we use the limits of this search in our recast to stay conservative regarding the potential power of the LHC in constraining ALP couplings in this channel. We follow the same recast procedure as for

the top plus jets search, but this time, the probability of an ALP decaying outside of the detector ($ct \geq 10$ m) has to be taken into account, which is given by the efficiency factor $e^{-\frac{10\,\mathrm{m}}{\gamma c \tau_{\mathrm{ALP}}}}$. The arising bound is shown by the blue region in Figures V.15 and V.16. As for the top plus jets search dashed lines are the limits for $\mathrm{Br}(t \to au)$, and solid lines are for $\mathrm{Br}(t \to ac)$.
Additionally, in the region where the ALP is stable on collider scales single top plus MET searches without FCNCs can also impose a bound on the parameter space. These searches, however, are typically performed for DM candidates with masses $\mathcal{O}(100)$ GeV [441–444]. They require at least 200 GeV of MET for hadronic top decays. However, in our scenario the typical amount of MET will be $\lesssim m_t/2$ if the ALP escapes undetected (indeed, the mean transverse momenta of ALPs with $m_a = 2$ GeV and $m_a = 10$ GeV are $p_T = 93.1$ GeV and $p_T = 93.4$ GeV, based on a MC simulation with 10000 events). Therefore, these analyses are not applicable to the here considered scenario as most signal events would fail the experimental selection. The p_T distribution of charming ALPs in the signal process is shown for two masses $m_a = 2$ GeV and $m_a = 10$ GeV in Appendix V.C.

V.2.3 Search Strategy and LHC Prospects for Top Decays to Long-Lived Particles

After considering model independent bounds on exotic top decays and recasting both a single top plus jets and a single top plus MET search, it is clear that there is a large part of the parameter space with intermediate charming ALP lifetimes unconstrained. In the following, we propose a search for this part of the parameter space.

V.2.3.1 Signal Properties

The here proposed search focuses on ALPs that are produced in flavour violating top decays. More precisely, top-pair production where one of the tops decays via its main SM decay mode to Wb and the other to an ALP and either an up or charm quark, see Fig. V.12, is studied. For this process the signal production cross section is

$$\sigma_{\mathrm{signal}} = \sigma_{t\bar{t}} \times \mathrm{Br}(t \to Wb) \times \mathrm{Br}(t \to aq) \tag{V.104}$$

with $\sigma_{t\bar{t}} \sim 830$ pb [409], $\mathrm{Br}(t \to Wb) \sim 0.96$ [351] and $\mathrm{Br}(t \to aq)$ given in Eq. (V.100). Assuming couplings $(c_{u_R})_{ij}$ of order one and $\frac{1}{f_a} \sim \mathcal{O}(10^{-9} - 10^{-5})$ GeV^{-1} light ALPs

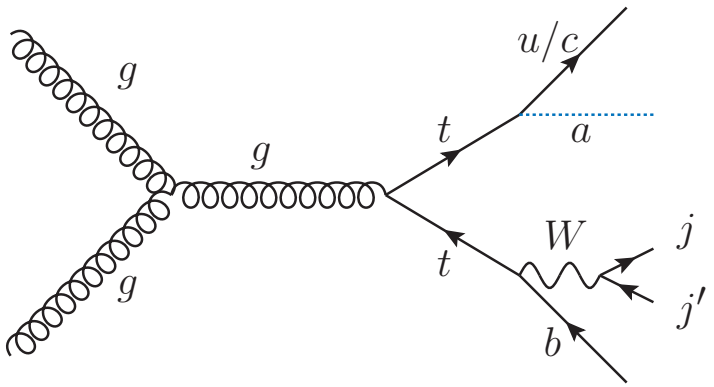

Figure V.12: The Feynman diagram for the signal: $t\bar{t}$ production where one of the top quarks decays to $q = u, c$ and an ALP.

with $m_a \sim (1-10)$ GeV have lifetimes of order millimeter to 100 m, while having $\mathrm{Br}(t \to aq) \lesssim 10^{-3}$. Light ALPs with these intermediate lifetimes decay mostly in the hadronic calorimeter or the muon spectrometer. Note that while the ALP decays to pairs of partons, it is highly boosted and decays displaced, so its decay products are mainly reconstructed as a single, narrow jet. Based on this information, we distinguish two cases: First, the case of ALP decays at the outer edge of the electromagnetic calorimeter or inside the hadronic calorimeter, and second, the case of decays in the muon spectrometer.
If ALPs decay at the outer edge of the electromagnetic calorimeter or inside the hadronic calorimeter, they will lead to a jet that deposits most of its energy in the hadronic calorimeter. Consequently, for such a jet the value of the hadronic to electromagnetic energy ratio $E_{\mathrm{had}}/E_{\mathrm{em}}$ is large. E_{had} and E_{em} denote the amount of energy deposited in the hadronic and electromagnetic calorimeter, respectively. In addition, we expect no tracks associated with the jet from the charming ALP decay since it is neutral. The other components of a signal event are one prompt light jet from the up or charm quark produced in the flavour violating decay $t \to aq$ ($q = u, c$) and one to three prompt jets, one of them being a b-jet, from the decay of the second top quark. For this process SM $t\bar{t}$ production where a jet consisting of (anti-) protons, $\pi^{\pm}$ and/or $K^{\pm}$, but no photons deposits the majority of its energy in the hadronic calorimeter and is, thus, reconstructed as a "displaced" jet, is the main background process. Such a "displaced jet" from the $t\bar{t}$ background leaves tracks, a feature that we use to distinguish signal from background.
For the second case where the ALP decays inside the muon spectrometer the signal consists of an event originating in the muon system with no associated tracks pointing to the PV, as well as the same prompt jets as for decays in the hadronic calorimeter, leading to a hit in the muon spectrometer without any associated tracks, as well as $2-4$ $(2-5)$ jets. We assume that such a signal would be background free.

V.2.3.2 Triggering and Event Selection

We study the case of charming ALP decays at the outer edge of the electromagnetic calorimeter or inside the hadronic calorimeter first, before moving to the case of charming ALPs decaying in the muon spectrometer. For the former the signal consists of the decay products of a SM top quark decay, a prompt light jet from the flavour violating top decay and one (or rarely two if the ALP decay products are seen as two jets) displaced jet(s) from the ALP decay. Thus, in total there are at minimum three and maximum five (six) jets, one (two) of them being displaced. In general, the fact that all decay products originate from a pair of top quarks could be used to reduce the background by reconstructing both top quark masses, one from the displaced jet and one additional jet, and the other from the remaining three jets. During our analysis we found, however, that focusing on the displaced jet provides sufficient background suppression, so that a reconstruction of the invariant top masses is not necessary. It is important to point out that for both studied cases we treat the top quark that decays to SM final states as a collider observable object. The experimental collaborations at CERN have demonstrated that they can trigger and identify top quark decays with high efficiency and accuracy, so that we expect only a marginal loss of sensitivity for an explicit implementation of top-tagging. Therefore, we do not explicitly implement top-tagging in our search, but we demand that the jets from the top decays are reconstructed with large enough transverse momenta. That way we ensure the sensitivity of the search is not overestimated.
For our analysis of ALPs decaying at the outer edge of the electromagnetic or inside the hadronic calorimeter events with $3-6$ $(3-5)$ jets with $p_T > 40$ GeV and $|\eta| < 2.5$ are selected. Furthermore, to identify the displaced jet from the ALP we follow the

requirements of the ATLAS Calorimeter Ratio trigger [445]. The decay products of neutral particles decaying in the outer layers of the electromagnetic calorimeter or in the hadronic calorimeter deposit most of their energy in the hadronic calorimeter. The trigger takes advantage of this property of displaced jets originating from neutral particles. More specifically, the Calorimeter Ratio trigger requires a τ-lepton like object with $E_T > 40$ GeV (which fits the jet originating from the ALP) with $\log_{10}(E_{\text{had}}/E_{\text{em}}) > 1.2$ and no tracks with $p_T > 1$ GeV in a (0.2×0.2) region in $(\Delta\eta \times \Delta\phi)$ around the jet direction.
In Figure V.13 the $\log_{10}(E_{\text{had}}/E_{\text{em}})$ distribution for the signal with $m_a = 2$ GeV (left) and $m_a = 10$ GeV (right) and ALP lifetimes $c\tau_{\text{ALP}} = 0.06$ m (red) and 0.4 m (blue), as well as for the $t\bar{t}$ (black) background is depicted. To obtain these distributions we modified the `FeynRules` [316,446] implementation of the linear ALP EFT model [333,334] to include the charming ALP couplings. Then, signal events were generated with `MadGraph5_aMC@NLO v2.6.4` [318] with showering and hadronization done with `Pythia v8.240` [315] and jet reconstruction performed by `FastJet v3.4.0` [447, 448] using the anti-k_t jet algorithm [322]. The energy deposit ratio $\log_{10}(E_{\text{had}}/E_{\text{em}})$ for the signal was assigned according to Figure 5b of [445]. For background estimation 100000 $t\bar{t}$ events were simulated with `MadGraph5_aMC@NLO v2.6.4` [318] with showering and hadronization done with `Pythia v8.240` [315] and fast detector simulation carried out by `Delphes v3.5.0` [449], from where the calorimeter energy deposit ratio was extracted.

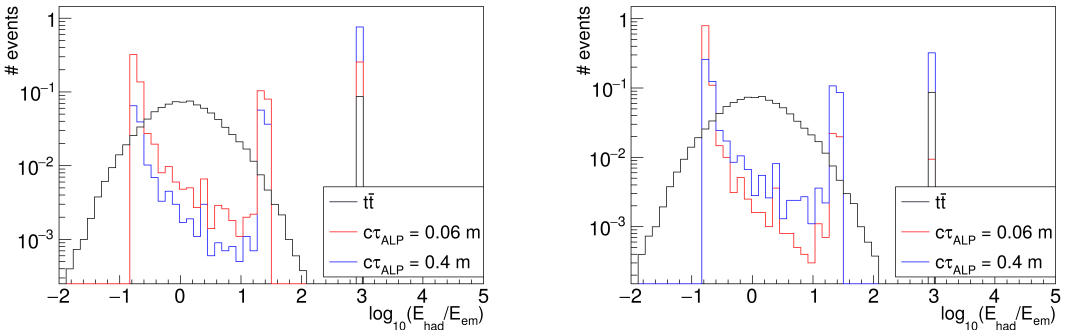

Figure V.13: Calorimeter energy deposit ratio $\log_{10}(E_{\text{had}}/E_{\text{em}})$ distribution for the $t\bar{t}$ background, as well as for the signal with $c\tau_{\text{ALP}} = 0.06$, 0.4 m and $m_a = 2$ GeV (**left**) and $m_a = 10$ GeV (**right**).

It can be seen that signal and background distributions show quite different features: The $t\bar{t}$ background in Figure V.13 is evenly distributed around $\log_{10}(E_{\text{had}}/E_{\text{em}}) \sim 0$, corresponding to an equal energy deposit in the hadronic and electromagnetic calorimeter, and has only one peak in the overflow bin at $\log_{10}(E_{\text{had}}/E_{\text{em}}) = 3$. This peak originates from jets with $E_{\text{em}} = 0$ and, therefore, $(E_{\text{had}}/E_{\text{em}}) = \infty$. In the `Delphes v3.5.0` card $(E_{\text{had}}/E_{\text{em}}) = \infty$ is defined as $(E_{\text{had}}/E_{\text{em}}) \equiv 1000$, leading to $\log_{10}(E_{\text{had}}/E_{\text{em}}) \equiv 3$. As described above, this is true for jets consisting of (anti-) protons, $\pi^{\pm}$ and/or $K^{\pm}$, but no photons. Such jets are, therefore, counted as background.
The signal, in contrast, has three peaks: The first peak at $\log_{10}(E_{\text{had}}/E_{\text{em}}) \sim -0.8$ corresponds to ALPs decaying close to the interaction point. Charming ALPs decaying further away from the interaction point only deposit a smaller amount of energy in the electromagnetic calorimeter and lead to the second peak at $\log_{10}(E_{\text{had}}/E_{\text{em}}) \gtrsim 1.2$. Specifically, this peak arises due to ALPs decaying in the outer layers of the electromagnetic calorimeter or inside the hadronic calorimeter. As ALPs are less boosted for

higher masses, the second signal peak is higher for $c\tau_{\text{ALP}} = 0.06$ m when $m_a = 2$ GeV and for $c\tau_{\text{ALP}} = 0.4$ m when $m_a = 10$ GeV, respectively. Finally, the signal has its third peak at $\log_{10}(E_{\text{had}}/E_{\text{em}}) = 3$, similar to the background peak. However, the signal peak has a different origin than the one of the background distribution. For the signal it shows the amount of ALPs decaying outside of the detector, defined by hand as having $(E_{\text{had}}/E_{\text{em}}) \equiv 1000$ and, consequently, $\log_{10}(E_{\text{had}}/E_{\text{em}}) \equiv 3$. Thus, the signal events in this peak do not count into the actual signal, while the background jets are counted.
Next, we consider the no track criterion of the Calorimeter Ratio trigger to further reduce the background of SM jets that appear displaced according to the Calorimeter Ratio trigger due to their particle content. We show the number of tracks or background jets

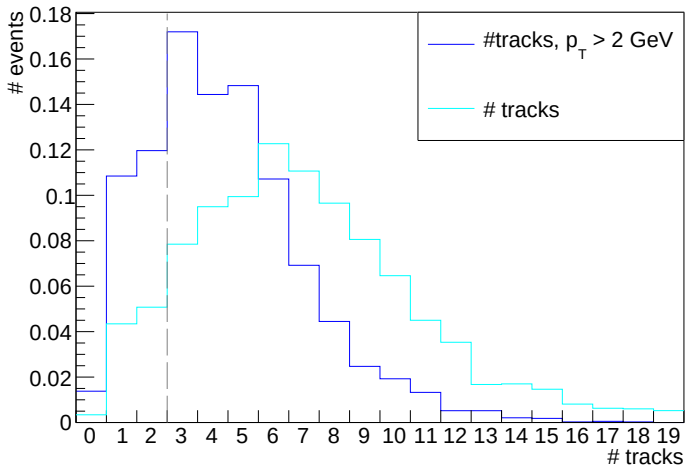

Figure V.14: Number of tracks of jets originating from $t\bar{t}$ with $\log_{10}(E_{\text{had}}/E_{\text{em}}) > 1.2$. The dark blue line shows the number of tracks with $p_T > 2$ GeV, the lighter blue line the number of all tracks for such a jet.

with $\log_{10}(E_{\text{had}}/E_{\text{em}}) > 1.2$ extracted from `Delphes v3.5.0` in Figure V.14. Here, the light and dark blue lines correspond to all tracks and to the tracks with $p_T > 2$ GeV of such a jet, respectively. In both cases, most jets have at least one track. In contrast, the number of tracks for signal events cannot be shown as signal events have no tracks pointing towards the decaying charming ALP at the level of our simulation. In reality, however, tracks pointing in the direction of the displaced decaying ALP can originate from pile-up events. Consequently, a very strict cut on the tracks could lead to less sensitivity. To avoid the possible loss of sensitivity we choose a less stringent cut on the number of tracks for background jets as the actual Calorimeter Ratio trigger, requiring that jets with $\log_{10}(E_{\text{had}}/E_{\text{em}}) > 1.2$ have less than two tracks with $p_T > 2$ GeV. This cut is indicated by the grey dashed line in Figure V.14. Only the events to the left of the grey dashed line are kept. It is obvious that even with this conservative cut most of the background is removed.
As a second scenario we consider a search for ALPs decaying in the muon spectrometer. Since we consider this search to be background free, we merely demand that signal events have $2-5$ prompt jets with $p_T > 40$ GeV and $|\eta| < 2.5$, while the ALP should decay inside the muon calorimeter (4.3 m $< L_{xy} <$ 10.7 m) and fulfill $p_T > 25$ GeV and $|\eta| < 2.5$.

V.2.3.3 LHC Sensitivity and Prospects at Future Colliders

To study the case where the charming ALPs decay at the outer edge of the electromagnetic calorimeter or inside the hadronic calorimeter and the case where they decay inside the muon spectrometer, we generate 10000 signal events for various charming ALP lifetimes between $c\tau_{\text{ALP}} = 0.001$ m and $c\tau_{\text{ALP}} = 100$ m for the two ALP masses $m_a = 2$ GeV and $m_a = 10$ GeV with `MadGraph5_aMC@NLO v2.6.4`, `Pythia v8.240` and `FastJet v3.4.0` as before. In `Pythia v8.240` we afterwards select events with $3-6$ $(3-5)$ jets, each with $p_T > 40$ GeV and $|\eta| < 2.5$. Furthermore, we demand that the jet from the ALP fulfils the $\log_{10}(E_{\text{had}}/E_{\text{em}}) > 1.2$ criterion of the Calorimeter Ratio trigger according to the energy deposit ratio as a function of the decay radius in Figure 5b of [445]. At the same time we also require that the ALP satisfies $p_T > 40$ GeV and $|\eta| < 2.5$.
For background estimation from the 100000 $t\bar{t}$ events generated with `MadGraph5_aMC@NLO v2.6.4`, `Pythia v8.240` and `Delphes v3.5.0`, we select events with $3-6$ $(3-5)$ jets with $p_T > 40$ GeV and $|\eta| < 2.5$. In addition, we require that at least one of these jets has $\log_{10}(E_{\text{had}}/E_{\text{em}}) > 1.2$ and that this jet has no more than two tracks with $p_T > 2$ GeV.
The experimental testing grounds we consider for our search are LHC with $\sqrt{s} = 13$ TeV and an expected total integrated luminosity after run 3 of $\mathcal{L} = 350$ fb^{-1}, as well as the high-luminosity phase of LHC with $\sqrt{s} = 14$ TeV and a total integrated luminosity $\mathcal{L} = 4000$ fb^{-1}.
In Table V.2 the cut flow (of the efficiencies) for the signal for $m_a = 2$ GeV and $m_a = 10$ GeV with $c\tau_{\text{ALP}} = 0.1$ m and $\text{Br}(t \to aq) = 0.001$, as well as for the background is shown for $\sqrt{s} = 13$ TeV and the expected total integrated luminosity $\mathcal{L} = 350$ fb^{-1} for requiring $3-6$ jets. It can be seen in Table V.2 that already the cut of minimal three and

	$\mathbf{m_a = 2}$ **GeV**	$\mathbf{m_a = 10}$ **GeV**	$\mathbf{t\bar{t}}$
total	(1) 2.79×10^5	(1) 2.79×10^5	(1) 2.91×10^8
$3-6$ jets with $p_T > 40$ GeV & $\lvert\eta\rvert < 2.5$	(0.8439) 2.35×10^5	(0.8414) 2.35×10^5	(0.71801) 2.09×10^8
1 jet with $\log_{10}\left(\frac{E_{\text{had}}}{E_{\text{em}}}\right) > 1.2$	(0.1436) 4.00×10^4	(0.0775) 2.16×10^4	(0.01244) 3.61×10^6
displaced jet has ≤ 2 tracks with $p_T > 2$ GeV	(0.1436) 4.00×10^4	(0.0775) 2.16×10^4	(0.00022) 6.39×10^4

Table V.2: Cut flow of the expected number of events for signal and background events for LHC run 3 with $\sqrt{s} = 13$ TeV and $\mathcal{L} = 350$ fb^{-1}. The values in brackets are the efficiencies after each cut. For the signal $c\tau_{\text{ALP}} = 0.1$ m and $\text{Br}(t \to aq) = 0.001$ is chosen.

maximal six jets with $p_T > 40$ GeV and $|\eta| < 2.5$ reduces the background compared to the signal, however the cuts on $\log_{10}(E_{\text{had}}/E_{\text{em}})$ and the number of tracks are significantly stronger and allow to clearly distinguish signal and background. Depending on the mass and lifetime of the ALP up to $\sim 15\%$ of the ALP signal passes these cuts, while each of them reduces the number of background events by about two orders of magnitude. In Table V.3 the same cut flow is shown for choosing events with three to five jets with $p_T > 40$ GeV and $|\eta| < 2.5$. This reduces signal and background in a similar way and, thus, does not improve the signal to background ratio. Consequently, we show the resulting detection prospects only for the $3-6$ jets cut. To do so, based on the above described selection criteria, we perform a cut-and-count analysis and use $S/\sqrt{S+B} = 2$ to find the expected 2σ exclusion region. Systematic effects are not included in our sensitivity estimate because we expect that the backgrounds can be further suppressed.
Here, we do not show a cut flow for charming ALPs decaying inside the muon spectrometer

since we assume such a signal to be background free. Therefore, we merely require ten signal events, again based on a cut-and-count analysis with the selection criteria for the decays in the muon spectrometer, for a discovery at the 3σ level. In Figure V.15 the

	$\mathbf{m_a = 2\ GeV}$	$\mathbf{m_a = 10\ GeV}$	$\mathbf{t\bar{t}}$
total	(1) 2.79×10^5	(1) 2.79×10^5	(1) 2.91×10^8
$3-5$ jets with $p_T > 40$ GeV & $\lvert\eta\rvert < 2.5$	(0.7815) 2.18×10^5	(0.7779) 2.17×10^5	(0.65997) 1.92×10^8
1 jet with $\log_{10}\left(\frac{E_{had}}{E_{em}}\right) > 1.2$	(0.1330) 3.71×10^4	(0.0699) 1.95×10^4	(0.01022) 2.97×10^6
displaced jet has ≤ 2 tracks with $p_T > 2$ GeV	(0.1330) 3.71×10^4	(0.0699) 1.95×10^4	(0.00018) 5.23×10^4

Table V.3: Cut flow for signal and background, same as Table V.2, but for requiring $3-5$ jets.

resulting expected 2σ exclusion region of the here proposed search for $\sqrt{s} = 13$ TeV and $\mathcal{L} = 350$ fb^{-1} is shown as the red line further on the right. Bounds from recasting the top plus jets and single top plus missing energy searches, as discussed in Section V.2.2.2, are displayed as purple and blue regions, respectively. In both cases, the dashed lines represent the constraints arising from the *tua* coupling and the solid lines the one arising from the *tca* coupling. Finally, we show the 10-event discovery lines for the above discussed search in the muon system (blue line) and for a background free search in the hadronic calorimeter (red line further to the left), to highlight the potential reach of further improved searches. In the upper panel we use $m_a = 2$ GeV and in the lower panel $m_a = 10$ GeV.
For small ALP lifetimes $c\tau_{\text{ALP}} \lesssim 0.006$ m ($c\tau_{\text{ALP}} \lesssim 0.02$ m) the top plus jets search is the most sensitive constraint and excludes branching ratios down to $\text{Br}(t \to aq) \sim 0.001$ for $m_a = 2$ GeV ($m_a = 10$ GeV). Top plus jets searches can probe the exotic top ALP coupling up to $c\tau_{\text{ALP}} \sim 30$ m ($c\tau_{\text{ALP}} \sim 100$ m) for large enough branching ratios. These bounds arise for ALPs decaying inside 2.5 cm $< r <$ 2 m. On the other hand, the single top plus missing energy search only becomes sensitive for $c\tau_{\text{ALP}} \gtrsim 0.01$ m ($c\tau_{\text{ALP}} \gtrsim 0.1$ m) and is more sensitive than our newly proposed search for $c\tau_{\text{ALP}} \gtrsim 1$ m ($c\tau_{\text{ALP}} \gtrsim 10$ m). In this region $\text{Br}(t \to aq) \gtrsim 10^{-4}$ is excluded for both masses. Single top searches leave the intermediate lifetime region ($c\tau_{\text{ALP}} \sim 0.006-1$ m for $m_a = 2$ GeV and $c\tau_{\text{ALP}} \sim 0.02-10$ m for $m_a = 10$ GeV) largely unconstrained. The here proposed search is sensitive in this region as shown in Figure V.15. For both $m_a = 2$ GeV and $m_a = 10$ GeV exotic top decays with branching ratios smaller than $\text{Br}(t \to aq) = 10^{-4}$ can be probed with 2σ significance by using the Calorimeter Ratio trigger requirements as event selection criteria. Different masses influence at which lifetimes this search reaches its highest sensitivity since ALPs with larger masses are less boosted. Here, for $m_a = 2$ (10) GeV the search is most sensitive at $c\tau_{\text{ALP}} \sim 0.04$ (0.3) m. Lastly, we assume that with a more advanced search strategy the search for charming ALPs in exotic top decays could be made basically background free. This could be received, for example, by exploiting the differences in the calorimeter showers between signal and background: a jet arising from an ALP decay inside the hadronic calorimeter should look quite different from a jet that travels through the electromagnetic and the full hadronic calorimeter. Additionally, due to the small ALP mass and the large boost factor, the jets originating from charming ALPs should also be unusually narrow. As can be seen in Figure V.15 the 10-event discovery lines for such a search and for a similarly background free search in the muon spectrometer suggest that probing the intermediate lifetime regime down to branching ratios as small as $\text{Br}(t \to aq) \sim 10^{-7}$ is possible.

We also study the prospect of such searches at HL-LHC. In Figure V.16 we show in addition to the results for LHC run 3 the expected discovery lines for background free searches for decays in the hadronic calorimeter and the muon system for the HL-LHC by dotted red and blue lines. At HL-LHC branching ratios as low as 10^{-8} can be reached. Note that since the same p_T requirement as for LHC have been used for the jets and the ALPs, optimizing them for HL-LHC could move the expected 10-event lines to even smaller branching ratios. Finally, one should point out that embedding the charming ALP into the UV completion discussed in Chapter III (cf. also Section V.1 of Chapter V) would lead to other interesting final states. While emerging jets from mediator pair production could be studied in a similar way as in Chapter IV, in addition, the spectacular signature of emerging jets from flavour violating top decays also arises.

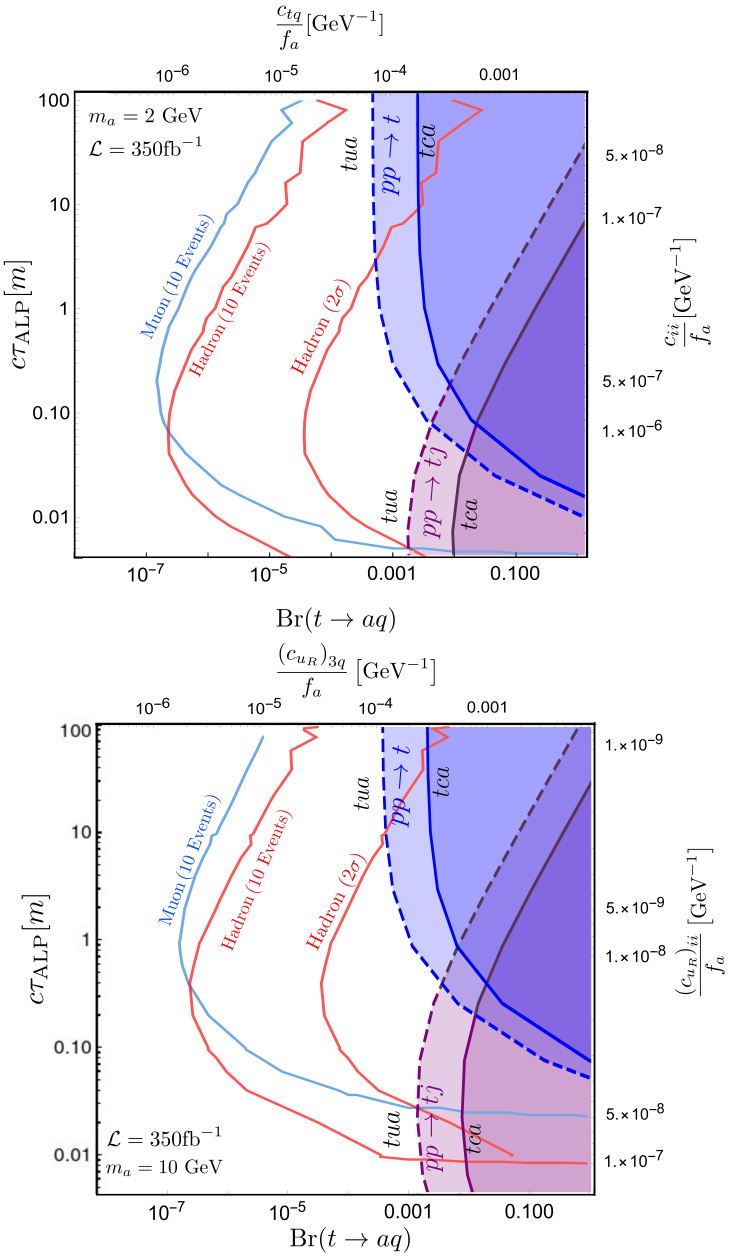

Figure V.15: The expected bounds as a function of lifetime ($c\tau_{\rm ALP}$) and the branching ratio of the exotic top decay Br($t \to aq$) for $m_a = 2$ GeV (**top**) and $m_a = 10$ GeV (**bottom**). The red lines furthest to the right represents the conservative exclusion limit of $\frac{S}{\sqrt{S+B}} = 2$ with the cuts in Table V.2 and assuming $\mathcal{L} = 350$ fb^{-1} integrated luminosity. The red (blue) solid lines on the left are the potential discovery lines where 10 signal events are produced in the hadronic (muon) calorimeter in case a background free search can be designed. Finally, the shaded regions indicate the current bounds on the model. The purple regions are derived from the top + jet [432] final state and the blue regions are from the single leptonic top search [440, 450]. The dashed lines are for the constraints on the tua coupling and the solid ones are that of the tca coupling. This figure was created in collaboration with a collaborator and modified for this thesis by the author.

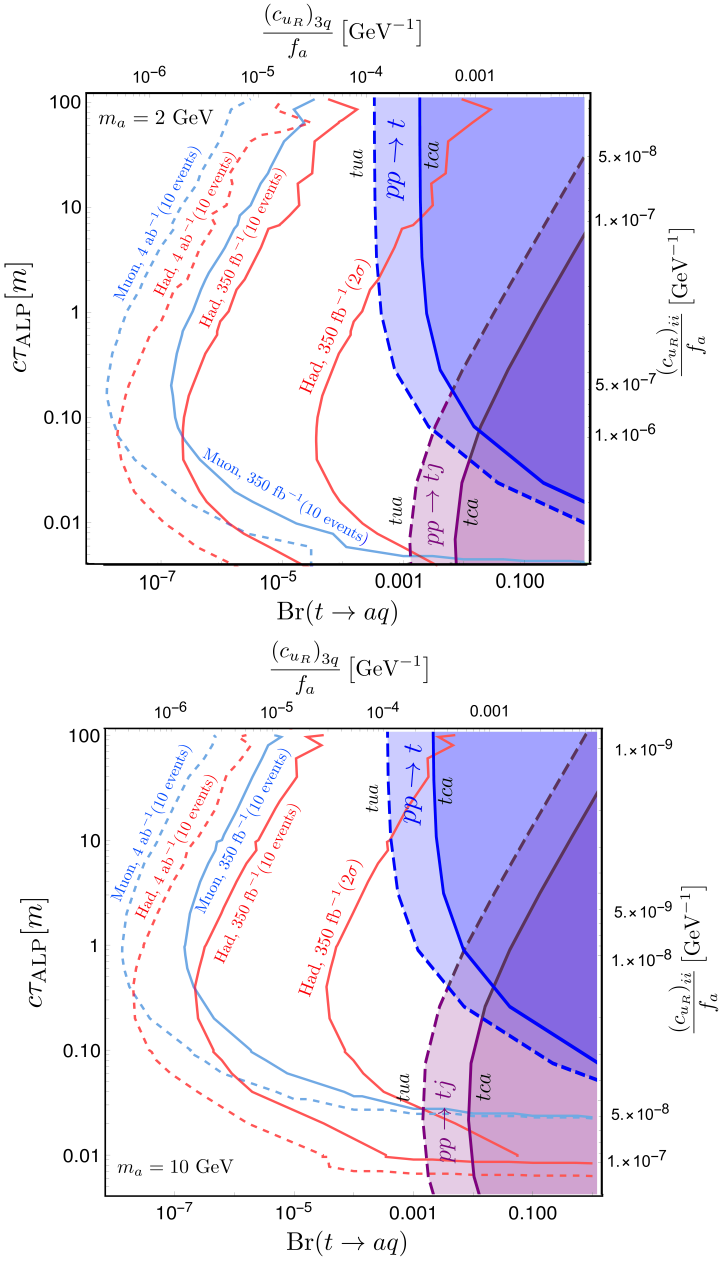

Figure V.16: The expected bounds as a function of lifetime ($c\tau_{\rm ALP}$) and the branching ratio of the exotic top decay Br($t \to aq$), same figure as Figure V.15, but additionally the expected 10 events lines at the HL-LHC with $\sqrt{s} = 14$ TeV, and $\mathcal{L} = 4$ ab^{-1} integrated luminosity are shown by dashed lines. The red dashed line represents an ALP that decays within the hadronic calorimeter and the dashed blue one when the ALP decays within the muon calorimeter. This figure was created in collaboration with a collaborator and modified for this thesis by the author.

V.3 Conclusion

In Chapter V the parameter space and detection possibilities of charming ALPs were studied over a large range of ALP masses. We denote light pNGBs having only tree-level couplings to RH up-type quarks, including non-zero off-diagonal couplings, as charming ALPs.

First, we studied various examples of theories that naturally feature charming ALPs and the phenomenology associated with their low energy EFT. Namely, as benchmark scenarios we considered a t-channel QCD-like dark sector with tree-level couplings only to the RH up-type quarks via a heavy mediator with hypercharge $Y_X = -2/3$ where we identified the two diagonal dark pions π_D^3 and π_D^8 with the charming ALP, and a FN like model where only the RH up-type quarks and a heavy scalar are charged under the new $U(1)$ symmetry. For comparison, as a fourth benchmark point we introduced an anarchic scenario with equal values for all entries of the coupling matrix c_{u_R}. For all four benchmark scenarios constraints arising from flavour experiments, astrophysics and cosmology, as well as the discovery prospect at planned fixed target experiments and LHC forward detectors were investigated. In our analysis, we demonstrated how future collider and fixed target experiments can probe these models for charming ALP masses up to the charm threshold. It was found that these experiments could be perfectly complemented by the measurement of the exotic decay $D \to \pi + invisible$, which is currently unavailable. In the absence of a dedicated search we showed instead the limit from recasting the three-body decay $D \to \tau\nu \to \pi\nu\nu$. Similarly, we recast the constraints on the branching ratios of flavour violating meson decays in the down sector, more precisely $B \to K/\pi\nu\nu$ decays. In addition, we used existing dedicated searches for the flavour violating Kaon decay $K \to \pi X$, where X is a massive invisible particle to obtain constraints on the parameter space.
In contrast to the low mass region where flavour, astrophysical and cosmological bounds constrain the parameter space we found that above the charm threshold all scenarios still feature a large unexplored parameter space. In a second step, this part of the parameter space was explored via flavour violating top decays. In order to do so we moved away from the previous benchmark points and instead considered the entries of the coupling matrix as free parameters. Choosing $(c_{u_R})_{12} = (c_{u_R})_{21} = 0$ we were able to exchange the diagonal and remaining off-diagonal couplings against the charming ALP lifetime $c\tau_{ALP}$ and the branching ratio $\mathrm{Br}(t \to aq_i)$ with $q_i = u, c$. Then, we focused on the top pair production channel where one of the top quarks decays via its SM decay $t \to Wb$ and the other one decays to an ALP together with an up- or charm-quark. The ALP subsequently decays in the hadronic calorimeter, thus, leading to a large value of the hadronic to electromagnetic energy ratio E_{had}/E_{em}. In our analysis a cut on this ratio together with a veto on the number of tracks was used enabling us to suppress the $t\bar{t}$ background enough to test exotic top branching ratios down to $\mathrm{Br}(t \to aq) \sim 10^{-4}$ $(q = u, c)$ for charming ALP masses $m_a \sim \mathcal{O}(1)$ GeV in the next run of LHC. In addition, the prospect of more refined searches, as well as the projections for HL-LHC were studied and shown. The results were combined with recasts of existing single top searches where we calculated new constraints for both prompt ALP decays, as well as for detector stable ALPs to cover the whole ALP lifetime range. It was found that in the intermediate ALP lifetime region with $c\tau \sim \mathcal{O}(1)$ cm to $\mathcal{O}(1)$ m our newly proposed search strategy can increase the sensitivity by nearly two orders of magnitude compared to the single top searches.
At the LHC the large number of $t\bar{t}$ events might facilitate further improvements of our search strategy. For example, the shape of the shower in the calorimeters can be used to further discriminate between signal and background as an ALP decaying inside the

hadronic calorimeter should look quite differently to a SM jet going through the electromagnetic and the hadronic calorimeter. Furthermore, jets from the ALP decay products should also be unusually narrow because the small ALP mass leads to a large boost. Analogously, we assumed that a search in the muon spectrometer could be virtually background free. With the assumption that both a search in the hadronic calorimeter and a search in the muon spectrometer can be background free as few as ten events might be enough to observe this exotic top decay. Then, branching ratios as low as 10^{-7} can be probed. Under the same assumption and without further adjustments of the search strategy the larger amount of events at HL-LHC will improve the testable region by another order of magnitude allowing to search down to $\mathrm{Br}(t \to aq) \sim 10^{-8}$.
Here, it is important to point out that some of the phenomenology studied for charming ALPs may change when the charming ALP is embedded in a more UV complete theory such as the dark QCD scenario. For example, the flavour phenomenology could change due to non-trivial interplay between the complete set of pNGBs in some regions of the parameter space. Considering the complete dark-QCD model will also allow more spectacular signatures. In particular, the decay of a top quark to a jet and an emerging jet (in analogy to the flavour violating top decay discussed here) is a spectacular signature, that should easily stand out. Moreover, these experimental signatures can then be connected with the DM phenomenology of the model.
Finally, it should be mentioned that there is a parameter space region that is left unexplored in the above studies. More precisely, we did not study charming ALPs with very small masses and couplings. In this region the charming ALP would be a stable DM candidate. Such charming ALP DM could be produced either by a freeze-out or a freeze-in scenario. However, here, only the freeze-in scenario is viable as the freeze-out scenario is excluded for $m_a \gtrsim 100$ eV due to DM overproduction for such a DM candidate [395] and for the whole parameter space when taking structure formation bounds into account [408]. For the freeze-in scenario, though, there exists in principle a parameter space region where the ALP can be a stable DM candidate [408].

Appendix

V.A Wilson Coefficients for $D^0 - \bar{D}^0$ − Mixing

In this Appendix the WCs for $D^0 - \bar{D}^0$ − mixing are calculated. Starting with the ALP effective Lagrangian

$$\begin{aligned}\mathcal{L} &= \frac{1}{2}(\partial_\mu a)(\partial^\mu a) - \frac{m_a^2}{2}a^2 + \frac{\partial_\mu a}{f_a}(c_{u_R})_{ij}\bar{u}_{Ri}\gamma^\mu u_{Rj} \\ &= \frac{1}{2}a\left(-\partial_\mu^2 - m_a^2\right)a - \frac{a}{f_a}(c_{u_R})_{ij}\partial_\mu\left(\bar{u}_{Ri}\gamma^\mu u_{Rj}\right) \\ &= \frac{1}{2}a\mathcal{O}a - \frac{a}{f_a}(c_{u_R})_{ij}\partial_\mu\left(\bar{u}_{Ri}\gamma^\mu, u_{Rj}\right) ,\end{aligned} \tag{V.105}$$

where $\mathcal{O} = \left(-\partial_\mu^2 - m_a^2\right)$, we use equations of motions

$$\delta\mathcal{L} = \delta a\mathcal{O}a - \frac{\delta a}{f_a}(c_{u_R})_{ij}\partial_\mu\left(\bar{u}_{Ri}\gamma^\mu u_{Rj}\right) = 0 = \delta a\left(\mathcal{O}a - \frac{(c_{u_R})_{ij}}{f_a}\partial_\mu\left(\bar{u}_{Ri}\gamma^\mu u_{Rj}\right)\right) \tag{V.106}$$

to obtain

$$\mathcal{O}a = \frac{(c_{u_R})_{ij}}{f_a}\partial_\mu\left(\bar{u}_{Ri}\gamma^\mu u_{Rj}\right) \tag{V.107}$$

and with $\mathcal{R} = \frac{(c_{u_R})_{ij}}{f_a}\partial_\mu\left(\bar{u}_{Ri}\gamma^\mu u_{Rj}\right)$

$$a = \mathcal{O}^{-1}\frac{(c_{u_R})_{ij}}{f_a}\partial_\mu\left(\bar{u}_{Ri}\gamma^\mu u_{Rj}\right) = \mathcal{O}^{-1}\mathcal{R}. \tag{V.108}$$

Then, the ALP effective Lagrangian can be written as

$$\begin{aligned}\mathcal{L} &= \frac{1}{2}a\mathcal{O}a - a\mathcal{R} = \frac{1}{2}\mathcal{O}^{-1}\mathcal{R}\mathcal{O}\mathcal{O}^{-1}\mathcal{R} - \mathcal{O}^{-1}\mathcal{R}\mathcal{R} \\ &= \frac{1}{2}\mathcal{O}^{-1}\mathcal{R}\mathcal{R} - \mathcal{O}^{-1}\mathcal{R}\mathcal{R} = -\frac{1}{2}\mathcal{O}^{-1}\mathcal{R}\mathcal{R}.\end{aligned} \tag{V.109}$$

Reinserting $\mathcal{O}$ and $\mathcal{R}$ we find

$$\begin{aligned}\mathcal{L} &= -\frac{1}{2}\left(\frac{1}{-\partial_\mu^2 - m_a^2}\right)\frac{1}{f_a^2}\partial_\mu\left(\bar{u}_{Ri}\gamma^\mu u_{Rj}\right)(c_{u_R})_{ij}\partial_\nu\left(\bar{u}_{Rp}\gamma^\mu u_{Rq}\right)(c_{u_R})_{pq} \\ &= \frac{1}{2}\left(\frac{1}{-\partial_\mu^2 - m_a^2}\right)\frac{1}{f_a^2}i\partial_\mu\left(\bar{u}_{Ri}\gamma^\mu u_{Rj}\right)i\partial_\nu\left(\bar{u}_{Rp}\gamma^\mu u_{Rq}\right)(c_{u_R})_{ij}(c_{u_R})_{pq}.\end{aligned} \tag{V.110}$$

From Equation V.110 the WCs for the $D^0 - \bar{D}^0$ − mixing can be found by using

$$\begin{aligned} i\partial\!\!\!/ u_{Ri} &= m_i u_{Li} \quad i\partial_\mu \bar{u}_{Ri}\gamma^\mu = -m_i \bar{u}_{Li} \\ i\partial\!\!\!/ u_{Li} &= m_i u_{Ri} \quad i\partial_\mu \bar{u}_{Li}\gamma^\mu = -m_i \bar{u}_{Ri} \end{aligned} \tag{V.111}$$

with m_i the respective quark mass. More precisely, we find

$$\begin{aligned} \mathcal{L} &= \frac{1}{2}\left(\frac{1}{-\partial_\mu^2 - m_a^2}\right)\frac{1}{f_a^2} i\partial_\mu \left(\bar{u}_{Ri}\gamma^\mu u_{Rj}\right) i\partial_\nu \left(\bar{u}_{Rp}\gamma^\mu u_{Rq}\right)(c_{u_R})_{ij}(c_{u_R})_{pq} \\ &= \frac{1}{2}\frac{(c_{u_R})_{ij}(c_{u_R})_{pq}}{-\partial_\mu^2 - m_a^2}\frac{1}{f_a^2}\left(\bar{u}_{Ri}u_{Lj}m_j - \bar{u}_{Li}u_{Rj}m_i\right)\left(\bar{u}_{Rp}u_{Lq}m_q - \bar{u}_{Lp}u_{Rq}m_p\right). \end{aligned} \tag{V.112}$$

Since $-\partial_\mu = p^2$ and, here, $p^2 = m_c^2$, we use $-\partial_\mu = p^2 = m_c^2$ as a final step to find the short and long distance effects of charming ALPs to $D^0 - \bar{D}^0$ − mixing. For $m_a \gg m_c$ the charm quark mass can be neglected, so that we have

$$\begin{aligned} \mathcal{L} = = &-\frac{1}{2m_a^2 f_a^2}\left(\bar{u}_{Ri}u_{Lj}\right)\left(\bar{u}_{Rp}u_{Lq}\right) m_j m_q (c_{u_R})_{ij}(c_{u_R})_{pq} \\ &- \frac{1}{2m_a^2 f_a^2}\left(\bar{u}_{Li}u_{Rj}\right)\left(\bar{u}_{Lp}u_{Rq}\right) m_i m_p (c_{u_R})_{ij}(c_{u_R})_{pq} \\ &+ \frac{1}{2m_a^2 f_a^2}\left(\bar{u}_{Ri}u_{Lj}\right)\left(\bar{u}_{Lp}u_{Rq}\right) m_j m_q (c_{u_R})_{ij}(c_{u_R})_{pq} \\ &+ \frac{1}{2m_a^2 f_a^2}\left(\bar{u}_{Li}u_{Rj}\right)\left(\bar{u}_{Rp}u_{Lq}\right) m_i m_q (c_{u_R})_{ij}(c_{u_R})_{pq}. \end{aligned} \tag{V.113}$$

Lastly, with $\mathcal{H} = -\mathcal{L}$ and $i = p = 2$ and $j = q = 1$, respectively, one obtains for the WCs in Equations V.57 for large ALP masses

$$\tilde{C}_2 = \frac{(c_{u_R})_{21}^2}{2m_a^2}\frac{m_c^2}{f_a^2},\ C_2 = \tilde{C}_2\frac{m_u^2}{m_c^2},\ C_4 = -2\tilde{C}_2\frac{m_u}{m_c} \tag{V.114}$$

and zero for all other operators. Here, $(c_{u_R})_{21}$ is the WC at the matching scale m_a and the running from the cut-off scale $4\pi f_a$ has been neglected.
On the other hand, for large distance physics ($m_a \ll m_c$) the ALP mass m_a in the denominator can be neglected and from Equation V.112 the WCs are found analogously to be

$$\tilde{C}_2 = -\frac{(c_{u_R})_{21}^2}{2f_a^2},\ C_2 = \tilde{C}_2\frac{m_u^2}{m_c^2},\ C_4 = -2\tilde{C}_2\frac{m_u}{m_c}, \tag{V.115}$$

while again all other WCs vanish.

V.B Transformation of the Operator Basis

Here, we show how the operator basis of [353] can be transformed to our operator basis in order to calculate the running of the WCs. In the following, we denote the operators in the basis of [353] as $\mathcal{Q}_i$, while the operators in our basis are labeled $\mathcal{O}_i$ (cf. Equation V.60). The operators in [353] are

$$\begin{aligned}
\mathcal{Q}_1 &= (\bar{u}_L\gamma_\mu c_L)\,(\bar{u}_L\gamma^\mu c_L)\,, & \mathcal{Q}_5 &= (\bar{u}_R\sigma_{\mu\nu} c_L)\,(\bar{u}_R\sigma^{\mu\nu} c_L)\,,\\
\mathcal{Q}_2 &= (\bar{u}_L\gamma_\mu c_L)\,(\bar{u}_R\gamma^\mu c_R)\,, & \mathcal{Q}_6 &= (\bar{u}_R\gamma_\mu c_R)\,(\bar{u}_R\gamma^\mu c_R)\,,\\
\mathcal{Q}_3 &= (\bar{u}_L c_R)\,(\bar{u}_R c_L)\,, & \mathcal{Q}_7 &= (\bar{u}_L c_R)\,(\bar{u}_L c_R)\,,\\
\mathcal{Q}_4 &= (\bar{u}_R c_L)\,(\bar{u}_R c_L)\,, & \mathcal{Q}_8 &= (\bar{u}_L\sigma_{\mu\nu} c_R)\,(\bar{u}_L\sigma^{\mu\nu} c_R)\,.
\end{aligned} \tag{V.116}$$

Comparing the two operator bases it is clear that

$$\mathcal{Q}_1 = \mathcal{O}_1\,, \quad \mathcal{Q}_3 = \mathcal{O}_4\,, \quad \mathcal{Q}_4 = \mathcal{O}_2\,, \quad \mathcal{Q}_6 = \tilde{\mathcal{O}}_1 \quad \text{and} \quad \mathcal{Q}_7 = \tilde{\mathcal{O}}_2\,. \tag{V.117}$$

On the other hand, we find

$$\begin{aligned}
\mathcal{Q}_2 &= (\bar{c}_L^\alpha\gamma^\mu u_L^\alpha)(\bar{c}_R^\beta\gamma_\mu u_R^\beta) = -2(\bar{c}_L^\alpha u_R^\beta)(\bar{c}_R^\beta u_L^\alpha) = -2(\bar{c}_L^\beta u_R^\alpha)(\bar{c}_R^\alpha u_L^\beta) = -2(\bar{c}_R^\alpha u_L^\beta)(\bar{c}_L^\beta u_R^\alpha)\\
&= -2\mathcal{O}_5,
\end{aligned} \tag{V.118}$$

where in the first step we used Fierz identity and in the second switched the names of the dummy indices α and β. Similarly, for the remaining operators we get

$$\mathcal{Q}_5 = -4\mathcal{O}_3 - 2\mathcal{O}_2 \quad \text{and} \quad \mathcal{Q}_8 = -4\tilde{\mathcal{O}}_3 - 2\tilde{\mathcal{O}}_2. \tag{V.119}$$

As discussed above, to first order approximation (neglecting all terms proportional to m_u/m_c) in our case the only operator with non-zero WC is $\tilde{\mathcal{O}}_2$. $\tilde{\mathcal{O}}_2$ shows up in the operators $\mathcal{Q}_7$ and $\mathcal{Q}_8$. Consequently, we have to consider the running of the corresponding WCs. Following [353] the running for the WCs C_7 and C_8 from the scale of integration Λ to the scale μ can be written as

$$\begin{pmatrix} C_7(\mu) \\ C_8(\mu) \end{pmatrix} = \begin{pmatrix} A & B \\ C & D \end{pmatrix} \begin{pmatrix} C_7(\Lambda) \\ C_8(\Lambda) \end{pmatrix} = P \begin{pmatrix} C_7(\Lambda) \\ C_8(\Lambda) \end{pmatrix} \tag{V.120}$$

with

$$\begin{aligned}
A &= r(\mu,\Lambda)^{(1+\sqrt{241})/6}\left(\frac{1}{2} - \frac{8}{\sqrt{241}}\right) + r(\mu,\Lambda)^{(1-\sqrt{241})/6}\left(\frac{1}{2} + \frac{8}{\sqrt{241}}\right)\\
B &= -r(\mu,\Lambda)^{(1+\sqrt{241})/6}\frac{30}{\sqrt{241}} + r(\mu,\Lambda)^{(1-\sqrt{241})/6}\frac{30}{\sqrt{241}}\\
C &= r(\mu,\Lambda)^{(1+\sqrt{241})/6}\frac{1}{8\sqrt{241}} - r(\mu,\Lambda)^{(1-\sqrt{241})/6}\frac{1}{8\sqrt{241}}\\
D &= r(\mu,\Lambda)^{(1+\sqrt{241})/6}\left(\frac{1}{2} + \frac{8}{\sqrt{241}}\right) + r(\mu,\Lambda)^{(1-\sqrt{241})/6}\left(\frac{1}{2} - \frac{8}{\sqrt{241}}\right)
\end{aligned} \tag{V.121}$$

and

$$r(\mu,\Lambda) = \left(\frac{\alpha_s(\Lambda)}{\alpha_s(m_t)}\right)^{2/7}\left(\frac{\alpha_s(m_t)}{\alpha_s(m_b)}\right)^{6/23}\left(\frac{\alpha_s(m_b)}{\alpha_s(\mu)}\right)^{6/25}, \tag{V.122}$$

where α_s is the strong coupling constant at the given scale. The running of α_s is obtained using the `RunDec` package [354, 355]. Moreover, the WCs in the basis of [353] can be transformed to our basis via

$$\begin{aligned}\begin{pmatrix} C_7 \\ C_8 \end{pmatrix} &= \begin{pmatrix} 1 & 0 \\ -2 & -4 \end{pmatrix} \begin{pmatrix} \tilde{C}_2 \\ \tilde{C}_3 \end{pmatrix} = R \begin{pmatrix} \tilde{C}_2 \\ \tilde{C}_3 \end{pmatrix} \\ \Rightarrow \begin{pmatrix} \tilde{C}_2 \\ \tilde{C}_3 \end{pmatrix} &= R^{-1} \begin{pmatrix} C_7 \\ C_8 \end{pmatrix} = \begin{pmatrix} 1 & 0 \\ -\frac{1}{2} & -\frac{1}{4} \end{pmatrix} \begin{pmatrix} C_7 \\ C_8 \end{pmatrix}. \end{aligned} \tag{V.123}$$

Now, we can use the matrices P and R to get the running of $\tilde{C}_2$ and $\tilde{C}_2$ in the following way

$$\begin{aligned}\begin{pmatrix} C_7(\mu) \\ C_8(\mu) \end{pmatrix} &= P \begin{pmatrix} C_7(\Lambda) \\ C_8(\Lambda) \end{pmatrix} = PR \begin{pmatrix} \tilde{C}_2(\Lambda) \\ \tilde{C}_3(\Lambda) \end{pmatrix} \\ \Rightarrow R \begin{pmatrix} \tilde{C}_2(\mu) \\ \tilde{C}_3(\mu) \end{pmatrix} &= PR \begin{pmatrix} \tilde{C}_2(\Lambda) \\ \tilde{C}_3(\Lambda) \end{pmatrix} \\ \Rightarrow \begin{pmatrix} \tilde{C}_2(\mu) \\ \tilde{C}_3(\mu) \end{pmatrix} &= R^{-1} PR \begin{pmatrix} \tilde{C}_2(\Lambda) \\ \tilde{C}_3(\Lambda) \end{pmatrix}. \end{aligned} \tag{V.124}$$

Again, neglecting $\mathcal{O}(m_u/m_c)$ effects at the UV we finally obtain

$$\begin{aligned}\tilde{C}_2(\mu) &= \left[r(\mu,\Lambda)^{\frac{1-\sqrt{241}}{6}} \left(\frac{1}{2} - \frac{52}{\sqrt{241}} \right) \right. \\ &\quad \left. + r(\mu,\Lambda)^{\frac{1+\sqrt{241}}{6}} \left(\frac{1}{2} + \frac{52}{\sqrt{241}} \right) \right] \tilde{C}_2(\Lambda), \\ \tilde{C}_3(\mu) &= \frac{705}{32\sqrt{241}} \left[r(\mu,\Lambda)^{\frac{1-\sqrt{241}}{6}} - r(\mu,\Lambda)^{\frac{1+\sqrt{241}}{6}} \right] \tilde{C}_2(\Lambda). \end{aligned} \tag{V.125}$$

V.C Momentum Distribution of Charming ALPs

In our recast of experimental single top plus MET searches we have only considered searches including flavour violating top couplings. However, searches for single top plus MET could also set bounds on the parameter space. The top plus MET searches without flavour violating top couplings [441–444] require at least 200 GeV of MET for the hadronic top decays, while the amount of MET for the charming ALP signal of Figure V.12 will be $\lesssim m_t/2$ if the ALP escapes undetected. The mean transverse momenta for $m_a = 2$ GeV and $m_a = 10$ GeV are given in the main text. In addition, we show in this appendix the transverse momentum distribution from a simulation with 10000 events and $c\tau = 10$ m for the above ALP masses in Figure V.17. Here, $m_a = 2$ GeV is depicted in the left panel and $m_a = 10$ GeV in the right one.

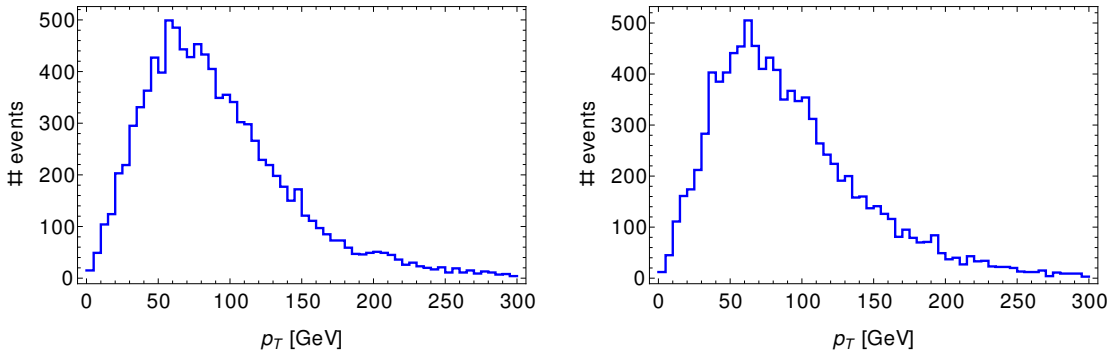

Figure V.17: Charming ALP transverse momentum distribution for the signal of Figure V.12. **Left:** $m_a = 2$ GeV. **Right:** $m_a = 10$ GeV.

Part II

Extended Scalar Sector

With the discovery of a scalar resonance at about 125 GeV [27, 28] the last missing piece of the SM was found. Now, one of the main goals of particle physics is to measure the properties of this scalar [451] and establish if the scalar sector is minimal, i.e. containing only the SM Higgs field, or if there are several. Models with extended scalar sectors feature additional scalar singlets, doublets, triplets and so forth. These kinds of models have a rich phenomenology leading to not only additional states, but also modifying the SM Higgs couplings. As such these models inspire new search channels at experiments, which can give insight into the missing parts of the SM.
An important part of testing the SM Higgs bosons is probing its spin [452, 453] and CP transformation properties [454]. The latter is especially interesting in light of the so far unexplained matter-antimatter asymmetry of the universe [85] because CP violation is one of the Sakharov conditions, cf. Chapter II. As described above, the CP violation in the SM, observed first in Kaon decay [455], then also found [456] in the B sector and more recently in D meson decays [457], is not sufficient to explain the observed baryon asymmetry of the universe. Thus, BSM physics is necessary to introduce an additional source of CP violation. This can, for example, be done in the scalar sector. While the observed scalar boson is so far in agreement with the predicted CP-even SM Higgs boson, an enhanced scalar sector might introduce CP violation. Even though no additional scalar particles have been found to date, extra scalars that mix only weakly with the SM Higgs boson are still viable and can have CP violating properties.
Here, we focus on the THDM [263], which extends the scalar sector by a second $SU(2)_L$ doublet charged under the same quantum numbers as the SM Higgs field. In its most general form the THDM allows CP violation in the scalar sector, being the minimal setup where this is possible. In a THDM with CP violation the scalar potential mixes the interaction eigenstates, that have definite CP properties leading to the mass eigenstates being an admixture of CP-even and CP-odd interaction eigenstates.
Several methods to test CP violation in the THDM have been discussed in the literature. The top quark associated production cross section of an extra scalar H_i is sensitive to the relative magnitudes of the CP-even and CP-odd coefficients of the $t\bar{t}H_i$ couplings. Thus, in case of the discovery of an extra scalar H_i this cross section could be used to determine its CP properties. [458–462]. A disadvantage of this strategy is, however, that the effect is suppressed by the smaller cross section of a three particle final state.
Another way to test the CP properties of extra scalars is to make use of the decay $H_i \to ZZ$. Here, two possibilities have been proposed, both based on the fact that only CP-even scalar bosons couple to pairs of Z bosons: First, the angular momentum of the final state muons in $H_i \to ZZ \to 4\mu$ events, where $4\mu \equiv \mu^-\mu^+\mu^-\mu^+$ (and analogue $4l \equiv l^-l^+l^-l^+$), can be used. Since CP-odd scalars only couple to Z bosons on one-loop levels leading to a different angular correlation than for tree-level decays of CP-even scalars, the asymmetry in the angular distribution of the muons in the final state could be used to determine the CP properties of extra scalars [452, 463–469]. Second, if loop-level contributions to $H_i \to ZZ$ can be neglected, the simultaneous observation of three Higgs bosons with interactions with Z bosons, will be a clear sign for CP violation in the THDM. Again, the reason is the absence of tree-level couplings to Z bosons of CP-odd scalars. Because in the CP conserving THDM all scalars are pure CP-eigenstates, the observation of three Higgs scalars in the decay chain $H_i \to ZZ \to 4\mu$ is only possible in the CP violating THDM where the mass eigenstates are admixtures of CP-even and CP-odd interaction eigenstates. However, it is important to note that the observation of three scalars in decays to ZZ is a clear sign for CP violation only in the THDM. In other models the third resonance could stem from an additional CP-even scalar boson.

Finally, the decay of extra scalars H_i to pairs of τ can give insight into their CP transformation properties since the correlation of the tau polarisation planes is directly linked to the CP properties of the scalars they are originating from. The polarisation planes can be reconstructed from hadronic tau decays [470–475].
In the second part of this thesis, the possibilities to discover CP violation via decays of extra scalars to Z boson and tau pairs are explored at LHC and HL-LHC on the basis of the CP violating THDM. The THDM is introduced in detail in Chapter VI. There, constraints on the parameter space are also discussed. Afterwards, Chapter VII investigates two ways of testing the CP properties of extra scalars. First, in Section VII.1 the prospect to discover CP violation in the scalar sector in decays to tau pairs, which in turn decay hadronically, is investigated. Then, making use of the fact that CP-odd scalars do not interact with Z bosons at tree-level the angular distributions of the four-lepton final state in $H_i \to ZZ \to 4\mu$ decays, and the possibility of observing three Higgs bosons in the invariant mass spectrum of these decays are explored in Section VII.2. Finally, a fit to current ATLAS four-lepton data is performed in Section VII.3.

CHAPTER VI

Two-Higgs-Doublet Model

VI.1 CP Violating Two-Higgs-Doublet Model

THE THDM was introduced in [263] and is the simplest extension of the SM scalar sector that adds a new source of CP violation. It extends the SM scalar sector with an additional scalar $SU(2)_L$-doublet field with the same quantum numbers under the SM gauge symmetry as the SM Higgs fields. The Lagrangian of the model can be decomposed as

$$\mathcal{L}_{\text{THDM}} = \mathcal{L}_{\text{SM,kin}} + \mathcal{L}_{\phi,\text{kin}} + V_\phi + Y_\phi \,. \tag{VI.1}$$

Here, $\mathcal{L}_{\text{SM,kin}}$ contains the kinetic terms of the SM gauge fields and fermions, $\mathcal{L}_{\phi,\text{kin}}$ includes the kinetic terms for the two scalar fields ϕ_1 and ϕ_2 of the model, V_ϕ is the scalar potential and Y_ϕ entails the Yukawa terms of the model. The most general scalar potential for the two scalar fields

$$\phi_1 = \begin{pmatrix} \eta_1^+ \\ (v_1 + h_1 + ih_3)/\sqrt{2} \end{pmatrix} \quad \text{and} \quad \phi_2 = \begin{pmatrix} \eta_2^+ \\ (v_2 + h_2 + ih_4)/\sqrt{2} \end{pmatrix} , \tag{VI.2}$$

where h_i, $i = 1, ..., 4$ are real neutral fields with $h_{1,2}$ being CP-even and $h_{3,4}$ CP-odd, η_i^+, $i = 1, 2$ charged (complex) fields and v_i, $i = 1, 2$ the by convention real and positive vevs, is

$$\begin{aligned} V_\phi = {} & m_{11}^2(\phi_1^\dagger\phi_1) + m_{22}^2(\phi_2^\dagger\phi_2) - \left[m_{12}^2(\phi_1^\dagger\phi_2) + h.c\right] \\ & + \lambda_1(\phi_1^\dagger\phi_1)^2 + \lambda_2(\phi_2^\dagger\phi_2)^2 + \lambda_3(\phi_1^\dagger\phi_1)(\phi_2^\dagger\phi_2) + \lambda_4(\phi_1^\dagger\phi_2)(\phi_2^\dagger\phi_1) \\ & + \frac{1}{2}\left[\lambda_5(\phi_1^\dagger\phi_2)^2 + \lambda_6(\phi_1^\dagger\phi_1)(\phi_1^\dagger\phi_2) + \lambda_7(\phi_2^\dagger\phi_2)(\phi_1^\dagger\phi_2) + h.c.\right] , \end{aligned} \tag{VI.3}$$

where $\lambda_{i\neq 5}$ are real, while the possible complex phases of the parameters $\lambda_5 = |\lambda_5|e^{i\eta(\lambda_5)}$ and $m_{12} = |m_{12}|e^{i\eta(m_{12})}$ allow CP violation in the scalar sector.
Generally, in the THDM FCNCs at tree-level are possible. They can be avoided by introducing a global Z_2 symmetry [476] under which the scalar fields transform as

$$\phi_1 \to \phi_1, \qquad \phi_2 \to -\phi_2 \,. \tag{VI.4}$$

Since tree-level FCNCs are absent when the contributions to the mass matrices for each fermion stem from a single source [476, 477], they can be prevented in the THDM by ensuring that all RH quarks of a given charge couple to a single $SU(2)_L$-doublet field via their charge assignment under the discrete Z_2 symmetry. Typically, four different types of the THDM are distinguished based on the Z_2 charges of the fermions as shown in

	up-type	down-type	leptons
type-I	ϕ_2	ϕ_2	ϕ_2
type-II	ϕ_2	ϕ_1	ϕ_1
lepton-specific	ϕ_2	ϕ_2	ϕ_1
flipped	ϕ_2	ϕ_1	ϕ_2

Table VI.1: Realizations of the Yukawa-types in the THDM with a softly broken Z_2 symmetry. For a given realization of the THDM the scalar to which the fermions couple is given.

Table VI.1 [478]. Here, we consider the THDM "type-I" where all quarks and charged leptons couple only to one of the scalar doublet fields, conventionally chosen to be ϕ_2. Other realizations of the THDM include the "type-II" with the up-type (down-type) quarks and leptons couple conventionally only to ϕ_2 (ϕ_1), the "lepton-specific" scenario where all quarks couple to ϕ_2 while the leptons couple to ϕ_1 and the "flipped" model where RH leptons couple to ϕ_2 like the up-type quarks. Consequently, in the THDM type-I the Yukawa term reads

$$-Y_\phi = Y_u \bar{Q}_L i\sigma_2 \phi_2^* u_R + Y_d \bar{Q}_L \phi_2 d_R + Y_e \bar{L}_L \phi_2 e_R + \text{h.c.} \tag{VI.5}$$

with the Yukawa coupling matrices Y_u, Y_d, Y_e.
In addition to preventing FCNCs at tree-level, the Z_2 symmetry also enforces $\lambda_6 = \lambda_7 = m_{12} = 0$ in the scalar potential for the transformations of the scalar fields given in Equation VI.4. Thus, for an exact Z_2 symmetry no CP violation occurs in the scalar sector as the only complex parameter would be λ_5 and its effect can be absorbed into a global field redefinition. To allow CP violation, therefore, we consider a softly broken Z_2 symmetry, so that both possible complex parameters λ_5 and m_{12} are present. Then, the scalar potential reads

$$\begin{aligned} V_\phi = {} & m_{11}^2(\phi_1^\dagger\phi_1) + m_{22}^2(\phi_2^\dagger\phi_2) - \left[m_{12}^2(\phi_1^\dagger\phi_2) + h.c\right] + \lambda_1(\phi_1^\dagger\phi_1)^2 + \lambda_2(\phi_2^\dagger\phi_2)^2 \\ & + \lambda_3(\phi_1^\dagger\phi_1)(\phi_2^\dagger\phi_2) + \lambda_4(\phi_1^\dagger\phi_2)(\phi_2^\dagger\phi_1) + \frac{1}{2}\left[\lambda_5(\phi_1^\dagger\phi_2)^2 + H.c\right], \end{aligned} \tag{VI.6}$$

where again λ_5 and m_{12} can be written as $\lambda_5 = |\lambda_5|e^{i\eta(\lambda_5)}$ and $m_{12} = |m_{12}|e^{i\eta(m_{12})}$.
The tadpole equations obtained from minimizing the scalar potential after spontaneous EWSB require

$$\frac{\partial V}{\partial h_1} = \frac{1}{2}v_1 v_2^2 \,\mathrm{Re}(\lambda_5) - v_2 \,\mathrm{Re}(m_{12}^2) + \lambda_1 v_1^3 + m_{11}^2 v_1 + \frac{1}{2}\lambda_3 v_1 v_2^2 + \frac{1}{2}\lambda_4 v_1 v_2^2 = 0, \tag{VI.7}$$

$$\frac{\partial V}{\partial h_2} = \frac{1}{2}v_1^2 v_2 \,\mathrm{Re}(\lambda_5) - v_1 \,\mathrm{Re}(m_{12}^2) + \frac{1}{2}\lambda_3 v_1^2 v_2 + \frac{1}{2}\lambda_4 v_1^2 v_2 + \lambda_2 v_2^3 + m_{22}^2 v_2 = 0, \tag{VI.8}$$

$$\frac{\partial V}{\partial h_3} = -\frac{1}{2}v_1 v_2^2 \,\mathrm{Im}(\lambda_5) + v_2 \,\mathrm{Im}(m_{12}^2) = 0, \tag{VI.9}$$

$$\frac{\partial V}{\partial h_4} = \frac{\partial V}{\partial h_3} \times \left(-\frac{v_1}{v_2}\right) = 0\,. \tag{VI.10}$$

In addition, the two vevs v_1 and v_2 of the respective scalar fields satisfy $v = \sqrt{v_1^2 + v_2^2}$, where $v = 246$ GeV is the SM vev, and we define $\tan\beta = v_2/v_1$. By solving Equations VI.7 and VI.8 m_{11}^2 and m_{22}^2 can be rewritten as functions of λ_i, $i = 1, ..., 5$, m_{12} and the vevs

and, thus, removed in all equations, while from Equation VI.9 the condition

$$\mathrm{Im}(m_{12}^2) = \frac{1}{2} v_1 v_2 \,\mathrm{Im}(\lambda_5) \tag{VI.11}$$

is found. As a consequence, $\mathrm{Im}(m_{12}^2)$ can be replaced with $\frac{1}{2} v_1 v_2 \,\mathrm{Im}(\lambda_5)$ in all equations, leaving in addition to the $\lambda_{i\neq 5}$

$$\mathrm{Re}(m_{12}^2) \quad \text{and} \quad \lambda_5 = |\lambda_5|\, e^{i\eta(\lambda_5)} \tag{VI.12}$$

as the remaining free parameters. The only left complex parameter is, then, $|\lambda_5| e^{i\eta(\lambda_5)}$. Consequently, the complex phase $\eta(\lambda_5)$ governs the CP violation of the THDM.
The remaining free parameters also determine the masses of the physical scalar bosons. For the neutral scalars the tree-level mass matrix is

$$(\mathcal{M}^2)_{ij} = \left. \frac{\partial^2 V}{\partial h_i \partial h_j} \right|_{h_i = 0} , \tag{VI.13}$$

where h_i $(i = 1, 2, 3, 4)$ are the neutral components of ϕ_1 and ϕ_2, cf. Equation VI.2, including the Goldstone boson that is absorbed by the Z boson after spontaneous EWSB. In the here considered model the mass matrix for the four neutral states in the Higgs basis h_1, h_2, h_3, h_4 reads

$$\mathcal{M} = \begin{pmatrix} D_1 & O_1 & O_2 & O_3 \\ O_1 & D_2 & O_4 & O_5 \\ O_2 & O_4 & D_3 & O_6 \\ O_3 & O_5 & O_6 & D_4 \end{pmatrix} , \tag{VI.14}$$

where the diagonal elements are

$$\begin{aligned} D_1 &= 3\lambda_1 v_1^2 + \frac{v_2^2 \lambda_3}{2} + \frac{v_2^2 \lambda_4}{2} + m_{11}^2 + \frac{1}{2} v_2^2 \,\mathrm{Re}(\lambda_5) , \\ D_2 &= \frac{\lambda_3 v_1^2}{2} + \frac{\lambda_4 v_1^2}{2} + \frac{1}{2} \,\mathrm{Re}(\lambda_5) v_1^2 + 3 v_2^2 \lambda_2 + m_{22}^2 , \\ D_3 &= \lambda_1 v_1^2 + \frac{v_2^2 \lambda_3}{2} + \frac{v_2^2 \lambda_4}{2} + m_{11}^2 - \frac{1}{2} v_2^2 \,\mathrm{Re}(\lambda_5) , \\ D_4 &= \frac{\lambda_3 v_1^2}{2} + \frac{\lambda_4 v_1^2}{2} - \frac{1}{2} \,\mathrm{Re}(\lambda_5) v_1^2 + v_2^2 \lambda_2 + m_{22}^2 \end{aligned} \tag{VI.15}$$

$$\tag{VI.16}$$

and the off-diagonal entries are

$$\begin{aligned} O_1 &= v_1 v_2 \lambda_3 + v_1 v_2 \lambda_4 + v_1 v_2 \,\mathrm{Re}(\lambda_5) - \mathrm{Re}(m_{12}^2) , \\ O_2 &= -\frac{1}{2} v_2^2 \,\mathrm{Im}(\lambda_5) , \\ O_3 &= \frac{1}{2} v_1 v_2 \,\mathrm{Im}(\lambda_5) , \\ O_4 &= -O_3 , \\ O_5 &= \frac{1}{2} v_1^2 \,\mathrm{Im}(\lambda_5) , \\ O_6 &= v_1 v_2 \,\mathrm{Re}(\lambda_5) - \mathrm{Re}(m_{12}^2) . \end{aligned} \tag{VI.17}$$

By diagonalizing the mass matrix in Equation VI.14 the masses of the neutral physical scalar bosons, three massive Higgs bosons H_1, H_2 and H_3 and one massless neutral field H_0, are obtained. The masses of these physical scalar bosons can either, under certain simplifying conditions, be evaluated analytically as a function of the model parameters, see for example [479, 480], or numerically, which we do in the following. Generally, the mass eigenstates violate the CP symmetry. However, with $\mathrm{Im}(\lambda_5)$ being the only source of CP violation the CP conserving THDM can be recovered for $\mathrm{Im}(\lambda_5) \to 0$, as for this choice the off-diagonal entries of the mass matrix $O_{2,3,4,5}$ vanish. Then, $\mathcal{M}$ becomes a block diagonal matrix with the the upper 2×2 block consisting of D_1, D_2 and O_1 and the lower block consisting of D_3, D_4 and O_6. Consequently, the two blocks can be diagonalized independently of each other.
In general, the squared neutral scalar boson matrix in Equation VI.14 is diagonalized via a 4×4 matrix R, so that

$$R^\dagger \mathcal{M}^2 R = \mathcal{M}^2_{diag} = \mathrm{diag}(0, M^2_{H_1}, M^2_{H_2}, M^2_{H_3})\,. \tag{VI.18}$$

Then the physical Higgs mass eigenstates H_i, $i = 0, 1, 2, 3$ are related to the interaction eigenstates h_i as

$$h_i = \sum_i R_{ij} H_j\,. \tag{VI.19}$$

As described above, in the absence of the CP violating phase $\eta(\lambda_5)$ $\mathcal{M}$ is a block diagonal matrix $\mathcal{M}$, so that each block can be diagonalized independently, causing the mass eigenstates H_0 and H_1 to only be related to the CP-even interaction eigenstates h_1 and h_2. Analogously, the mass eigenstates H_2 and H_3 are only related to the CP-odd interaction eigenstates h_3 and h_4. On the other hand, if $\eta(\lambda_5) \neq 0$, all mass eigenstates H_i, $i = 1, 2, 3, 4$ are admixtures of both the CP-even and the CP-odd interaction eigenstates because all entries of $\mathcal{M}$ will be non-zero.
We identify the massless scalar boson H_0 with the Goldstone boson eaten by the Z boson and H_1 as the SM Higgs-like scalar resonance with mass $M_{H_1} \sim 125$ GeV. Furthermore, we assume, in the following, that the additional massive neutral scalar bosons H_2 and H_3 are heavier than H_1 and require without loss of generality the mass ordering to be $M_{H_1} \leq M_{H_2} \leq M_{H_3}$. We carry out the evaluation of both, the mass matrix $\mathcal{M}$ and the rotation matrix R numerically with `SPheno v3.8.8` [481, 482]. In addition to the three neutral Higgs bosons H_1, H_2 and H_3, the THDM also features one massive and one massless charged scalar where the latter is the Goldstone boson eaten by the charged $W^\pm$ boson. Again, the mass of the massive charged Higgs boson $H^\pm$ is evaluated with `SPheno v3.8.8`.

VI.2 Constraints

BEFORE evaluating two methods to study the CP properties of the Higgs bosons of the THDM type-I in Chapter VII, we first discuss the various constraints on the parameter space of the model from observations and measurements at collider and non-collider experiments, such as B-physics measurements, Higgs data from LHC, LEP and Tevatron and measurements of the electron electric dipole moment.

Theoretical Considerations

Besides limits from observations and measurements theoretical considerations also constrain the parameters of the THDM type-I. First, we require that all couplings satisfy $|\lambda_i| \lesssim 4\pi$ to ensure the model is perturbative. A second condition arises from vacuum stability. The scalar potential in Equation VI.6 should be positive for large values of ϕ_i, $i = 1, 2$, leading to [479, 483]

$$\lambda_1 > 0, \qquad \lambda_2 > 0, \qquad \lambda_3 + \sqrt{\lambda_1 \lambda_2} > 0, \qquad \lambda_3 + \lambda_4 - |\lambda_5| + \sqrt{\lambda_1 \lambda_2} > 0\,. \tag{VI.20}$$

Third, the S-matrix for elastic two-by-two Higgs-Higgs boson, Higgs-vector boson and vector-vector boson scattering processes has to be unitary, which also limits the magnitude of the λ_i, $i = 1 - 5$ parameters as discussed in [479, 483]. Finally, the oblique parameters given from the electroweak global fit in [484, 485]

$$S = 0.03 \pm 0.10, \qquad T = 0.05 \pm 0.12, \qquad U = 0.03 \pm 0.10\,, \tag{VI.21}$$

receive contributions from the THDM at loop-level and, thus, present an important independent constraint on the free parameters. The values of the oblique parameters for a given set of model parameters are calculated with `SPheno v3.8.8` and parameter points that exceed the errors in Equation VI.21 are rejected.

B-physics Data

Measurements of B meson decays put a limit on the THDM parameter space as the additional charged scalar $H^\pm$ contributes to these processes. Here, it is important to note that the couplings of $H^\pm$ are not sensitive to the parameters of the neutral scalar sector. Thus, the constraints from B meson decays are independent of the amount of CP violation in the model.
Similarly to the evaluation of the scalar masses and the oblique parameters of the model the flavour phenomenology is also assessed numerically. For this the tool `FlavorKit` [486] was used. For each given set of input parameters `FlavorKit` calculates flavour observables including the branching ratios of B and D mesons, as well as Kaons. For a general THDM the most stringent bound arises from the process $B \to X_s\gamma$. In particular, this process excludes masses of the charged scalar $m_{H^\pm} \lesssim 580$ GeV for $\tan\beta = 1$ in the THDM type-II. On the other hand, in the THDM type-I this quantity gets weaker with increasing $\tan\beta$, so that the strongest bound arises at $\tan\beta \leq 2$ [487, 488]. To constrain the parameter space we use the experimental bound reported in [89]

$$\mathrm{Br}_{E_\gamma \geq 1.6\,\mathrm{GeV}}(B \to X_s\gamma) \leq (3.32 \pm 0.15) \times 10^{-4}\,. \tag{VI.22}$$

Again, parameter points that result in larger branching ratios than this bound are excluded.

Higgs Data

As we have identified H_1 as the SM-like Higgs boson, its properties, together with the contributions from H_2 and H_3, have to be in agreement with the to date measurements of the SM Higgs properties. Measurements from LEP, Tevatron and LHC experiments are included in the global data set of the Higgs boson. The data from these experiments are combined and can be used to constrain the parameter space of models with additional scalar bosons such as the THDM with the numerical tool `HiggsBounds v5.3.2` [489]. In `HiggsBounds v5.3.2` the most sensitive channel for each Higgs boson H_i is identified separately, before the ratio of the theoretically predicted to the observed signal strength for heavy Higgs bosons for this channel is calculated as

$$\mathcal{K}_i = \frac{\sigma \times \mathrm{Br}(H_i)_{model}}{\sigma \times \mathrm{Br}(H_i)_{obs}}\,. \tag{VI.23}$$

Here, σ is the production cross section. This can be used to obtain a 95% CL for parameter space points where at least one observable with $\mathcal{K}_i > 1$ exists.
Furthermore, we use the numerical tool `HiggsSignals v2.2.3` [490], so that we not only exclude individual parameter space points, but can also determine the statistical compatibility of the chosen lightest SM-like Higgs boson H_1 with the scalar resonance observed at the LHC. Here, the SM-like Higgs mass and signal rates are compared with the various signal rates published by the experimental collaborations for a fixed Higgs mass hypothesis. More precisely, a NP model is tested at the Higgs mass peak observed in the channels with high mass resolutions, such as $h \to ZZ^* \to 4l$ and $h \to \gamma\gamma$ with h the SM Higgs boson and $l = e, \mu$. For a given NP model the signal strength modifier of a single channel is given by

$$\mu = \frac{(\sigma \times \mathrm{Br})_{model}}{(\sigma \times \mathrm{Br})_{SM}} \times \omega\,, \tag{VI.24}$$

where ω is the SM weight of the channel including the experimental efficiencies. Then, `HiggsSignals v2.2.3` performs a χ^2 test for the NP model hypothesis with local excesses in the observed data at a specific mass being matched by the model. The total χ^2 including both the signal strength modifiers and the corresponding predicted Higgs masses is

$$\chi^2_{tot} = \chi^2_{\mu} + \sum_{i=1}^{N_H} \chi^2_{m_{H_i}}. \tag{VI.25}$$

Above, χ^2_{μ} is the χ-squared measure calculated solely from the signal strength modifiers, while χ^2_m with i running over the number of neutral Higgs bosons N_H in the given model is the χ-squared measure determined from the neutral Higgs bosons masses. For χ_{μ} the intrinsic experimental statistical and systematic uncertainties within 1σ are

$$\chi^2_{\mu} = (\mu_{obs} - \mu_{model})^T C^{-1}_{ij} (\mu_{obs} - \mu_{model}) \tag{VI.26}$$

with C_{ij} the signal strength covariance matrix containing the uncorrelated intrinsic experimental statistical and systematic uncertainties in its diagonal entries.
From the best-fit value of the model under consideration here, $\Delta\chi^2_{best} = 1.049$, the 1σ and 2σ error is given by $1(2)\sigma = \Delta\chi^2_{best} + 2.3(5.9)$. The combined best fit values for the SM Higgs signal strength reported by CMS and ATLAS at $\sqrt{s} = 13$ TeV and integrated luminosities of $\mathcal{L} = 35.9$ fb^{-1} and $\mathcal{L} = 79.8$ fb^{-1} are $\mu_{best} = 1.17^{+0.1}_{-0.1}$ [491] and $\mu_{best} = 1.13^{+0.09}_{-0.08}$ [492], respectively. This not only puts a strong constraint on H_1 to have properties close to the SM Higgs boson, but also strongly limits the amount of mixing between H_1 and H_i, $i = 2, 3$.

Electric Dipole Moment

Lastly, we consider the impact of the THDM on low-energy observables. The presence of possibly large CP phases implies that the THDM gives rise to contributions to EDMs of SM particles, especially the electron EDM. Contributions to the electron EDM arise from the new neutral scalars, as well as from the charged scalar boson via Barr-Zee diagrams as discussed e.g. in [493, 494] and in [495] for two loop calculation. It was found that in particular the CP violating complex phase strongly affects the magnitude of the EDM, mainly by modifying the couplings of the Higgs bosons. The impact differs depending on which realization of the THDM is chosen. Generally, for fermions that couple to ϕ_1 (ϕ_2) the Yukawa coupling is enhanced (suppressed) by $\tan\beta$ ($\frac{1}{\tan\beta}$). Consequently, in the THDM type-I where all fermions couple to ϕ_2 all Yukawa couplings are proportional to $\frac{1}{\tan\beta}$, while in the THDM type-II the Yukawa couplings of down-type quarks and leptons are proportional to $\tan\beta$. Then, the electron EDM is suppressed in the THDM type-I by $\frac{1}{\tan\beta}$ and enhanced by $\tan\beta$ in the THDM type-II [496]. Here, we always consider large values of $\tan\beta$, so that the contributions to the electron EDM are suppressed. In all analyses in Chapter VII only parameter space points with electron EDM lower than the experimental limit, which is at $|d_e| < 1.1 \times 10^{-29}$ ecm [497], are considered.

Scanning the Parameter Space

A scan over the parameter space where the full parametric dependence of the physical properties of the scalar particles like their masses and interaction vertices are calculated allows us to find viable parameter space points satisfying the above listed constraints. We perform such a scan with `SPheno v3.3.8` combined with `HiggsBounds v5.3.2` and `HiggsSignals v2.2.3` where a number of flavour processes was calculated with the `FlavorKit` tool. The parameter ranges used were optimized to fulfill the constraints on the parameter space and are

$$\begin{aligned} 0 \;\leq\; \lambda_1 \;\leq\; 10, \qquad & 0.05 \;\leq\; \lambda_2 \;\leq\; 0.2, \\ 0 \;\leq\; \lambda_3 \;\leq\; 10, \qquad & -10 \;\leq\; \lambda_4 \;\leq\; 10, \\ -10 \;\leq\; |\lambda_5| \;\leq\; 10, \qquad & -1.0 \;\leq\; \eta(\lambda_5) \;\leq\; 1.0, \\ 2 \;\leq\; \tan\beta \;\leq\; 50, \qquad & -25\ \text{TeV}^2 \;\leq\; m_{12}^2 \;\leq\; 25\ \text{TeV}^2\,. \end{aligned} \tag{VI.27}$$

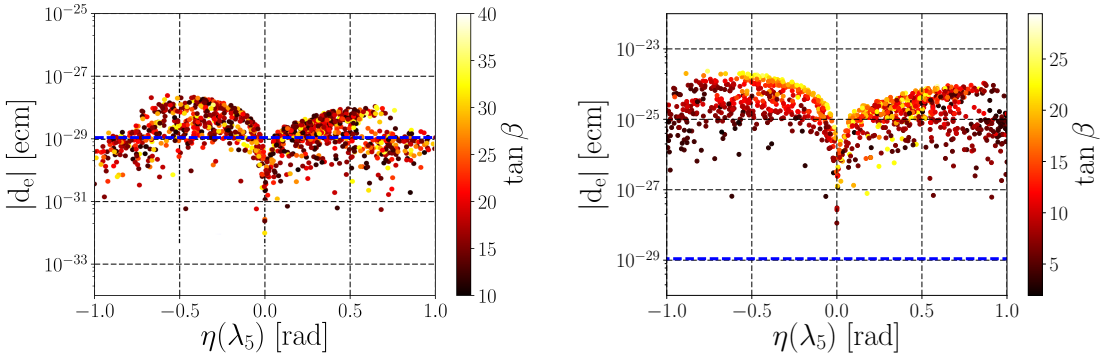

Figure VI.1: Electron EDM as a function of $\eta(\lambda_5)$ and $\tan\beta$ for the type-I (**left**) and type-II (**right**) THDM. The dotted blue lines show the current experimental limit $|d_e| < 1.1 \times 10^{-29}$. Points below the lines satisfy the constraint. This figure was created in collaboration with a collaborator and modified by the author for this thesis.

The contributions to the electron EDM, on the other hand, were calculated following the expressions in [493, 494]. The corresponding electron EDM for each parameter space point that satisfies all other constraints is shown in Figure VI.1 for the THDM type-I (left panel) and type-II (right panel) as a function of $\tan\beta$ and $\eta(\lambda_5)$. The dependence on $\tan\beta$ can be seen clearly. For the THDM type-II the lowest electron EDM values are obtained for low $\tan\beta$ and large η. For the here used scan resolution in the THDM type-II no viable parameter space point was found. This is in agreement with the literature, for example, the analysis in [498]. There, for small values of $\tan\beta$ a region in the parameter space of the type-II THDM was found that is not excluded by the electron EDM and the Higgs constraints. Since in the performed parameter space scan $\tan\beta \geq 2$ was used, this region is not visible in Figure VI.1. In contrast, in the type-I THDM where the couplings entering the contributions to the electron EDM are suppressed with $1/\tan\beta$ viable parameter space points were found for all values of $\eta(\lambda_5)$.
After also applying the electron EDM constraint in total around 5000 allowed parameter space points spanning a wide range of masses for H_2 and H_3 are left for the THDM type-I. The masses of the scalar bosons are shown as a function of $\tan\beta$ in Figure VI.2. It can

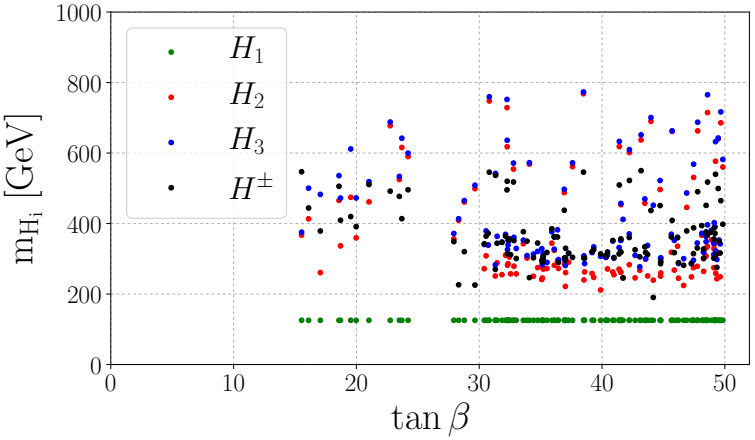

Figure VI.2: Scatter plot of the masses of the scalar bosons H_1 (green), H_2 (red), H_3 (blue) and $H^\pm$ (black) as a function of $\tan\beta$.

be seen that for all values of $\tan\beta$ it is possible to recover a SM-like Higgs boson in H_1, while the masses of H_2 and H_3 are between about 200 and 700 GeV. Moreover, H_2 is slightly lighter with most of the possible masses around 200 to 300 GeV and H_3 heavier with masses closer to 400 GeV. From the set of allowed parameter space points we choose benchmark points for our analyses.

CHAPTER VII

Testing the CP Properties of the THDM Type-I

VII.1 Discovering CP Violation in $H_{2,3} \to \tau^-\tau^+$ Decays

As a first approach to test the CP properties of the CP violating THDM type-I we use the decays of the two heavy scalars H_2 and H_3 to pairs of taus. As described above, the correlation of the tau polarisation planes can be used to test the CP properties of a model with extra Higgs bosons. To extract the transverse spin correlation we use the impact parameter method. This method was first introduced in [470] and is used in the decay chain of a field that is an admixture of a scalar and a pseudoscalar field. For simplicity, in the following, we denote such a field S. Note that this method is independent of the production mechanism of S. Instead, it translates directly into correlations among its decay products.
In our analysis the decay chain is $S \to \tau^-\tau^+$ where each tau decays hadronically via $\tau^\pm \to \pi^\pm\bar{\nu}_\tau(\nu_\tau)$ and S corresponds to H_2 and H_3. The branching ratio for the decay $\tau^\pm \to \pi^\pm\bar{\nu}_\tau(\nu_\tau)$ is 11% [499]. Thus, this choice of decay chain limits the statistics of the analysis. However, it also provides a clear signal. Therefore, the results obtained in our analysis are a conservative estimate for the sensitivity to distinguish CP properties.
The impact parameter method makes use of the visible decay products of the taus, $\tau_{had} = \pi^\pm$, to extract an asymmetry in the so-called acoplanarity angle ϕ of the two tau leptons. The acoplanarity angle is the angle between the two decay planes and sensitive to the CP properties of S via its scalar and pseudoscalar coupling component. The Yukawa interaction of the scalar field S to taus reads

$$\mathcal{L}_y = y_{S\tau}\ (\bar{\tau}\,(C_S + C_P\ i\gamma_5)\,\tau)\,S\,, \tag{VII.1}$$

where $y_{S\tau}$ is the effective Yukawa coupling between S and tau, C_P, C_S the scalar and pseudoscalar components of the coupling, respectively, and $C_S^2 + C_P^2 = 1$. Furthermore, we define the effective mixing angle $\theta_{\tau\tau}$ as

$$\tan(\theta_{\tau\tau}) = \frac{C_P}{C_S}\,. \tag{VII.2}$$

This angle measures the mixing of CP eigenstates. For example, $\theta_{\tau\tau} = 0$ corresponds to pure scalar and $\theta_{\tau\tau} = \frac{\pi}{2}$ to pure pseudoscalar couplings.
From the angle between the tau decay planes the $\tau^-\tau^+$ spin correlation can be inferred. The angular correlation in the decay width for the here considered $\tau^\pm \to \pi^\pm\bar{\nu}_\tau(\nu_\tau)$ decay

is [470]

$$\frac{1}{\Gamma}\frac{d\Gamma}{d\phi} = \frac{1}{2\pi}\left(1 - \frac{\pi^2}{16}\frac{C_S^2 - C_P^2}{C_S^2 + C_P^2}\cos\phi\right) = \frac{1}{2\pi}\left(1 - \frac{\pi^2}{16}\left(\cos^2\theta_{\tau\tau} - \sin^2\theta_{\tau\tau}\right)\cos\phi\right) \quad \text{(VII.3)}$$

with C_P, C_S and $\theta_{\tau\tau}$ as defined above and ϕ again the acoplanarity angle. Equation VII.3 is given for the case where ϕ and $2\pi - \phi$ are indistinguishable by summing over both cases [470]. We show in Figure VII.1 the angular correlation in the decay width in Equation VII.3 as a function of the acoplanarity angle for three values of $\theta_{\tau\tau}$, $\theta_{\tau\tau} = \frac{\pi}{2}$ (blue), $\theta_{\tau\tau} = \frac{\pi}{4}$ (yellow) and $\theta_{\tau\tau} = 0$ (green). It is clear due to the different shapes of $\frac{1}{\Gamma}\frac{d\Gamma}{d\phi}$ for the three values of $\theta_{\tau\tau}$ that if measurable (which means if a sufficient number of signal events would be produced), this distribution will allow inferring the CP properties of extra scalars.

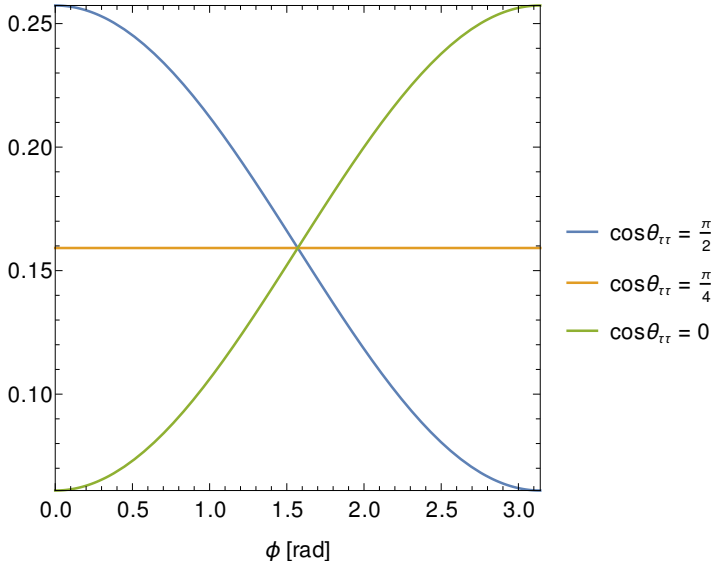

Figure VII.1: The angular correlation in the decay width $\frac{1}{\Gamma}\frac{d\Gamma}{d\phi}$ (cf. Equation VII.3) as a function of the acoplanarity angle ϕ for $\theta_{\tau\tau}$, $\theta_{\tau\tau} = \frac{\pi}{2}$ (blue), $\theta_{\tau\tau} = \frac{\pi}{4}$ (yellow) and $\theta_{\tau\tau} = 0$ (green).

VII.1.1 The Zero-Momentum-Frame

In the here considered case the impact parameter is the shortest path from the PV to the pion momentum vector extended, so that it points in the direction of the tau decay point. We introduce the impact parameter vector

$$\vec{n}^{\pm} = \frac{\vec{P}_{\pi^\pm} \times \vec{P}_{\tau^-}}{|\vec{P}_{\pi^\pm} \times \vec{P}_{\tau^-}|}\,, \quad \text{(VII.4)}$$

where $\vec{P}_{\pi^\pm}$ and $\vec{P}_{\tau^-}$ are the momenta of the pions and taus, respectively. From the impact parameter vector the acoplanarity angle can be reconstructed as

$$\phi = \arccos\left(\vec{n}^{-} \cdot \vec{n}^{+}\right). \quad \text{(VII.5)}$$

However, due to the presence of tau neutrinos as one of the taus decay products it is nearly impossible to reconstruct the tau lepton momenta. To avoid this problem we use the "Zero-Momentum-Frame" (ZMF) of the tau decay products, here, the pions. The

ZMF of the pions is defined as the frame where $\vec{P}^*_{\pi^+} = -\vec{P}^*_{\pi^-}$. Note that here and in the following quantities in the ZMF are marked with an asterisk (*). Using the ZMF of the pions instead of the taus does not affect the correlation of the decay planes [470] and, thus, it is no longer necessary to reconstruct the exact direction of the taus. It is worth pointing out that also Equation VII.3 remains invariant when going to the pion ZMF (cf. also [470]), so that

$$\frac{1}{\Gamma}\frac{d\Gamma}{d\phi^*} = \frac{1}{\Gamma}\frac{d\Gamma}{d\phi}\bigg|_{\phi\to\phi^*} = \frac{1}{2\pi}\left(1 - \frac{\pi^2}{16}\left(\cos^2\theta_{\tau\tau} - \sin^2\theta_{\tau\tau}\right)\cos\phi^*\right) . \tag{VII.6}$$

Next, a four-vector for the normalized impact parameter is defined in the ZMF as $n^{*\pm} = (0, \vec{n}^{*\pm})$ for each tau. Then, the acoplanarity angle in the ZMF can be reconstructed from these vectors via

$$\phi^* = \arccos\left(\vec{n}^{*-}_{\perp} \cdot \vec{n}^{*+}_{\perp}\right) , \tag{VII.7}$$

where $\vec{n}^{*\pm}_{\perp}$ are the components of $n^{*\pm}$ orthogonal to the pion momentum. The resulting distribution of ϕ^* between 0 and π differs for CP-even and CP-odd eigenstates and, consequently, allows for a clear distinction between the two cases. In the following, using a benchmark point obtained from the above described parameter space scan, we explore how well this method can be used at current and future experiments to test the CP properties of extra scalars.

VII.1.2 Analysis

For our analysis of the CP properties of extra scalars in the THDM with decays to tau pairs we use the HL-LHC with a center-of-mass energy $\sqrt{s} = 14$ TeV and a total integrated luminosity of $\mathcal{L} = 3$ ab^{-1}. The two dominant production modes of neutral Higgs bosons at pp colliders are gluon fusion, which makes up $\sim 90\%$ of Higgs boson production, and vector boson fusion producing nearly 10% of the Higgs bosons. The effective Higgs-gluon-gluon couplings for H_2 and H_3 were calculated with `SPheno v3.3.8` and the production cross sections by including this vertex in `MadGraph5_aMC@NLO v3.4.0` [318]. In addition, the QCD corrections from [500] were included.
In Figure VII.2 the cross section of the process $gg \to H_i \to \tau^-\tau^+$ is shown for HL-LHC with $\sqrt{s} = 14$ TeV as a function of the masses of the extra Higgs bosons H_2 and H_3 in red and blue, respectively. Only parameter space points satisfying all of the above discussed constraints are shown. As the CP properties of the extra scalars is encoded in the angular correlations of their decay products and, thus, can only be accessed statistically, we are interested in a benchmark point where a large amount of signal events can be expected. From Figure VII.2 it can be seen that parameter space points exist with production cross sections larger than a few femtobarn. With the expected total luminosity at HL-LHC these points would yield a few thousand events. Generally, this is a sufficiently large number of signal events to study the CP properties of the extra Higgs bosons. However, difficulties could arise due to large backgrounds and reconstruction uncertainties. Subsequently, we evaluate a specific benchmark point with high cross section for the process $gg \to H_i \to \tau^-\tau^+$ to assess the prospect of testing CP violation in decays to tau pairs.

VII.1.2.1 Signal Reconstruction for a Benchmark Point at HL-LHC

The chosen benchmark point has $m_{H_2} = 250$ GeV and $m_{H_3} = 300$ GeV based on the model parameters $\tan\beta = 31$, $\theta_{\tau\tau} = 0.68 = \frac{\pi}{4.6}$ (which corresponds to $\eta(\lambda_5) = 0.7$),

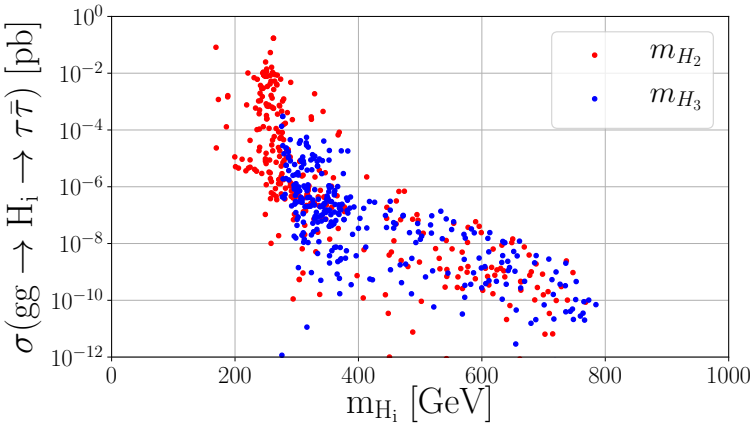

Figure VII.2: Production cross section of tau pairs in $gg \to H_i \to \tau^-\tau^+$ processes at HL-LHC with $\sqrt{s} = 14$ TeV as a function of the mass of H_2 (red) and H_3 (blue) for all parameter space points satisfying the discussed constrains. This figure was created in collaboration with a collaborator and modified by the author for this thesis.

$\lambda_1 = 0.039$, $\lambda_2 = 0.104$, $\lambda_3 = 2.215$, $\lambda_4 = -0.023$, $\mathrm{Re}(\lambda_5) = 0.337$ and $m_{12}^2 = -1.919 \times 10^4$ GeV^2. As discussed in the previous Chapter VI, the parameters m_{11}^2 and m_{22}^2 are fixed due to the tadpole equations in Equations VI.7 and VI.8. This benchmark point fulfills all constraints. It has an electron EDM of $|d_e| \approx 7.4 \times 10^{-30}$ ecm and a branching ratio $\mathrm{Br}(B \to X_s\gamma) \approx 3.04 \times 10^{-4}$. Both values are close to the experimental limit and, consequently, can be used as complementary probes of our benchmark point. It is worth pointing out that the benchmark point is stable against small changes in the model parameters, more precisely, changes in the input parameters of $\mathcal{O}(5\%)$ lead to changes in the masses of $\mathcal{O}(0.1\%)$, while still all above discussed constraints are fulfilled.
Here we focus on the inclusive signal process

$$pp \to H_i \to \tau^-\tau^+ \tag{VII.8}$$

and include interference between H_2 and H_3. The main irreducible backgrounds for this process are $Z \to \tau^-\tau^+$, as well as single top and $t\bar{t}$ with tau jet pairs produced from the W decay [501]. Additional backgrounds arise from the misidentification of light jets as tau jets for instance in W boson plus jets or multijets events. The cross sections of the considered backgounds are listed in Table VII.1.
For the signal we simulated 20 millions events and for each background 30 millions with `MadGraph5_aMC@NLO v3.4.0` [318] where parton shower, hadronisation and spin correlation of the tau lepton decay are taken care of by `Pythia v8.240` [314]. The fast detector simulation was done with `Delphes v3.5.0` [449] where the tau jet tagging was performed with a reconstruction efficiency of 70% and a misidentification rate of QCD jets of 5×10^{-3} was used, both implemented on the analysis level. Following [503] we use a background reconstruction efficency of 60%. Moreover, we require two tau-tagged jets with $p_T > 20$ GeV for event reconstruction and reject events with b-tagged jets. Furthermore, we improve the quality of the events with a cut on the track impact parameter at $d_0 \geq 50$ μm.
From our signal simulation we find that for the chosen benchmark point the interference between the H_i is small and increases the total cross section only by about 5%. More specifically, the interference between H_2 and H_3 is small because it is suppressed by the small H_3 total cross section $\sigma_{H_3\tau\tau} \sim 1.5 \times 10^{-5}$ pb, compared to the significantly larger total cross section $\sigma_{H_2\tau\tau} \sim 0.3$ pb. Consequently, for our analysis we solely focus on H_2

Background	$\sigma_{(\textbf{HL-LHC})}$ **[pb]**
$Z \to \tau^-\tau^+$	1537
QCD jets	$10^8 \times \epsilon^2$
$W + J, W \to \tau\ \nu_\tau$	22
$t\bar{t}$	6
$WW, W \to \tau\ \nu_\tau$	0.9

Table VII.1: Cross sections of the dominant background processes considered in our analysis. The following cuts have been used: $p_T(j) \geq 20$ GeV, $p_T(l) \geq 10$ GeV. The efficiency of QCD jets to be mistagged as tau jets is taken from the CMS paper [502], which gives the fake rate $\epsilon = 5 \times 10^{-3}$.

and study an exclusive sample of the process $H_2 \to \tau^-\tau^+$.

VII.1.2.2 Shape Analysis to Establish CP Violation

As a first step of the analysis we separate signal and background using a Boosted Decision Tree (BDT) by using the *Tool for Multi-Variate Analysis* package (TMVA) [504]. For the BDT we only use the simulated distributions from the process $pp \to H_2 \to \tau^-\tau^+$ neglecting the small contributions from H_1 and H_3. The variables we use are the invariant mass of the reconstructed tau pair, MET and $\Delta R(\tau_{had}, \tau_{had})$, where $\Delta R = \sqrt{(\Delta\eta)^2 + (\Delta\phi)^2}$ with $\Delta\eta$ the pseudorapidity and $\Delta\phi$ the azimuthal angle difference between the two final state pions. The input parameters are ranked by the BDT algorithm according to their ability to separate between signal and background. The ranges of the BDT classifiers are -1 to 1 where events with discriminant value close to 1 are classified as signal, while those near -1 are considered as background-like events. In Figure VII.3 the BDT response for signal (blue) and background (red) is shown in the left panel. In the right panel the optimization

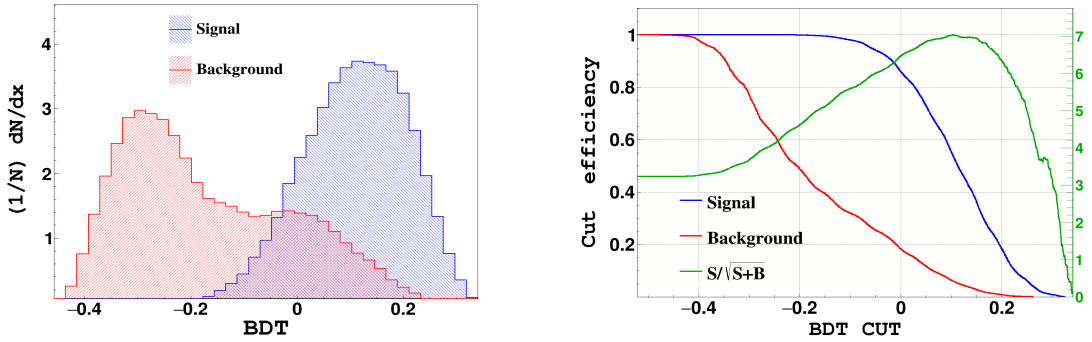

Figure VII.3: Results of BDT for $H_2 \to \tau^-\tau^+$: The **left** panel shows the distribution of the BDT response to signal (blue) and background (red). The **right** panel depicts the cut efficiency that maximizes the BDT cut: For a cut value greater than 0.104 one can get $\frac{S}{\sqrt{S+B}} = 7.04\sigma$ with 2043 signal events and 82212 background events after the BDT cuts. The cut efficiency for the signal is 0.57 and for the background it is 0.00059. This figure was created by a collaborator.

of the signal significance as a function of signal and background cut efficiency is pictured again in blue and red, respectively. In addition the $S/\sqrt{S+B}$ is shown in green. It can be seen that the maximum cut efficiency is reached at BDT classifier ≥ 0.193. There, the signal significance is 7σ (cf. green line), while the signal efficiency and background rejection efficiency are at 0.57 and 0.0059, respectively. For our benchmark point with $\theta_{\tau\tau} \approx 0.68$ 2043 signal and 82212 background events are obtained via the BDT. Both, the p_T cut and the cut on the impact parameter are taken into account in the analysis and for the reported event numbers.
In addition to the above described benchmark point we also simulate distributions for the same input parameters, only changing the CP mixing angle, using $\theta_{\tau\tau} = 0,\ \pi/8,\ 3/8\pi,\ \pi/2$. Those points are only used for comparison and were not checked to satisfy all constraints for corresponding parameter space points.
In the next step we analyze the shape of the acoplanarity angle distribution aiming to infer the CP mixing angle $\theta_{\tau\tau}$ from the simulated data. For all benchmark points we consider the decay $H_2 \to \tau^-\tau^+$ where both taus subsequently decay into a charged pion and a tau-neutrino. We use the tracks inside of the tau jets to reconstruct the above defined acoplanarity angle ϕ^* between the decay planes of the two taus because they carry information on the spin correlation between the taus and the pions. As described above, we boost the four-vectors of the pion candidates' tracks to the ZMF. Then, the acoplanarity angle can be evaluated according to Equation VII.7.
For our analysis of the shape of the ϕ^* distribution between 0 and π the distributions for the samples of 2043 events labelled "2K" and corresponding to the expected event yield of the benchmark point at the HL-LHC were considered. In addition, simulated samples with 2 million events were used as an "infinite statistics" limit labelled "2M". The "2M" samples have a much smaller statistical than systematic uncertainty. The systematic uncertainties arise from uncertainties related to hadronisation, detector simulation and the reconstruction of tau leptons. The distributions of both the small and large versions of the five signal samples are pictured in Figure VII.4. The distributions from the simulation are given with 20 bins each, from $\phi^* = 0$ to $\phi^* = \pi$. Furthermore, in the figure the theory predictions for $1/\Gamma d\Gamma/d\phi^*$ as given in Equation VII.6 are shown as blue lines. Comparing the shape of the distributions obtained from the simulations with the theory prediction in Equation VII.3 (blue lines) it can be seen that the shapes are very similar. Based on this observation we define the reconstructed distributions in the ZMF frame for our numerical fit to the data as

$$\frac{1}{\Gamma}\frac{d\Gamma}{d\phi^*}(\theta_{\tau\tau}) = a(\theta_{\tau\tau}) - b(\theta_{\tau\tau})\cos\phi^* \tag{VII.9}$$

with the fit parameters a and b. Excellent agreement was found between the fitted values of a and b and the theoretical values in Equation VII.3 $a_{\theta_{\tau\tau}} = 1/2\pi$ and $b_{\theta_{\tau\tau}} = \pi/32\left(\cos^2\theta_{\tau\tau} - \sin^2\theta_{\tau\tau}\right)$. Consequently, we can directly compare the reconstructed distributions with the theory predictions in Equation VII.6. As an outcome of our analysis we also found that the background is completely flat with respect to the signal.
Based on the 20 bins of each distribution we create a χ^2 fit for different values of $\theta_{\tau\tau}$ using

$$\chi^2(\theta_{\text{fit}}) = \frac{\left(S_i^{\theta_{\tau\tau}} - \frac{n_S}{\Gamma}\frac{d\Gamma}{d\phi_i^*}(\theta_{\text{fit}})\right)^2}{(\delta S_i)^2 + \delta^2_{\text{syst}}}\,. \tag{VII.10}$$

Here, $\theta_{\tau\tau}$ is the mixing angle of a given benchmark point, θ_{fit} an input of the theoretical distribution, $S_i^{\theta_{\tau\tau}}$ the signal distribution in bin i and $n_S = 2043$ is the total number of

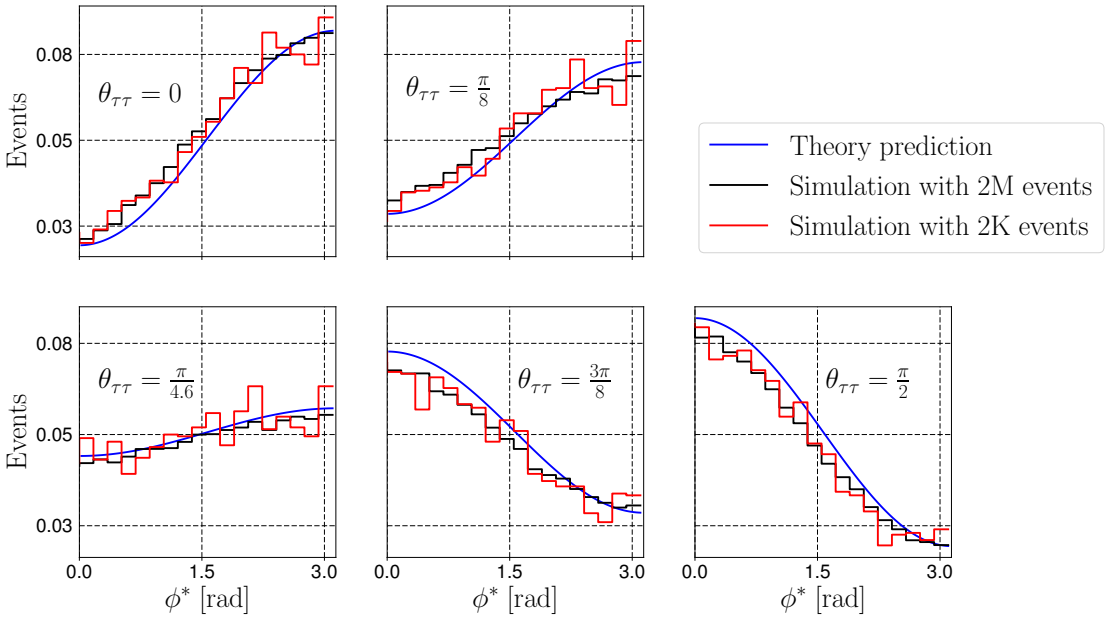

Figure VII.4: Distributions of the τ-acoplanarity angle ϕ^* in the ZMF for $pp \to H_2 \to \tau^-\tau^+$ events. The red lines illustrate the results from the MC simulation with `MadGraph5_aMC@NLO v3.4.0` for 2043 events as expected for the chosen benchmark point at the HL-LHC. The black lines depict the distribution for samples with 2M events corresponding to the infinite statistics limit. Finally, the blue lines depict the theory prediction of the distribution calculated with Equation. VII.3. For all distributions the total number of events is normalised to one. In the **top left** panel the distributions for $\theta_{\tau\tau} = 0$ and in the **top right** panel the ones for $\theta_{\tau\tau} = \frac{\pi}{8}$ are shown. The **lower left** panel depicts the distributions of the original benchmark point with $\theta_{\tau\tau} = \frac{\pi}{4.6}$. Finally, the **lower middle** and **lower right** panels illustrate $\theta_{\tau\tau} = \frac{3\pi}{8}$ and $\theta_{\tau\tau} = \frac{\pi}{2}$. This figure was created by a collaborator and modified for this thesis by the author.

signal events. Furthermore,

$$\delta S_i = \sqrt{S_i}, \qquad \delta_{\text{syst}} = \alpha \frac{N_{\text{bkg}}}{N_{\text{bins}}}, \tag{VII.11}$$

where the total number of background events after the BDT cut is $N_{\text{bkg}} = 82212$ and α is the precision with which the background can be controlled experimentally. As a conservative, realistic and optimistic value we choose $\alpha = 5\%, 1\%$, and 0.5%, respectively. The minimum for θ_{fit} obtained from the χ^2 fits for all benchmark points for both the small and the large samples agrees with high accuracy with the input value $\theta_{\tau\tau}$ of the respective benchmark point. The 90% CL for excluding the pure CP-even or CP-odd hypothesis from the $\Delta\chi^2$ corresponds for 20 bins (which corresponds to the number of observables) minus one fitting parameter (θ_{fit}) to $\Delta\chi^2 = 27.2$. It is found from our analysis that for $\alpha = 5\%$ and 1% no statistically meaningful statement on CP violation is possible at the 90% CL for our benchmark point at the HL-LHC. On the other hand, for $\alpha = 0.5\%$ for our benchmark point at all chosen mixing angles $\theta_{\tau\tau}$ CP violation can be probed. This can be seen in Figure VII.5. Our procedure allows to determine the CP mixing angle $\theta_{\tau\tau} \simeq \pi/4.6 \pm 0.3$ at 90% CL for our original benchmark point with $\theta_{\tau\tau} = 0.68 \approx \pi/4.6$ and the HL-LHC sample with 2043 signal events. Therefore, CP conservation can be excluded at more than 90% CL for this benchmark point.

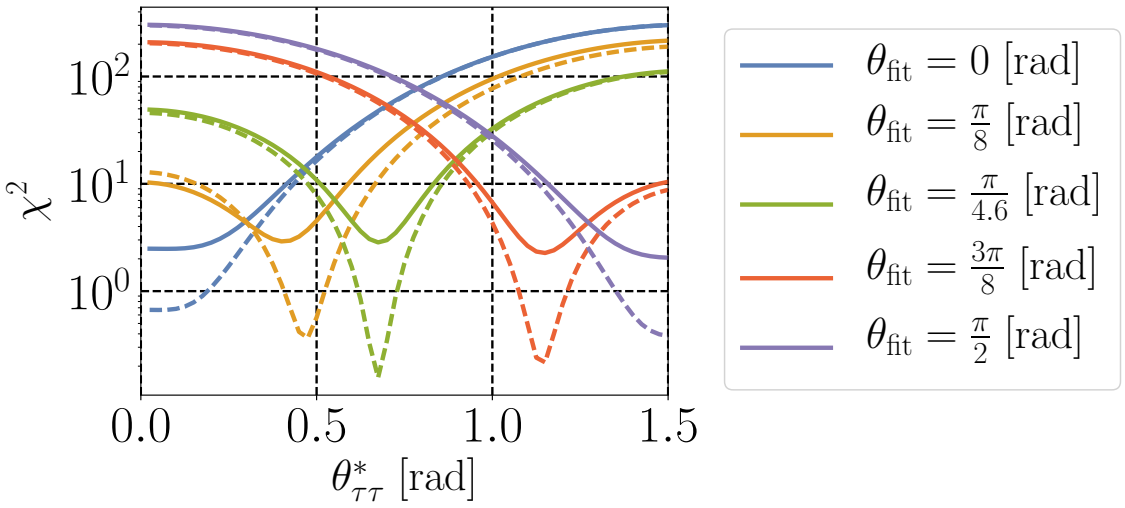

Figure VII.5: Absolute value of the χ^2 for our benchmark point with the five different values of CP-mixing $\theta_{\tau\tau} = 0$ (blue), $\theta_{\tau\tau} = \pi/8$ (yellow), $\theta_{\tau\tau} = \pi/4.6 \approx 0.68$ (green), $\theta_{\tau\tau} = 3\pi/8$ (red) and $\theta_{\tau\tau} = \pi/2$ (lila) with $\delta_{sys} = 0.5\% \cdot (N_{bkg}/N_{bins})$. Solid lines correspond to the small event samples (HL-LHC), while dashed lines show the results for the large event samples ("infinite statistics"). This figure was created by a collaborator and modified for this thesis by the author.

VII.2 Testing CP Properties of Extra Scalars in $H_{2,3} \to ZZ$ Decays

USING the parameter space points from Chapter VI, next, we explore the prospect of testing the CP properties of H_2 and H_3 in decays to Z boson pairs. First, the angular correlation of the final state muons as a test for CP violation is studied. Subsequently, the possibility to infer the CP properties of H_2 and H_3 from the four lepton invariant mass spectrum from $H_i \to ZZ \to 4l$ decays is investigated.

VII.2.1 Angular Correlation in $H_i \to ZZ \to 4\mu$ Decays

The possibility of testing the CP properties of extra scalars via the angular correlation of the final state leptons in $H_i \to ZZ \to 4l$ processes was previously discussed, for example, in [452, 463–469]. Respective searches were performed by both the ATLAS [505] and CMS [506] collaborations. As mentioned above, this strategy is based on the fact that CP-odd fields couple to pairs of Z bosons only at loop level. The respective Feynman diagrams are shown in Figure VII.6. The dominant contribution is from top quarks in

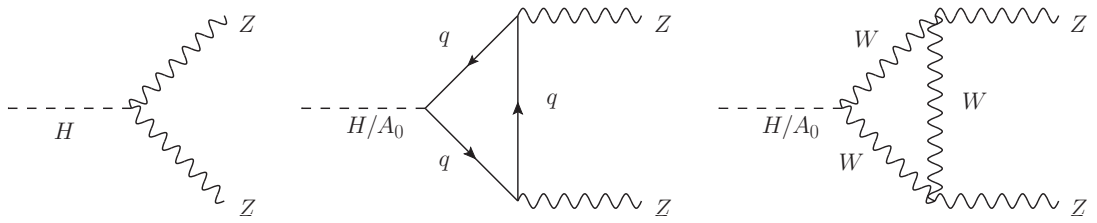

Figure VII.6: Feynman diagrams for Z boson pair production at tree-level from CP-even (H) and on loop-level for CP-even and CP-odd (A_0) scalars.

the loop. A specific angular correlation in the four lepton final state arises from the pseudoscalar couplings of the top quarks to the CP-odd scalar field. To determine if these final state correlations can be observed at future experiments, the branching ratios of extra scalar bosons decaying to Z boson pairs needs to be studied.
First, we investigate the case of a pure CP-even scalar H and a pure CP-odd scalar A_0. The general matrix element for the decay of a Higgs boson to a pair of Z bosons is

$$\begin{aligned} i\mathcal{M} &= i\mathcal{M}^{\text{tree}}_{(H\to ZZ)} + i\mathcal{M}^{\text{one-loop}}_{(H/A_0\to ZZ)} \\ &= C_1\,\epsilon_1^*\epsilon_2^* + C_2\,(p_2\epsilon_1^*)(p_1\epsilon_2^*) + C_3\,\mathcal{E}_{\mu\nu\alpha\beta}p_1^\mu p_2^\nu \epsilon_1^{*\alpha}\epsilon_2^{*\beta} \end{aligned} \tag{VII.12}$$

with $\epsilon_1^*, \epsilon_2^*$ the polarization vectors, p_1 and p_2 the momenta for the outgoing gauge bosons and $\mathcal{E}_{\mu\nu\alpha\beta}$ the total anti-symmetric tensor. The coefficient C_1 gives the strength of the coupling of the CP-even boson to ZZ at tree-level, while C_2 and C_3 are the coupling strength of the CP-even and CP-odd scalars at one-loop level, respectively. The difference in the correlations of the four muon final state of the $H/A_0 \to ZZ \to 4\mu$ process arises from the contraction of the momenta with the anti-symmetric tensor in the last term of Equation VII.12. The coefficients C_i, $i = 1, 2, 3$, are

$$C_1 = \frac{igM_Z\ \sin(\beta-\alpha)}{\cos\theta_W},$$

$$C_2 = \frac{i\ \sin\alpha\ g^3 m_t^2}{18\pi^2 m_H^4 \sin\beta\cos\theta_W^2 m_W}\left(3m_H^2 + m_t^2\ln(\chi_t)^2 + \sqrt{m_H^4 - 4m_H^2 m_t^2}\ln(\chi_t)\right)$$

$$
\begin{aligned}
&+ \frac{i\ \sin(\beta-\alpha)\ g^3 m_W \cos\theta_W^2}{4\pi^2 m_H^4} \\
&\times \left(-30m_H^2 + (m_H^2 - m_W^2)\ln(\chi_W)^2 - 10\sqrt{m_H^4 - 4m_H^2 m_W^2}\ln(\chi_W)\right), \\
C_3 = &\frac{-ig^3 m_t^2}{18\pi^2 m_{A_0}^4 \tan\beta \cos\theta_W^2 m_W} \\
&\times \left(2m_{A_0}^2 + (4\sin\theta_W^4 - 3\sin\theta_W^2)m_{A_0}^2 \ln(\chi_t)^2 - 9\sqrt{m_{A_0}^4 - 4m_{A_0}^2 m_t^2}\ln(\chi_t)\right). \quad \text{(VII.13)}
\end{aligned}
$$

There, α is the mixing angle between the CP-even Higgs bosons, θ_W is the weak mixing angle and

$$\chi_a = \frac{\sqrt{m_\phi^4 - 4m_\phi^2 m_a^2} + 2m_a^2 - m_\phi^2}{2m_a^2} \tag{VII.14}$$

with m_ϕ the masses of the decaying Higgs bosons (H or A_0) and m_a the masses of the loop particles. To calculate all expressions in Equation VII.13 `FeynCalc` [507] and `Package-X` [508] have been used.
With this information the CP properties of a CP-odd scalar A_0 can be found from measurements of the angular distribution of the four leptons in the final state. To do so successfully a large amount of $A_0 \to ZZ \to 4\mu$ is necessary and, therefore, a large branching ratio $\mathrm{Br}(A_0 \to ZZ)$ is needed. However, the dominant decay channels of the CP-odd scalar A_0 are

$$
\begin{aligned}
&A_0 \to \bar{t}t \propto (y_t \cos\beta)^2 \\
&A_0 \to \bar{b}b \propto (y_b \sin\beta)^2 \\
&A_0 \to H^\pm W^\mp \propto (g_2 \sin 2\beta (P_A - P_W))^2 \\
&A_0 \to HZ \propto (\sin(\alpha-\beta)\sqrt{g_1^2 + g_2^2}(P_A - P_Z))^2 . \quad \text{(VII.15)}
\end{aligned}
$$

These are tree-level decays dominating over the loop-level decay $A_0 \to ZZ$. Consequently, the branching ratio $\mathrm{Br}(A_0 \to ZZ)$ is comparatively small in the THDM, maximally $\mathrm{Br}(A_0 \to ZZ) \sim 10^{-3}$ [509]. In addition, the branching ratio of the Z decays $Z \to \mu^-\mu^+ \simeq 10^{-3}$ leads to a further suppression of this process. The total production cross section of A_0 is not larger than $\sigma_{A_0} = 1$ pb, so that the cross section for the process under consideration is at most $\sigma_{A_0 \to ZZ \to 4\mu} \sim 10^{-7}$ pb. Furthermore, cuts applied for background suppression also reduce the signal production cross section and, thus, the number of signal events available for the analysis. It is clear that, even with the total integrated luminosity of HL-LHC of 4 ab^{-1}, the loop-suppressed decay $A_0 \to ZZ \to 4\mu$ is too suppressed to be used for studying the CP properties of the extra scalars in the THDM based on the angular correlation of the final state leptons in $H_i \to ZZ \to 4\mu$ decays. This conclusion, of course, also holds true for the CP-odd component of a scalar that is not purely CP-odd, but an admixture of CP-even and CP-odd states as the coupling of the CP-odd component is suppressed in the same way.

VII.2.2 Higgs Spectrum from $H_i \to ZZ \to 4\mu$

As we concluded in the previous Section VII.2.1 using the angular correlation in the decay $H_i \to ZZ \to 4\mu$ to infer the CP properties is not feasible at HL-LHC. Next, we investigate the prospect of testing the CP properties of the extra Higgs states of the

THDM from the reconstructed invariant mass spectrum of the Higgs decay products. For such a search $pp \to H \to ZZ \to 4\mu$ is a promising channel because it has a very clear SM prediction and, thus, when extra scalars H_i contribute substantially to it, this could lead to their discovery. Another promising channel would be $H_i \to H_1 H_1$ with $i = 2, 3$ [510], which we do not consider here.

Above it was already discussed that purely CP-odd scalars only decay to pairs of Z bosons at loop-level and that this decay is, therefore, too suppressed to be observed at HL-LHC. If, however, an additional scalar state is an admixture of CP-even and CP-odd eigenstates, it will decay to pairs of Z bosons at tree-level and, consequently, might be visible in the invariant mass spectrum of the four-muon final state. In particular, in the THDM with $\eta(\lambda_5) \neq 0$, so that CP violation is present, three neutral Higgs boson resonances would be observed in the four-muon final state. Such an observation is, then, a clear sign for CP violation in the complex THDM. However, it is important to state again that the simultaneous observation of three resonances in the four-muon final state is not a universal signature of CP violation, but it is specific to the THDM model. While seeing three resonances in the four-muon final state is a definite sign for NP, for models featuring three or more neutral CP-even scalar bosons no statements about the CP properties can be made from such an observation.

Nonetheless, since the observation of three scalar resonances in the invariant mass spectrum of the four-muon final state is a certain sign for CP violation in the THDM type-I, we study its prospect at HL-LHC in the following. In Figure VII.7 the total cross section of the process $gg \to H_i \to ZZ$ at HL-LHC with $\sqrt{s} = 14$ TeV is shown for all points of the parameter space scan in Chapter VI satisfying the discussed constraints. The cross section for H_2 is shown in red and the one for H_3 in blue. It can be seen that total production cross sections of up to $\sigma_{gg \to H_i \to ZZ} \sim 10^{-2}$ pb can be found for both H_2 and H_3. We select a benchmark point that satisfies all

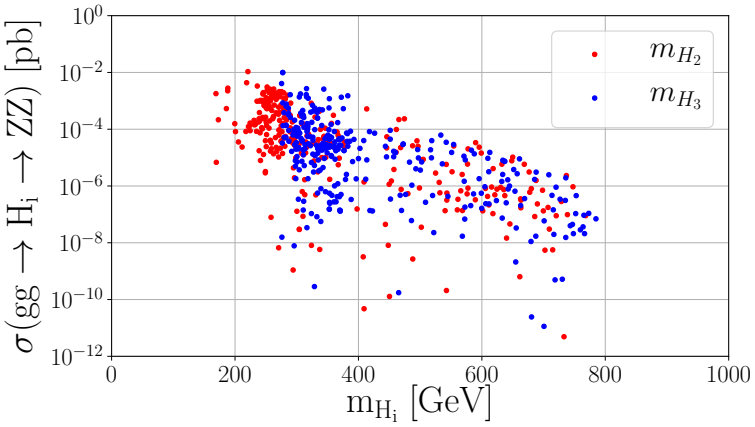

Figure VII.7: Production cross section of Z boson pairs in $gg \to H_i \to ZZ$ processes at HL-LHC with $\sqrt{s} = 14$ TeV as a function of the mass of H_2 (red) and H_3 (blue) for all parameter space points satisfying the discussed constrains. This figure was created in collaboration with a collaborator and modified for this thesis by the author.

discussed constraints and has a reasonable large total production cross section for the process $gg \to H_i \to ZZ$. More specifically, our chosen benchmark point has $m_{H_2} = 260$ GeV and $m_{H_3} = 500$ GeV based on the model parameters $\tan\beta = 4$, $\lambda_1 = 0.172$, $\lambda_2 = 0.0828$, $\lambda_3 = 5.149$, $\lambda_4 = -0.313$, $\mathrm{Re}(\lambda_5) = -4.6431, \eta(\lambda_5) = 0.81$ and $m_{12}^2 = 1.091 \times 10^4$ GeV^2. As before, the parameters m_{11} and m_{22} are fixed from the given

parameters by the tadpole equations in Equations VI.7 and VI.8. The invariant mass spectrum of this benchmark point in the four-muon final state is shown in Figure VII.8. The distribution was created from an inclusive simulation of the signal sample with 20 millions events in `MadGraph5_aMC@NLO v3.4.0` with showering and hadronization done with `Pythia v8.240` and the fast detector simulation carried out with `Delphes v3.5.0`. The observation of such a spectrum in experimental data would be a clear sign for CP violation in the THDM.

In our analysis of the invariant mass spectrum we consider as backgrounds the dominant

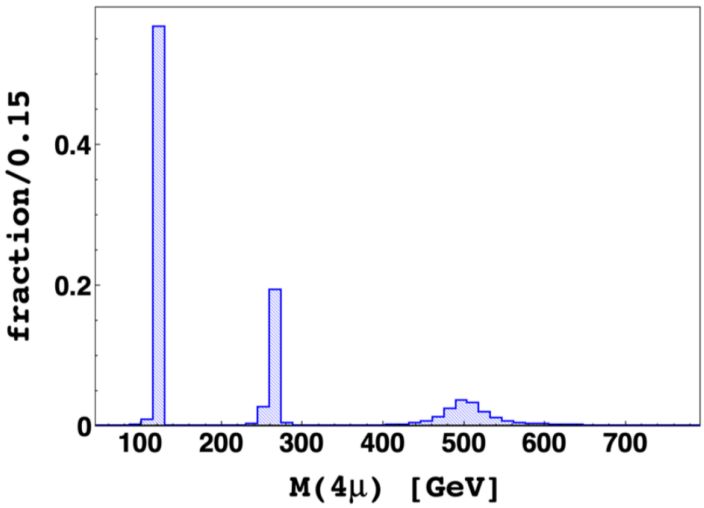

Figure VII.8: Total invariant mass distribution of the four-muon final state from the process $pp \to H_i \to ZZ \to 4\mu$ for the chosen benchmark point in the THDM type-I. This figure was created by a collaborator.

SM production of Z pairs leading to the four-muon final state, as well as WW and WZ production where one final state jet is misidentified as a muon. Further backgrounds are $t\bar{t}$ and $t\bar{t}Z$ production, single top production in association with a W boson (tWb) and triple W boson production. However, the background from three gauge boson production is highly suppressed by the large amount of missing energy in the process. Therefore, we do not consider it here. The production cross section of the remaining background processes are given in Table VII.2 at HL-LHC after cuts on the transverse momentum of the jets and leptons, namely $p_T(j) \geq 20$ GeV, $p_T(l) \geq 10$ GeV). These backgrounds can be reduced by employing the following cuts. The WW and ZZ backgrounds can be reduced sufficiently by requiring a tight isolation criteria for the hard final state muons, so that less jets are misidentified as muons, while backgrounds involving top quarks ($t\bar{t}$, tWb and $t\bar{t}Z$) can be suppressed by a veto on b-jets.

To distinguish signal and background we again use a BDT where we reconstruct all possible kinematic variables. The result of the optimized signal and background classifiers are shown in the left panel of Figure VII.9. As a result of the BDT analysis the invariant mass of the four final state muons is the most important variable for separating signal and background. This is due to the three resonances from the three neutral scalar bosons of the THDM appearing in the invariant mass spectrum, cf. Figure VII.8. The fact that all three resonances are visible is a clear indication for CP violation in the THDM.

In the right panel of Figure VII.9 we also show the signal significance as a function of signal and background cut efficiency. It can be seen that the maximum cut efficiency is at

Backgrounds	$\sigma_{(\textbf{HL-LHC})}$ **[pb]**
$pp \to ZZ \to 4\mu$	0.0065
$pp \to \bar{t}t$, where $t \to$ leptons	6.7
$pp \to \bar{t}tZ$	0.0002
$pp \to WZ \to 3\mu + \nu_\mu$	0.099
$pp \to tWb$, where $t \to$ leptons	7.1

Table VII.2: Dominant background processes for the analysis of the Higgs invariant mass spectrum and their total cross sections. The samples have been produced in `MadGraph5_aMC@NLO v.3.4.0` after cuts on the jet momenta $p_T(j) \geq 20$ GeV and lepton momenta $p_T(l) \geq 10$ GeV.

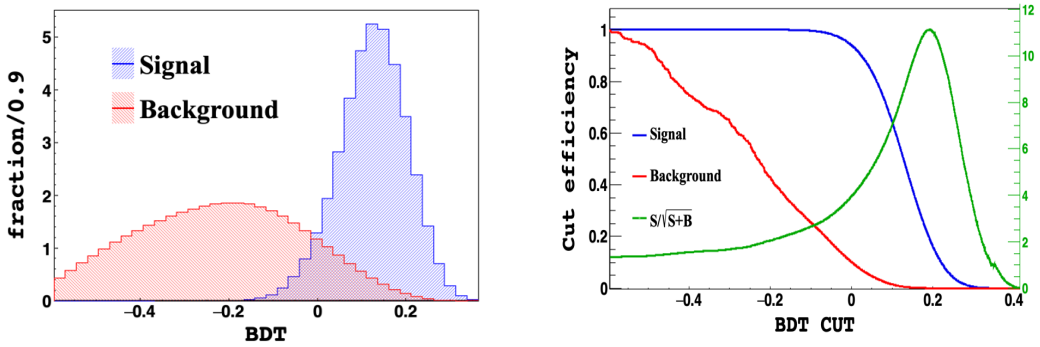

Figure VII.9: **Left:** Distribution of the BDT response to signal (blue) and background (red). **Right:** Cut efficiency that leads to the maximum BDT cut. For a cut value greater than 0.193 one can get $S/\sqrt{S+B} = 11\sigma$ with 939 signal events and 6185 background events. The cut efficiency for the signal is 0.187 and for the background 0.0004. This figure was created by a collaborator.

≥ 0.194 with a signal significance of 11σ and signal efficiency 0.187, while the background rejection efficiency is 0.0004. This demonstrates the excellent discovery potential for our benchmark point in this channel.

VII.3 Fitting the THDM to ATLAS Four-Lepton Data

Now that we have established the $H_i \to ZZ \to 4\mu$ channel as a discovery channel for extra scalar particles and a viable probe of CP violation in the complex THDM we fit a benchmark point to existing four-lepton data from ATLAS. We do this to study how the existence of two additional heavy Higgs bosons could be seen in experimental data. Both, ATLAS and CMS search for NP, for example in final states with four b quarks [511], two tau leptons [512,513], and two photons [514]. In addition, there are searches for exotic resonances for instance in semi-leptonic final states [515–518]. To date no NP has been found in the scalar sector, however, excesses in final states with leptons [517, 519, 520] and di-photons [521–524] indicate there might be additional scalar DOF. For example, excesses around 240 GeV and 700 GeV have been observed at ATLAS in the $ZZ \to 4l$ and $ZZ \to l^+l^-\nu\bar{\nu}$ final states using 2015 and 2016 data [517], though they have not been confirmed with the full data set [516]. The four-lepton channel is of particular interest in the search for NP as it has small and controllable SM backgrounds. Possible excesses in the four-lepton analyses of ATLAS [13, 517] and CMS [525, 526] at high invariant masses are discussed, for example, in [527–530].

Here, we fit a "double peak" from the two heavy neutral scalar bosons of the THDM with CP violation to these excesses above 500 GeV. The data we fit the model to are the measurements of the differential cross-sections in four-lepton events with the 139 fb^{-1} data set of ATLAS [13]. More precisely, we use the four-lepton differential cross section and the invariant mass spectrum (M_{4l}). For both we digitize the observed event rates, their errors and the SM theory prediction. In the analysis we only consider the eight bins of M_{4l} between 500 GeV and 900 GeV. In six out of these eight bins the observed event count exceeds the SM prediction. By subtracting the SM theory prediction from the observed event rates we obtain a sample of excess events. Note that in a given bin the obtained number of "excess events" might be negative if the SM predicts more events than were observed. At the time our analysis was performed from CMS a four-lepton analysis was only available with 35.9 fb^{-1} data [531]. As this is a much smaller data set than the one from the ATLAS analysis, we do not include it in the fit. Nonetheless, the compatibility of our fit with the CMS measurements is discussed below.

In our fit procedure we consider only benchmark points that satisfy all constraints discussed in Section VI.2. For each chosen benchmark point the inclusive process $pp \to H_2, H_3 \to 4l$ was calculated in `MadGraph5_aMC@NLO v3.4.0` including the effective gluon-Higgs vertex found using `SPheno v3.3.8` and QCD corrections [500]. It is worth pointing out that the four-lepton invariant mass spectrum is simulated including the interference between the heavy scalars. Interference with the SM-like Higgs boson H_1 are found to be negligible for the considered masses of H_2 and H_3. Showering and hadronization was performed with `Pythia v8.240`, while the fast detector simulation was done with 500000 events per benchmark point with `Delphes v3.5.0` using the standard ATLAS detector card. Then, the invariant mass spectra can be found from the reconstructed events. Here, we use the same selection criteria as in [13]. These are that the leading and subleading leptons have $p_T > 20$ Gev and $p_T > 10$ GeV, respectively, $m_{ll} > 5$ GeV, $\Delta R > 0.05$ between two leptons and that electrons (muons) fulfill $p_T > 7$ GeV, $|\eta| > 2.47$ ($p_T > 5$ GeV, $|\eta| > 2.7$). We find that the signal efficiency based on these criteria is $\epsilon_{4l} \sim 0.3$ and mostly independent of the scalar mass.

VII.3.1 First Approximation

From the parameter space scan discussed in Chapter VI we select benchmark points with masses $m_{H_2} \sim 500$ GeV and $m_{H_3} \sim 700$ GeV, and with similar magnitudes of the cross section for the $H_i \to ZZ \to 4l$ process. As a first benchmark point we choose the point P_1 with $m_{H_2}^{P_1} = 535$ GeV and $m_{H_3}^{P_1} = 703$ GeV, as well as total four-lepton cross sections $\sigma_{H_2\to 4\ell}^{P_1} = 1.3$ fb and $\sigma_{H_3\to 4\ell}^{P_1} = 0.86$ fb. For P_1 the processes $pp \to H_2 \to 4\ell$ and $pp \to H_3 \to 4\ell$ were simulated exclusively and the corresponding invariant mass spectra ρ_{H_2} and ρ_{H_3} obtained. Thus, in this first step the interference between H_2 and H_3 was not yet taken into account.
For the obtained invariant mass spectra we perform a simple χ^2 analysis by varying the signal peaks of the spectra with the parameters δm_j with $j = 2, 3$, so that the masses are given by $m_{H_j} = m_{H_j}^{P_1} + \delta m_j$. Moreover, the signal strength multipliers s_j which are multiplied with the invariant mass spectra ρ_{H_j} are introduced. With these parameters the χ^2 is constructed as

$$\chi^2_{\text{sig}}(\delta m_2, \delta m_3, s_2, s_3) = \sum_i \frac{(b_{sig,i}(\delta m_2, \delta m_3, s_2, s_3) - b_i)^2}{\delta^2_{obs,i} + \delta^2_{sys,i}}. \tag{VII.16}$$

In Equation VII.16 i is the bin number, b_i the measured event rate, $\delta_{obs,i} = \sqrt{b_i}$ and $\delta_{syst,i} = 10\%$ corresponds to the uncertainty quoted in the ATLAS analysis. The signal rate for bin i is

$$b_{sig,i}(\delta m_2, \delta m_3, s_2, s_3) = b_{SM,i} + \int_i (s_2 \cdot \rho_{H_2}(E - \delta m_2) + s_3 \cdot \rho_{H_3}(E - \delta m_3))dE\,, \tag{VII.17}$$

where $b_{SM,i}$ is the SM prediction, ρ_{H_j} the signal distributions and the parameters δm_j and s_j are varied to minimize the χ^2. The signal strength as defined in Equation VII.17 distorts the invariant mass spectra. Consequently, it is disconnected from the underlying benchmark point. Nonetheless, the masses and event rates preferred by the fit to the data can be found from the distorted spectra.

VII.3.2 Iterative Analysis

Based on benchmark point P_1 we acquire best-fit values for the masses and the total four-lepton cross section. They are converted from the fiducial cross section by using the signal selection efficiency and the integrated luminosity. These are, then, used as selection criteria for a new benchmark point. In order to find the best possible benchmark point a fine grained parameter space scan around the best fit values was performed with `SPheno v3.3.8`. Again, all parameter space points were checked against the constraints in Section VI.2 and only those satisfying all were kept. From the new set of parameter space points we select a point P_2 with masses m_{H_j} and cross section $\sigma_{H_j\to 4l}$ as close as possible to the best-fit values from P_1. We continue with this procedure iteratively. For each selected point P_n with $n > 1$ we create an inclusive four-lepton invariant mass spectrum $\rho_{incl}^{P_n}$ with two peaks around m_{H_2} and m_{H_3}, including, now, the interference between H_2 and H_3. This spectrum is then separated into $\rho_{H_2}^{P_n}$ and $\rho_{H_3}^{P_n}$ at the minimum between the two peaks. Finally, the parameters δm_j and s_j with $j = 2, 3$ are fitted to the data and the best fit values are used to select a new benchmark point P_{n+1} from the fine grained parameter space scan. Once the iterative analysis converges sufficiently, so that a benchmark point with a spectrum providing a good fit was found, a Bayesian fit of the

parameters δm_j and s_j with $j = 2, 3$ is performed to establish the Bayesian confidence limits on the parameters.
We find that the iterative analysis converges sufficiently after six iterations. The 90% Bayesian confidence interval around the sixth iteration's best-fit parameters are

$$\begin{aligned} 521.1 \text{ GeV} \leq m_{H_2} \leq 562.9 \text{ GeV}, \quad 602.2 \text{ GeV} \leq m_{H_3} \leq 655.9 \text{ GeV}, \\ 0.6 \text{ fb} \leq \sigma_{tot} \leq 1.2 \text{ fb}, \qquad\qquad 0.5 \leq r \leq 2.0\,. \end{aligned} \tag{VII.18}$$

Here, we introduced the total signal strength $\sigma_{tot} = \sigma_{pp\to H_2,H_3\to 4\ell}$ and the relative signal strength $r = b_{sig,2}/b_{sig,3}$, which is the ratio of the quantity defined in Equation VII.17.
The 90% Bayesian confidence intervals are used to perform an even more fine grained scan of the parameter space with `SPheno v3.3.8`. In this scan parameter space points with masses m_{H_2}, m_{H_3}, inclusive signal cross section $\sigma_{pp\to H_2,H_3\to 4\ell}$ and relative signal strength r consistent with the 90% Bayesian confidence intervals above were selected where we approximate the signal strength parameter as $r = \sigma_2/\sigma_3$ with σ_i the exclusive signal strengths for $pp \to H_i \to 4\ell$. It is important to note that we continue to consider only parameter space points that satisfy the bounds from Section VI.2. Consequently, the SM Higgs signal strength constraint is still used as an input parameter to our parameter space scan to ensure compatibility with observations. We obtain $\sim$ 10000 allowed parameter space points from the scan after applying all constraints. In these we find a benchmark point P_7 with $m_{H_2}^{P_7} = 544$ GeV and $m_{H_3}^{P_7} = 629$ GeV based on the model parameters $\tan\beta = 21$, $\eta = 0.663$, $\lambda_1 = 0.73$, $\lambda_2 = 0.099$, $\lambda_3 = 4.76$, $\lambda_4 = 6.45$ and $\mathrm{Re}(\lambda_5) = 1.63$. The point P_7 has $\sigma_{tot}^{P_7} = 0.77$ fb, $r = 1.17$ fb. In the following, we call P_7 the "best-fit benchmark point" because it provides a very good fit to the spectrum with a $\chi^2 = 5.76$. The SM value for the bins above 500 GeV is $\chi^2_{SM} = 21.0$ (16.9) corresponding to an upward fluctuation with a p-value of 0.007 (0.03) considering statistical errors only (all errors).
In Figure VII.10 we show the contributions of H_2 and H_3 to the four-lepton invariant mass spectrum. There, the striking feature of the spectrum, namely that it covers a wide

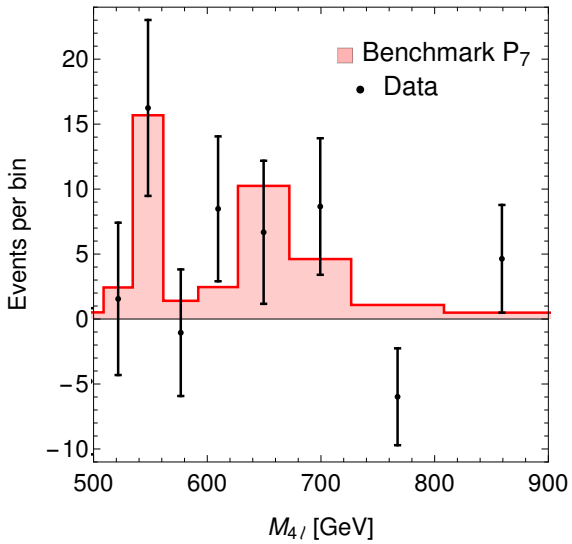

Figure VII.10: Contribution to the four-lepton invariant mass spectrum of H_2 and H_3 from the best-fit benchmark point P_7. The difference between observed and predicted data from the four-lepton invariant mass spectrum in [13] is depicted by the black dots with error bars. This figure was created by a collaborator.

range of M_{4l}, can be seen. This is, on one hand, due to the widths of H_2 and H_3, which

are $\Gamma_{H_2} \sim \mathcal{O}(10)$ GeV and $\Gamma_{H_3} \sim \mathcal{O}(50)$ GeV (cf. Figure VII.11 where the total decay width for H_2 (left) and H_3 (right) is shown from the final fine grained parameter space scan) and, on the other hand, due to the interference between the two heavy scalars. It is

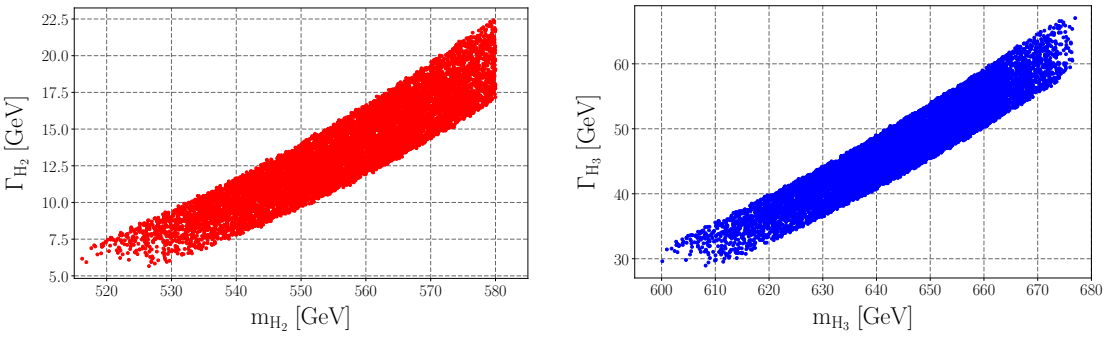

Figure VII.11: Total decay widths for the scalars H_2 (**left**, red) and H_3 (**right**, blue) as a function of the respective scalar mass obtained from the final fine grained parameter space scan. This figure was created by a collaborator and modified for this thesis by the author.

also clear from Figure VII.10 that the best-fit benchmark point P_7 provides an excellent fit to the four-lepton invariant mass data from the ATLAS analysis [13] in the high mass region. Furthermore, similar masses of the two heavy scalars, $m_{H_2} \sim 500$ GeV and $m_{H_3} \sim 700$ GeV, and similar contributions to the inclusive cross section of the four-lepton final state are preferred by the fit. Note that while the here performed fit can explain the observed excess events in the high mass region, the observed data is also in agreement with the SM. Nonetheless, a confirmed observation of such excess events over a wide mass range in the high mass region combined with the facts that, on one hand, the THDM adds one CP-even and one CP-odd scalar to the SM scalar sector and, on the other hand, the CP-odd field does not decay into Z boson pairs at tree-level, implies that the mass eigenstates of the model must be strongly CP-mixed if the THDM is the cause of such excesses. From the allowed parameter space points of the final fine grained scan in the 90% Bayesian confidence interval of P_7 we find, indeed, that η lies in the range $0.63 \leq \eta \leq 0.68$. A complementary probe of the CP properties of heavy Higgs bosons, that might be observed in the four-lepton invariant mass spectrum, is the method discussed in Section VII.1 where the CP properties are inferred from the angular correlation in $H_i \to \tau^+\tau^-$, $i = 2, 3$ decays. It was already mentioned above that the excesses in the high mass region of the invariant mass spectrum of [13] are in agreement with the SM. Therefore, it is important to point out that the here performed fit is not meant to establish statistical evidence for the existence of a THDM signal in the M_{4l} spectrum of the considered ATLAS analysis. The current data set at most can be interpreted as a hint for the THDM. The large mass window considered leads to a large look-elsewhere effect, which reduces the significance. Consequently, higher statistics in the four-lepton data and possibly also in the other channels are required to establish a global significance for the THDM. Furthermore, the scalar H_1, while tested against current SM Higgs measurements with `HiggsBounds v5.3.2` and `HiggsSignals v2.2.3`, is slightly different from the SM Higgs boson and would need to be included into the fit as well. Therefore, while the fit should not be interpreted as providing statistical evidence for the THDM, it shows how the four-lepton invariant mass spectrum can be used to probe CP violation in the THDM and how excesses in M_{4l}, if they become statistical relevant, can be explained by a double peak of two heavy scalar particles.

VII.3.3 CMS Data and Additional H_i Decay Channels

The heavy scalars H_2 and H_3 generally decay not only to pairs of Z bosons, but also to other SM particles. Thus, after finding a benchmark point that is in good agreement with the reported ATLAS invariant four-lepton mass spectrum we investigate the possibilities to make quantitative predictions for H_i $(i = 2, 3)$ decays to $t\bar{t}$, W^+W^-, and $\gamma\gamma$. First, however, we discuss the compatibility of the best-fit benchmark point P_7 with the CMS four-lepton data from [531].

CMS Four-Lepton Spectrum

The CMS four lepton-data from [531] includes about a quarter of the data of the ATLAS analysis, namely 35.9 fb^{-1} pp data, compared to the 139 fb^{-1} data in the ATLAS analysis. To not dilute the statistical significance of our fit we did not include the CMS data in the fit because, when simply including both data sets in the fit, events from the smaller CMS data set would be weighted more strongly than events from the larger ATLAS data set. The best-fit point P_7, however, should still be in agreement with the CMS data set.
To prove the compatibility of P_7 with the CMS data we again consider the mass region from 500 GeV to 900 GeV. In the CMS analysis this region of M_{4l} is divided into 23 bins with non-zero event counts, most of which have only one event with error bars that are larger than one event. Based on P_7 we calculated the THDM theory prediction. Doing this it was found that P_7 is compatible with the CMS data with $\chi^2/dof = 23/23$, mostly driven from the "s_2" part of the signal. On the other hand, in the SM $\chi^2/dof = 10/23$. These results show once more that the CMS data has little statistical weight compared to the ATLAS data.

Di-Top Channel

Next, we investigate the $pp \to H_2, H_3 \to t\bar{t}$ channel. For this process the best-fit benchmark point P_7 has the inclusive cross section $\sigma_{pp\to H_2,H_3\to t\bar{t}} = 28.3$ fb. This is much smaller than the current uncertainty of the recent measurements of the total di-top production cross section $\sigma_{t\bar{t}} = 830 \pm 36(\text{stat}) \pm 14(\text{syst})$ pb by ATLAS [409] and $\sigma_{t\bar{t}} = 791 \pm 25$ pb by CMS [532]. Moreover, we show in Figure VII.12 the projections of the di-top inclusive cross sections for the ~ 10000 allowed parameter space points from the final fine grained scan as a function of m_{H_2} (left) and m_{H_3} (right), as well as the four-lepton inclusive cross section $\sigma_{pp\to H_2,H_3\to 4\ell}$ illustrated by the colour coding. It is obvious that for all parameter space points the inclusive production cross section is smaller than the current uncertainties.

Semi-Leptonic WW Channel

No enhancement in the semi-leptonic final states from WW or ZZ decays was reported in [515]. The best-fit benchmark point P_7 should be in agreement with these measurements. The sum of WW and ZZ cross section for P_7 is

$$\sum_{V=W,Z} \sigma_{pp\to H_2,H_3\to VV} = 330 \text{ fb}\,. \tag{VII.19}$$

Here, V denotes the vector bosons W and Z. This value is comparable with the 2σ upper limits on the production cross section, which are ~ 250 fb and ~ 150 fb for scalar bosons with masses of 560 GeV and 640 GeV, respectively, from [515]. There, as an example for a heavy scalar boson, the radion was used. As for the di-top channel we show in Figure VII.13 the projections of the inclusive W boson pair production cross sections

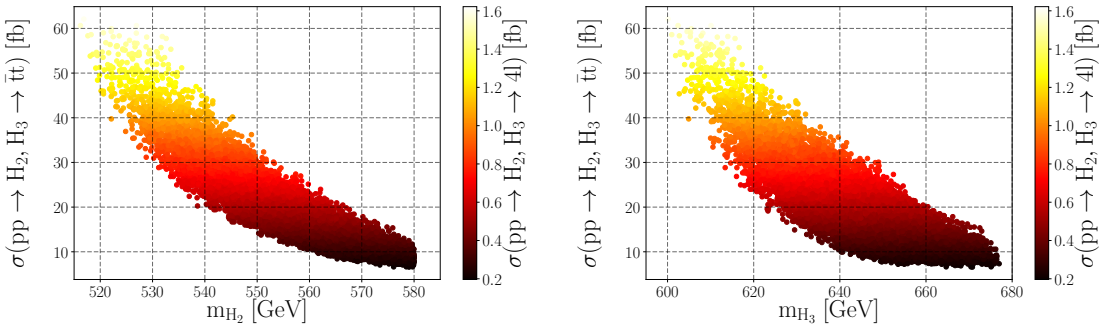

Figure VII.12: Projections of the di-top inclusive cross sections from the final fine grained scan as a function of m_{H_2} (**left**) and m_{H_3} (**right**). The colour coding depicts the four-lepton inclusive cross section $\sigma_{pp\to H_2,H_3\to 4\ell}$. This figure was created by a collaborator and modified for this thesis by the author.

for the allowed parameter space points from the final fine grained scan as a function of m_{H_2} (left) and m_{H_3} (right). Again, the four-lepton inclusive cross section $\sigma_{pp\to H_2,H_3\to 4\ell}$ is illustrated by the colour coding. Illustrated by the dashed blue line is the current 90%

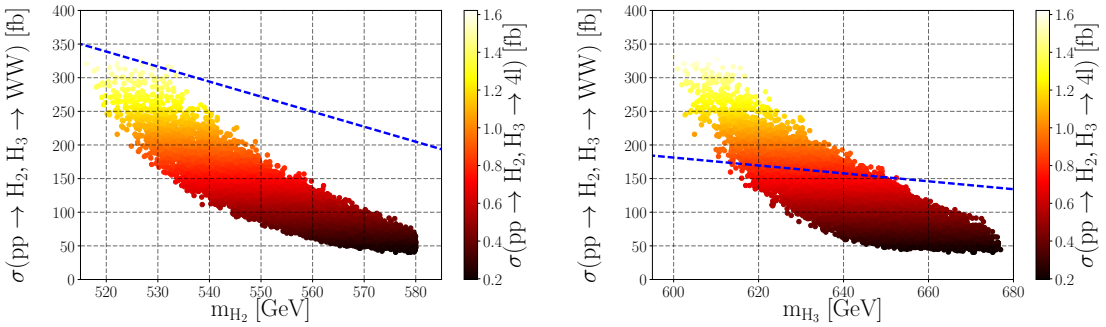

Figure VII.13: Projections of the WW inclusive cross sections, same as Figure VII.12. Here, in addition, the dashed blue lines show the current 90% upper limit on the semi-leptonic cross section from ATLAS [515]. This figure was created by a collaborator and modified for this thesis by the author.

upper limit on the semi-leptonic cross section from ATLAS [515]. Clearly, a large amount of parameter space points is below the current bounds. The cross sections of vector boson quadruplet production processes such as $pp \to H_{j>1} \to 2H_1 + X \to 4V + X$ might be substantially enhanced in the THDM. Consequently, they could become relevant in the future [533].

4b Channel

A small enhancement of the $b\bar{b}b\bar{b} = 4b$ final state for invariant masses above 500 GeV was observed in [511]. This apparent enhancement could be another hint for the THDM process $pp \to H_2, H_3 \to ZZ$. The corresponding cross section is expected to be

$$\sigma_{pp\to H_2,H_3\to 4b} \geq \left(\frac{\mathrm{Br}(Z\to b\bar{b})}{\mathrm{Br}(Z\to \ell^+\ell^-)}\right)^2 \epsilon_b^4 \frac{\epsilon_{4b}}{\epsilon_{4\ell}}\,, \tag{VII.20}$$

where $\epsilon_b \simeq 0.7$ is the b-tagging and $\epsilon_{4b} \sim 0.1$ the selection efficiency. Additional $4b$ events arise from the process $pp \to H_i \to 2H_1 \to 4b$.

From Equation VII.20 16.5 additional signal events are obtained in the $4b$ final state. This result is in agreement with the observed $\sim$ 20 excess events of the background for $M_{4b} \geq 500$ GeV.

Di-Photon Channel

For the di-photon channel the best-fit point P_7 has an inclusive production cross section of $\sigma_{pp\to H_2,H_3\to\gamma\gamma} = 0.8$ fb. Meanwhile, limits on the production cross section are at 1.15 fb and 0.83 fb at 2σ for resonances with masses corresponding to 544 GeV and 629 GeV, respectively, from the ATLAS di-photon search in [514]. Thus, P_7 is in a slight tension at $\sim 1\sigma$ with the ATLAS data. However, we note that in the current data some upward fluctuations of the observed event counts exist at around 540 GeV and 680 GeV, so that P_7 might still be considered as compatible.
The projections of the di-photon inclusive cross sections for the allowed parameter space points from the final fine grained scan can be seen in Figure VII.14 as a function of m_{H_2} (left) and m_{H_3} (right), as well as the four-lepton inclusive cross section $\sigma_{pp\to H_2,H_3\to 4\ell}$, which is depicted by the colour coding. Moreover, the dashed blue line shows the 90% upper limits from ATLAS [514]. Similar to the best-fit benchmark point P_7 a part of

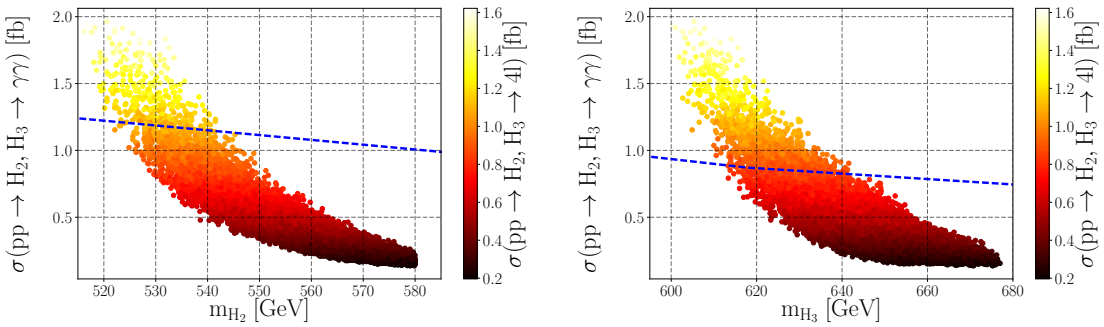

Figure VII.14: Projections of the di-photon inclusive cross sections, same as Figure VII.12. Here, in addition, with the dashed blue lines the current 90% CL upper limit on the di-photon cross section from ATLAS [514] is shown. This figure was created by a collaborator and modified for this thesis by the author.

the parameter space points from the final fine grained scan are in tension with di-photon 90% CL upper limits. This makes it clear that future analyses with more data should be able to test the di-photon channel of P_7 and put a strong constraint on the parameter space of the THDM type-I.

Di-Tau Channel

The last channel we investigate is the di-tau channel. As discussed in Section VII.1, the di-tau channel can be used as a complementary probe of CP violation in the THDM and is, therefore, of special interest. The best-fit benchmark point P_7 has a inclusive cross section of $\sigma_{pp\to H_2,H_3\to\tau^-\tau^+} = 0.015$ fb. Searches for di-tau resonances by ATLAS [512] and CMS [513] found no evidence for additional τ production leading to a current upper bound of $\sigma_{\tau\tau} < \mathcal{O}(100)$ ($\mathcal{O}(1)$) fb for resonances around 500 (1000) GeV. Obviously, P_7 is below this bound. However, from the projections shown in Figure VII.15 of the di-tau inclusive cross sections for the allowed parameter space points from the final fine grained scan as a function of m_{H_2} (left) and m_{H_3} (right) it is also clear that it is unlikely for our

parameter space points to produce an observable signal in this final state due to small production cross sections.

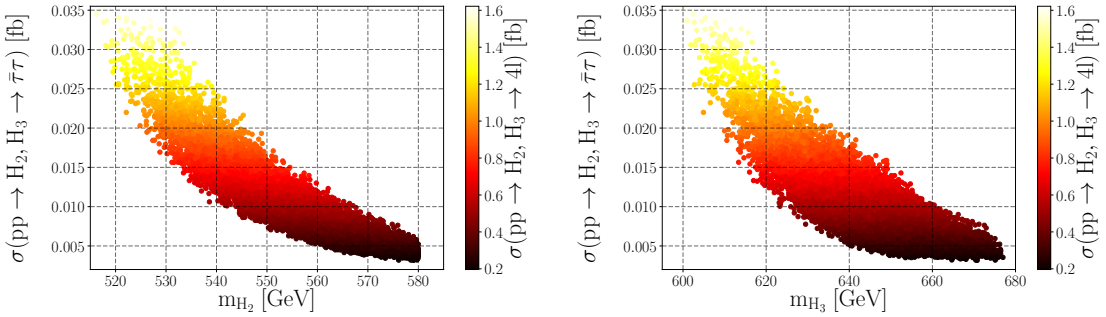

Figure VII.15: Projections of the di-tau inclusive cross sections, same as Figure VII.12. This figure was created by a collaborator and modified for this thesis by the author.

Electric Dipole Moment

As already discussed in Section VI.2 a large phase η, which is preferred from the fit, leads to contributions to the EDM of SM particles, particularly, to the electron EDM. In all parameter space scans only points that satisfy the electron EDM constraint, which is currently at $|d_e| < 1.1 \times 10^{-29}$ ecm from the ACME collaboration [497], were kept. We found that for the final fine grained scan the majority, more precisely $\gtrsim 90\%$ of all points, has $10^{-30} \leq \frac{|d_e|}{\text{ecm}} \leq 1.09 \cdot 10^{-29}$.

VII.4 Conclusion

THE second part of this thesis studied the implications and possible probes of introducing CP violation in the scalar sector. Additional sources of CP violation are necessary since the observed baryon asymmetry of the universe can not be explained by the CP violation in SM processes. Here, we used the THDM where a $SU(2)_L$ doublet with same quantum numbers as the SM Higgs field is added to the SM scalar sector, so that CP mixing between the scalar mass eigenstates is possible, to provide an additional source of CP violation. There are several ways, how CP violation in the scalar sector can be observed at LHC and HL-LHC, including, for example, the simultaneous observation of specific processes, top-quark associated production modes, and angular momentum correlations in decays, such as $H_i \to ZZ \to 4\mu$ or $H_i \to \tau^-\tau^+$, where H_i are extra scalar bosons. Both the simultaneous observation of three resonances in the four-lepton invariant mass spectrum and the angular momentum correlations in di-tau and four-muon final states were investigated in Chapter VII.

First, in Chapter VI the THDM was reviewed and the model parameter space established. As a concrete scenario the THDM type-I was chosen. Then, the mass eigenstates were evaluated numerically and without any assumptions on the parameters. Subsequently, the viable parameter space was determined by a numerical scan over all independent parameters of the Lagrangian of the model. By excluding parameter space points inconsistent with the constraints from theoretical considerations, B-physics data, Higgs property measurements and the upper bound of the electron EDM the available parameter space was found. As a result, scalar bosons with masses with $m_{H_i} \sim \mathcal{O}(100)$ GeV, that can be reached at HL-LHC, are allowed for $\tan\beta \gtrsim 2$ and $-\frac{Pi}{2} \leq \eta(\lambda_5) \leq \frac{Pi}{2}$.
Next, the prospect of establishing CP violating in $H_i \to \tau^-\tau^+$ was investigated for a selected benchmark point using a BDT, where the SM $Z \to \tau^-\tau^+$, $t\bar{t}$, single top and light jet misidentification backgrounds were included. After signal and background discrimination with the BDT the decay $\tau \to \pi\nu$ was used to quantify the detectibility of CP violation via a χ^2 fit of the theoretically predicted distribution to the reconstructed tau decay planes from the simulated data. Here, we found that for our selected benchmark point CP conservation can be excluded at 90% CL where the selected benchmark point has a CP mixing angle $\theta_{\tau\tau} \sim \frac{Pi}{4.6}$ close to the maximum ($\theta_{\tau\tau} = \frac{Pi}{4}$) and we assumed that the SM backgrounds can be controlled with a relative accuracy of 0.5%. Note that, while it is not clear that this accuracy can be reached by future experiments, our analysis only includes the decay $\tau \to \pi\nu$ with a branching ratio of $\mathrm{Br}(\tau \to \pi\nu) \sim 0.11$ [499], so that the inclusion of other decay modes probably leads to less accuracy needed.
Subsequently, we studied the possibility to test CP violation in a similar way in the angular distribution in $H_i \to ZZ \to 4\mu$ decays. This, however, was found to not be feasible since the coupling of the CP-odd component of a scalar that is an admixture of CP-even and CP-odd eigenstates to pairs of Z bosons occurs only on loop-level and is strongly suppressed. As a consequence not enough signal events would be produced at HL-LHC to allow a statistically relevant statement about the CP properties of an extended scalar sector. Instead, the simultaneous observation of three resonances in the four-lepton mass spectrum can be used as a probe of CP violation in the THDM. In the THDM only three neutral scalar exist. For CP vonservation one of them would be purely CP-odd and coupling only on loop-level and, thus, strongly suppressed, to Z boson pairs. Consequently, the observation of three such resonance implies that the scalars are admixtures of CP-even and -odd eigenstates. We remind once more that this statement is not unambiguous as models with larger scalar sectors could produce such a signal without the need for CP

violation. Nonetheless, we showed via a BDT analysis of the $H_i \to ZZ \to 4\mu$ process the excellent discovery prospect for CP violation in the THDM in this channel since the invariant mass spectrum of the four-muon final state is the best classifier to distinguish between signal and background.
Finally, to demonstrate how the three resonances of the THDM would show up in experimental data we fitted a benchmark point to the four-lepton invariant mass spectrum of the analysis in [13]. With an iterative method based on a χ^2-fit we found the best-fit benchmark point P_7, which is in excellent agreement ($\chi^2 = 5.67$ for 8 bins) with the observed four-lepton invariant mass spectrum of [13], which shows slight excesses around 500 GeV and 700 GeV. The best-fit benchmark point P_7 is also in agreement with a similar CMS measurement [531]. A particular interesting feature, here, is the "double peak" from two heavy resonances, that are relatively close in mass. This double peak can explain excesses appearing in a wide mass range. We, furthermore, investigated the prediction of P_7 for other decay channels, such as $\bar{t}t$, VV, $\gamma\gamma$, $4b$ and $\tau^-\tau^+$. We found inclusive cross sections of $\sigma_{t\bar{t}} \sim 28$ fb, $\sigma_{WW} \sim 159$ fb and $\sigma_{\gamma\gamma} \sim 0.8$ fb consistent with current constraint. Similarly, the 16.5 additional events expected in the $4b$ channel are in agreement with an observed excess of ~ 20 events for $M_{4b} \geq 500$ GeV. The inclusive cross section in the di-tau channel is $\sigma_{\tau\tau} = 0.015$ fb, which is also below the current bound. Due to this small cross section it is unlikely that the CP properties of the best-fit point P_7 can be tested in this channel. Lastly, the THDM, especially with large $\eta(\lambda_5)$ as preferred by the fit, contributes to the electron EDM. As P_7 and all parameter space points inside the 90% Bayesian limits of it have electron EDMs close to the experimental limit, measurements of the electron EDM provide an example of a complementary test of the here considered THDM type-I.

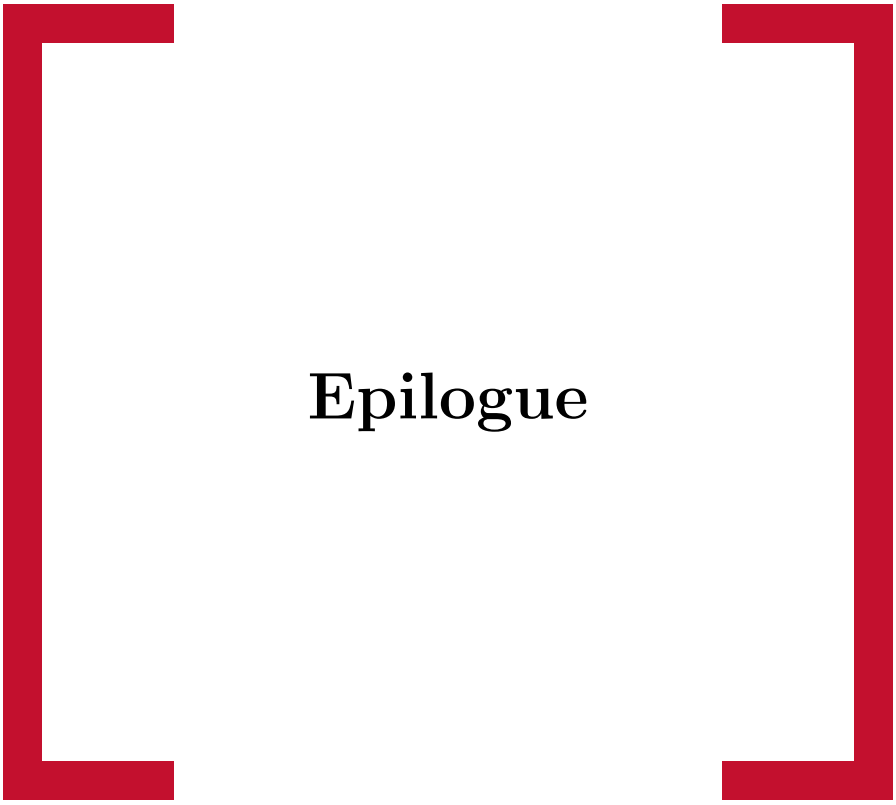
Epilogue

CHAPTER VIII

Conclusion and Outlook

The SM describes all to date known particles and their fundamental interactions. It has successfully predicted several elementary particles, that were later confirmed by experimental discoveries. Examples are the weak gauge bosons, heavy quarks and, most famously, the Higgs boson. The power of the SM also shows itself through the fact that a lot of quantities are measured to be in great agreement with the SM predicted values. Nevertheless, there are several measurements and observations that cannot be explained solely by SM phenomena and, consequently, require BSM physics. In this thesis, two of these open questions, the origin and nature of DM and the source of additional CP violation needed for the baryon asymmetry of the universe, were investigated with NP models. Here, the main focus was on defining the allowed parameter space of viable models and, subsequently, on studying their collider phenomenology, as well as complementary probes of the NP scenarios.

First, in Part I two manifestations of a t-channel dark sector model were studied as examples for DM models with a complex structure. The model in question was reviewed in detail in Chapter III. In a first step, in Chapter IV the parameter space and phenomenology of the model were investigated for the case where the bi-fundamental mediator X_D has hypercharge $Y_X = -\frac{1}{3}$ and connects the dark sector with the visible sector via its coupling to down-type quarks. This model setup had been previously studied, for example, in [10,12, 310]. Based on these studies we investigated for the first time the whole range of dark pion lifetimes including both the limit where dark pions decay promptly and the limit where they are stable on collider scales. In addition, bounds from flavour observables, direct detection experiments, fixed target experiments and cosmology were considered. Here, at first an unflavoured scenario with only the diagonal couplings being non-zero and the dark pions lifetime degenerated, was studied. It was found that in the region where dark pions decay promptly ($c\tau_{\pi_D} \lesssim 1$ mm) mediator masses $m_X \gtrsim 400$ GeV are excluded, while in the intermediate lifetime region (1 mm $\lesssim c\tau_{\pi_D} \lesssim 1$ m) $m_X \lesssim 1.5$ TeV and in the large lifetime region $m_X \lesssim 1.3$ TeV are excluded. Note that only the search used to constrain the large lifetime region uses the full LHC run 2 data set. Furthermore, we showed that these limits are stable when changing the mass of the dark pion in the $\sim 1 - 50$ GeV region. The only non-collider bounds on the parameter space relevant in the unflavoured scenario are direct detection bounds. They are shown together with the collider bounds in the usual DM mass - mediator mass plane. Thereby, it was seen that the coupling to down quarks has a strong influence on which search strategy is the most promising: For large couplings to down quarks the direct detection bound already constrains large parts of the parameter space, smaller couplings relax this bound. Especially in a strange dark sector where the coupling to down quarks is significantly smaller than the one to strange and bottom quarks collider searches are the most likely discovery mode.

The study of two flavoured scenarios, one with $n_D = 2$ and one with $n_D = 3$, showed that the same search strategies as for the unflavoured scenario can be used. Generally, the same shape of constraints was obtained. This allowed us to combine the constraints from the unflavoured scenario with the bounds derived for several flavoured scenarios in [10]. Here, we found that in most of the remaining parameter space a jets plus MET search is the most sensitive and only a small part with large m_{π_D} and κ_0 could be probed with an emerging jets search.
In the next step, in Chapter V we turned to the case of $Y_X = \frac{2}{3}$. Then, the mediator couples to up-type quarks and dark quarks. In contrast to the previous case we did not study the phenomenology of the full model, but explicitly the one of single dark pions. A single dark pion is comparable to an ALP. Specifically, a dark pion in a QCD-like dark sector with a mediator connecting it with up-type quarks can be treated as an ALP with only couplings to up-type quarks, a charming ALP. The parameter space of charming ALPs for four benchmark couplings, two inspired by dark QCD, one by FN models and one anarchic scenario, was studied in detail in Section V.1. Bounds from flavour, astrophysics and cosmology were applied and the discovery prospect at fixed target experiments and dedicated detectors for long-lived particles in the forward direction were investigated. By comparing the benchmark scenarios it became clear that the coupling of ALPs to top quarks influences the allowed parameter space since loops with top quarks are the main contribution to loop-level processes, for example B meson and Kaon decays. Thus, small ALP couplings to top quarks relax the bounds from such processes. For all four benchmark points it was found that large parts of the remaining parameter space below the charm threshold can be probed by fixed target experiments and dedicated detectors for long-lived particles. Nonetheless, there exists parameter space that is so far unprobed in the small mass region and for $m_a \gtrsim 5$ GeV. In the small mass region, that has not yet been studied, charming ALPs could be a DM candidate if considering a freeze-in scenario. The only bound on the $m_a \gtrsim 5$ GeV region arises from $D^0 - \bar{D}^0$ − mixing. This region can be probed, for example, in flavour violating top decays.
A detailed study of this part of the parameter space was performed in Section V.2. A more general setup of charming ALPs was used where the coupling to up-type quarks were not defined from a UV-completion, but are, instead, free parameters. To avoid the constraint from $D^0 - \bar{D}^0$ − mixing $(c_{u_R})_{12} = (c_{u_R})_{21} = 0$ was chosen. After finding that the lifetime of charming ALPs is mainly varied by the diagonal couplings and the branching ratio $\mathrm{Br}(t \to aq)$, $q = u, c$ clearly depends only on the couplings $(c_{u_R})_{3q}$, instead of the diagonal and off-diagonal couplings the lifetime and branching ratio can be used as free parameters. Here, changes in the ALP decay constant f_a can be absorbed in changes of the couplings. We found that parts of both the small and large ALP lifetime regions are excluded due to recasts of single top plus jets and single top plus MET searches. However, the intermediate lifetime region (1 cm $\lesssim c\tau_{ALP} \lesssim$ 1 m) is not accessible with these searches. Thus, we proposed a search strategy for this region based on the energy deposit ratio in the hadronic and electromagnetic calorimeter E_{had}/E_{em}. In addition, the fact that neutral particles such as charming ALPs do not leave tracks was used. We showed that such a search can probe branching ratios $\mathrm{Br}(t \to aq) \gtrsim 10^{-4}$. Moreover, it was found that, if background free searches are possible, branching ratios as low as $\mathrm{Br}(t \to aq) \sim 10^{-7}$ can be probed for both decays in the hadronic calorimeter and in the muon spectrometer. Finally, with more data from HL-LHC without any further adjustments on the search strategy another order of magnitude becomes accessible.
In Part II of this thesis the possibility to introduce a source of CP violation in the scalar sector, which might be part of an explanation for the baryon asymmetry of the universe,

was discussed. Here, after introducing the model and its parameter space in Chapter VI, the focus was on testing the CP properties of the extra scalars in the model at hadron colliders. Three strategies were investigated in Chapter VII: using the correlation of the decay planes in $H_{2,3} \to \tau^-\tau^+$ decays, using the angular correlation in $H_{2,3} \to ZZ \to 4\mu$ decays and the observation of three heavy resonances in the four-muon invariant mass spectrum. While the former two are universal tests of CP violation in decays of heavy scalars, the latter is specific to the THDM as other models can have this signature without the need for CP violation.
For the di-tau final state we showed in Section VII.1 based on a benchmark point with large branching ratios $\mathrm{Br}(H_i \to \tau^-\tau^+)$ $(i = 2, 3)$ with a shape analysis of the acoplanarity angle distribution in the ZMF that for the chosen benchmark point CP conservation can be ruled out at 90% CL at HL-LHC. Here, it was assumed that the background can be controlled with a relative accuracy of 0.5%. Contrariwise, the angular distribution in the 4μ final state cannot be used to test the CP properties of the THDM. The total cross section of the process is suppressed since the CP-odd component of the scalars couples to Z boson pairs only on loop-level. Consequently, not enough events would be available for a statistical analysis of the angular distributions, even at HL-LHC. Nonetheless, the CP properties of the THDM can still be inferred from the four-muon invariant mass spectrum. A BDT analysis showed that, if two heavy scalars that are admixtures of CP-even and CP-odd eigenstates are present in the process $H_i \to ZZ \to 4\mu$ $(i = 1, 2, 3)$, the four-muon invariant mass spectrum is the main discriminator between signal and background. To show how such a signal would show up in experimental data we fitted the THDM to the four-lepton invariant mass spectrum of [13]. With an iterative fitting procedure we obtained a benchmark point that is in great agreement with the experimental data and, generally, also in agreement with measurements of other decay channels and CMS data. Furthermore, this benchmark point has an electron EDM close to the current experimental limit, which makes this an excellent possibility for a complementary probe.
In conclusion, in this thesis two of the open questions in contemporary particle physics, namely the origin and nature of dark DM and the source of additional CP violation needed for the baryon asymmetry of the universe, were addressed. To investigate these questions several ways to search for NP at current and future experiments were discussed ranging from cosmological and astrophysical probes over flavour observables to collider searches. While the discussed search strategies already are promising in the search for NP, further improvements can be made both on the theoretical and the experimental side. Especially, dark sectors with a non-trivial flavour structure can require dedicated search strategies as different dark pion species can have varying lifetimes. The study of scenarios where most or none of them are seen as MET will give further insight into the dark sector phenomenology. Similarly, an investigation of the impact of the mass hierarchies between π_D and ρ_D can lead to new insights. Furthermore, the case of $n_D \geq 4$ provides interesting mechanisms for the production of the DM relic abundance. When focusing on the t-channel model with $Y - X = \frac{2}{3}$ interesting phenomenological consequences such as top decays to emerging jets occur when studying the full model. Finally, the search for CP violation in the scalar sector, for example through the THDM, can be improved by including more decay channels and more data. Overall, with the ongoing theoretical and experimental efforts in the search for BSM physics, including the improvement of simulation tools, the proposal for new signatures and the amount of proposed and planned new experiments, the prospect of unraveling some of nature's mysteries seems bright.

Acknowledgements

All names and personal references were removed from the acknowledgements in the electronic publication of this dissertation.

At the end of this thesis I want to express my gratitude to all, who made this work possible, each in their own way.
First and foremost, I thank my supervisor, who gave me the opportunity to perform this work and who always made sure to create an inspiring and enjoyable work environment. During my PhD studies he provided me with guidance and helped me grow as a scientist. I very much look forward to continued collaboration beyond my PhD.
Next, I want to thank all committee members who took the time to read and evaluate my PhD thesis.
When writing this thesis, I realized how much I learned in the last few years. Therefore, I want to express my gratitude to all those from and with whom I learned. Besides my supervisor, this includes the complete faculty of THEP, but especially my supervisor when I first came to Mainz as an internship student, who introduced me to the world of high energy physics research. I also thank my collaborators from whom I learned a lot during our work together and had many inspiring discussions with. In the same way, I am grateful for my "Basel collaborators" for the collaboration and sharing of knowledge, starting with my master thesis and continuing till today. Moreover, I thank my office mates, the "second floor people" and all past and current members of THEP, who provided a great and friendly enviroment, which I truly appreciated. I enjoyed all the time spend together, be that in discussions of physics and life, over coffee or lunch, at conferences and summer schools, or just in daily life. A special thank you also to all my colleagues, who helped proof read this thesis.
I am also grateful to the administrative staff to always provide their support, also on short notice if necessary.
I acknowledge the support from the graduate school Mainz Physics Academy, both financially and through helpful workshops, retreats and summer schools.
Last but not least I am truly thankful to my family. Without their love and support I wouldn't be where I am today. I know everyone says they have the best and most supportive parents, but in my case it is actually true. Thank you, Mama and Papa, for always being there for me and ensuring I could follow my dreams. Mama, who always encouraged me to do my best and to follow my path no matter what other might think, and Papa, who always provided his stability and discussions about music, recent science and politics, were always my biggest cheerleaders and I couldn't wish for better ones. I'm also very thankful to my siblings, who were there for me every step of my way.

List of Figures

Chapter VI

Chapter VII

List of Tables

List of Abbreviations

4l - $l^-l^+l^-l^+$
4μ - $\mu^-\mu^+\mu^-\mu^+$
ΛCDM - Standard Model of cosmology
ALP - axion-like particle
BDT - Boosted Decision Tree
BBN - BigBang Nucleosynthesis
Br - branching ratio
BSM - beyond the Standard Model
C - charge
CDM - cold dark matter
ChPT - chiral perturbation theory
CKM - Cabibbo-Kobayashi-Maskawa matrix
CL - confidence level
CMB - cosmic microwave background
CP - charge and parity
DGLAP - Dokshitzer-Gribov-Lipatov-Altarelli-Parisi evolution equations
DM - dark matter
DOF - degrees of freedom
EDM - electric dipole moment
EFT - effective field theory
$\mathbf{E_T^{miss}}$ - negative scalar sum of transverse momenta
$\vec{\mathbf{E}}_\mathbf{T}^\mathbf{miss}$ - negative vector sum of transverse momenta
EWSB - electroweak symmetry breaking
FCNC - flavour changing neutral current
FN - Froggatt-Nielsen
HDM - hot dark matter
$\mathbf{H_T}$ - scalar sum of transverse momenta
$\vec{\mathbf{H}}_\mathbf{T}$ - vector sum of transverse momenta
HV - Hidden Valley
IR - infrared
LH - left-handed
$\mathbf{M_{4l}}$ - four-lepton invariant mass spectrum
MACHO - massive compact halo object
MC - Monte Carlo
MET - missing transverse energy (also H_T^{miss} or E_T^{miss})
MOND - modified newtonian dynamics
NP - new physics
OPE - operator product expansion
P - parity
PDF - parton distribution function
pNGB - pseudo-Nambu-Goldstone boson
pp - proton-proton
PQ - Peccei-Quinn
$\mathbf{p_T}$ - transverse momentum
PV - primary vertex
QCD - quantum chromodynamics
QED - quantum electrodynamics
QFT - quantum field theory
RGE - renormalization group equation
RH - right-handed
SM - Standard Model of Particle Physics
THDM - Two-Higgs-Doublet model
TMVA - Tool for Multi-Variate Analysis
UFO - Universal Feynrules Output
UV - ultraviolet
vev - vacuum expectation value
WC - Wilson coefficient
WIMP - weakly interacting massive particles
ZMF - zero-momentum-frame

List of Experiments

Collider Facilities, Experiments and Detectors

- **CERN** - European Organisation for Nuclear Research
  - **LHC** - Large Hadron Collider
    - **ALICE** - A Large Ion Collider Experiment
    - **ATLAS** - A Toroidal LHC ApparatuS
    - **CMS** - Compact Muon Solenoid
    - **FASER** - ForwArd Search ExpeRiment at the LHC
    - **FASERν** - ForwArd Search ExpeRiment neutrino detector
    - **LHCb** - LHC beauty
    - **SND@LHC** - Scattering and Neutrino Detector at the LHC
  - **HL-LHC**
    - **FPF** - Forward Physics Facility, includes
      FASER2 - Second stage of the ForwArd Search ExpeRiment
    - **MATHUSLA** - MAssive Timing Hodoscope for Ultra Stable neutraL pArticles
  - **Sp$\bar{\text{p}}$S** - Super Proton-Antiproton Synchrotron
    - **UA1** Underground Area 1
    - **UA2** Underground Area 2
  - **SPS** - Super Proton Synchrotron
    - **CHARM** - CERN-Hamburg-Amsterdam-Rome-Moscow Collaboration
    - **NA62** - North Area 62 (fixed target experiment)
    - **SHiP** - Search for Hidden Particles (fixed target experiment)
  - **LEP** - Large Electron-Proton Collider
- **Fermilab** - Fermi National Accelerator Laboratory
  - **Tevatron** - proton-antiproton collider

Dark Matter Experiments

Direct Detection

- **CREST-III** - Third stage of Cryogenic Rare Event Search with Superconducting Thermometers
- **DAMA/LIBRA** - DArk MAtter/Large sodium Iodide Bulk for RAre processes
- **DAMIC** - Dark Matter in CCDs (charge-coupled devices)
- **DARWIN** - DARk matter WImp search with liquid xenoN
- **SENSEI** - Sub-Electron-Noise Skipper-CCD Experimental Instrument
- **SuperCDMS** - Super Cryogenic Dark Matter Search
- **XENON1T** - XENON Experiment

Indirect Detection via Gamma-Ray Spectra Surveys

- **Fermi-LAT** - Fermi Large Area Telescope
- **H.E.S.S.** - High Energy Stereoscopic System
- **MAGIC** - Major Atmospheric Gamma Imaging Cherenkov Telescopes

Dedicated Axion/ALP/Light Particle Experiments

- **ABRACADABRA** - A Broadband/Resonant Approach to Cosmic Axion Detection with an Amplifying B-field Ring Apparatus
- **ALPS** - Any Light Particle Search
- **ALPS-II** - Second stage of Any Light Particle Search
- **CAST** - CERN Axion Solar Telescope
- **IAXO** - International Axion Observatory
- **OSQAR** - Optical Search for QED Vacuum Bifringence, Axions and Photon Regeneration

Other

- **ACME** - Advanced Cold Molecule Electron EDM
- **BaBar** - B factory
- **Belle II** - B factory
- **Planck** - Planck satellite
- **WMAP** - Wilkinson Microwave Anisotrope Probe

Bibliography

[1] S. Antusch, O. Fischer, A. Hammad and C. Scherb, *Testing CP Properties of Extra Higgs States at the HL-LHC*, *JHEP* **03** (2021) 200 [2011.10388].

[2] H. Mies, C. Scherb and P. Schwaller, *Collider constraints on dark mediators*, *JHEP* **04** (2021) 049 [2011.13990].

[3] A. Carmona, C. Scherb and P. Schwaller, *Charming ALPs*, *JHEP* **08** (2021) 121 [2101.07803].

[4] S. Antusch, O. Fischer, A. Hammad and C. Scherb, *Explaining excesses in four-leptons at the LHC with a double peak from a CP violating Two Higgs Doublet Model*, 2112.00921.

[5] A. Carmona, F. Elahi, C. Scherb and P. Schwaller, *The ALPs from the Top: Searching for long lived axion-like particles from exotic top decays*, 2202.09371.

[6] L. A. Anchordoqui et al., *The Forward Physics Facility: Sites, Experiments, and Physics Potential*, 2109.10905.

[7] J. L. Feng et al., *The Forward Physics Facility at the High-Luminosity LHC*, 2203.05090.

[8] G. Albouy et al., *Theory, phenomenology, and experimental avenues for dark showers: a Snowmass 2021 report*, 2203.09503.

[9] S. Antusch, O. Fischer, A. Hammad and C. Scherb, *Low scale type II seesaw: Present constraints and prospects for displaced vertex searches*, *JHEP* **02** (2019) 157 [1811.03476].

[10] S. Renner and P. Schwaller, *A flavoured dark sector*, *JHEP* **08** (2018) 052 [1803.08080].

[11] Y. Bai and P. Schwaller, *Scale of dark QCD*, *Phys. Rev. D* **89** (2014) 063522 [1306.4676].

[12] P. Schwaller, D. Stolarski and A. Weiler, *Emerging Jets*, *JHEP* **05** (2015) 059 [1502.05409].

[13] ATLAS collaboration, *Measurements of differential cross-sections in four-lepton events in 13 TeV proton-proton collisions with the ATLAS detector*, *JHEP* **07** (2021) 005 [2103.01918].

[14] D. Binosi and L. Theussl, *JaxoDraw: A Graphical user interface for drawing Feynman diagrams*, *Comput. Phys. Commun.* **161** (2004) 76 [hep-ph/0309015].

[15] D. Binosi, J. Collins, C. Kaufhold and L. Theussl, *JaxoDraw: A Graphical user interface for drawing Feynman diagrams. Version 2.0 release notes*, *Comput. Phys. Commun.* **180** (2009) 1709 [0811.4113].

[16] R. H. L. K. G. D. L. F. M.R.I., *I. nineteenth century clouds over the dynamical theory of heat and light*, *The London, Edinburgh, and Dublin Philosophical Magazine and Journal of Science* **2** (1901) 1.

[17] S. L. Glashow, *Partial Symmetries of Weak Interactions*, *Nucl. Phys.* **22** (1961) 579.

[18] S. Weinberg, *A Model of Leptons*, *Phys. Rev. Lett.* **19** (1967) 1264.

[19] A. Salam, *Weak and Electromagnetic Interactions*, *Conf. Proc. C* **680519** (1968) 367.

[20] G. 't Hooft and M. J. G. Veltman, *Regularization and Renormalization of Gauge Fields*, *Nucl. Phys. B* **44** (1972) 189.

[21] F. Englert and R. Brout, *Broken Symmetry and the Mass of Gauge Vector Mesons*, *Phys. Rev. Lett.* **13** (1964) 321.

[22] P. W. Higgs, *Broken symmetries, massless particles and gauge fields*, *Phys. Lett.* **12** (1964) 132.

[23] P. W. Higgs, *Broken Symmetries and the Masses of Gauge Bosons*, *Phys. Rev. Lett.* **13** (1964) 508.

[24] G. S. Guralnik, C. R. Hagen and T. W. B. Kibble, *Global Conservation Laws and Massless Particles*, *Phys. Rev. Lett.* **13** (1964) 585.

[25] P. W. Higgs, *Spontaneous Symmetry Breakdown without Massless Bosons*, *Phys. Rev.* **145** (1966) 1156.

[26] T. W. B. Kibble, *Symmetry breaking in nonAbelian gauge theories*, *Phys. Rev.* **155** (1967) 1554.

[27] ATLAS collaboration, *Observation of a new particle in the search for the Standard Model Higgs boson with the ATLAS detector at the LHC*, *Phys. Lett. B* **716** (2012) 1 [1207.7214].

[28] CMS collaboration, *Observation of a New Boson at a Mass of 125 GeV with the CMS Experiment at the LHC*, *Phys. Lett. B* **716** (2012) 30 [1207.7235].

[29] C.-N. Yang and R. L. Mills, *Conservation of Isotopic Spin and Isotopic Gauge Invariance*, *Phys. Rev.* **96** (1954) 191.

[30] M. Gell-Mann, *A Schematic Model of Baryons and Mesons*, *Phys. Lett.* **8** (1964) 214.

[31] G. Zweig, *An SU(3) model for strong interaction symmetry and its breaking. Version 1*, .

[32] H. Fritzsch, M. Gell-Mann and H. Leutwyler, *Advantages of the Color Octet Gluon Picture*, *Phys. Lett. B* **47** (1973) 365.

[33] D. J. Gross and F. Wilczek, *Ultraviolet Behavior of Nonabelian Gauge Theories*, *Phys. Rev. Lett.* **30** (1973) 1343.

[34] H. D. Politzer, *Reliable Perturbative Results for Strong Interactions?*, *Phys. Rev. Lett.* **30** (1973) 1346.

[35] F. Braun, *Ueber ein verfahren zur demonstration und zum studium des zeitlichen verlaufes variabler ströme*, *Annalen der Physik* **296** (1897) 552 [https://onlinelibrary.wiley.com/doi/pdf/10.1002/andp.18972960313].

[36] P. E. R. F.R.S., *Lxxix. the scattering of and particles by matter and the structure of the atom*, *The London, Edinburgh, and Dublin Philosophical Magazine and Journal of Science* **21** (1911) 669.

[37] E. O. Lawrence and M. S. Livingston, *The production of high speed light ions without the use of high voltages*, *Phys. Rev.* **40** (1932) 19.

[38] P. J. Bryant, *A Brief history and review of accelerators*, in *CERN Accelerator School: Course on General Accelerator Physics*, pp. 1–16, 1992.

[39] UA1 collaboration, *Experimental Observation of Isolated Large Transverse Energy Electrons with Associated Missing Energy at* $\sqrt{s} = 540$ *GeV*, *Phys. Lett. B* **122** (1983) 103.

[40] UA1 collaboration, *Experimental Observation of Lepton Pairs of Invariant Mass Around 95-GeV/c**2 at the CERN SPS Collider*, *Phys. Lett. B* **126** (1983) 398.

[41] UA2 collaboration, *Evidence for* $Z^0 \to e^+e^-$ *at the CERN* $\bar{p}p$ *Collider*, *Phys. Lett. B* **129** (1983) 130.

[42] UA2 collaboration, *Observation of Single Isolated Electrons of High Transverse Momentum in Events with Missing Transverse Energy at the CERN anti-p p Collider*, *Phys. Lett. B* **122** (1983) 476.

[43] M. E. Peskin and D. V. Schroeder, *An Introduction to quantum field theory*. Addison-Wesley, Reading, USA, 1995.

[44] M. D. Schwartz, *Quantum Field Theory and the Standard Model*. Cambridge University Press, 3, 2014.

[45] S. Weinberg, *The Quantum theory of fields. Vol. 1: Foundations*. Cambridge University Press, 6, 2005.

[46] S. Weinberg, *The quantum theory of fields. Vol. 2: Modern applications*. Cambridge University Press, 8, 2013.

[47] S. Tomonaga, *On a relativistically invariant formulation of the quantum theory of wave fields*, *Prog. Theor. Phys.* **1** (1946) 27.

[48] J. S. Schwinger, *On Quantum electrodynamics and the magnetic moment of the electron*, *Phys. Rev.* **73** (1948) 416.

[49] J. S. Schwinger, *Quantum electrodynamics. I A covariant formulation*, *Phys. Rev.* **74** (1948) 1439.

[50] R. P. Feynman, *The Theory of positrons*, *Phys. Rev.* **76** (1949) 749.

[51] R. P. Feynman, *Space - time approach to quantum electrodynamics*, *Phys. Rev.* **76** (1949) 769.

[52] R. P. Feynman, *Mathematical formulation of the quantum theory of electromagnetic interaction*, *Phys. Rev.* **80** (1950) 440.

[53] N. Cabibbo, *Unitary Symmetry and Leptonic Decays*, *Phys. Rev. Lett.* **10** (1963) 531.

[54] M. Kobayashi and T. Maskawa, *CP Violation in the Renormalizable Theory of Weak Interaction*, *Prog. Theor. Phys.* **49** (1973) 652.

[55] J. R. Ellis, M. Gaillard, D. V. Nanopoulos and C. T. Sachrajda, *Is the Mass of the Higgs Boson About 10-GeV?*, *Phys. Lett. B* **83** (1979) 339.

[56] J. Campbell, J. Huston and F. Krauss, *The Black Book of Quantum Chromodynamics: A Primer for the LHC Era*. Oxford University Press, 12, 2017.

[57] J. Collins, *Foundations of perturbative QCD*, vol. 32. Cambridge University Press, 11, 2013.

[58] T. Muta, *Foundations of Quantum Chromodynamics: An Introduction to Perturbative Methods in Gauge Theories, (3rd ed.)*, vol. 78 of *World scientific Lecture Notes in Physics*. World Scientific, Hackensack, N.J., 3rd ed., 2010.

[59] F. J. Yndurain, *The Theory of Quark and Gluon Interactions*, Theoretical and Mathematical Physics. Springer, Berlin, Germany, 2006, 10.1007/3-540-33210-3.

[60] W. Greiner, S. Schramm and E. Stein, *Quantenchromodynamik*. 2007.

[61] F. Halzen and A. D. Martin, *QUARKS AND LEPTONS: AN INTRODUCTORY COURSE IN MODERN PARTICLE PHYSICS*. 1984.

[62] A. Deur, S. J. Brodsky and G. F. de Teramond, *The QCD Running Coupling*, *Nucl. Phys.* **90** (2016) 1 [1604.08082].

[63] Y. Nambu, *Quasiparticles and Gauge Invariance in the Theory of Superconductivity*, *Phys. Rev.* **117** (1960) 648.

[64] J. Goldstone, *Field theories with "superconductor" solutions*, *Nuovo Cimento* **19** (1960) 154.

[65] TASSO collaboration, *Evidence for Planar Events in e+ e- Annihilation at High-Energies*, *Phys. Lett. B* **86** (1979) 243.

[66] D. P. Barber et al., *Discovery of Three Jet Events and a Test of Quantum Chromodynamics at PETRA Energies*, *Phys. Rev. Lett.* **43** (1979) 830.

[67] PLUTO collaboration, *Evidence for Gluon Bremsstrahlung in e+ e- Annihilations at High-Energies*, *Phys. Lett. B* **86** (1979) 418.

[68] JADE collaboration, *Observation of Planar Three Jet Events in e+ e- Annihilation and Evidence for Gluon Bremsstrahlung*, *Phys. Lett. B* **91** (1980) 142.

[69] E598 collaboration, *Experimental Observation of a Heavy Particle J*, *Phys. Rev. Lett.* **33** (1974) 1404.

[70] SLAC-SP-017 collaboration, *Discovery of a Narrow Resonance in e^+e^- Annihilation*, *Phys. Rev. Lett.* **33** (1974) 1406.

[71] S. W. Herb et al., *Observation of a Dimuon Resonance at 9.5-GeV in 400-GeV Proton-Nucleus Collisions*, *Phys. Rev. Lett.* **39** (1977) 252.

[72] D0 collaboration, *Observation of the top quark*, *Phys. Rev. Lett.* **74** (1995) 2632 [hep-ex/9503003].

[73] CDF collaboration, *Evidence for top quark production in $\bar{p}p$ collisions at $\sqrt{s} = 1.8$ TeV*, *Phys. Rev. D* **50** (1994) 2966.

[74] D. Hanneke, S. F. Hoogerheide and G. Gabrielse, *Cavity Control of a Single-Electron Quantum Cyclotron: Measuring the Electron Magnetic Moment*, *Phys. Rev. A* **83** (2011) 052122 [1009.4831].

[75] B. C. Odom, D. Hanneke, B. D'Urso and G. Gabrielse, *New Measurement of the Electron Magnetic Moment Using a One-Electron Quantum Cyclotron*, *Phys. Rev. Lett.* **97** (2006) 030801.

[76] SNO collaboration, *Direct evidence for neutrino flavor transformation from neutral current interactions in the Sudbury Neutrino Observatory*, *Phys. Rev. Lett.* **89** (2002) 011301 [nucl-ex/0204008].

[77] Super-Kamiokande collaboration, *Evidence for oscillation of atmospheric neutrinos*, *Phys. Rev. Lett.* **81** (1998) 1562 [hep-ex/9807003].

[78] K. G. Wilson, *The Renormalization Group and Strong Interactions*, *Phys. Rev. D* **3** (1971) 1818.

[79] G. F. Giudice, *Naturalness after LHC8*, *PoS* **EPS-HEP2013** (2013) 163 [1307.7879].

[80] G. Bertone, D. Hooper and J. Silk, *Particle dark matter: Evidence, candidates and constraints*, *Phys. Rept.* **405** (2005) 279 [hep-ph/0404175].

[81] G. Bertone and D. Hooper, *History of dark matter*, *Rev. Mod. Phys.* **90** (2018) 045002 [1605.04909].

[82] R. J. Crewther, P. Di Vecchia, G. Veneziano and E. Witten, *Chiral Estimate of the Electric Dipole Moment of the Neutron in Quantum Chromodynamics*, *Phys. Lett. B* **88** (1979) 123.

[83] C. Abel et al., *Measurement of the Permanent Electric Dipole Moment of the Neutron*, *Phys. Rev. Lett.* **124** (2020) 081803 [2001.11966].

[84] Planck collaboration, *Planck 2018 results. VI. Cosmological parameters*, *Astron. Astrophys.* **641** (2020) A6 [1807.06209].

[85] A. D. Sakharov, *Violation of CP Invariance, C asymmetry, and baryon asymmetry of the universe*, *Pisma Zh. Eksp. Teor. Fiz.* **5** (1967) 32.

[86] V. A. Kuzmin, V. A. Rubakov and M. E. Shaposhnikov, *On the Anomalous Electroweak Baryon Number Nonconservation in the Early Universe*, *Phys. Lett. B* **155** (1985) 36.

[87] A. G. Cohen, D. B. Kaplan and A. E. Nelson, *Baryogenesis at the weak phase transition*, *Nucl. Phys. B* **349** (1991) 727.

[88] N. Turok and J. Zadrozny, *Dynamical generation of baryons at the electroweak transition*, *Phys. Rev. Lett.* **65** (1990) 2331.

[89] HFLAV collaboration, *Averages of b-hadron, c-hadron, and τ-lepton properties as of 2018*, *Eur. Phys. J. C* **81** (2021) 226 [1909.12524].

[90] ATLAS, CMS, LHCb collaboration, *Flavour anomalies: a review*, *J. Phys. Conf. Ser.* **1137** (2019) 012025 [1807.11373].

[91] Muon g-2 collaboration, *Measurement of the Positive Muon Anomalous Magnetic Moment to 0.46 ppm*, *Phys. Rev. Lett.* **126** (2021) 141801 [2104.03281].

[92] F. Zwicky, *Die Rotverschiebung von extragalaktischen Nebeln*, *Helv. Phys. Acta* **6** (1933) 110.

[93] V. C. Rubin and W. K. Ford, Jr., *Rotation of the Andromeda Nebula from a Spectroscopic Survey of Emission Regions*, *Astrophys. J.* **159** (1970) 379.

[94] M. Markevitch, A. H. Gonzalez, D. Clowe, A. Vikhlinin, L. David, W. Forman et al., *Direct constraints on the dark matter self-interaction cross-section from the merging galaxy cluster 1E0657-56*, *Astrophys. J.* **606** (2004) 819 [astro-ph/0309303].

[95] D. Clowe, A. Gonzalez and M. Markevitch, *Weak lensing mass reconstruction of the interacting cluster 1E0657-558: Direct evidence for the existence of dark matter*, *Astrophys. J.* **604** (2004) 596 [astro-ph/0312273].

[96] S. M. Faber and R. E. Jackson, *Velocity dispersions and mass to light ratios for elliptical galaxies*, *Astrophys. J.* **204** (1976) 668.

[97] E. Corbelli and P. Salucci, *The Extended Rotation Curve and the Dark Matter Halo of M33*, *Mon. Not. Roy. Astron. Soc.* **311** (2000) 441 [astro-ph/9909252].

[98] S. W. Allen, A. E. Evrard and A. B. Mantz, *Cosmological Parameters from Observations of Galaxy Clusters*, *Ann. Rev. Astron. Astrophys.* **49** (2011) 409 [1103.4829].

[99] X.-P. Wu, T. Chiueh, L.-Z. Fang and Y.-J. Xue, *A comparison of different cluster mass estimates: consistency or discrepancy ?*, *Mon. Not. Roy. Astron. Soc.* **301** (1998) 861 [astro-ph/9808179].

[100] P. Natarajan et al., *Mapping substructure in the HST Frontier Fields cluster lenses and in cosmological simulations*, *Mon. Not. Roy. Astron. Soc.* **468** (2017) 1962 [1702.04348].

[101] A. Refregier, *Weak gravitational lensing by large scale structure*, *Ann. Rev. Astron. Astrophys.* **41** (2003) 645 [astro-ph/0307212].

[102] WMAP collaboration, *Five-Year Wilkinson Microwave Anisotropy Probe (WMAP) Observations: Cosmological Interpretation*, *Astrophys. J. Suppl.* **180** (2009) 330 [0803.0547].

[103] WMAP collaboration, *Nine-Year Wilkinson Microwave Anisotropy Probe (WMAP) Observations: Cosmological Parameter Results*, *Astrophys. J. Suppl.* **208** (2013) 19 [1212.5226].

[104] C. J. Copi, D. N. Schramm and M. S. Turner, *Big bang nucleosynthesis and the baryon density of the universe*, *Science* **267** (1995) 192 [astro-ph/9407006].

[105] LIGO Scientific, Virgo, Fermi-GBM, INTEGRAL collaboration, *Gravitational Waves and Gamma-rays from a Binary Neutron Star Merger: GW170817 and GRB 170817A*, *Astrophys. J. Lett.* **848** (2017) L13 [1710.05834].

[106] A. Y. Ignatiev, V. A. Kuzmin and M. E. Shaposhnikov, *Is the Electric Charge Conserved?*, *Phys. Lett. B* **84** (1979) 315.

[107] S. D. McDermott, H.-B. Yu and K. M. Zurek, *Turning off the Lights: How Dark is Dark Matter?*, *Phys. Rev. D* **83** (2011) 063509 [1011.2907].

[108] A. Davidson and K. C. Wali, *Minimal Flavor Unification via Multigenerational Peccei-Quinn Symmetry*, *Phys. Rev. Lett.* **48** (1982) 11.

[109] B. Audren, J. Lesgourgues, G. Mangano, P. D. Serpico and T. Tram, *Strongest model-independent bound on the lifetime of Dark Matter*, *JCAP* **12** (2014) 028 [1407.2418].

[110] S. W. Randall, M. Markevitch, D. Clowe, A. H. Gonzalez and M. Bradac, *Constraints on the Self-Interaction Cross-Section of Dark Matter from Numerical Simulations of the Merging Galaxy Cluster 1E 0657-56*, *Astrophys. J.* **679** (2008) 1173 [0704.0261].

[111] T. D. Brandt, *Constraints on MACHO Dark Matter from Compact Stellar Systems in Ultra-Faint Dwarf Galaxies*, *Astrophys. J. Lett.* **824** (2016) L31 [1605.03665].

[112] L. Randall, J. Scholtz and J. Unwin, *Cores in Dwarf Galaxies from Fermi Repulsion*, *Mon. Not. Roy. Astron. Soc.* **467** (2017) 1515 [1611.04590].

[113] M. Nori, R. Murgia, V. Iršič, M. Baldi and M. Viel, *Lyman α forest and non-linear structure characterization in Fuzzy Dark Matter cosmologies*, *Mon. Not. Roy. Astron. Soc.* **482** (2019) 3227 [1809.09619].

[114] V. Iršič et al., *New Constraints on the free-streaming of warm dark matter from intermediate and small scale Lyman-α forest data*, *Phys. Rev. D* **96** (2017) 023522 [1702.01764].

[115] H. Baer, K.-Y. Choi, J. E. Kim and L. Roszkowski, *Dark matter production in the early Universe: beyond the thermal WIMP paradigm*, *Phys. Rept.* **555** (2015) 1 [1407.0017].

[116] H.-Y. Chiu, *Symmetry between particle and anti-particle populations in the universe*, *Phys. Rev. Lett.* **17** (1966) 712.

[117] Y. b. Zeldovich, *Survey of Modern Cosmology*, *Adv. Astron. Astrophys.* **3** (1965) 241.

[118] L. J. Hall, K. Jedamzik, J. March-Russell and S. M. West, *Freeze-In Production of FIMP Dark Matter*, *JHEP* **03** (2010) 080 [0911.1120].

[119] J. McDonald, *Thermally generated gauge singlet scalars as selfinteracting dark matter*, *Phys. Rev. Lett.* **88** (2002) 091304 [hep-ph/0106249].

[120] G. Jungman, M. Kamionkowski and K. Griest, *Supersymmetric dark matter*, *Phys. Rept.* **267** (1996) 195 [hep-ph/9506380].

[121] P. Gondolo and G. Gelmini, *Cosmic abundances of stable particles: Improved analysis*, *Nucl. Phys. B* **360** (1991) 145.

[122] E. W. Kolb and M. S. Turner, *The Early Universe*, vol. 69. 1990, 10.1201/9780429492860.

[123] M. W. Goodman and E. Witten, *Detectability of Certain Dark Matter Candidates*, *Phys. Rev. D* **31** (1985) 3059.

[124] MAGIC, Fermi-LAT collaboration, *Limits to Dark Matter Annihilation Cross-Section from a Combined Analysis of MAGIC and Fermi-LAT Observations of Dwarf Satellite Galaxies*, *JCAP* **02** (2016) 039 [1601.06590].

[125] S. Hoof, A. Geringer-Sameth and R. Trotta, *A Global Analysis of Dark Matter Signals from 27 Dwarf Spheroidal Galaxies using 11 Years of Fermi-LAT Observations*, *JCAP* **02** (2020) 012 [1812.06986].

[126] Fermi-LAT collaboration, *Updated search for spectral lines from Galactic dark matter interactions with pass 8 data from the Fermi Large Area Telescope*, *Phys. Rev. D* **91** (2015) 122002 [1506.00013].

[127] H.E.S.S. collaboration, *Search for dark matter annihilations towards the inner Galactic halo from 10 years of observations with H.E.S.S*, *Phys. Rev. Lett.* **117** (2016) 111301 [1607.08142].

[128] XENON collaboration, *Dark Matter Search Results from a One Ton-Year Exposure of XENON1T*, *Phys. Rev. Lett.* **121** (2018) 111302 [1805.12562].

[129] CRESST collaboration, *First results from the CRESST-III low-mass dark matter program*, *Phys. Rev. D* **100** (2019) 102002 [1904.00498].

[130] SuperCDMS collaboration, *First Dark Matter Constraints from a SuperCDMS Single-Charge Sensitive Detector*, *Phys. Rev. Lett.* **121** (2018) 051301 [1804.10697].

[131] DAMIC collaboration, *Constraints on Light Dark Matter Particles Interacting with Electrons from DAMIC at SNOLAB*, *Phys. Rev. Lett.* **123** (2019) 181802 [1907.12628].

[132] SENSEI collaboration, *SENSEI: Direct-Detection Constraints on Sub-GeV Dark Matter from a Shallow Underground Run Using a Prototype Skipper-CCD*, *Phys. Rev. Lett.* **122** (2019) 161801 [1901.10478].

[133] Fermi-LAT collaboration, *Fermi-LAT Observations of High-Energy γ-Ray Emission Toward the Galactic Center*, *Astrophys. J.* **819** (2016) 44 [1511.02938].

[134] R. K. Leane and T. R. Slatyer, *Revival of the Dark Matter Hypothesis for the Galactic Center Gamma-Ray Excess*, *Phys. Rev. Lett.* **123** (2019) 241101 [1904.08430].

[135] AMS collaboration, *Antiproton Flux, Antiproton-to-Proton Flux Ratio, and Properties of Elementary Particle Fluxes in Primary Cosmic Rays Measured with the Alpha Magnetic Spectrometer on the International Space Station*, *Phys. Rev. Lett.* **117** (2016) 091103.

[136] I. Cholis, T. Linden and D. Hooper, *A Robust Excess in the Cosmic-Ray Antiproton Spectrum: Implications for Annihilating Dark Matter*, *Phys. Rev. D* **99** (2019) 103026 [1903.02549].

[137] R. Bernabei et al., *First model independent results from DAMA/LIBRA-phase2*, *Nucl. Phys. Atom. Energy* **19** (2018) 307 [1805.10486].

[138] G. Adhikari et al., *An experiment to search for dark-matter interactions using sodium iodide detectors*, *Nature* **564** (2018) 83 [1906.01791].

[139] K. Petraki and R. R. Volkas, *Review of asymmetric dark matter*, *Int. J. Mod. Phys. A* **28** (2013) 1330028 [1305.4939].

[140] K. M. Zurek, *Asymmetric Dark Matter: Theories, Signatures, and Constraints*, *Phys. Rept.* **537** (2014) 91 [1308.0338].

[141] B. Holdom, *Two u(1)'s and charge shifts*, *Physics Letters B* **166** (1986) 196.

[142] B. Patt and F. Wilczek, *Higgs-field portal into hidden sectors*, hep-ph/0605188.

[143] A. Falkowski, J. Juknevich and J. Shelton, *Dark Matter Through the Neutrino Portal*, 0908.1790.

[144] M. J. Strassler and K. M. Zurek, *Echoes of a hidden valley at hadron colliders*, *Phys. Lett. B* **651** (2007) 374 [hep-ph/0604261].

[145] M. T. Frandsen, F. Kahlhoefer, A. Preston, S. Sarkar and K. Schmidt-Hoberg, *LHC and Tevatron Bounds on the Dark Matter Direct Detection Cross-Section for Vector Mediators*, *JHEP* **07** (2012) 123 [1204.3839].

[146] O. Buchmueller, M. J. Dolan and C. McCabe, *Beyond Effective Field Theory for Dark Matter Searches at the LHC*, *JHEP* **01** (2014) 025 [1308.6799].

[147] H. Dreiner, D. Schmeier and J. Tattersall, *Contact Interactions Probe Effective Dark Matter Models at the LHC*, *EPL* **102** (2013) 51001 [1303.3348].

[148] O. Buchmueller, M. J. Dolan, S. A. Malik and C. McCabe, *Characterising dark matter searches at colliders and direct detection experiments: Vector mediators*, *JHEP* **01** (2015) 037 [1407.8257].

[149] K. Hamaguchi, S. P. Liew, T. Moroi and Y. Yamamoto, *Isospin-Violating Dark Matter with Colored Mediators*, *JHEP* **05** (2014) 086 [1403.0324].

[150] P. Harris, V. V. Khoze, M. Spannowsky and C. Williams, *Constraining Dark Sectors at Colliders: Beyond the Effective Theory Approach*, *Phys. Rev. D* **91** (2015) 055009 [1411.0535].

[151] T. Jacques and K. Nordström, *Mapping monojet constraints onto Simplified Dark Matter Models*, *JHEP* **06** (2015) 142 [1502.05721].

[152] S. P. Liew, M. Papucci, A. Vichi and K. M. Zurek, *Mono-X Versus Direct Searches: Simplified Models for Dark Matter at the LHC*, *JHEP* **06** (2017) 082 [1612.00219].

[153] C. Englert, M. McCullough and M. Spannowsky, *S-Channel Dark Matter Simplified Models and Unitarity*, *Phys. Dark Univ.* **14** (2016) 48 [1604.07975].

[154] E. Bernreuther, F. Kahlhoefer, M. Krämer and P. Tunney, *Strongly interacting dark sectors in the early Universe and at the LHC through a simplified portal*, *JHEP* **01** (2020) 162 [1907.04346].

[155] H.-C. Cheng, L. Li, E. Salvioni and C. B. Verhaaren, *Light Hidden Mesons through the Z Portal*, *JHEP* **11** (2019) 031 [1906.02198].

[156] T. Cohen, M. Lisanti, H. K. Lou and S. Mishra-Sharma, *LHC Searches for Dark Sector Showers*, *JHEP* **11** (2017) 196 [1707.05326].

[157] H. An, L.-T. Wang and H. Zhang, *Dark matter with t-channel mediator: a simple step beyond contact interaction*, *Phys. Rev. D* **89** (2014) 115014 [1308.0592].

[158] S. Chang, R. Edezhath, J. Hutchinson and M. Luty, *Effective WIMPs*, *Phys. Rev. D* **89** (2014) 015011 [1307.8120].

[159] Y. Bai and J. Berger, *Fermion Portal Dark Matter*, *JHEP* **11** (2013) 171 [1308.0612].

[160] M. Papucci, A. Vichi and K. M. Zurek, *Monojet versus the rest of the world I: t-channel models*, *JHEP* **11** (2014) 024 [1402.2285].

[161] M. Garny, A. Ibarra, S. Rydbeck and S. Vogl, *Majorana Dark Matter with a Coloured Mediator: Collider vs Direct and Indirect Searches*, *JHEP* **06** (2014) 169 [1403.4634].

[162] Y. Hochberg, E. Kuflik, T. Volansky and J. G. Wacker, *Mechanism for Thermal Relic Dark Matter of Strongly Interacting Massive Particles*, *Phys. Rev. Lett.* **113** (2014) 171301 [1402.5143].

[163] K. R. Dienes, F. Huang, S. Su and B. Thomas, *Dynamical Dark Matter from Strongly-Coupled Dark Sectors*, *Phys. Rev. D* **95** (2017) 043526 [1610.04112].

[164] S.-M. Choi, H. M. Lee and M.-S. Seo, *Cosmic abundances of SIMP dark matter*, *JHEP* **04** (2017) 154 [1702.07860].

[165] M. Heikinheimo, K. Tuominen and K. Langæble, *Hidden strongly interacting massive particles*, *Phys. Rev. D* **97** (2018) 095040 [1803.07518].

[166] H. Beauchesne, E. Bertuzzo and G. Grilli Di Cortona, *Dark matter in Hidden Valley models with stable and unstable light dark mesons*, *JHEP* **04** (2019) 118 [1809.10152].

[167] T. Cohen, M. Lisanti and H. K. Lou, *Semivisible Jets: Dark Matter Undercover at the LHC*, *Phys. Rev. Lett.* **115** (2015) 171804 [1503.00009].

[168] N. Daci, I. De Bruyn, S. Lowette, M. H. G. Tytgat and B. Zaldivar, *Simplified SIMPs and the LHC*, *JHEP* **11** (2015) 108 [1503.05505].

[169] Z. Chacko, H.-S. Goh and R. Harnik, *The Twin Higgs: Natural electroweak breaking from mirror symmetry*, *Phys. Rev. Lett.* **96** (2006) 231802 [hep-ph/0506256].

[170] N. Craig, A. Katz, M. Strassler and R. Sundrum, *Naturalness in the Dark at the LHC*, *JHEP* **07** (2015) 105 [1501.05310].

[171] R. Barbieri, D. Greco, R. Rattazzi and A. Wulzer, *The Composite Twin Higgs scenario*, *JHEP* **08** (2015) 161 [1501.07803].

[172] M. Blennow, B. Dasgupta, E. Fernandez-Martinez and N. Rius, *Aidnogenesis via Leptogenesis and Dark Sphalerons*, *JHEP* **03** (2011) 014 [1009.3159].

[173] T. Hur, D.-W. Jung, P. Ko and J. Y. Lee, *Electroweak symmetry breaking and cold dark matter from strongly interacting hidden sector*, *Phys. Lett. B* **696** (2011) 262 [0709.1218].

[174] T. Hur and P. Ko, *Scale invariant extension of the standard model with strongly interacting hidden sector*, *Phys. Rev. Lett.* **106** (2011) 141802 [1103.2571].

[175] M. T. Frandsen, S. Sarkar and K. Schmidt-Hoberg, *Light asymmetric dark matter from new strong dynamics*, *Phys. Rev. D* **84** (2011) 051703 [1103.4350].

[176] M. R. Buckley and E. T. Neil, *Thermal dark matter from a confining sector*, *Phys. Rev.* **D87** (2013) 043510 [1209.6054].

[177] T. Hambye and A. Strumia, *Dynamical generation of the weak and Dark Matter scale*, *Phys. Rev. D* **88** (2013) 055022 [1306.2329].

[178] J. M. Cline, Z. Liu, G. D. Moore and W. Xue, *Composite strongly interacting dark matter*, *Phys. Rev. D* **90** (2014) 015023 [1312.3325].

[179] K. K. Boddy, J. L. Feng, M. Kaplinghat and T. M. P. Tait, *Self-Interacting Dark Matter from a Non-Abelian Hidden Sector*, *Phys. Rev. D* **89** (2014) 115017 [1402.3629].

[180] Y. Hochberg, E. Kuflik, H. Murayama, T. Volansky and J. G. Wacker, *Model for Thermal Relic Dark Matter of Strongly Interacting Massive Particles*, *Phys. Rev. Lett.* **115** (2015) 021301 [1411.3727].

[181] O. Antipin, M. Redi, A. Strumia and E. Vigiani, *Accidental Composite Dark Matter*, *JHEP* **07** (2015) 039 [1503.08749].

[182] I. Garcia Garcia, R. Lasenby and J. March-Russell, *Twin Higgs WIMP Dark Matter*, *Phys. Rev.* **D92** (2015) 055034 [1505.07109].

[183] Y. Hochberg, E. Kuflik and H. Murayama, *SIMP Spectroscopy*, *JHEP* **05** (2016) 090 [1512.07917].

[184] S. J. Lonsdale, M. Schroor and R. R. Volkas, *Asymmetric Dark Matter and the hadronic spectra of hidden QCD*, *Phys. Rev. D* **96** (2017) 055027 [1704.05213].

[185] H. Davoudiasl, P. P. Giardino, E. T. Neil and E. Rinaldi, *Unified Scenario for Composite Right-Handed Neutrinos and Dark Matter*, *Phys. Rev. D* **96** (2017) 115003 [1709.01082].

[186] S.-M. Choi, H. M. Lee, P. Ko and A. Natale, *Resolving phenomenological problems with strongly-interacting-massive-particle models with dark vector resonances*, *Phys. Rev. D* **98** (2018) 015034 [1801.07726].

[187] A. Berlin, N. Blinov, S. Gori, P. Schuster and N. Toro, *Cosmology and Accelerator Tests of Strongly Interacting Dark Matter*, *Phys. Rev. D* **97** (2018) 055033 [1801.05805].

[188] J. Halverson, B. D. Nelson and F. Ruehle, *String Theory and the Dark Glueball Problem*, *Phys. Rev. D* **95** (2017) 043527 [1609.02151].

[189] B. S. Acharya, M. Fairbairn and E. Hardy, *Glueball dark matter in non-standard cosmologies*, *JHEP* **07** (2017) 100 [1704.01804].

[190] M. J. Strassler and K. M. Zurek, *Discovering the Higgs through highly-displaced vertices*, *Phys. Lett. B* **661** (2008) 263 [hep-ph/0605193].

[191] J. Alexander et al., *Dark Sectors 2016 Workshop: Community Report*, 8, 2016, 1608.08632.

[192] B. Batell, J. Pradler and M. Spannowsky, *Dark Matter from Minimal Flavor Violation*, *JHEP* **08** (2011) 038 [1105.1781].

[193] P. Agrawal, S. Blanchet, Z. Chacko and C. Kilic, *Flavored Dark Matter, and Its Implications for Direct Detection and Colliders*, *Phys. Rev. D* **86** (2012) 055002 [1109.3516].

[194] L. Calibbi, A. Crivellin and B. Zaldívar, *Flavor portal to dark matter*, *Phys. Rev. D* **92** (2015) 016004 [1501.07268].

[195] R. Harnik and T. Wizansky, *Signals of New Physics in the Underlying Event*, *Phys. Rev. D* **80** (2009) 075015 [0810.3948].

[196] T. Han, Z. Si, K. M. Zurek and M. J. Strassler, *Phenomenology of hidden valleys at hadron colliders*, *JHEP* **07** (2008) 008 [0712.2041].

[197] J. E. Juknevich, *Pure-glue hidden valleys through the Higgs portal*, *JHEP* **08** (2010) 121 [0911.5616].

[198] M. J. Strassler, *On the Phenomenology of Hidden Valleys with Heavy Flavor*, 0806.2385.

[199] J. E. Juknevich, D. Melnikov and M. J. Strassler, *A Pure-Glue Hidden Valley I. States and Decays*, *JHEP* **07** (2009) 055 [0903.0883].

[200] L. Carloni and T. Sjostrand, *Visible Effects of Invisible Hidden Valley Radiation*, *JHEP* **09** (2010) 105 [1006.2911].

[201] L. Carloni, J. Rathsman and T. Sjostrand, *Discerning Secluded Sector gauge structures*, *JHEP* **04** (2011) 091 [1102.3795].

[202] G. D. Kribs and E. T. Neil, *Review of strongly-coupled composite dark matter models and lattice simulations*, *Int. J. Mod. Phys. A* **31** (2016) 1643004 [1604.04627].

[203] H. Beauchesne and G. Grilli di Cortona, *Classification of dark pion multiplets as dark matter candidates and collider phenomenology*, *JHEP* **02** (2020) 196 [1910.10724].

[204] R. D. Peccei and H. R. Quinn, *CP Conservation in the Presence of Instantons*, *Phys. Rev. Lett.* **38** (1977) 1440.

[205] R. D. Peccei and H. R. Quinn, *Constraints Imposed by CP Conservation in the Presence of Instantons*, *Phys. Rev.* **D16** (1977) 1791.

[206] S. Weinberg, *A New Light Boson?*, *Phys. Rev. Lett.* **40** (1978) 223.

[207] F. Wilczek, *Problem of Strong P and T Invariance in the Presence of Instantons*, *Phys. Rev. Lett.* **40** (1978) 279.

[208] R. D. Peccei, *The Strong CP problem and axions*, *Lect. Notes Phys.* **741** (2008) 3 [hep-ph/0607268].

[209] J. Redondo, *Alternative dark matter candidates: axions and ALPs*, *PoS* **NOW2018** (2019) 083.

[210] B. Gripaios, A. Pomarol, F. Riva and J. Serra, *Beyond the Minimal Composite Higgs Model*, *JHEP* **04** (2009) 070 [0902.1483].

[211] G. Ferretti and D. Karateev, *Fermionic UV completions of Composite Higgs models*, *JHEP* **03** (2014) 077 [1312.5330].

[212] A. Belyaev, G. Cacciapaglia, H. Cai, G. Ferretti, T. Flacke, A. Parolini et al., *Di-boson signatures as Standard Candles for Partial Compositeness*, *JHEP* **01** (2017) 094 [1610.06591].

[213] B. Gripaios, M. Nardecchia and T. You, *On the Structure of Anomalous Composite Higgs Models*, *Eur. Phys. J. C* **77** (2017) 28 [1605.09647].

[214] D. Buarque Franzosi, G. Cacciapaglia, X. Cid Vidal, G. Ferretti, T. Flacke and C. Vázquez Sierra, *Exploring new possibilities to discover a light pseudo-scalar at LHCb*, *Eur. Phys. J. C* **82** (2022) 3 [2106.12615].

[215] H.-C. Cheng, L. Li and E. Salvioni, *A theory of dark pions*, *JHEP* **01** (2022) 122 [2110.10691].

[216] B. Bellazzini, A. Mariotti, D. Redigolo, F. Sala and J. Serra, *R-axion at colliders*, *Phys. Rev. Lett.* **119** (2017) 141804 [1702.02152].

[217] D. Gorbunov, V. Ilyin and B. Mele, *Sgoldstino events in top decays at LHC*, *Phys. Lett. B* **502** (2001) 181 [hep-ph/0012150].

[218] C. D. Froggatt and H. B. Nielsen, *Hierarchy of Quark Masses, Cabibbo Angles and CP Violation*, *Nucl. Phys.* **B147** (1979) 277.

[219] P. Svrcek and E. Witten, *Axions In String Theory*, *JHEP* **06** (2006) 051 [hep-th/0605206].

[220] A. Arvanitaki, S. Dimopoulos, S. Dubovsky, N. Kaloper and J. March-Russell, *String Axiverse*, *Phys. Rev. D* **81** (2010) 123530 [0905.4720].

[221] F. Wilczek, *Axions and Family Symmetry Breaking*, *Phys. Rev. Lett.* **49** (1982) 1549.

[222] D. B. Reiss, *Can the Family Group Be a Global Symmetry?*, *Phys. Lett.* **115B** (1982) 217.

[223] Z. G. Berezhiani and M. Y. Khlopov, *Physical and astrophysical consequences of breaking of the symmetry of families. (In Russian)*, *Sov. J. Nucl. Phys.* **51** (1990) 935.

[224] Z. G. Berezhiani and M. Y. Khlopov, *The Theory of broken gauge symmetry of families. (In Russian)*, *Sov. J. Nucl. Phys.* **51** (1990) 739.

[225] J. L. Feng, T. Moroi, H. Murayama and E. Schnapka, *Third generation familons, b factories, and neutrino cosmology*, *Phys. Rev.* **D57** (1998) 5875 [hep-ph/9709411].

[226] M. E. Albrecht, T. Feldmann and T. Mannel, *Goldstone Bosons in Effective Theories with Spontaneously Broken Flavour Symmetry*, *JHEP* **10** (2010) 089 [1002.4798].

[227] M. Bauer, T. Schell and T. Plehn, *Hunting the Flavon*, *Phys. Rev. D* **94** (2016) 056003 [1603.06950].

[228] Y. Ema, K. Hamaguchi, T. Moroi and K. Nakayama, *Flaxion: a minimal extension to solve puzzles in the standard model*, *JHEP* **01** (2017) 096 [1612.05492].

[229] L. Calibbi, F. Goertz, D. Redigolo, R. Ziegler and J. Zupan, *Minimal axion model from flavor*, *Phys. Rev.* **D95** (2017) 095009 [1612.08040].

[230] Y. Ema, D. Hagihara, K. Hamaguchi, T. Moroi and K. Nakayama, *Supersymmetric Flaxion*, *JHEP* **04** (2018) 094 [1802.07739].

[231] M. Heikinheimo, K. Huitu, V. Keus and N. Koivunen, *Cosmological constraints on light flavons*, *JHEP* **06** (2019) 065 [1812.10963].

[232] Q. Bonnefoy, E. Dudas and S. Pokorski, *Chiral Froggatt-Nielsen models, gauge anomalies and flavourful axions*, *JHEP* **01** (2020) 191 [1909.05336].

[233] M. Bauer, M. Neubert and A. Thamm, *Collider Probes of Axion-Like Particles*, *JHEP* **12** (2017) 044 [1708.00443].

[234] M. Bauer, M. Heiles, M. Neubert and A. Thamm, *Axion-Like Particles at Future Colliders*, *Eur. Phys. J. C* **79** (2019) 74 [1808.10323].

[235] K. Ehret et al., *New ALPS Results on Hidden-Sector Lightweights*, *Phys. Lett. B* **689** (2010) 149 [1004.1313].

[236] R. Bähre et al., *Any light particle search II —Technical Design Report*, *JINST* **8** (2013) T09001 [1302.5647].

[237] OSQAR collaboration, *New exclusion limits on scalar and pseudoscalar axionlike particles from light shining through a wall*, *Phys. Rev. D* **92** (2015) 092002 [1506.08082].

[238] CAST collaboration, *An Improved limit on the axion-photon coupling from the CAST experiment*, *JCAP* **04** (2007) 010 [hep-ex/0702006].

[239] E. Armengaud et al., *Conceptual Design of the International Axion Observatory (IAXO)*, *JINST* **9** (2014) T05002 [1401.3233].

[240] XENON collaboration, *Excess electronic recoil events in XENON1T*, *Phys. Rev. D* **102** (2020) 072004 [2006.09721].

[241] C. Gao, J. Liu, L.-T. Wang, X.-P. Wang, W. Xue and Y.-M. Zhong, *Reexamining the Solar Axion Explanation for the XENON1T Excess*, *Phys. Rev. Lett.* **125** (2020) 131806 [2006.14598].

[242] L. Di Luzio, M. Fedele, M. Giannotti, F. Mescia and E. Nardi, *Solar axions cannot explain the XENON1T excess*, *Phys. Rev. Lett.* **125** (2020) 131804 [2006.12487].

[243] P. Carenza, O. Straniero, B. Döbrich, M. Giannotti, G. Lucente and A. Mirizzi, *Constraints on the coupling with photons of heavy axion-like-particles from Globular Clusters*, *Phys. Lett. B* **809** (2020) 135709 [2004.08399].

[244] G. G. Raffelt, *Astrophysical axion bounds*, *Lect. Notes Phys.* **741** (2008) 51 [hep-ph/0611350].

[245] F. D'Eramo, R. Z. Ferreira, A. Notari and J. L. Bernal, *Hot Axions and the H_0 tension*, *JCAP* **11** (2018) 014 [1808.07430].

[246] F. Capozzi and G. Raffelt, *Axion and neutrino red-giant bounds updated with geometric distance determinations*, 2007.03694.

[247] P. Sikivie, *Experimental Tests of the Invisible Axion*, *Phys. Rev. Lett.* **51** (1983) 1415.

[248] J. L. Ouellet et al., *First Results from ABRACADABRA-10 cm: A Search for Sub-μeV Axion Dark Matter*, *Phys. Rev. Lett.* **122** (2019) 121802 [1810.12257].

[249] C. Dessert, J. W. Foster and B. R. Safdi, *X-ray Searches for Axions from Super Star Clusters*, *Phys. Rev. Lett.* **125** (2020) 261102 [2008.03305].

[250] R. Hlozek, D. Grin, D. J. E. Marsh and P. G. Ferreira, *A search for ultralight axions using precision cosmological data*, *Phys. Rev. D* **91** (2015) 103512 [1410.2896].

[251] V. Poulin, T. L. Smith, D. Grin, T. Karwal and M. Kamionkowski, *Cosmological implications of ultralight axionlike fields*, *Phys. Rev. D* **98** (2018) 083525 [1806.10608].

[252] J. Wess and B. Zumino, *Supergauge Transformations in Four-Dimensions*, *Nucl. Phys. B* **70** (1974) 39.

[253] S. P. Martin, *A Supersymmetry primer*, *Adv. Ser. Direct. High Energy Phys.* **18** (1998) 1 [hep-ph/9709356].

[254] Particle Data Group collaboration, *Review of Particle Physics*, *PTEP* **2020** (2020) 083C01.

[255] D. Buttazzo, G. Degrassi, P. P. Giardino, G. F. Giudice, F. Sala, A. Salvio et al., *Investigating the near-criticality of the Higgs boson*, *JHEP* **12** (2013) 089 [1307.3536].

[256] J. R. Espinosa, *Implications of the top (and Higgs) mass for vacuum stability*, *PoS* **TOP2015** (2016) 043 [1512.01222].

[257] W. Konetschny and W. Kummer, *Nonconservation of Total Lepton Number with Scalar Bosons*, *Phys. Lett. B* **70** (1977) 433.

[258] M. Magg and C. Wetterich, *Neutrino Mass Problem and Gauge Hierarchy*, *Phys. Lett. B* **94** (1980) 61.

[259] J. Schechter and J. W. F. Valle, *Neutrino Masses in SU(2) x U(1) Theories*, *Phys. Rev. D* **22** (1980) 2227.

[260] T. P. Cheng and L.-F. Li, *Neutrino Masses, Mixings and Oscillations in SU(2) x U(1) Models of Electroweak Interactions*, *Phys. Rev. D* **22** (1980) 2860.

[261] R. N. Mohapatra and G. Senjanovic, *Neutrino Masses and Mixings in Gauge Models with Spontaneous Parity Violation*, *Phys. Rev. D* **23** (1981) 165.

[262] G. Lazarides, Q. Shafi and C. Wetterich, *Proton Lifetime and Fermion Masses in an SO(10) Model*, *Nucl. Phys. B* **181** (1981) 287.

[263] T. D. Lee, *A Theory of Spontaneous T Violation*, *Phys. Rev. D* **8** (1973) 1226.

[264] G. D. Kribs, A. Martin, B. Ostdiek and T. Tong, *Dark Mesons at the LHC*, *JHEP* **07** (2019) 133 [1809.10184].

[265] J. M. Butterworth, L. Corpe, X. Kong, S. Kulkarni and M. Thomas, *New sensitivity of LHC measurements to composite dark matter models*, *Phys. Rev. D* **105** (2022) 015008 [2105.08494].

[266] J. Kang and M. A. Luty, *Macroscopic Strings and 'Quirks' at Colliders*, *JHEP* **11** (2009) 065 [0805.4642].

[267] S. Knapen, S. Pagan Griso, M. Papucci and D. J. Robinson, *Triggering Soft Bombs at the LHC*, *JHEP* **08** (2017) 076 [1612.00850].

[268] ALICE collaboration, *The ALICE experiment at the CERN LHC*, *JINST* **3** (2008) S08002.

[269] ATLAS collaboration, *The ATLAS Experiment at the CERN Large Hadron Collider*, *JINST* **3** (2008) S08003.

[270] CMS collaboration, *The CMS Experiment at the CERN LHC*, *JINST* **3** (2008) S08004.

[271] LHCb collaboration, *The LHCb Detector at the LHC*, *JINST* **3** (2008) S08005.

[272] ATLAS collaboration, *Improved luminosity determination in pp collisions at sqrt(s) = 7 TeV using the ATLAS detector at the LHC*, *Eur. Phys. J. C* **73** (2013) 2518 [1302.4393].

[273] ATLAS collaboration, *Luminosity determination in pp collisions at $\sqrt{s}$ = 8 TeV using the ATLAS detector at the LHC*, *Eur. Phys. J. C* **76** (2016) 653 [1608.03953].

[274] ATLAS collaboration, *Luminosity determination in pp collisions at $\sqrt{s} = 13$ TeV using the ATLAS detector at the LHC*, .

[275] S. Fartoukh et al., *LHC Configuration and Operational Scenario for Run 3*, .

[276] FASER collaboration, *Technical Proposal: FASERnu*, 2001.03073.

[277] SHiP collaboration, *SND@LHC*, 2002.08722.

[278] *High-Luminosity Large Hadron Collider (HL-LHC): Technical Design Report V. 0.1*, .

[279] NA62 collaboration, *The Beam and detector of the NA62 experiment at CERN*, *JINST* **12** (2017) P05025 [1703.08501].

[280] P. Agrawal, M. Blanke and K. Gemmler, *Flavored dark matter beyond Minimal Flavor Violation*, *JHEP* **10** (2014) 072 [1405.6709].

[281] Planck collaboration, *Planck 2013 results. XVI. Cosmological parameters*, *Astron. Astrophys.* **571** (2014) A16 [1303.5076].

[282] S. Nussinov, *Technocosmology — could a technibaryon excess provide a "natural" missing mass candidate?*, *Phys. Lett. B* **165** (1985) 55.

[283] D. B. Kaplan, *A Single explanation for both the baryon and dark matter densities*, *Phys. Rev. Lett.* **68** (1992) 741.

[284] S. M. Barr, R. S. Chivukula and E. Farhi, *Electroweak Fermion Number Violation and the Production of Stable Particles in the Early Universe*, *Phys. Lett. B* **241** (1990) 387.

[285] S. M. Barr, *Baryogenesis, sphalerons and the cogeneration of dark matter*, *Phys. Rev. D* **44** (1991) 3062.

[286] S. Dodelson, B. R. Greene and L. M. Widrow, *Baryogenesis, dark matter and the width of the Z*, *Nucl. Phys. B* **372** (1992) 467.

[287] M. Fujii and T. Yanagida, *A Solution to the coincidence puzzle of Omega(B) and Omega (DM)*, *Phys. Lett. B* **542** (2002) 80 [hep-ph/0206066].

[288] R. Kitano and I. Low, *Dark matter from baryon asymmetry*, *Phys. Rev. D* **71** (2005) 023510 [hep-ph/0411133].

[289] G. R. Farrar and G. Zaharijas, *Dark matter and the baryon asymmetry*, *Phys. Rev. Lett.* **96** (2006) 041302 [hep-ph/0510079].

[290] S. B. Gudnason, C. Kouvaris and F. Sannino, *Towards working technicolor: Effective theories and dark matter*, *Phys. Rev. D* **73** (2006) 115003 [hep-ph/0603014].

[291] R. Kitano, H. Murayama and M. Ratz, *Unified origin of baryons and dark matter*, *Phys. Lett. B* **669** (2008) 145 [0807.4313].

[292] D. E. Kaplan, M. A. Luty and K. M. Zurek, *Asymmetric Dark Matter*, *Phys. Rev. D* **79** (2009) 115016 [0901.4117].

[293] J. Shelton and K. M. Zurek, *Darkogenesis: A baryon asymmetry from the dark matter sector*, *Phys. Rev. D* **82** (2010) 123512 [1008.1997].

[294] H. Davoudiasl, D. E. Morrissey, K. Sigurdson and S. Tulin, *Hylogenesis: A Unified Origin for Baryonic Visible Matter and Antibaryonic Dark Matter*, *Phys. Rev. Lett.* **105** (2010) 211304 [1008.2399].

[295] M. R. Buckley and L. Randall, *Xogenesis*, *JHEP* **09** (2011) 009 [1009.0270].

[296] T. Cohen, D. J. Phalen, A. Pierce and K. M. Zurek, *Asymmetric Dark Matter from a GeV Hidden Sector*, *Phys. Rev. D* **82** (2010) 056001 [1005.1655].

[297] W.-Z. Feng and J.-H. Yu, *Twin Cogenesis*, 2005.06471.

[298] P. Barnes, Z. Johnson, A. Pierce and B. Shakya, *Simple Hidden Sector Dark Matter*, *Phys. Rev. D* **102** (2020) 075019 [2003.13744].

[299] M. Ibe, S. Matsumoto and T. T. Yanagida, *The GeV-scale dark matter with B–L asymmetry*, *Phys. Lett. B* **708** (2012) 112 [1110.5452].

[300] W.-Z. Feng, P. Nath and G. Peim, *Cosmic Coincidence and Asymmetric Dark Matter in a Stueckelberg Extension*, *Phys. Rev. D* **85** (2012) 115016 [1204.5752].

[301] K. Kumar, A. Menon and T. M. P. Tait, *Magnetic Fluffy Dark Matter*, *JHEP* **02** (2012) 131 [1111.2336].

[302] G. Krnjaic and K. Sigurdson, *Big Bang Darkleosynthesis*, *Phys. Lett. B* **751** (2015) 464 [1406.1171].

[303] W. Detmold, M. McCullough and A. Pochinsky, *Dark Nuclei I: Cosmology and Indirect Detection*, *Phys. Rev. D* **90** (2014) 115013 [1406.2276].

[304] G. Arcadi, Y. Mambrini and F. Richard, *Z-portal dark matter*, *JCAP* **03** (2015) 018 [1411.2985].

[305] T. Jubb, M. Kirk and A. Lenz, *Charming Dark Matter*, *JHEP* **12** (2017) 010 [1709.01930].

[306] M. Blanke, S. Das and S. Kast, *Flavoured Dark Matter Moving Left*, *JHEP* **02** (2018) 105 [1711.10493].

[307] E. C. Poggio, H. R. Quinn and S. Weinberg, *Smearing method in the quark model*, *Phys. Rev. D* **13** (1976) 1958.

[308] M. A. Shifman, *Quark hadron duality*, in *8th International Symposium on Heavy Flavor Physics*, vol. 3, (Singapore), pp. 1447–1494, World Scientific, 7, 2000, hep-ph/0009131, DOI.

[309] G. D. Kribs, A. Martin and T. Tong, *Effective Theories of Dark Mesons with Custodial Symmetry*, *JHEP* **08** (2019) 020 [1809.10183].

[310] CMS collaboration, *Search for new particles decaying to a jet and an emerging jet*, *JHEP* **02** (2019) 179 [1810.10069].

[311] V. N. Gribov and L. N. Lipatov, *Deep inelastic e p scattering in perturbation theory*, *Sov. J. Nucl. Phys.* **15** (1972) 438.

[312] G. Altarelli and G. Parisi, *Asymptotic Freedom in Parton Language*, *Nucl. Phys. B* **126** (1977) 298.

[313] Y. L. Dokshitzer, *Calculation of the Structure Functions for Deep Inelastic Scattering and e+ e- Annihilation by Perturbation Theory in Quantum Chromodynamics.*, *Sov. Phys. JETP* **46** (1977) 641.

[314] T. Sjostrand, S. Mrenna and P. Z. Skands, *A Brief Introduction to PYTHIA 8.1*, *Comput. Phys. Commun.* **178** (2008) 852 [0710.3820].

[315] T. Sjöstrand, S. Ask, J. R. Christiansen, R. Corke, N. Desai, P. Ilten et al., *An introduction to PYTHIA 8.2*, *Comput. Phys. Commun.* **191** (2015) 159 [1410.3012].

[316] A. Alloul, N. D. Christensen, C. Degrande, C. Duhr and B. Fuks, *FeynRules 2.0 - A complete toolbox for tree-level phenomenology*, *Comput. Phys. Commun.* **185** (2014) 2250 [1310.1921].

[317] C. Degrande, C. Duhr, B. Fuks, D. Grellscheid, O. Mattelaer and T. Reiter, *UFO - The Universal FeynRules Output*, *Comput. Phys. Commun.* **183** (2012) 1201 [1108.2040].

[318] J. Alwall, R. Frederix, S. Frixione, V. Hirschi, F. Maltoni, O. Mattelaer et al., *The automated computation of tree-level and next-to-leading order differential cross sections, and their matching to parton shower simulations*, *JHEP* **07** (2014) 079 [1405.0301].

[319] "Hidden valley processes, pythia8." http://home.thep.lu.se/~torbjorn/pythia82php/HiddenValleyProcesses.php?filepath=files/.

[320] CMS collaboration, *Search for supersymmetry in proton-proton collisions at 13 TeV in final states with jets and missing transverse momentum*, *JHEP* **10** (2019) 244 [1908.04722].

[321] ATLAS collaboration, *A search for pair-produced resonances in four-jet final states at $\sqrt{s} = 13$ TeV with the ATLAS detector*, *Eur. Phys. J. C* **78** (2018) 250 [1710.07171].

[322] M. Cacciari, G. P. Salam and G. Soyez, *The anti-k_t jet clustering algorithm*, *JHEP* **04** (2008) 063 [0802.1189].

[323] CMS Collaboration collaboration, *Search for new particles decaying to a jet and an emerging jet*, tech. rep., CERN, Geneva, 2018.

[324] DARWIN collaboration, *DARWIN: towards the ultimate dark matter detector*, *JCAP* **11** (2016) 017 [1606.07001].

[325] Planck collaboration, *Planck 2015 results. XIII. Cosmological parameters*, *Astron. Astrophys.* **594** (2016) A13 [1502.01589].

[326] NA62 collaboration, *Searches for very weakly-coupled particles beyond the Standard Model with NA62*, in *13th Patras Workshop on Axions, WIMPs and WISPs*, pp. 145–148, 2018, 1711.08967, DOI.

[327] SHiP Collaboration collaboration, *SHiP Experiment - Progress Report*, Tech. Rep. CERN-SPSC-2019-010. SPSC-SR-248, CERN, Geneva, Jan, 2019.

[328] BaBar collaboration, *Search for $B \to K^{(*)}\nu\overline{\nu}$ and invisible quarkonium decays*, *Phys. Rev. D* **87** (2013) 112005 [1303.7465].

[329] A. J. Buras, J. Girrbach-Noe, C. Niehoff and D. M. Straub, *$B \to K^{(*)}\nu\overline{\nu}$ decays in the Standard Model and beyond*, *JHEP* **02** (2015) 184 [1409.4557].

[330] Belle-II collaboration, *The Belle II Physics Book*, *PTEP* **2019** (2019) 123C01 [1808.10567].

[331] H. Georgi, D. B. Kaplan and L. Randall, *Manifesting the Invisible Axion at Low-energies*, *Phys. Lett.* **169B** (1986) 73.

[332] K. Choi, K. Kang and J. E. Kim, *Effects of η' in Low-energy Axion Physics*, *Phys. Lett.* **B181** (1986) 145.

[333] I. Brivio, M. B. Gavela, L. Merlo, K. Mimasu, J. M. No, R. del Rey et al., "ALPsEFT - FeynRules."

[334] I. Brivio, M. B. Gavela, L. Merlo, K. Mimasu, J. M. No, R. del Rey et al., *ALPs Effective Field Theory and Collider Signatures*, *Eur. Phys. J.* **C77** (2017) 572 [1701.05379].

[335] M. B. Gavela, R. Houtz, P. Quilez, R. Del Rey and O. Sumensari, *Flavor constraints on electroweak ALP couplings*, *Eur. Phys. J.* **C79** (2019) 369 [1901.02031].

[336] W. A. Bardeen, R. D. Peccei and T. Yanagida, *Constraints on Variant Axion Models*, *Nucl. Phys.* **B279** (1987) 401.

[337] L. M. Krauss and M. B. Wise, *Constraints on Shortlived Axions From the Decay $\pi^+ \to e^+e^-e^+$ Neutrino*, *Phys. Lett.* **B176** (1986) 483.

[338] J. F. Kamenik and C. Smith, *FCNC portals to the dark sector*, *JHEP* **03** (2012) 090 [1111.6402].

[339] D. Egana-Ugrinovic, S. Homiller and P. Meade, *Light Scalars and the Koto Anomaly*, *Phys. Rev. Lett.* **124** (2020) 191801 [1911.10203].

[340] Q. Bonnefoy, P. Cox, E. Dudas, T. Gherghetta and M. D. Nguyen, *Flavoured Warped Axion*, 2012.09728.

[341] G. Alonso-Álvarez, F. Ertas, J. Jaeckel, F. Kahlhoefer and L. J. Thormaehlen, *Leading Logs in QCD Axion Effective Field Theory*, 2101.03173.

[342] M. Bauer, M. Carena and K. Gemmler, *Flavor from the Electroweak Scale*, *JHEP* **11** (2015) 016 [1506.01719].

[343] M. Bauer, M. Carena and K. Gemmler, *Creating the fermion mass hierarchies with multiple Higgs bosons*, *Phys. Rev.* **D94** (2016) 115030 [1512.03458].

[344] M. Bauer, M. Carena and A. Carmona, *Higgs Pair Production as a Signal of Enhanced Yukawa Couplings*, *Phys. Rev. Lett.* **121** (2018) 021801 [1801.00363].

[345] E. C. Poggio, H. R. Quinn and S. Weinberg, *Smearing the Quark Model*, *Phys. Rev.* **D13** (1976) 1958.

[346] K. Choi, S. H. Im, C. B. Park and S. Yun, *Minimal Flavor Violation with Axion-like Particles*, *JHEP* **11** (2017) 070 [1708.00021].

[347] J. Martin Camalich, M. Pospelov, P. N. H. Vuong, R. Ziegler and J. Zupan, *Quark Flavor Phenomenology of the QCD Axion*, *Phys. Rev. D* **102** (2020) 015023 [2002.04623].

[348] M. Chala, G. Guedes, M. Ramos and J. Santiago, *Running in the ALPs*, 2012.09017.

[349] M. Bauer, M. Neubert, S. Renner, M. Schnubel and A. Thamm, *The Low-Energy Effective Theory of Axions and ALPs*, 2012.12272.

[350] M. Bauer, M. Neubert, S. Renner, M. Schnubel and A. Thamm, *Flavor probes of axion-like particles*, 2110.10698.

[351] Particle Data Group collaboration, *Review of Particle Physics*, *PTEP* **2020** (2020) 083C01.

[352] A. Bazavov et al., *Short-distance matrix elements for D^0-meson mixing for $N_f = 2 + 1$ lattice QCD*, *Phys. Rev. D* **97** (2018) 034513 [1706.04622].

[353] E. Golowich, J. Hewett, S. Pakvasa and A. A. Petrov, *Relating D0-anti-D0 Mixing and D0 —> l+ l- with New Physics*, *Phys. Rev. D* **79** (2009) 114030 [0903.2830].

[354] K. G. Chetyrkin, J. H. Kuhn and M. Steinhauser, *RunDec: A Mathematica package for running and decoupling of the strong coupling and quark masses*, *Comput. Phys. Commun.* **133** (2000) 43 [hep-ph/0004189].

[355] F. Herren and M. Steinhauser, *Version 3 of RunDec and CRunDec*, *Comput. Phys. Commun.* **224** (2018) 333 [1703.03751].

[356] HFLAV collaboration, *Averages of b-hadron, c-hadron, and τ-lepton properties as of 2018*, 1909.12524.

[357] M. Bauer, M. Neubert, S. Renner, M. Schnubel and A. Thamm, *Consistent Treatment of Axions in the Weak Chiral Lagrangian*, *Phys. Rev. Lett.* **127** (2021) 081803 [2102.13112].

[358] ETM collaboration, *Scalar and vector form factors of $D \to \pi(K)\ell\nu$ decays with $N_f = 2 + 1 + 1$ twisted fermions*, *Phys. Rev. D* **96** (2017) 054514 [1706.03017].

[359] J. A. Bailey et al., *$B \to Kl^+l^-$ Decay Form Factors from Three-Flavor Lattice QCD*, *Phys. Rev. D* **93** (2016) 025026 [1509.06235].

[360] N. Gubernari, A. Kokulu and D. van Dyk, *$B \to P$ and $B \to V$ Form Factors from B-Meson Light-Cone Sum Rules beyond Leading Twist*, *JHEP* **01** (2019) 150 [1811.00983].

[361] N. Carrasco, P. Lami, V. Lubicz, L. Riggio, S. Simula and C. Tarantino, *$K \to \pi$ semileptonic form factors with $N_f = 2 + 1 + 1$ twisted mass fermions*, *Phys. Rev. D* **93** (2016) 114512 [1602.04113].

[362] CLEO collaboration, *Precision Measurement of B(D+ —> mu+ nu) and the Pseudoscalar Decay Constant f(D+)*, *Phys. Rev. D* **78** (2008) 052003 [0806.2112].

[363] BESIII collaboration, *Observation of the leptonic decay $D^+ \to \tau^+\nu_\tau$*, *Phys. Rev. Lett.* **123** (2019) 211802 [1908.08877].

[364] R. Brun and F. Rademakers, *ROOT: An object oriented data analysis framework*, *Nucl. Instrum. Meth. A* **389** (1997) 81.

[365] A. L. Read, *Presentation of search results: The CL(s) technique*, *J. Phys. G* **28** (2002) 2693.

[366] BESIII collaboration, *Precision measurements of B[ψ(3686)$\to\pi+\pi$-J/ψ] and B[J/$\psi\to$l+l-]*, *Phys. Rev. D* **88** (2013) 032007 [1307.1189].

[367] E949, E787 collaboration, *Measurement of the K+ –> pi+ nu nu branching ratio*, *Phys. Rev. D* **77** (2008) 052003 [0709.1000].

[368] CLEO collaboration, *Search for the familon via B+- —> pi+- X0, B+- —> K+- X0, and B0 —> K0(S)X0 decays*, *Phys. Rev. Lett.* **87** (2001) 271801 [hep-ex/0106038].

[369] NA62 collaboration, *Search for a feebly interacting particle X in the decay $K^+ \to \pi^+ X$*, 2011.11329.

[370] BaBar collaboration, *A search for the decay $B^+ \to K^+\nu\bar{\nu}$*, *Phys. Rev. Lett.* **94** (2005) 101801 [hep-ex/0411061].

[371] A. J. Buras, D. Buttazzo, J. Girrbach-Noe and R. Knegjens, *$K^+ \to \pi^+\nu\bar{\nu}$ and $K_L \to \pi^0\nu\bar{\nu}$ in the Standard Model: status and perspectives*, *JHEP* **11** (2015) 033 [1503.02693].

[372] S. Martellotti, *The NA62 Experiment at CERN*, in *12th Conference on the Intersections of Particle and Nuclear Physics*, 10, 2015, 1510.00172.

[373] H. Haber, G. L. Kane and T. Sterling, *The Fermion Mass Scale and Possible Effects of Higgs Bosons on Experimental Observables*, *Nucl. Phys. B* **161** (1979) 493.

[374] H. E. Haber, A. S. Schwarz and A. E. Snyder, *Hunting the Higgs in B Decays*, *Nucl. Phys. B* **294** (1987) 301.

[375] M. L. Mangano and P. Nason, *Radiative quarkonium decays and the NMSSM Higgs interpretation of the hyperCP $\Sigma+ \to p\mu^+\mu^-$ events*, *Mod. Phys. Lett. A* **22** (2007) 1373 [0704.1719].

[376] F. Domingo, U. Ellwanger, E. Fullana, C. Hugonie and M.-A. Sanchis-Lozano, *Radiative Upsilon decays and a light pseudoscalar Higgs in the NMSSM*, *JHEP* **01** (2009) 061 [0810.4736].

[377] P. Fayet, *U(1)(A) Symmetry in two-doublet models, U bosons or light pseudoscalars, and psi and Upsilon decays*, *Phys. Lett. B* **675** (2009) 267 [0812.3980].

[378] L. Merlo, F. Pobbe, S. Rigolin and O. Sumensari, *Revisiting the production of ALPs at B-factories*, *JHEP* **06** (2019) 091 [1905.03259].

[379] M. Vysotsky, *Strong Interaction Corrections to Semiweak Decays: Calculation of the V —> H gamma Decay Rate with alpha-S Accuracy*, *Phys. Lett. B* **97** (1980) 159.

[380] P. Nason, *QCD Radiative Corrections to Υ Decay Into Scalar Plus γ and Pseudoscalar Plus γ*, *Phys. Lett. B* **175** (1986) 223.

[381] J. Polchinski, S. R. Sharpe and T. Barnes, *Bound State Effects in $\Upsilon \to$ Zeta (8.3) γ*, *Phys. Lett. B* **148** (1984) 493.

[382] J. T. Pantaleone, M. E. Peskin and S. Tye, *Bound State Effects in $\Upsilon \to \gamma$ + Resonance*, *Phys. Lett. B* **149** (1984) 225.

[383] I. Aznaurian, S. Grigorian and S. G. Matinyan, *Relativistic Effects in $V \to H^0\gamma$ Decay*, *JETP Lett.* **43** (1986) 646.

[384] CLEO collaboration, *Search for the Decay J/psi -¿ gamma + invisible*, *Phys. Rev. D* **81** (2010) 091101 [1003.0417].

[385] G. G. Raffelt, *Stars as laboratories for fundamental physics: The astrophysics of neutrinos, axions, and other weakly interacting particles*. 5, 1996.

[386] N. Bar, K. Blum and G. D'Amico, *Is there a supernova bound on axions?*, *Phys. Rev. D* **101** (2020) 123025 [1907.05020].

[387] N. Cabibbo, E. C. Swallow and R. Winston, *Semileptonic hyperon decays*, *Ann. Rev. Nucl. Part. Sci.* **53** (2003) 39 [hep-ph/0307298].

[388] R. L. Jaffe and A. Manohar, *The G(1) Problem: Fact and Fantasy on the Spin of the Proton*, *Nucl. Phys. B* **337** (1990) 509.

[389] J. H. Chang, R. Essig and S. D. McDermott, *Revisiting Supernova 1987A Constraints on Dark Photons*, *JHEP* **01** (2017) 107 [1611.03864].

[390] J. H. Chang, R. Essig and S. D. McDermott, *Supernova 1987A Constraints on Sub-GeV Dark Sectors, Millicharged Particles, the QCD Axion, and an Axion-like Particle*, *JHEP* **09** (2018) 051 [1803.00993].

[391] W. Keil, H.-T. Janka, D. N. Schramm, G. Sigl, M. S. Turner and J. R. Ellis, *A Fresh look at axions and SN-1987A*, *Phys. Rev. D* **56** (1997) 2419 [astro-ph/9612222].

[392] S. Hannestad and G. Raffelt, *Supernova neutrino opacity from nucleon-nucleon Bremsstrahlung and related processes*, *Astrophys. J.* **507** (1998) 339 [astro-ph/9711132].

[393] A. Bartl, R. Bollig, H.-T. Janka and A. Schwenk, *Impact of Nucleon-Nucleon Bremsstrahlung Rates Beyond One-Pion Exchange*, *Phys. Rev. D* **94** (2016) 083009 [1608.05037].

[394] F. Ertas and F. Kahlhoefer, *On the interplay between astrophysical and laboratory probes of MeV-scale axion-like particles*, *JHEP* **07** (2020) 050 [2004.01193].

[395] D. Cadamuro and J. Redondo, *Cosmological bounds on pseudo Nambu-Goldstone bosons*, *JCAP* **02** (2012) 032 [1110.2895].

[396] M. Millea, L. Knox and B. Fields, *New Bounds for Axions and Axion-Like Particles with keV-GeV Masses*, *Phys. Rev. D* **92** (2015) 023010 [1501.04097].

[397] P. F. Depta, M. Hufnagel and K. Schmidt-Hoberg, *Robust cosmological constraints on axion-like particles*, *JCAP* **05** (2020) 009 [2002.08370].

[398] S. Alekhin et al., *A facility to Search for Hidden Particles at the CERN SPS: the SHiP physics case*, *Rept. Prog. Phys.* **79** (2016) 124201 [1504.04855].

[399] FASER collaboration, *FASER's physics reach for long-lived particles*, *Phys. Rev. D* **99** (2019) 095011 [1811.12522].

[400] MATHUSLA collaboration, *A Letter of Intent for MATHUSLA: A Dedicated Displaced Vertex Detector above ATLAS or CMS.*, 1811.00927.

[401] MATHUSLA collaboration, *An Update to the Letter of Intent for MATHUSLA: Search for Long-Lived Particles at the HL-LHC*, 2009.01693.

[402] CHARM collaboration, *Search for Axion Like Particle Production in 400-{GeV} Proton - Copper Interactions*, *Phys. Lett. B* **157** (1985) 458.

[403] NA62 collaboration, *Search for Hidden Sector particles at NA62*, *PoS* **EPS-HEP2017** (2017) 301.

[404] SHiP Collaboration collaboration, *Heavy Flavour Cascade Production in a Beam Dump*, .

[405] J. D. Clarke, R. Foot and R. R. Volkas, *Phenomenology of a very light scalar (100 MeV $< m_h <$ 10 GeV) mixing with the SM Higgs*, *JHEP* **02** (2014) 123 [1310.8042].

[406] HERA-B collaboration, *Measurement of D0, D+, D+(s) and D*+ Production in Fixed Target 920-GeV Proton-Nucleus Collisions*, *Eur. Phys. J. C* **52** (2007) 531 [0708.1443].

[407] M. Cacciari, M. Greco and P. Nason, *The P(T) spectrum in heavy flavor hadroproduction*, *JHEP* **05** (1998) 007 [hep-ph/9803400].

[408] S. Baumholzer, V. Brdar and E. Morgante, *Structure Formation Limits on Axion-Like Dark Matter*, 2012.09181.

[409] ATLAS collaboration, *Measurement of the $t\bar{t}$ production cross-section in the lepton+jets channel at $\sqrt{s} = 13$ TeV with the ATLAS experiment*, *Phys. Lett. B* **810** (2020) 135797 [2006.13076].

[410] J. Bonilla, I. Brivio, M. B. Gavela and V. Sanz, *One-loop corrections to ALP couplings*, *JHEP* **11** (2021) 168 [2107.11392].

[411] ATLAS collaboration, *Jet energy measurement with the ATLAS detector in proton-proton collisions at $\sqrt{s} = 7$ TeV*, *Eur. Phys. J. C* **73** (2013) 2304 [1112.6426].

[412] CDF collaboration, *Direct Measurement of the Total Decay Width of the Top Quark*, *Phys. Rev. Lett.* **111** (2013) 202001 [1308.4050].

[413] CMS collaboration, *Jet energy scale and resolution in the CMS experiment in pp collisions at 8 TeV*, *JINST* **12** (2017) P02014 [1607.03663].

[414] ATLAS collaboration, *Jet energy scale and resolution measured in proton–proton collisions at $\sqrt{s} = 13$ TeV with the ATLAS detector*, *Eur. Phys. J. C* **81** (2021) 689 [2007.02645].

[415] CMS collaboration, *Bounding the top quark width using final states with two charged leptons and two jets at* $\sqrt{s} = 13$ TeV, .

[416] ATLAS collaboration, *Direct top-quark decay width measurement in the* $t\bar{t}$ *lepton+jets channel at* $\sqrt{s}$*=8 TeV with the ATLAS experiment*, *Eur. Phys. J. C* **78** (2018) 129 [1709.04207].

[417] A. Baskakov, E. Boos and L. Dudko, *On the top-quark width measurement using a combination of resonant and non resonant cross sections.*, *EPJ Web Conf.* **158** (2017) 04007.

[418] A. Baskakov, E. Boos and L. Dudko, *Model independent top quark width measurement using a combination of resonant and nonresonant cross sections*, *Phys. Rev. D* **98** (2018) 116011 [1807.11193].

[419] A. Baskakov, E. Boos and L. Dudko, *The top quark width constrains from the single top quark production channel*, *EPJ Web Conf.* **222** (2019) 03022.

[420] C. Herwig, T. Ježo and B. Nachman, *Extracting the Top-Quark Width from Nonresonant Production*, *Phys. Rev. Lett.* **122** (2019) 231803 [1903.10519].

[421] D0 collaboration, *An Improved determination of the width of the top quark*, *Phys. Rev. D* **85** (2012) 091104 [1201.4156].

[422] CMS collaboration, *Measurement of the ratio* $\mathcal{B}(t \to Wb)/\mathcal{B}(t \to Wq)$ *in pp collisions at* $\sqrt{s} = 8$ *TeV*, *Phys. Lett. B* **736** (2014) 33 [1404.2292].

[423] ATLAS collaboration, *Search for flavour-changing neutral current top-quark decays* $t \to qZ$ *in proton-proton collisions at* $\sqrt{s} = 13$ *TeV with the ATLAS detector*, *JHEP* **07** (2018) 176 [1803.09923].

[424] CMS collaboration, *Search for associated production of a Z boson with a single top quark and for tZ flavour-changing interactions in pp collisions at* $\sqrt{s} = 8$ *TeV*, *JHEP* **07** (2017) 003 [1702.01404].

[425] CMS collaboration, *Search for flavour changing neutral currents in top quark production and decays with three-lepton final state using the data collected at sqrt(s) = 13 TeV*, .

[426] CMS collaboration, *Search for Anomalous Single Top Quark Production in Association with a Photon in pp Collisions at* $\sqrt{s} = 8$ *TeV*, *JHEP* **04** (2016) 035 [1511.03951].

[427] ATLAS collaboration, *Search for flavour-changing neutral currents in processes with one top quark and a photon using 81* fb^{-1} *of pp collisions at* $\sqrt{s} = 13$ *TeV with the ATLAS experiment*, *Phys. Lett. B* **800** (2020) 135082 [1908.08461].

[428] ATLAS collaboration, *Search for top-quark decays* $t \to Hq$ *with 36* fb^{-1} *of pp collision data at* $\sqrt{s} = 13$ *TeV with the ATLAS detector*, *JHEP* **05** (2019) 123 [1812.11568].

[429] CMS collaboration, *Search for top quark decays via Higgs-boson-mediated flavor-changing neutral currents in pp collisions at* $\sqrt{s} = 8$ *TeV*, *JHEP* **02** (2017) 079 [1610.04857].

[430] CMS collaboration, *Search for the flavor-changing neutral current interactions of the top quark and the Higgs boson which decays into a pair of b quarks at* $\sqrt{s} =$ *13 TeV*, *JHEP* **06** (2018) 102 [1712.02399].

[431] ATLAS collaboration, *Search for single top-quark production via flavour-changing neutral currents at 8 TeV with the ATLAS detector*, *Eur. Phys. J. C* **76** (2016) 55 [1509.00294].

[432] CMS collaboration, *Search for anomalous Wtb couplings and flavour-changing neutral currents in t-channel single top quark production in pp collisions at $\sqrt{s} = 7$ and 8 TeV*, *JHEP* **02** (2017) 028 [1610.03545].

[433] S. Balaji, *CP asymmetries in the rare top decays $t \to c\gamma$ and $t \to cg$*, *Phys. Rev. D* **102** (2020) 113010 [2009.03315].

[434] J. Andrea, B. Fuks and F. Maltoni, *Monotops at the LHC*, *Phys. Rev. D* **84** (2011) 074025 [1106.6199].

[435] J. F. Kamenik and J. Zupan, *Discovering Dark Matter Through Flavor Violation at the LHC*, *Phys. Rev. D* **84** (2011) 111502 [1107.0623].

[436] S. Banerjee, M. Chala and M. Spannowsky, *Top quark FCNCs in extended Higgs sectors*, *Eur. Phys. J. C* **78** (2018) 683 [1806.02836].

[437] J. Ebadi, F. Elahi, M. Khatiri and M. Mohammadi Najafabadi, *Same-sign top pair plus W production in flavor changing vector and scalar models*, *Phys. Rev. D* **98** (2018) 075012 [1806.03463].

[438] N. Castro, M. Chala, A. Peixoto and M. Ramos, *Novel flavour-changing neutral currents in the top quark sector*, *JHEP* **10** (2020) 038 [2005.09594].

[439] CMS collaboration, *Identification of heavy-flavour jets with the CMS detector in pp collisions at 13 TeV*, *JINST* **13** (2018) P05011 [1712.07158].

[440] R. Goldouzian and B. Clerbaux, *Photon initiated single top quark production via flavor-changing neutral currents at the LHC*, *Phys. Rev. D* **95** (2017) 054014 [1609.04838].

[441] ATLAS collaboration, *Search for large missing transverse momentum in association with one top-quark in proton-proton collisions at $\sqrt{s} = 13$ TeV with the ATLAS detector*, *JHEP* **05** (2019) 041 [1812.09743].

[442] ATLAS collaboration, *Search for dark matter produced in association with a single top quark in $\sqrt{s} = 13$ TeV pp collisions with the ATLAS detector*, *Eur. Phys. J. C* **81** (2021) 860 [2011.09308].

[443] CMS collaboration, *Search for dark matter produced in association with a single top quark or a top quark pair in proton-proton collisions at $\sqrt{s} = 13$ TeV*, *JHEP* **03** (2019) 141 [1901.01553].

[444] CMS collaboration, *Search for dark matter in events with energetic, hadronically decaying top quarks and missing transverse momentum at $\sqrt{s} = 13$ TeV*, *JHEP* **06** (2018) 027 [1801.08427].

[445] ATLAS collaboration, *Triggers for displaced decays of long-lived neutral particles in the ATLAS detector*, *JINST* **8** (2013) P07015 [1305.2284].

[446] N. D. Christensen and C. Duhr, *FeynRules - Feynman rules made easy*, *Comput. Phys. Commun.* **180** (2009) 1614 [0806.4194].

[447] M. Cacciari, G. P. Salam and G. Soyez, *FastJet User Manual*, *Eur. Phys. J. C* **72** (2012) 1896 [1111.6097].

[448] M. Cacciari and G. P. Salam, *Dispelling the N^3 myth for the k_t jet-finder*, *Phys. Lett. B* **641** (2006) 57 [hep-ph/0512210].

[449] DELPHES 3 collaboration, *DELPHES 3, A modular framework for fast simulation of a generic collider experiment*, *JHEP* **02** (2014) 057 [1307.6346].

[450] R. Goldouzian and B. Clerbaux, *Search for anomalous tqγ FCNC Couplings in direct single top quark production at the LHC*, in *9th International Workshop on Top Quark Physics*, 12, 2016, 1612.01795.

[451] ATLAS, CMS collaboration, *Measurements of the Higgs boson production and decay rates and constraints on its couplings from a combined ATLAS and CMS analysis of the LHC pp collision data at $\sqrt{s} = 7$ and 8 TeV*, *JHEP* **08** (2016) 045 [1606.02266].

[452] S. Y. Choi, D. J. Miller, M. M. Muhlleitner and P. M. Zerwas, *Identifying the Higgs spin and parity in decays to Z pairs*, *Phys. Lett. B* **553** (2003) 61 [hep-ph/0210077].

[453] Y. Gao, A. V. Gritsan, Z. Guo, K. Melnikov, M. Schulze and N. V. Tran, *Spin Determination of Single-Produced Resonances at Hadron Colliders*, *Phys. Rev. D* **81** (2010) 075022 [1001.3396].

[454] J. R. Dell'Aquila and C. A. Nelson, *P or CP Determination by Sequential Decays: V1 V2 Modes With Decays Into $\bar{\ell}$epton (A) $\ell(B)$ And/or $\bar{q}$ (A) $q(B)$*, *Phys. Rev. D* **33** (1986) 80.

[455] J. H. Christenson, J. W. Cronin, V. L. Fitch and R. Turlay, *Evidence for the 2π Decay of the K_2^0 Meson*, *Phys. Rev. Lett.* **13** (1964) 138.

[456] Belle collaboration, *Observation of large CP violation in the neutral B meson system*, *Phys. Rev. Lett.* **87** (2001) 091802 [hep-ex/0107061].

[457] LHCb collaboration, *Observation of CP Violation in Charm Decays*, *Phys. Rev. Lett.* **122** (2019) 211803 [1903.08726].

[458] J. F. Gunion and X.-G. He, *Determining the CP nature of a neutral Higgs boson at the LHC*, *Phys. Rev. Lett.* **76** (1996) 4468 [hep-ph/9602226].

[459] F. Boudjema, R. M. Godbole, D. Guadagnoli and K. A. Mohan, *Lab-frame observables for probing the top-Higgs interaction*, *Phys. Rev. D* **92** (2015) 015019 [1501.03157].

[460] D. Goncalves and D. Lopez-Val, *Pseudoscalar searches with dileptonic tops and jet substructure*, *Phys. Rev. D* **94** (2016) 095005 [1607.08614].

[461] S. Amor Dos Santos et al., *Probing the CP nature of the Higgs coupling in $t\bar{t}h$ events at the LHC*, *Phys. Rev. D* **96** (2017) 013004 [1704.03565].

[462] M. R. Buckley and D. Goncalves, *Boosting the Direct CP Measurement of the Higgs-Top Coupling*, *Phys. Rev. Lett.* **116** (2016) 091801 [1507.07926].

[463] C. P. Buszello, I. Fleck, P. Marquard and J. J. van der Bij, *Prospective analysis of spin- and CP-sensitive variables in H —> Z Z —> l(1)+ l(1)- l(2)+ l(2)- at the LHC*, *Eur. Phys. J. C* **32** (2004) 209 [hep-ph/0212396].

[464] R. M. Godbole, D. J. Miller and M. M. Muhlleitner, *Aspects of CP violation in the H ZZ coupling at the LHC*, *JHEP* **12** (2007) 031 [0708.0458].

[465] D. Chang, W.-Y. Keung and I. Phillips, *CP odd correlation in the decay of neutral Higgs boson into Z Z, W+ W-, or t anti-t*, *Phys. Rev. D* **48** (1993) 3225 [hep-ph/9303226].

[466] F. Ferreira, B. Fuks, V. Sanz and D. Sengupta, *Probing CP-violating Higgs and gauge-boson couplings in the Standard Model effective field theory*, *Eur. Phys. J. C* **77** (2017) 675 [1612.01808].

[467] A. De Rujula, J. Lykken, M. Pierini, C. Rogan and M. Spiropulu, *Higgs Look-Alikes at the LHC*, *Phys. Rev. D* **82** (2010) 013003 [1001.5300].

[468] S. Bolognesi, Y. Gao, A. V. Gritsan, K. Melnikov, M. Schulze, N. V. Tran et al., *On the spin and parity of a single-produced resonance at the LHC*, *Phys. Rev. D* **86** (2012) 095031 [1208.4018].

[469] P. Artoisenet et al., *A framework for Higgs characterisation*, *JHEP* **11** (2013) 043 [1306.6464].

[470] S. Berge and W. Bernreuther, *Determining the CP parity of Higgs bosons at the LHC in the tau to 1-prong decay channels*, *Phys. Lett. B* **671** (2009) 470 [0812.1910].

[471] R. Harnik, A. Martin, T. Okui, R. Primulando and F. Yu, *Measuring CP Violation in $h \to \tau^+\tau^-$ at Colliders*, *Phys. Rev. D* **88** (2013) 076009 [1308.1094].

[472] S. Berge, W. Bernreuther and S. Kirchner, *Prospects of constraining the Higgs boson's CP nature in the tau decay channel at the LHC*, *Phys. Rev. D* **92** (2015) 096012 [1510.03850].

[473] A. Bhardwaj, P. Konar, P. Sharma and A. K. Swain, *Exploring CP phase in τ-lepton Yukawa coupling in Higgs decays at the LHC*, *J. Phys. G* **46** (2019) 105001 [1612.01417].

[474] K. Lasocha, E. Richter-Was, M. Sadowski and Z. Was, *Deep neural network application: Higgs boson CP state mixing angle in $H \to \tau\tau$ decay and at the LHC*, *Phys. Rev. D* **103** (2021) 036003 [2001.00455].

[475] A. K. Swain, *M_{T2} as a probe of CP phase in $h \to \tau\tau$ at the LHC*, 2008.11127.

[476] S. L. Glashow and S. Weinberg, *Natural Conservation Laws for Neutral Currents*, *Phys. Rev. D* **15** (1977) 1958.

[477] E. A. Paschos, *Diagonal Neutral Currents*, *Phys. Rev. D* **15** (1977) 1966.

[478] G. C. Branco, P. M. Ferreira, L. Lavoura, M. N. Rebelo, M. Sher and J. P. Silva, *Theory and phenomenology of two-Higgs-doublet models*, *Phys. Rept.* **516** (2012) 1 [1106.0034].

[479] I. F. Ginzburg and M. Krawczyk, *Symmetries of two Higgs doublet model and CP violation*, *Phys. Rev. D* **72** (2005) 115013 [hep-ph/0408011].

[480] D. Fontes, M. Mühlleitner, J. C. Romão, R. Santos, J. a. P. Silva and J. Wittbrodt, *The C2HDM revisited*, *JHEP* **02** (2018) 073 [1711.09419].

[481] W. Porod, *SPheno, a program for calculating supersymmetric spectra, SUSY particle decays and SUSY particle production at e+ e- colliders*, *Comput. Phys. Commun.* **153** (2003) 275 [hep-ph/0301101].

[482] W. Porod and F. Staub, *SPheno 3.1: Extensions including flavour, CP-phases and models beyond the MSSM*, *Comput. Phys. Commun.* **183** (2012) 2458 [1104.1573].

[483] A. Arhrib, E. Christova, H. Eberl and E. Ginina, *CP violation in charged Higgs production and decays in the Complex Two Higgs Doublet Model*, *JHEP* **04** (2011) 089 [1011.6560].

[484] M. Baak, M. Goebel, J. Haller, A. Hoecker, D. Ludwig, K. Moenig et al., *Updated Status of the Global Electroweak Fit and Constraints on New Physics*, *Eur. Phys. J. C* **72** (2012) 2003 [1107.0975].

[485] M. Baak, M. Goebel, J. Haller, A. Hoecker, D. Kennedy, R. Kogler et al., *The Electroweak Fit of the Standard Model after the Discovery of a New Boson at the LHC*, *Eur. Phys. J. C* **72** (2012) 2205 [1209.2716].

[486] W. Porod, F. Staub and A. Vicente, *A Flavor Kit for BSM models*, *Eur. Phys. J. C* **74** (2014) 2992 [1405.1434].

[487] M. Misiak and M. Steinhauser, *Weak radiative decays of the B meson and bounds on $M_{H^\pm}$ in the Two-Higgs-Doublet Model*, *Eur. Phys. J. C* **77** (2017) 201 [1702.04571].

[488] T. Enomoto and R. Watanabe, *Flavor constraints on the Two Higgs Doublet Models of Z_2 symmetric and aligned types*, *JHEP* **05** (2016) 002 [1511.05066].

[489] P. Bechtle, O. Brein, S. Heinemeyer, O. Stål, T. Stefaniak, G. Weiglein et al., HiggsBounds – 4*: Improved Tests of Extended Higgs Sectors against Exclusion Bounds from LEP, the Tevatron and the LHC*, *Eur. Phys. J. C* **74** (2014) 2693 [1311.0055].

[490] P. Bechtle, S. Heinemeyer, O. Stål, T. Stefaniak and G. Weiglein, *HiggsSignals: Confronting arbitrary Higgs sectors with measurements at the Tevatron and the LHC*, *Eur. Phys. J. C* **74** (2014) 2711 [1305.1933].

[491] CMS collaboration, *Combined measurements of the Higgs boson's couplings at $\sqrt{s} = 13$ TeV*, .

[492] ATLAS collaboration, *Combined measurements of Higgs boson production and decay using up to 80 fb^{-1} of proton–proton collision data at $\sqrt{s} = 13$ TeV collected with the ATLAS experiment*, .

[493] T. Abe, J. Hisano, T. Kitahara and K. Tobioka, *Gauge invariant Barr-Zee type contributions to fermionic EDMs in the two-Higgs doublet models*, *JHEP* **01** (2014) 106 [1311.4704].

[494] E. J. Chun, J. Kim and T. Mondal, *Electron EDM and Muon anomalous magnetic moment in Two-Higgs-Doublet Models*, *JHEP* **12** (2019) 068 [1906.00612].

[495] W. Altmannshofer, S. Gori, N. Hamer and H. H. Patel, *Electron EDM in the complex two-Higgs doublet model*, *Phys. Rev. D* **102** (2020) 115042 [2009.01258].

[496] D. Egana-Ugrinovic and S. Thomas, *Higgs Boson Contributions to the Electron Electric Dipole Moment*, 1810.08631.

[497] ACME collaboration, *Improved limit on the electric dipole moment of the electron*, *Nature* **562** (2018) 355.

[498] K. Cheung, A. Jueid, Y.-N. Mao and S. Moretti, *Two-Higgs-doublet model with soft CP violation confronting electric dipole moments and colliders*, *Phys. Rev. D* **102** (2020) 075029 [2003.04178].

[499] ALEPH collaboration, *Branching ratios and spectral functions of tau decays: Final ALEPH measurements and physics implications*, *Phys. Rept.* **421** (2005) 191 [hep-ex/0506072].

[500] A. Belyaev, N. D. Christensen and A. Pukhov, *CalcHEP 3.4 for collider physics within and beyond the Standard Model*, *Comput. Phys. Commun.* **184** (2013) 1729 [1207.6082].

[501] ATLAS collaboration, *Evidence for the Higgs-boson Yukawa coupling to tau leptons with the ATLAS detector*, *JHEP* **04** (2015) 117 [1501.04943].

[502] CMS collaboration, *Analysis of the CP structure of the Yukawa coupling between the Higgs boson and τ leptons in proton-proton collisions at $\sqrt{s} = 13$ TeV*, .

[503] G. Bagliesi, *Tau tagging at Atlas and CMS*, in *17th Symposium on Hadron Collider Physics 2006 (HCP 2006)*, 7, 2007, 0707.0928.

[504] A. Hocker et al., *TMVA - Toolkit for Multivariate Data Analysis*, physics/0703039.

[505] ATLAS collaboration, *Study of the spin and parity of the Higgs boson in diboson decays with the ATLAS detector*, *Eur. Phys. J. C* **75** (2015) 476 [1506.05669].

[506] CMS collaboration, *Combined search for anomalous pseudoscalar HVV couplings in VH($H \to b\bar{b}$) production and $H \to VV$ decay*, *Phys. Lett. B* **759** (2016) 672 [1602.04305].

[507] V. Shtabovenko, R. Mertig and F. Orellana, *FeynCalc 9.3: New features and improvements*, *Comput. Phys. Commun.* **256** (2020) 107478 [2001.04407].

[508] H. H. Patel, *Package-X: A Mathematica package for the analytic calculation of one-loop integrals*, *Comput. Phys. Commun.* **197** (2015) 276 [1503.01469].

[509] W. Bernreuther, P. Gonzalez and M. Wiebusch, *Pseudoscalar Higgs Boson Decays into W and Z Bosons Revisited*, 0909.3772.

[510] A. Hammad, S. Khalil and S. Moretti, *LHC signals of a B-L supersymmetric standard model CP -even Higgs boson*, *Phys. Rev. D* **93** (2016) 115035 [1601.07934].

[511] ATLAS collaboration, *Search for the $HH \to b\bar{b}b\bar{b}$ process via vector-boson fusion production using proton-proton collisions at $\sqrt{s} = 13$ TeV with the ATLAS detector*, *JHEP* **07** (2020) 108 [2001.05178].

[512] ATLAS collaboration, *Search for heavy Higgs bosons decaying into two tau leptons with the ATLAS detector using pp collisions at $\sqrt{s} = 13$ TeV*, *Phys. Rev. Lett.* **125** (2020) 051801 [2002.12223].

[513] CMS collaboration, *Search for heavy resonances decaying to tau lepton pairs in proton-proton collisions at $\sqrt{s} = 13$ TeV*, *JHEP* **02** (2017) 048 [1611.06594].

[514] ATLAS collaboration, *Search for resonances decaying into photon pairs in 139 fb^{-1} of pp collisions at $\sqrt{s}$=13 TeV with the ATLAS detector*, *Phys. Lett. B* **822** (2021) 136651 [2102.13405].

[515] ATLAS collaboration, *Search for heavy diboson resonances in semileptonic final states in pp collisions at $\sqrt{s} = 13$ TeV with the ATLAS detector*, *Eur. Phys. J. C* **80** (2020) 1165 [2004.14636].

[516] ATLAS collaboration, *Search for heavy resonances decaying into a pair of Z bosons in the $\ell^+\ell^-\ell'^+\ell'^-$ and $\ell^+\ell^-\nu\bar{\nu}$ final states using 139* fb^{-1} *of proton–proton collisions at $\sqrt{s} = 13$ TeV with the ATLAS detector*, *Eur. Phys. J. C* **81** (2021) 332 [2009.14791].

[517] ATLAS collaboration, *Search for heavy ZZ resonances in the $\ell^+\ell^-\ell^+\ell^-$ and $\ell^+\ell^-\nu\bar{\nu}$ final states using proton–proton collisions at $\sqrt{s} = 13$ TeV with the ATLAS detector*, *Eur. Phys. J. C* **78** (2018) 293 [1712.06386].

[518] ATLAS collaboration, *Search for a heavy Higgs boson decaying into a Z boson and another heavy Higgs boson in the $\ell\ell bb$ and $\ell\ell WW$ final states in pp collisions at $\sqrt{s} = 13$ TeV with the ATLAS detector*, *Eur. Phys. J. C* **81** (2021) 396 [2011.05639].

[519] W. Abdallah, S. Khalil and S. Moretti, *Double Higgs peak in the minimal SUSY B-L model*, *Phys. Rev. D* **91** (2015) 014001 [1409.7837].

[520] S. Buddenbrock, A. S. Cornell, Y. Fang, A. Fadol Mohammed, M. Kumar, B. Mellado et al., *The emergence of multi-lepton anomalies at the LHC and their compatibility with new physics at the EW scale*, *JHEP* **10** (2019) 157 [1901.05300].

[521] CMS collaboration, *Search for new resonances in the diphoton final state in the mass range between 70 and 110 GeV in pp collisions at $\sqrt{s} = 8$ and 13 TeV*, .

[522] P. J. Fox and N. Weiner, *Light Signals from a Lighter Higgs*, *JHEP* **08** (2018) 025 [1710.07649].

[523] U. Haisch and A. Malinauskas, *Let there be light from a second light Higgs doublet*, *JHEP* **03** (2018) 135 [1712.06599].

[524] T. Biekötter, M. Chakraborti and S. Heinemeyer, *The "96 GeV excess" at the LHC*, *Int. J. Mod. Phys. A* **36** (2021) 2142018 [2003.05422].

[525] CMS collaboration, *Measurements of properties of the Higgs boson in the four-lepton final state at $\sqrt{s} = 13$ TeV*, .

[526] CMS collaboration, *Measurements of properties of the Higgs boson decaying into four leptons in pp collisions at sqrts = 13 TeV*, .

[527] M. Consoli and L. Cosmai, *Experimental signals for a second resonance of the Higgs field*, 2111.08962.

[528] F. Richard, *Indications for extra scalars at LHC? – BSM physics at future e^+e^- colliders*, 2001.04770.

[529] P. Cea, *Evidence of the true Higgs boson H_T at the LHC Run 2*, *Mod. Phys. Lett. A* **34** (2019) 1950137 [1806.04529].

[530] F. Richard, *Global interpretation of LHC indications within the Georgi-Machacek Higgs model Talk presented at the International Workshop on Future Linear Colliders (LCWS2021), 15-18 March 2021. C21-03-15.1*, in *International Workshop on Future Linear Colliders*, 3, 2021, 2103.12639.

[531] CMS collaboration, *Search for a new scalar resonance decaying to a pair of Z bosons in proton-proton collisions at $\sqrt{s} = 13$ TeV*, *JHEP* **06** (2018) 127 [1804.01939].

[532] CMS collaboration, *Measurement of differential $t\bar{t}$ production cross sections in the full kinematic range using lepton+jets events from proton-proton collisions at $\sqrt{s} = 13$ TeV*, *Phys. Rev. D* **104** (2021) 092013 [2108.02803].

[533] N. Darvishi and M. R. Masouminia, *Signature of the Maximally Symmetric 2HDM via $W^\pm/Z$-Quadruplet Productions at the LHC*, *Phys. Rev. D* **103** (2021) 095031 [2012.14746].